Irregular aluminium foam and phase change material composite in transient thermal management

A thesis submitted to Newcastle University for the Degree of Doctor of Philosophy in Chemical Engineering

By

AHMAD FADHLAN BIN MUSTAFFAR

School of Chemical Engineering and Advanced Materials

Newcastle University

June 2016

CONFIDENTIAL

Abstract

Traction systems generate high loads of waste heat, which need to be removed for efficient operations. A new transient heat sink is proposed, which is based on salt hydrate phase change material (PCM). The heat sink would absorb heat during the short stationary phase i.e. at stations in which the PCM melts, a process accelerated by aluminium foam as it increases the rate of heat transfer within the PCM. When the train moves, the PCM is solidified via a forced convection stack. This creates a passive and efficient thermal solution, especially once heat pipe is employed as heat conduit.

At the outset, the characteristics of the foam needed to be accurately determined. The foam was uncommon as its pore morphology was irregular, therefore it was scanned in a medical computed tomography (CT) scanner, which allowed for the construction of a three dimensional (3D) model. The model accuracy was enhanced by software, resulting in an extremely useful analytical tool. The model enabled important structural parameters to be measured e.g. porosity and specific surface area, which were crucial for the subsequent thermal and fluid flow analyses. A defect dense region was also detected, the effect of which was further investigated. Interestingly in the volume devoid of this defect, the porosity and specific surface area were uniform.

A test rig was constructed that mimicked liquid cooling (or in the planned application, heat pipe cooling) in power electronics. At the core was a heat sink of salt hydrate PCM, impregnated within the foam. The sink with its current specifications (with liquid cooling) was able to absorb a thermal load consistent from a group of 4-5 IGBTs, which dissipated a low power of 20W per module during stops. The heating period of 1600-3500s per cycle meant the sink could be fitted to intercity locomotives. The foam increased the effective thermal conductivity by a factor of 24, from 0.45 to 10.83 W/m.K. 3D volume averaged numerical simulation was validated by experiment, which could be used to facilitate scale up or redesign for further optimization.

As well as a support structure for the storage component of the system, the foam could replace conventional fins in forced convection, adding value to the potential manufacturer of the system. Heat transfer coefficient calculation incorporated the actual surface area that was derived from the 3D model, a first for metal foam studies. Results have shown a good Nu/Re correlation, comparable with other metal foam works.

Keywords: Transient heat sink; irregular metal foam; thermal energy storage; phase change material; computed tomography (CT); effective thermal conductivity; numerical simulation; steady state cooling

Acknowledgement

To my hero, Hillary Clinton

Table of Contents

List of Figures

List of Tables

Nomenclature

Abbreviations

2D/3D	Two/three-dimensional	
A,B,C	Reactant A, products B, C (in thermochemical storage)	
BET	Brunauer–Emmett–Teller	
BP	Boomsba and Poulikakos model	
CFD	Computational fluid dynamics	
CSP	Concentrated solar power	
CT	Computed tomography	
μCT	Microtomography	
DICOM	Digital Imaging and Communications in Medicine	
DSC	Differential scanning calorimetry	
EGW	Ethylene glycol-water mixture	
EP	Enthalpy porosity	
FE	Finite element	
GTO	Gate turn-off thyristor	
IGBT	Insulated gate bipolar transistor	
IGCT	Integrated gate-commutated thyristor	
LMTD	Log mean temperature difference	(K)
LPM	Litre per minute	(L/min)
MOSFET	Metal-oxide-semiconductor field effect transistor	
MRI	Magnetic resonance image	
OEM	Original equipment manufacturer	
PCM	Phase change material	
PPI	Pore per inch (pore density)	
ROI	Regions of interest	
RSQ	Root mean square (R^2)	
SSA	Specific surface area	(m^2/m^3)
S46	Salt hydrate '46' phase change material	
TC	Thermocouple	
TCR	Thermal contact resistance	(K/W)
TES	Thermal energy storage	
UDF	User-defined functions	
VOF	Volume of fluid	

Nomenclature

a	Permeability	(m^2)	
A	Surface area	(m^2)	
A	Cross-sectional area	(m^2)	for Chapter 5
A_c	Cross-sectional area	(m^2)	for Chapter 6
C	Form drag coefficient	(m^{-1})	
C	Mush coefficient	(kg/m^3s)	for Chapter 5
Cp	Specific heat	(J/kgK)	
D	Diameter	(m)	
d	Size, diameter	(m)	for Chapter 5
dT	Differential temperature	(°C)	
E	Percentage error	(%)	
g	Gravitational acceleration	(m/s^2)	
G	Specific air velocity	(kg/m^2s)	
h	Height of fluid	(mm)	
h	Sensible enthalpy	(J/kgK)	for Chapter 5
h	Convective coefficient	(W/m^2K)	for Chapter 6
$\bar{h}$	Mean heat transfer coefficient	(W/m^2K)	
H	Foam height	(m)	
H	Latent enthalpy	(J/kg)	for Chapter 5

I	X-ray beam intensity through scanned object	(keV)	
l	Characteristic length	(m)	for Chapter 4,5
I	Inertial coefficient		for Chapter 5
I_o	X-ray source beam intensity	(keV)	
k	Thermal conductivity	(W/mK)	
K	Thermal conductivity	(W/mK)	for Chapter 4
K	Permeability	(m^2)	
L	Length	(mm or m)	
L	Latent heat	(J/kg)	for Chapter 4,5
L_c	Corrected length	(m)	
L_{min}	Minimum entrance length	(m)	
m	Mass	(kg)	
m	Mass flow rate	(kg/s)	for Chapter 6
Nu	Nusselt number		
p	Pressure	(Pa, N/m^2)	
P	Pressure	(Pa, N/m^2)	for Chapter 6
q	Thermal energy	(W, J/s)	for Chapter 5
Q	Thermal energy	(W, J/s)	
r	Radius	(mm)	
Re	Reynolds number		
s	Length of strut curve	(m)	
S	Source term		
t	Thickness of the scanned object	(mm)	
t	Time	(s)	for Chapter 4
$\bar{t}$	Mean temperature	(K or °C)	
T	Temperature	(K or °C)	
u	fluid velocity	(m/s)	
U	Heat transfer coefficient	(W/m^{2}K)	
U_{LOSS}	heat loss coefficient	(W/m^{2}K)	
v	Velocity	(m/s)	
V	Volume	(L or m^3)	
V	Darcian velocity	(m/s)	for Chapter 6
$\dot{V}$	Volumetric flow rate	(m^3/s)	
W	Width of container	(mm)	
Δh	Specific enthalpy (latent heat)	(J/kg)	
ΔH	Enthalpy differential	(J)	
ΔHR	Chemical reaction enthalpy	(J/mol)	
ΔP	Pressure drop	(Pa, N/m^2)	
ΔT	Temperature differential	(K or °C)	

Subscript

0	Reference	
air,in	Inlet air	
a	Ambient	
a	Air	for Chapter 6
actual	Actual impregnation	
AL	Aluminium	
avg	Average	
b	Bulk	
base	Foam base cross-section	
comp	Composite	
DL	Data logger	
e	Ending	
eff	Effective	
f/fluid	Fluid phase (PCM or air)	

f	Foam strut		for Chapter 5
h	Hydraulic		
HC	Heater circulator		
i	Initial/starting		
i,j	Vector denoting x,y, and z-axis, respectively		for Chapter 5
ideal	Ideal impregnation		
in	Inlet		
l	liquid phase, liquidus		
-L	Liquid phase		
LOSS	Heat loss		
out	Outlet		
p	Pore		
PCM	Phase change material		
R	Random error		
ref	Reference		
s/solid	Solid phase, solidus		
-S	Solid phase, solidus		for Chapter 4
S	Systematic error		
t	time	(s)	
T	Total		
TC	Thermocouple		
w	Wall (of foam struts)		
w	Water-side		for Chapter 6
W	Water		
W	Wall		for Chapter 5
v	Voidage		
x	Local		

Greek symbols

α	Impregnation ratio	(-)	
β	Liquid fraction		
ϵ	Volumetric porosity	(fraction or %)	
η	Efficiency	(%)	
ρ	Density	(kg/m3)	
τ	Tortuosity	(-)	
μ	Dynamic viscosity	(kg/ms or Pas)	
μ	Linear attenuation coefficient	(mm^{-1})	for Chapter 3
Υ	Fluid expansion factor	(K^{-1})	
ω	Small constant value		
∞	Ambient		

Chapter 1   Introduction

1.1   Research background

Thermacore Ltd. exhibited great interest in expanding their thermal management solutions especially in traction systems. Power electronics, which condition the locomotives and associated rolling stock, release high heat loads that must be removed for efficient operation. Current cooling and energy recovery technologies on offer include custom-built passive heat pipe/vapour chamber assemblies, and liquid cold plates.

Trains stop periodically at stations for short periods of time. During this stage, cooling can be done passively through a thermal energy storage technology called latent heat storage. Phase change material (PCM) forms the core of this heat sink, which recovers heat while melting. This isothermal, high load heat recovery is accelerated by locating the PCM within a conductivity-enhancing metal foam as PCMs are generally low in thermal conductivity. Once the train departs from its stationary phase, the melted PCM will be solidified through forced convection. This would be aided by heat pipes as they remove heat from the PCM/foam block as the train moves, and the heat sink will be reusable at the next stop. This melt/freeze cycle provides a simple, efficient, and passive transient thermal solution. Figure 1-1 illustrates the idea.
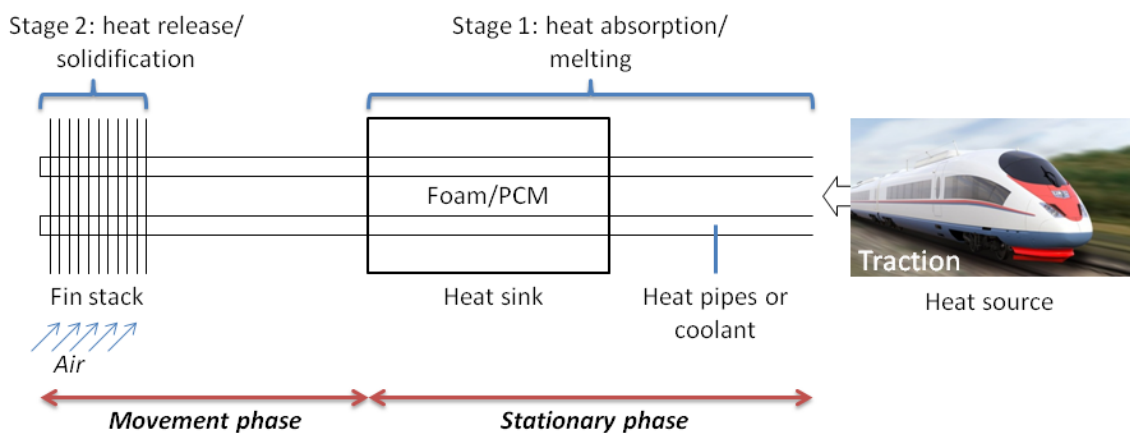
Figure 1-1 The development of a transient heat sink based on phase change material enhanced by metal foam.

1.2 Traction systems during the stationary phase

The following Table 1-1 lists the power dissipation, operating conditions, and stopping period for traction types (i.e. commuter, metro, intercity, long distance, and common trains) during the stationary phase. These data were gathered from various sources. Many of current systems employ pumped liquid cooling through cold plates or heat exchangers [2], especially in cooling high heat loads during the movement phase (close to 2 – 2.5 kW per IGBT module [2, 3]). Passive cooling system by using thermosiphon has been investigated by Perpina *et* al. [3]. Weng *et* al. [4] investigated heat pipe combined with PCM (pure eicosane) for electronics cooling, although not dedicated for IGBT in traction. Gernert, 2009 [5] from Thermacore in the USA, proved that cooling a group of six IGBT modules, which produced a total of 6kW power dissipation (during full operation) by using heat pipe/heat sink technology, performed better than an extruded aluminium heat sink.

Table 1-1 The data on power dissipation, operating conditions, and stopping period during the traction stationary phase.

	Value	Traction type	Reference
Total load (power dissipation) per IGBT module	20W*	Commuter/ common trains	[3]
	~ a few Watts	Trains equipped with high efficiency (98%) IGBT modules	[6]
Operating temperature	70 - 85°C (within 60 seconds)	Metro trains	[7]
	60°C	Common trains	[2]
Coolant flow rate	50 LPM		
Stopping period	~ 60 seconds	Metro trains	[3, 7]
	200 – 3000 seconds	Intercity trains	
	~ 1 hour or more	Long distance trains	

*For trains travelling at modest speeds of up to 70 km/h, the power dissipation peaks at ~2 to 2.5 kW/IGBT module, but drops to 20W/IGBT module at the station.

None of the works were dedicated toward the stationary phase cooling. As explained in Perpina *et* al. [3], the load per IGBT during this phase could drop to 20W per IGBT module. As explained in Figure 1-1, this project aims to supplement the current liquid cooling systems with phase change material to be used during the stationary phase, with

prospective use of heat pipe to create a fully passive cooling system. As a preliminary assessment, a heat sink with 165 x 116 x 54 mm dimensions, fully filled with salt hydrate S46 PCM, would provide a thermal capacity of 345 kJ or 0.096 kWh (based on latent heat only - the PCM thermophysical data are available in the following Chapter 2, Table 2-4), enough to cool a group of 4-5 IGBTs rated at 20W for a duration of 1 hour of stopping time (for intercity trains). If the train was stopping for much shorter periods, as is the norm, the storage demand would be much less.

Because PCM is generally slow in the energy charge/discharge process due to the low thermal conductivity (for the S46 PCM: 0.45 W/m.K), aluminium foam is to be embedded in the PCM to increase the process times. If 30% of the sink is occupied by the aluminium phase (i.e. 70% porosity foam), the thermal capacity of the sink is now 270 kJ or 0.075 kWh (latent heat only for the PCM and sensible heat for the aluminium foam with 40 K temperature lift – from ambient (20°C) to the maximum operating temperature (60°C)). With the aluminium foam, the heat sink is able to cool 3-4 IGBTs within an hour of train stopping time, but with an assurance that the process could be completed within this time period. This theory has to be tested through experimental work, and modelled for further scaling-up. Table 1-2 below summarizes the PCM heat sink thermal capacity as discussed. Although not investigated here, foams are rigid and act as structural members, lending strength to a PCM container, particularly if the foam is attached to the container walls – (also aiding conduction).

Table 1-2 Thermal capacity of transient heat sink based on PCM (latent heat only).
Note: 1) Sink dimension: 164 x 116 x 54 mm, 2) PCM: salt hydrate S46.

	In kJ	In kWh
Pure PCM	345	0.096
PCM plus aluminium foam* with 70% porosity.	270	0.075

*The contribution of the aluminium foam to the thermal capacity involved the sensible heat uptake by the aluminium (temperature lift of 40K).

The characterization of the transient cooling system based on the PCM/aluminium foam is an important research topic and therefore, it was investigated in this project.

1.3 Energy storage basics

Energy can be stored in many forms as shown in Figure 1-2. The concept has spurred research for decades and this will continue well into the future. Currently, lithium ion batteries and fuel cells are terms not unheard of. Often, the energy that needs to be stored is thermal energy, which may come from the sun (captured via a solar collector) or, for example, from an exothermic chemical reaction in a reactor. It is much more efficient to store it directly as thermal energy instead of converting it to and from other energy forms e.g. mechanical energy. The energy density, which determines the compactness of an energy store, is a prime motivation for research. For thermal stores, PCMs provide a compact solution compared to traditional methods.
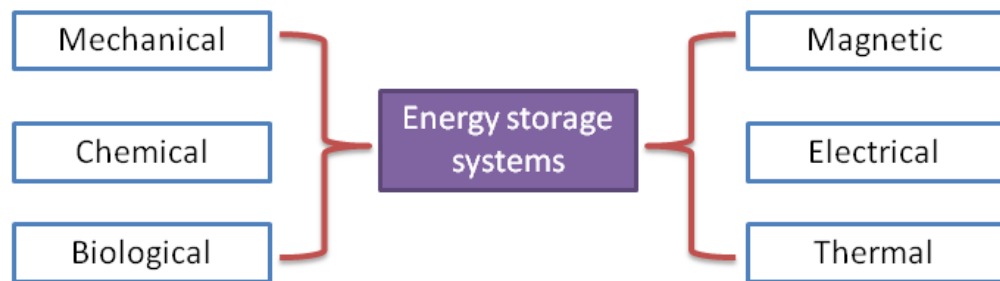
Figure 1-2 The many forms of energy storage.

1.4 The irregular metal foam

The metal foam supplied by Thermacore Europe Ltd. was unique if one compares it with common metal foams (Figure 1-3). A novel manufacturing process resulted in irregularity in its pore morphology. Analysis-wise, it was challenging as it defied any established theoretical/empirical models. These models enable the derivation of structural properties, especially porosity and surface area that are crucial for analyses. A new characterization method therefore must be devised that will be non-intrusive, as the foam prototype was to be returned to Thermacore Ltd. intact.

The research project was designed from the ground up: the foam was first characterized non-invasively. After this stage was completed, analyses on thermal and fluid flow performance were carried out. The foam prototype had to be kept intact, throughout the research programme.
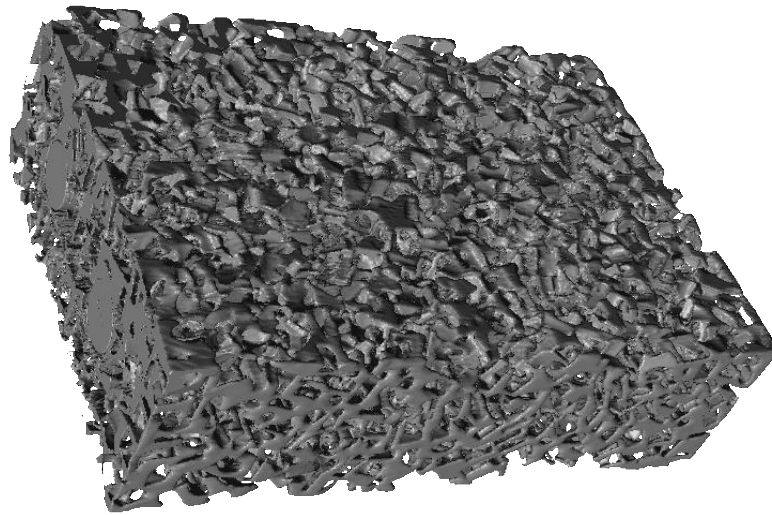
Figure 1-3 The irregular aluminium foam. "Irregularity" refers to its pore morphology.

1.5 Research objectives

The research project was planned to address five major objectives, which are tabulated below.

No	Description	Location
1	A state-of-the-art literature survey was carried out on thermal storage technologies, phase change materials, enhancement techniques, thermal and fluid flow simulation methods, metal foam characterization processes, and tests on metal foam as a forced convection heat sink in steady state cooling operation.	*Chapter 2*
2	The irregular foam prototype was scanned via a medical computed tomography (CT) scanner. This allowed the development of a three dimensional (3D) model, the accuracy of which was enhanced by software. The model was used to measure several parameters, e.g. porosity and specific surface area, that were important for subsequent chapters.	*Chapter 3*
3	A test rig was constructed, the operations of which aimed to mimic liquid cooling in power electronics. At the core was a heat sink of	*Chapter 4*

salt hydrate PCM, impregnated within the foam. Thermal analyses allowed 3D computer simulation of the melting process.

4   By using the model developed from the CT scan, an homogenization   ***Chapter 5***
analysis was carried out to assist the PCM melting simulation, which utilized the volume average method. The numerical results were validated with experimental profiles obtained from the previous chapter.

5   The foam prototype was subsequently tested in a forced convection   ***Chapter 6***
cooling mode, which allowed the characterization of steady state thermal and flow properties i.e. heat transfer coefficient and pressure drop. The surface area data obtained from the CT scan model allowed for the calculation of accurate values. It was envisaged to replace finned heat stacks, which would add value to Thermacore Ltd. technologies.

1.6   Thesis structure

This thesis is presented as a series of closely linked Chapters written by the candidate, Ahmad Mustaffar, under the supervision of Professors Adam Harvey and David Reay. Contributors to the thesis included Dr. Ross Maxwell for Chapter 3 and Professor Chris Underwood for Chapter 4. All experimental work was conducted by the candidate with some assistance from Prof. Reay and the lab technician, Brian Grover, during the PCM impregnation process.

Conclusions are presented in Chapter 7. The following Figure 1-4 visualizes how the major chapters are linked to each other.
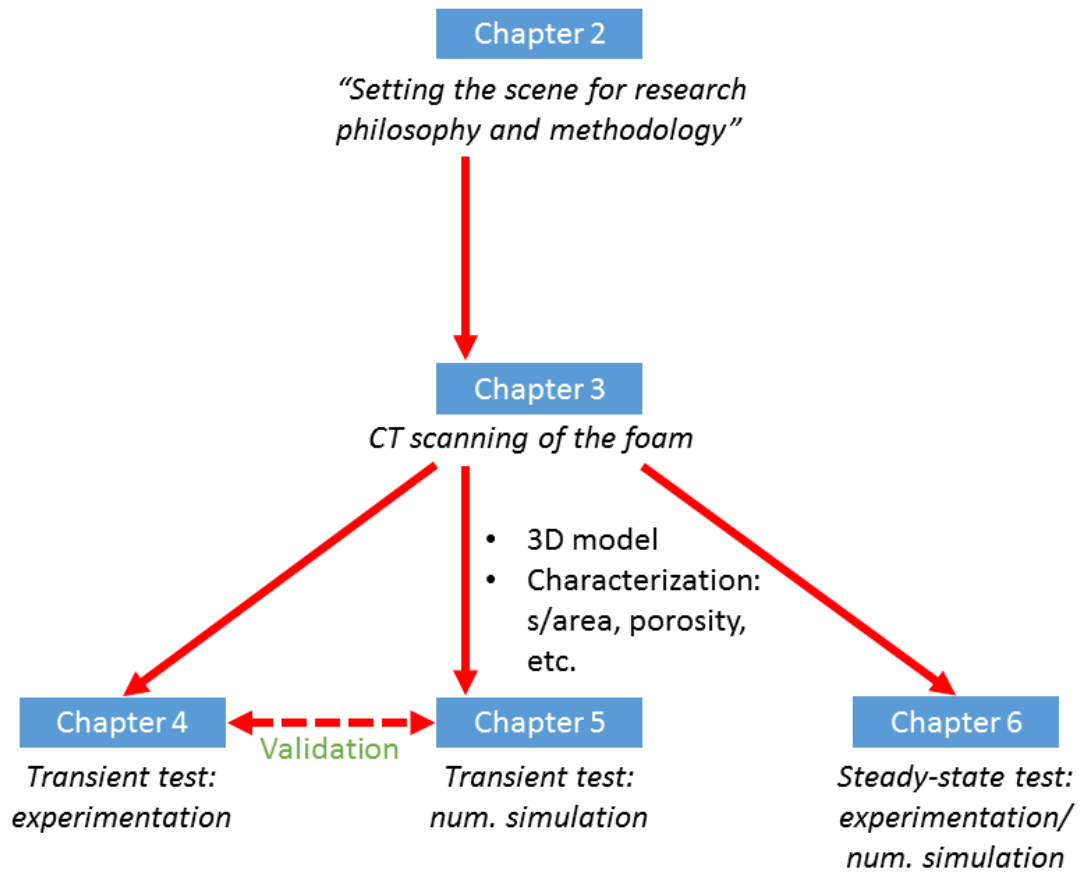
Figure 1-4 How major technical chapters are linked to each other.

Chapter 2   Literature survey

2.1   Abstract

The advent of thermal energy storage is due to the fact that it can fundamentally solve the energy demand and mismatch issue, which is one hurdle in renewable energy implementations. Energy density motivates the advancement of latent and thermochemical storage, the latter being in the earliest developmental stage. Phase change materials (PCMs), which provide isothermal latent heat storage have been well researched with extensive availability of their thermophysical data. Its common issue of low thermal conductivity can be mitigated by innovative enhancement techniques, one of these being to impregnate metal foam with a PCM. Metal foams are generally attractive due to their light weight, high specific surface area, and random/extensive solid network. Metal foam has also been identified as being a promising replacement for finned heat sinks in part due to its enhanced air mixing capability, tortuosity, and thermal dispersion. Recent advancements in computed tomography (CT) scanning enable the creation of realistic foam models, which can be used for accurate measurement of its structural and mechanical characteristics with further manipulations for micro-scale heat and flow simulations. For practical purposes, volume average simulation of the PCM phase change process in metal foam is preferred over the pore scale approach to enable a full-scale melting simulation within the means of available computational resources. Implementing metal foam in heat transfer applications depends on economic and technical considerations. A lingering issue of foam's uncompetitive cost can lead to the examination of alternatives, one being the use of metal mesh for PCM applications as it is more common, cheaper, and flexible but prospectively offering similar benefits to metal foam [8].

Keywords: Thermal energy storage; phase change material; metal foam; computed tomography; numerical simulation; heat sink; metal mesh

2.2 Introduction

Chapter 1 has already discussed the many forms of energy storage. Thermal energy storage (TES) forms the core of this project. To easily visualize one of the benefits of TES, an application is shown in Figure 2-1. During the intermittency of solar radiation at night time, the steam turbine in the concentrated solar thermal power (CSP) plant uses steam generated by the heat in the TES (in this example, molten salts, based upon sensible heat storage), enabling a round-the-clock electrical supply. TES therefore provides reliable zero carbon electricity as an alternative to coal or nuclear plants. Already a 200MW CSP plant integrated with TES is being built in Arizona [9].
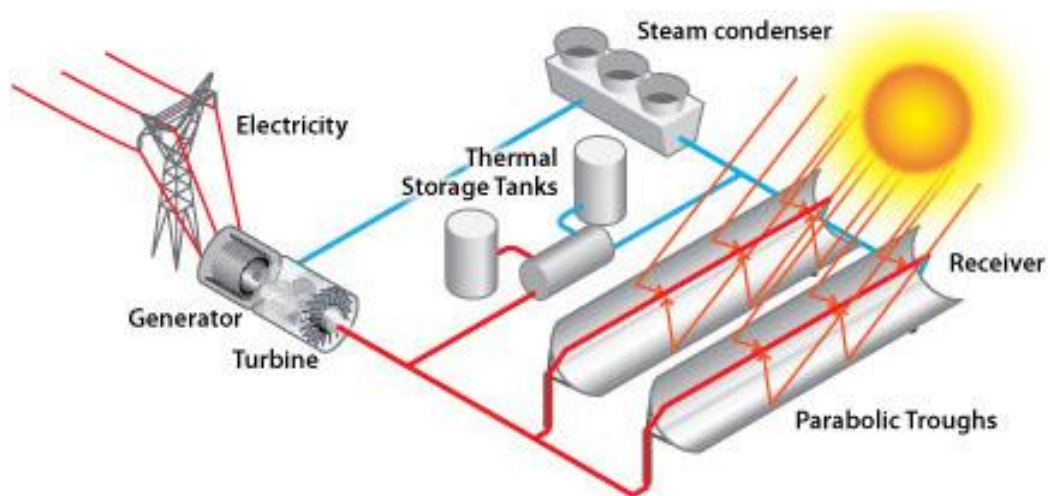
Figure 2-1 A concentrated solar power plant with an integrated TES component [9].

The previous example illustrates one of the many TES potentials. The applications are wide ranging with a huge spectrum of benefits. The literature survey presented in this chapter attempts to introduce the reader to the technology holistically, but concisely. To achieve this, a survey scope provides the boundary of discussion (Figure 2-2). In essence, this survey involves five sections:

1. An overview of thermal energy storage methods.
2. Latent heat storage: material and heat exchanger analyses.
3. Phase change material/metal foam composite.
4. Metal foam as a steady state heat sink.
5. The future prospects for, and barriers to phase change material and metal foams.

A state-of-the-art review in each section/subsection is followed by discussion and analysis.
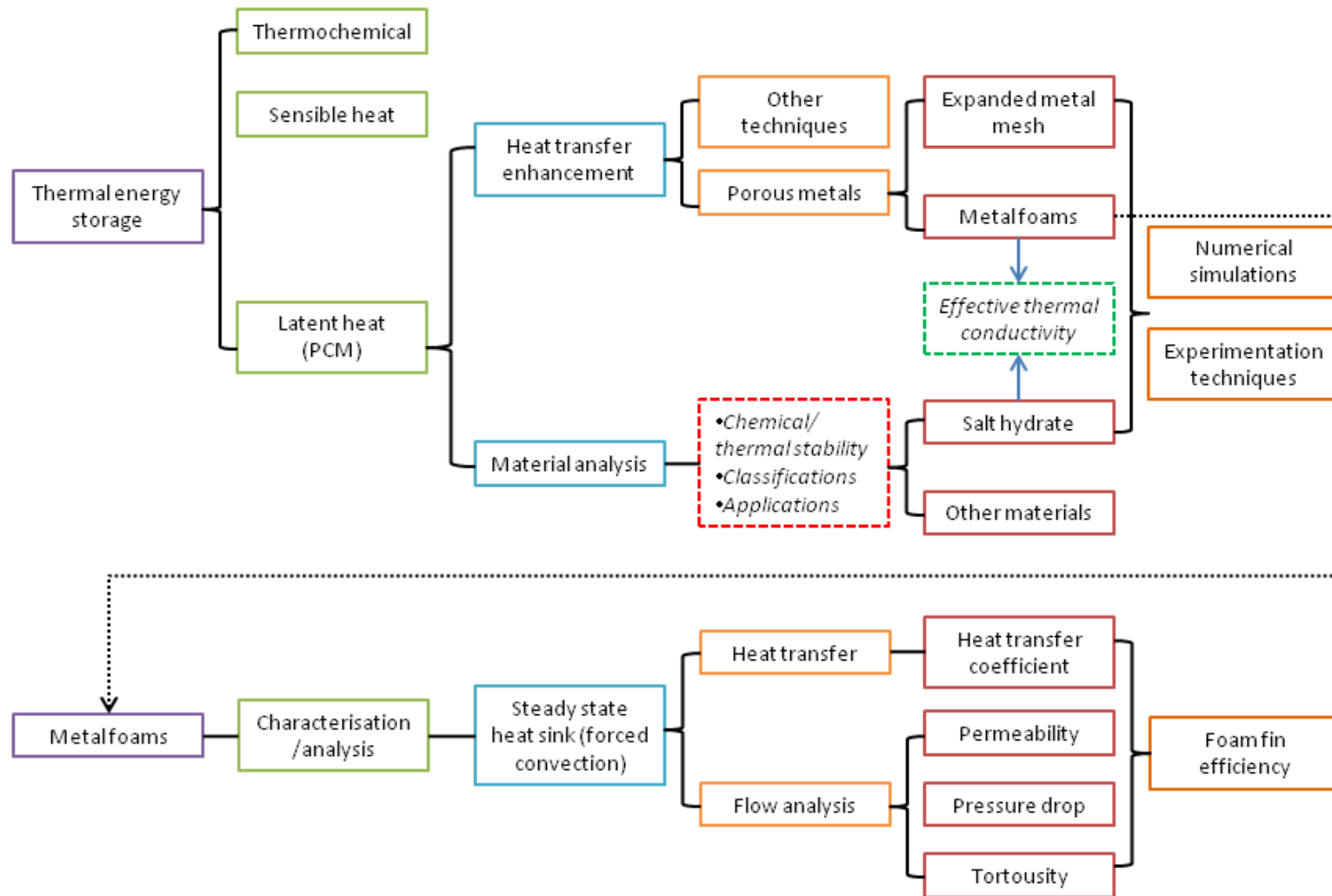
Figure 2-2 Scope of the literature survey.

2.3   Thermal energy storage

Thermal energy storage (TES) allows the storage of heat and cold so that they can be used later, therefore the storage method must be reversible, i.e. capable of being charged as well as discharged, repeatedly. Figure 2-3 shows the possible storage methods, which can be divided into physical and chemical processes.

```
                        Methods for thermal
                         energy storage

        Physical processes                      Chemical processes

 Sensible heat      Latent heat
                    -   Solid-liquid phase change
                    -   Liquid-vapor phase change
                    -   Solid-solid phase change
```
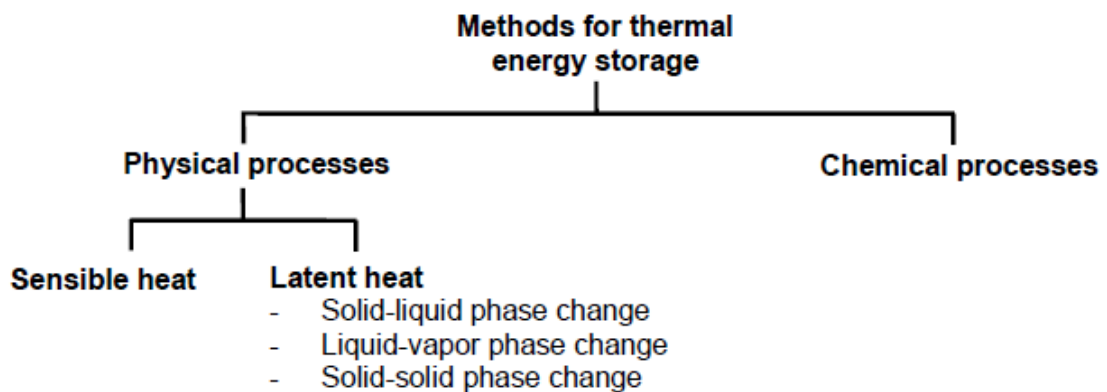
Figure 2-3 Methods for reversible heat and cold storage methods [1].

2.3.1   Sensible heat storage

Sensible heat storage method is based on changing a substance's temperature by changing its internal energy. Unlike PCM, it does not undergo any phase change during the storage process (Figure 2-4). The amount of energy stored, Q, is expressed by the following equations:

$$Q = m \times Cp \ \times \Delta T$$ Equation 2-1

$$Q = \rho \times Cp \ \times V \times \Delta T$$ Equation 2-2

Where: Q = amount of heat stored (kJ), m (kg) and ρ (kg/L) = the mass and density of the storage material, respectively. Cp = specific heat over the temperature range of operation (kJ/kg.K), V = volume of the storage material (L), and ΔT = temperature range of the operation (°C or K).

The amount of heat stored is dependent upon the temperature lift, mass, and heat capacity of the material. In choosing suitable material for sensible storage, the heat capacity plays the most important role. In addition, sensible heat stores should be

inexpensive, there should be storage space (volume) available, and the material should have a good thermal conductivity [10]. It is possible to store sensible energy in both solid and liquid phases. Sensible heat is currently the most common method for heat storage. Hot water heat storage is used for residential space heating and hot water provision in many households, although recent reports have indicated its decline due to the proliferation of condensing boilers [1].
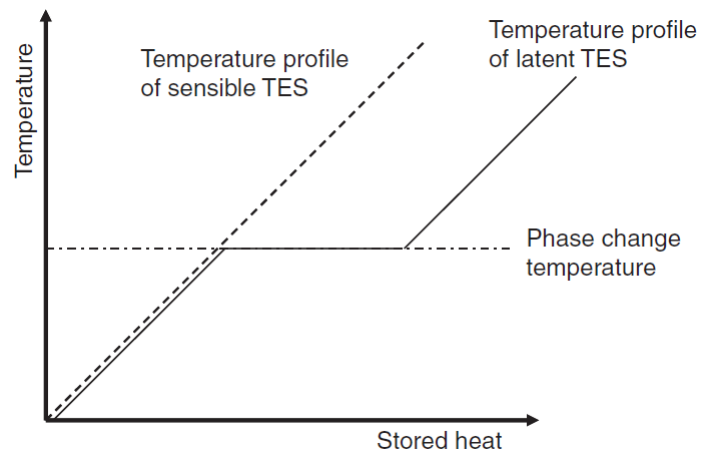
Figure 2-4 Thermal storage principles: sensible and latent heat methods [11].

2.3.2   Latent heat storage

When a material changes phase from solid to liquid, it absorbs a large quantity of energy to break the intermolecular bonds. The uptake of this thermal energy, also known as latent heat, happens whilst the temperature of the material remains constant or within a very close temperature range i.e. isothermal (Figure 2-4). This process is reversible i.e. the phase change from liquid to solid in which the latent heat is released. A small volume change usually follows the melting/solidification at around 10%. The amount of heat stored can be expressed as follows:

$\Delta Q = \Delta H = m.\Delta h$ Equation 2-3

The latent heat, ΔQ (kJ) is calculated from the differences of enthalpy between the two phases, ΔH. m is the mass of the storage (kg) and Δh is the specific enthalpy (kJ/kg). Heat storage via sensible heat is also involved prior and after the melting process (Figure 2-4). The heating could proceed further to involve liquid/vapour transformation. However,

this is deemed impractical in the vast majority of cases, as a heat storage method because under a constant volume (closed) system, evaporation increases the vapour pressure, which leads to a greater temperature increase for the phase change to occur. Under a constant pressure system, the volume change involved would prove too great to be practical [1]. (Note that the steam accumulator, not so widely used nowadays, is a liquid/vapour transformation process that was quite extensively used for thermal energy storage in industry).

2.3.3 Thermochemical storage

Thermochemical energy storage is potentially more interesting than latent heat storage as it is based upon a chemical reaction that is reversible, rather than a phase change. As the products of the reactions can be transported or stored, even at ambient temperatures, the longevity of storage can be extensive – over a season – before the heat-releasing reaction needs to be triggered. When a chemical reaction takes places, there is a difference in the enthalpy of the substances present at the beginning and end of the reaction. This enthalpy difference is termed the heat of reaction. Any chemical reaction with a high heat of reaction can be used for thermal energy storage if the products of the reaction can be stored and if the energy stored during the reaction can be released when the material reverts back to its original chemical composition:

$$A + \Delta H_R \Longleftrightarrow B + C$$
<div align="right">Equation 2-4</div>

During the charging step, heat is used to dissociate a chemical reactant (A) into products (B and C). This reaction is endothermic [ΔH_R = reaction enthalpy (kJ/mol)]. During the discharging step, the products return to the original state, A. This step is exothermic i.e. heat releasing. The products of both sides of this reversible reaction can be stored under ambient conditions or the working temperature. A simplified scheme of a thermochemical-based TES system is presented in Figure 2-5. A subset of the thermochemical storage method is sorption. In a sorption process, heat is stored by breaking the binding force between the sorbent and the sorbate in terms of chemical potential. An interesting example is the use of zeolites for seasonal storage, as is currently being examined by TNO in The Netherlands, 175 kg of zeolite was able to store

15 kWh [12]. Further information on sorption storage can be found in the literature such as Yu *et* al. [13] and Ristić *et* al. [14].
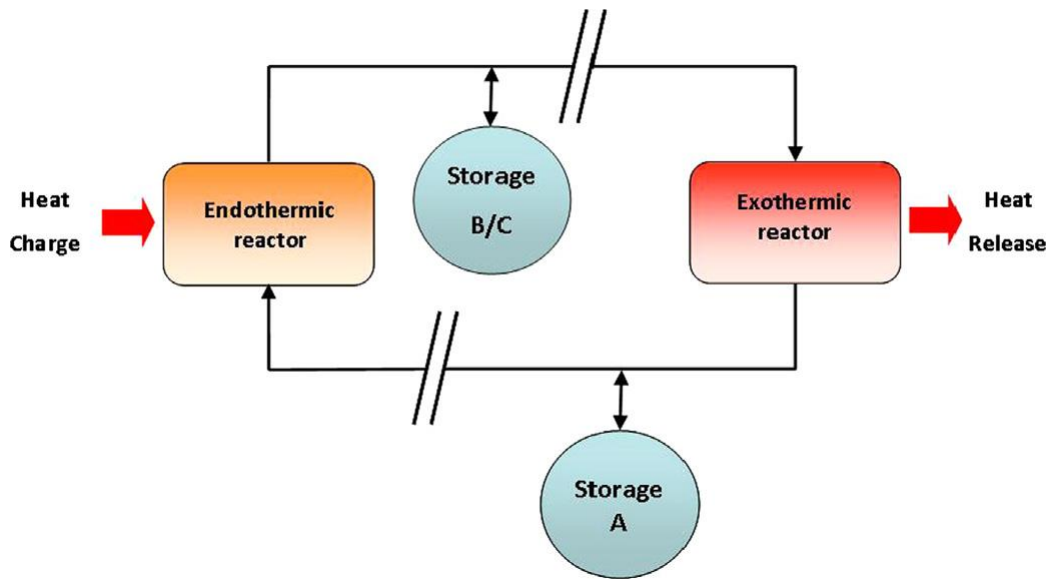
Figure 2-5 Simplified schematic of a thermochemical thermal storage system [15].

2.3.4 Discussion and analysis

The prime consideration in comparing the thermal storage methods is the energy density. Figure 2-6 illustrates the comparison: if one is to store 6.7GJ (over 1800 kWh) of thermal energy, sensible heat (water) would require a 34 m^3 storage volume, whilst a thermochemical storage would require the smallest volume: ~1m^3. Both latent heat storage and thermochemical storage are also highly advantageous against sensible storage as they reduce the volumetric requirement greatly. Table 2-1 lists the essential characteristics of the methods. It is apparent that thermochemical storage possesses one key advantage over sensible and latent heat storage: it stores thermal energy in chemical bonds, it negates the need for thermal insulation when the reactant(s) are being stored or transported, as there is no heat release or gain in these periods, unlike sensible and latent heat systems. However, the technology is still complex and remains at the laboratory scale. An example of an organization devoted to thermochemical TES research is the DLR Institute of Engineering Thermodynamics in Germany (www.dlr.de).
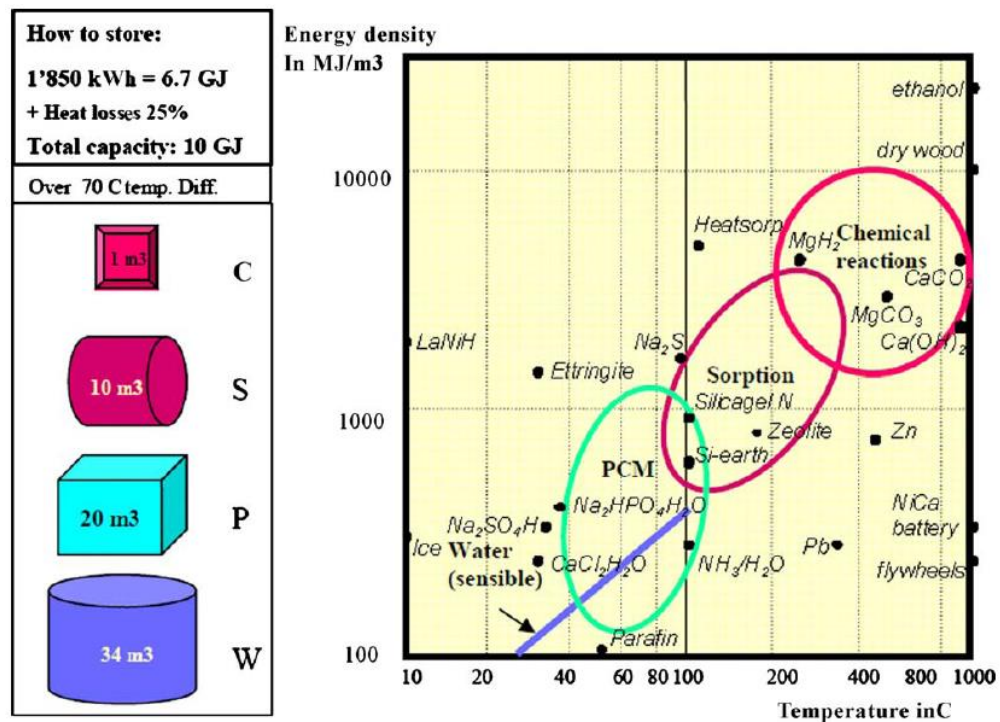
Figure 2-6 Energy density comparison of the thermal storage methods. Note: W: water (sensible), P: PCM (latent heat), S: sorption, and C: thermochemical [16].

Table 2-1 Key comparative factors of the thermal storage methods (adapted from [15]).

	Sensible	Latent	Thermochemical
Energy density	Low	Medium	High
Storage temperature	Charging temperature	Charging temperature	Ambient/charging temperature
Storage period	Limited (due to heat loss)	Limited (due to heat loss)	Unlimited (theoretically negligible heat loss)
Transport capability	Small distance	Small distance, unless well-insulated	Distance unlimited
Technology maturity	Industrial scale	Some commercial use	Laboratory scale
Technology complexity	Simple	Medium	Complex

2.4 Latent heat storage (phase change material)

The high energy density and (in theory) isothermal charging and discharging capability of latent heat storage are the main preference factors over sensible storage. The latent heat store is also known as phase change material (PCM) due to its heat storage principle, which is based on the solid/liquid phase change. The discussion in this

subsection establishes the fundamentals of PCM that leads to the PCM material and heat exchanger selection for the creation of a transient heat sink prototype.

2.4.1 Material analysis

2.4.1.1 Material classifications

Phase change material can be classified into organics (paraffins and fatty acids), inorganics (salts, salt hydrates, hydroxides, etc.) and eutectics (Figure 2-7). Organic PCMs have been attributed to possess good chemical compatibility and do not suffer from supercooling. Supercooling (or subcooling) is the phenomenon in which a temperature significantly below the melting temperature has to be reached, until a material begins to solidify and therefore, releasing its heat (Figure 2-8). If this temperature is not reached, the PCM will not solidify and thus, effectively only store sensible heat: this has the effect of a substantial reduction in storage capacity and unstable working temperatures [17]. PCM disadvantages include very low thermal conductivities (typically around 0.2 W/m.K), flammability, and inconsistent phase change temperatures. Inorganic PCMs generally possess a slightly higher thermal conductivity (mostly around 0.5 W/m.K), but are reportedly to show severe supercooling and to be corrosive towards container materials. Eutectics have sharp melting/solidification temperatures, but they tend to suffer a large volume change during the phase change process [18]. Other features, in addition to consideration of the melting temperature, are discussed in Section 2.4.1.2.
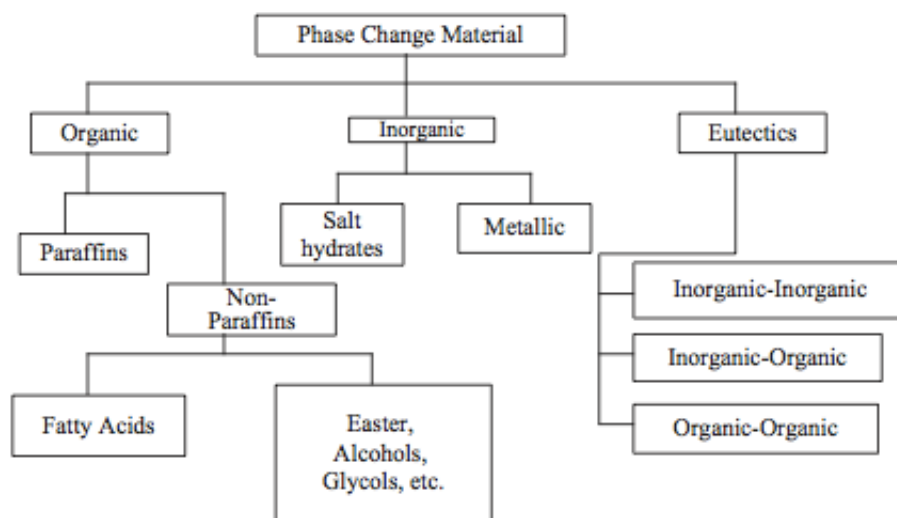
Figure 2-7 Material classifications of PCM [19].
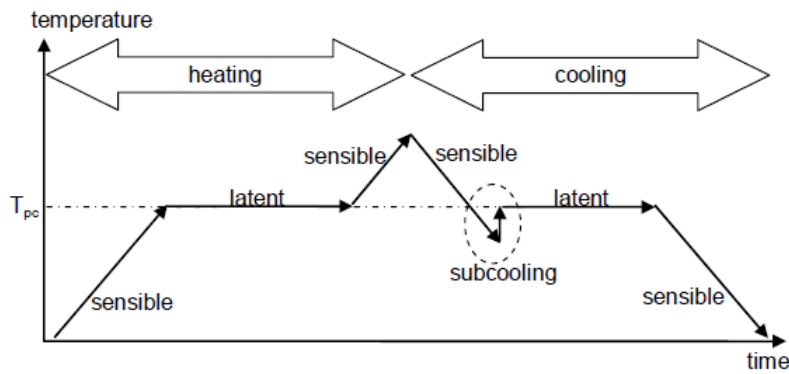
Figure 2-8 Heating (melting) and cooling (solidification) phases of the thermal storage process with PCM. Note: supercooling (subcooling) is marked [1].

2.4.1.2 Selection criteria

The initial selection of a PCM is generally based upon its melting temperature, as this would be the working temperature of the thermal storage process. Another important consideration is the melting enthalpy. This must be high to provide a high energy density. Figure 2-9 shows the typical range of melting temperatures and enthalpies of common PCM material classes. A closer inspection shows that energy density is roughly proportional to the melting temperature. This correlates with the 'theory of Richards', which states that melting enthalpy per unit volume is proportional to the melting temperature, the number of bonds per molecule, and the packing density of molecules or atoms, as mentioned by Mehling et al [1]. The aforementioned two criteria are important ones, but should be accompanied by other desirable physical, technical, and economic features (tabulated in Table 2-2). It is difficult to satisfy all criteria with one PCM, and compromises have to be made.
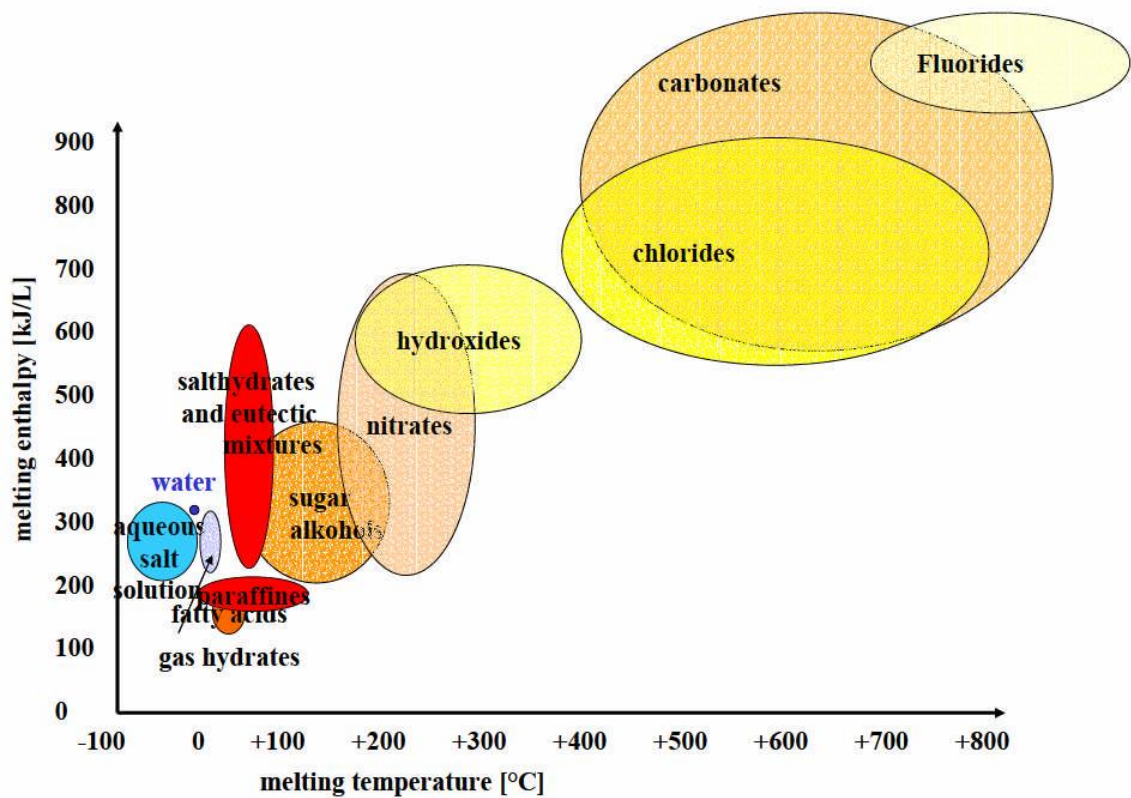
Figure 2-9 PCM classes with their range of melting temperatures and enthalpies [1].

Table 2-2 Selection criteria of PCM materials (adapted from [20]).

Thermodynamic requirements	• Correct range of melting temperature. • High latent heat per unit volume or mass. • High specific heat. • High density. • High thermal conductivity. • Small volume change upon melting. • Small vapour pressure at the operating temperature. • Melting congruency.
Kinetic requirements	• High nucleation rate to avoid/reduce supercooling. • High rate of crystal growth to meet demands of heat recovery from the PCM.
Chemical requirements	• Reversible melting/solidification cycles. • Chemical stability. • Thermal cycling capability i.e. no degradation after charge/discharge cycles. • Not corrosive toward container materials esp. metals. • Not toxic, flammable, or explosive.
Economic requirements	• Cost-effective. • Industrial-scale availability.

As listed in Table 2-2, the selection procedure for a PCM (and other storage media) is not limited to the thermal performance and operating temperature. As with any chemicals, the health and safety aspects must be considered and when a PCM is being

applied, particularly if it may come into contact with operators, those living in buildings where it may be used, or on transport, a health and safety assessment should be carried out and risks identified.

There are limited data on many PCMs regarding the operational lifetime. This is not so much a feature of steady degradation of the chemical(s) when in a quiescent state, but is a strong function of the number of charge/discharge cycles undertaken. If used for diurnal storage in a house, there will be several hundred cycles every year, and for a typical 20 year life this figure may well exceed 10,000. Much literature limits life tests to a few hundred cycles under controlled laboratory conditions, and some degradation is common. It is recognised that this is one property holding back long term and widespread adoption of PCMs in, for example, the built environment.

Encapsulation of PCMs in polymers (micro-encapsulation) is seen as one way of preventing the PCM corroding building materials, for example. With regard to PCM salts this can protect metals that might be used as containers, at the expense of efficiency as the polymer may well inhibit the rate of charge/discharge if the capsule wall is too thick.

The cost of PCMs depends upon the type used – organics such as waxes, used at modest temperatures, are relatively cheap and do not demand expensive containment. Salts often need corrosion-resistant materials as containers/enhancement materials, while at high temperature the PCMs themselves may be very expensive – an example being the miscible gap metal alloys invented in Australia some four years [21]. (In these alloys, one component melts, but is completely encapsulated by the second component that remains in the solid phase).

2.4.1.3   Salt hydrates

A salt hydrate consists of a salt and water in a fixed mixture ratio. It is an integral number of water molecules per ion pair of the salt, in which a stable crystal is formed. The bonds are typically ion-dipole or hydrogen bonds. The water molecules are located and oriented in a well-defined manner. In some structures, the water is more closely oriented to the salt anions and in others, to the cations. An example is shown in Figure

2-10 for MgCl$_2$.6H$_2$O (magnesium chloride hydrate). Because of this stable crystal structure, salt hydrate melting temperatures are higher than for water [1]. The pros and cons of the salt hydrates with regard to their application as PCM are given in Table 2-3. Because of their relatively high volumetric energy density, they are highly researched PCMs. A prime supplier of salt hydrate PCMs, PCM Products Ltd. [22], offers modified salt hydrates, in which they are thickened with additives to relieve the complication of phase separation from semicongruent and incongruent melting salt hydrates. Moreno *et* al. [23] performed corrosion analyses of different salt hydrates against common heat exchanger metals: copper, stainless/carbon steel, and aluminium.
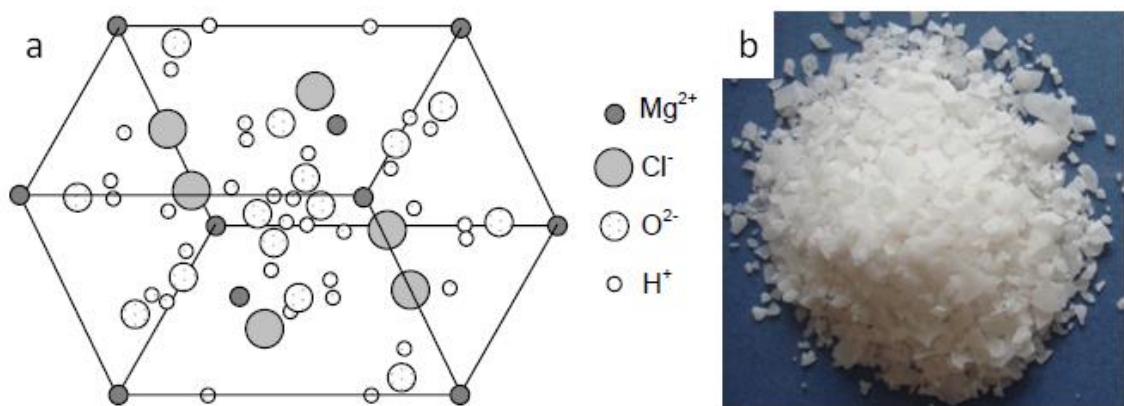
Figure 2-10 **Salt hydrate MgCl$_2$.6H$_2$O (a)** molecular structure [1], (**b**) physical form at room temperature [24].

Table 2-3 The advantages/disadvantages of salt hydrates (adapted from [1] and [23]).

Advantages	- Very high energy density with respect to mass and volume. - Moderate thermal conductivity (higher than organic PCMs). - Lower vapour pressure. - Acceptable volume change at melting: typically ~10 vol%. - Chemically very stable. - Commercially available and very inexpensive: €1-3/kg. - Robust corrosion dataset is available [23, 25, 26].
Disadvantages	- Most suffer from supercooling. - Potential phase separation between the salt and water phases.

2.4.1.4 Chemical/thermal stability and corrosion

For economic reasons, longevity of PCMs is of utmost importance. Rathod and Banerjee [19] defined a reliable PCM as a thermally, chemically, and physically stable material after repeated thermal cycles. Kenisarin and Mahkamov [27] concluded that a PCM should be tested for at least 1000 thermal cycles to be viable. Characterizing PCMs based on their stability is an important branch of PCM research with the simple aim of eliminating the undesirable, unstable materials from the many candidates. In addition, efforts are also under way to artificially stabilize PCMs with additives, etc. A typical technique involves accelerated thermal cycling tests, as described in Shukla *et* al. [17] and Risueño *et* al. [28]. So far, the stability of many PCM classes has been verified and is accessible in literature e.g. Sharma *et* al. [29] and Porisini *et* al. [30]. Because PCMs in operation are in contact with metal containers or heat exchanger surfaces, the corrosion resistance of PCMs is an important design consideration. Cabeza *et* al. [25] pioneered the immersion corrosion tests of salt hydrates against common metals and metal alloys. The tests were holistic in that the corrosion data included heating and cooling operations as well as being carried out over short and long term durations. Recently, Moreno *et* al. [23] carried out long terms tests (12 weeks) on commercial salt hydrates have concluded that stainless steel is the most compatible material. Unfortunately, this type of test has not been carried out for most other PCM classes.

2.4.1.5 Discussion and analysis

The fundamentals of PCM material analysis have been established. In this project, a PCM candidate must be selected to provide the base material for a transient heat sink device. For this application, it was decided to select a PCM with a melting temperature within the range of 40-50°C. It must be sourced commercially and locally (UK or EU). Two materials were shortlisted. Table 2-4 shows important information for the comparative analysis (discounting the costs). It is apparent that the salt hydrate is superior in terms of energy density, from considerations of both latent and sensible heat. In addition, it is also attractive in terms of thermal conductivity and volume expansion. The salt hydrate S46 has also been rigorously tested, as reported in Moreno *et* al. [23], therefore robust corrosion data against common metals are available, although it is also generally assumed that paraffin waxes are chemically stable/non-corrosive. The paper also

identified that the salt hydrate S46 has been thickened by the supplier with sepiolite (a naturally occurring clay mineral) and fumed silica to render it congruent. Due to these features, the salt hydrate was selected. In addition, there has been no work carried out on salt hydrate enhanced (for thermal performance) with metal foam, hence this would be an opportunity for study.

Table 2-4 Important thermophysical data for the candidate PCM materials.

Candidate material	Supplier	Melting temp. (°C)	Latent heat (kJ/kg)	Sensible heat (kJ/kg.K)	Thermal conductivity (W/m.K)	Volume expansion (vol %)
RT47 (paraffin)	Rubitherm (Germany)	41-48	170	2.0	0.20	12
S46 (salt hydrate)	PCM Products (UK)	46	210	2.4	0.45	10

2.4.2 Enhancing heat transfer performance in PCMs

It is apparent in Table 2-4 that common PCMs possess very low thermal conductivity (0.45 W/m.K for the salt hydrate). Metallic PCMs such as Al34-Mg6-Zn however, are an exception [31], but are less relevant in the temperature range of interest. To improve the efficiency of heat charging and discharging processes, the ability to transfer heat between the PCM 'core' and the heat sink (or source) must be increased as low heat transfer performance has been the main factor restricting the application of PCMs, particularly in situations requiring rapid energy storage and release. The techniques are presented in the following subsections.

2.4.2.1 Investigated techniques

So far, the techniques investigated can be categorized as shown in Figure 2-11. Some active methods e.g. ultrasonication [32, 33] and mechanical agitations are not discussed here – these of course require an extra energy input that may not be practicable and/or are costly to implement. The ensuing discussion introduces the techniques. There exist excellent reviews in literature such as Agyenim et al. [34] and Xu et al. [35] for in-depth discussions.
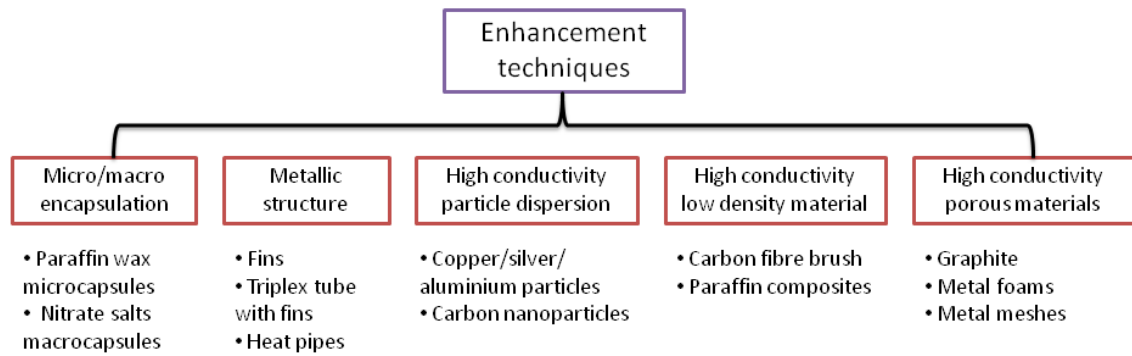
Figure 2-11 Categories of the investigated methods to enhance the thermal conductivity of PCMs.

- **Micro/macroencapsulation**

Microencapsulation is a process in which solid particles or liquid droplets are surrounded by a coating or embedded in a homogeneous or heterogeneous matrix to give small capsules having many useful properties. Microcapsules of PCM are defined as having a diameter less than 1000µm (Figure 2-12a shows a single capsule, and Figure 2.12b an SEM of a mass of microcapsules). Any larger diameter results in them being called macrocapsules [36]. There are many reasons to encapsulate PCMs: 1) to make it easier and safer to handle the PCM as there will be no leakage, 2) to reduce PCM reactivity with the outside environment, 3) to dampen the effect of volume change at melting, and 4) to improve heat transfer by increasing surface area – like a compact heat exchanger with many square metres of surface per unit volume, which tends to outweigh any limitation due to the extra wall resistance of the polymer, as mentioned earlier – Section 2.4.1.2. So far, the most common PCM class to be encapsulated is paraffin wax. The encapsulation process is typically carried out via spray drying, coacervation – (a form of *in situ* polymerisation), and suspension polymerisation. Most of the shell materials are polymer-based e.g. low density polyethylene, polystyrene, and polymethyl methacrylate. Applications of encapsulated PCM include agriculture, pharmaceuticals, foods, cosmetics, buildings, and fragrances [37, 38].
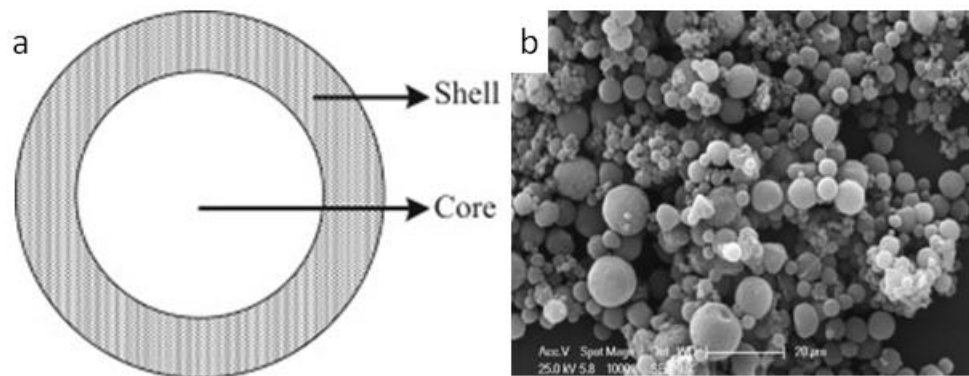
Figure 2-12 (**a**) PCM microcapsule [37], (**b**) SEM of prepared PCM microcapsules [39].

- **Metallic structures**

This category includes incorporating metallic fins, to increase the heat transfer within the PCM container. These may typically be longitudinal and radial fins [40], as well as pin fins [41] embedded within the PCM phase. Also included is the triplex-tube configuration i.e. heat transfer fluid flowing in the inner and outer tube, with PCM in the middle tube [42]. A heat pipe as a highly effective thermal conductor in the PCM has also been aggressively investigated by researchers such as Faghri *et* al. [43, 44]. These methods are by far the easiest solution as fabrication can be carried out in workshops and they are suitable for medium to large scale TES tanks, subject to correct heat exchanger design. They are also relatively easy to model and simulate on a computer for design optimisation. Figure 2-13 illustrates some of these methods.
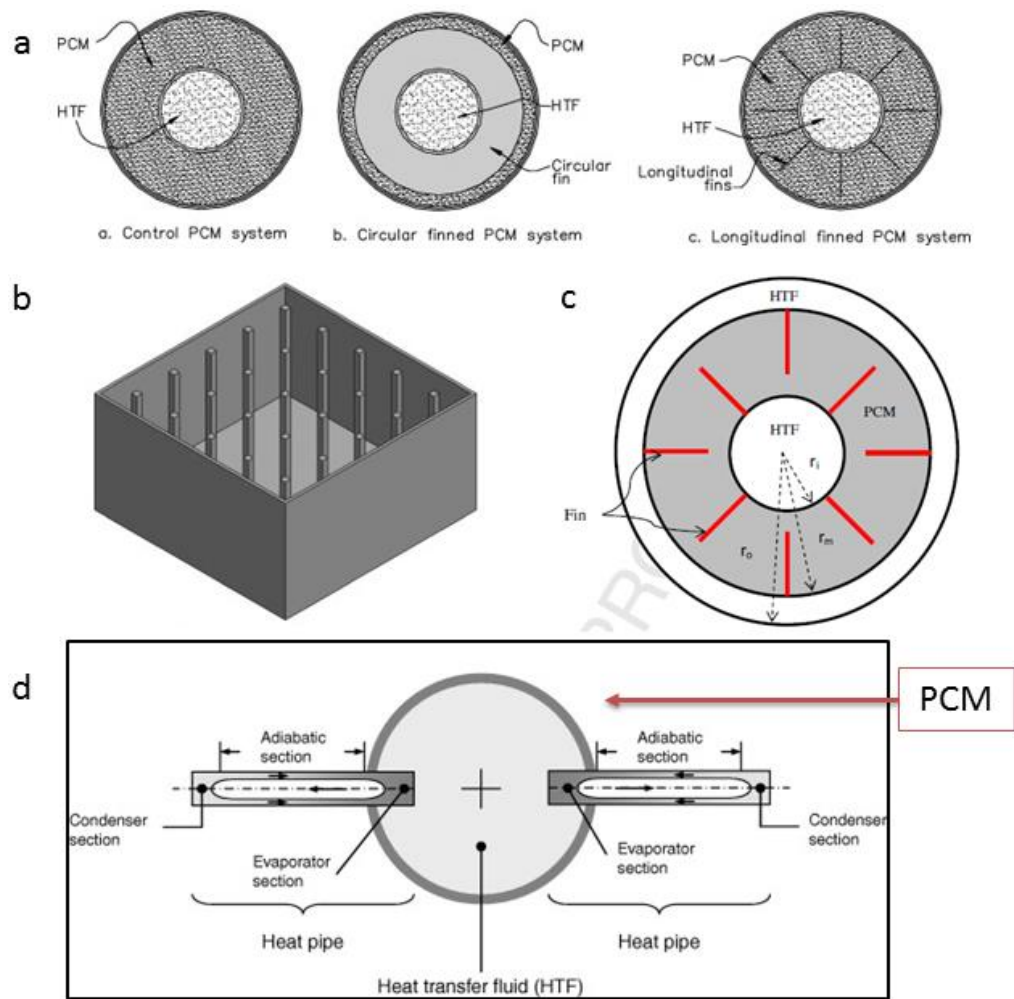
Figure 2-13 **Embedding metallic fins/high conductive materials in PCM** (**a**) longitudinal/radial fins [40], (**b**) pin fins [41], (**c**) triplex-tube with fins [42], (**d**) heat pipes in shell and tube heat exchanger configuration [43] with PCM filling the shell-side and the heat transfer fluid fills the tube-side.

In the case of the triplex tube with fins, the aim here is to take high thermal conductivity features (the fins) into the bulk PCM so that by conduction into or out of the fins, local solidification or melting of the PCM can occur. Obviously the distance between the fin surface and the bulk of the PCM is critical and the need is to retain a good PCM content for high heat storage, while minimising long conduction paths within the PCM. The reliance on convection that will occur at the melt/solid interface is likely to be unreliable as an enhancement measure.

- **Particle dispersions**

The dispersion of high conductivity metal particles in PCMs is a relatively simple method to increase the heat transfer i.e. by dispersing silver/copper/aluminium particles, metal nanoparticles [45], and carbon fibres [46] into PCMs. In general, for every case there is

a range of optimum particle fraction and it has been suggested that one should select the lower band values to ensure a high PCM mass to increase the amount of stored energy – an excess of metal will reduce the allowable storage volume of the PCM.

- **High conductivity, low density materials**

Interesting research carried out by Fukai *et* al. [47, 48] utilized randomly-oriented carbon fibres and carbon brushes embedded in paraffin wax to improve heat transfer through the PCM container (Figure 2-14). The motivation stems from the fact that carbon fibres are highly conductive (reportedly in the region of 1000 W/m.K) whilst being low in density (theoretically less than 1600 kg/m^3). This would create low-weight PCM storage systems. In addition, the resistance of carbon fibres to corrosion and chemical attacks could solve the common incompatibility issues between PCMs and metals. The results indicated the preference towards the brush and the authors recommended further investigations pertaining to different PCM types and cost considerations. Most recently, Nakaso *et* al. [49] discovered that carbon cloths had a better thermal performance than carbon brushes because the cloth structure was more continuous than the brush structure.
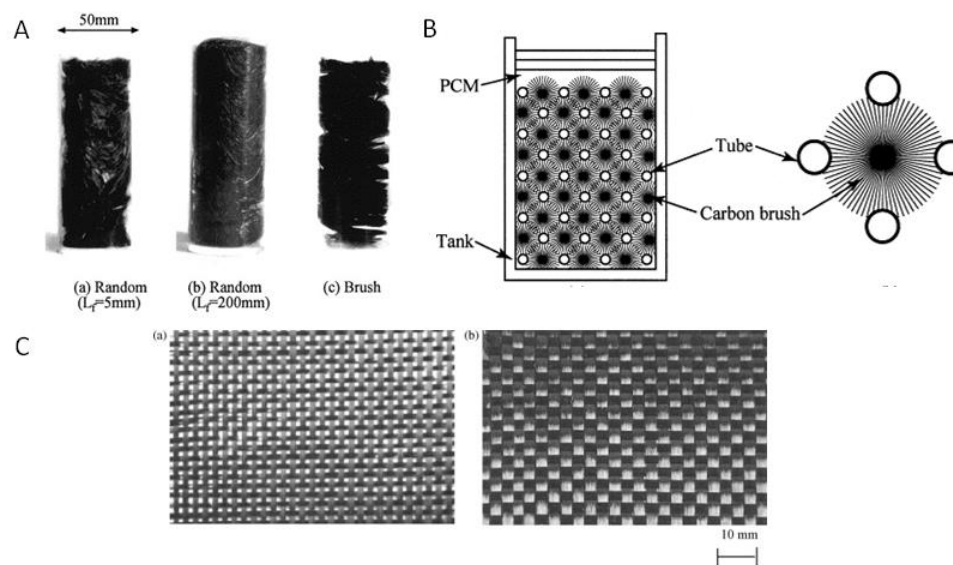
Figure 2-14 (**A**) Randomly-oriented carbon fibres and carbon brush, (**B**) schematic of the carbon brush/PCM TES unit, (**C**) carbon cloths [47, 49].

- **Other techniques**

It is worth mentioning some other techniques that have been investigated either numerically or experimentally to show the many possibilities for exploring PCM 'package' heat transfer improvements. Abdollahzadeh *et* al. [50] investigated numerically the solidification behaviour of nano-enhanced phase change material inside an enclosure with two wavy walls with positive results. Fauzi *et* al. [51] investigated the addition of acid-based surfactants in myristic acid/palmitic acid eutectic PCM with an interesting effect - the reduction of subcooling.

2.4.2.2   Porous matrices

An important consideration is the impregnation of high conductivity porous matrices in PCMs. The combination has gained increasing attention, particularly because of the matrix light weight and high specific surface area for heat transfer.

- **Metal foams**

Metal foam is a cellular structure consisting of a solid metal, containing a large volume fraction of gas-filled pores. These pores can be sealed i.e. a close-cell foam, or form an interconnected network i.e. open-cell foam (Figure 2-15a). It is an interesting heat exchanger device due to its characteristic of mixing air flow during forced convection (discussed further in Section 2.6). The core advantages of impregnating PCM in metal foam i.e. composite (Figure 2-15b) include: 1) the capability of the foam ligament network to conduct heat throughout the storage media – unlike other techniques, the distribution of the foam ligaments within the PCM phase should make the melting and solidification processes more uniform, and 2) its high specific surface area (per volume or mass) for heat transfer, which results in increasing the '*effective thermal conductivity*' of the PCM/foam composite[1]. An important parameter to consider is porosity, ε, defined as the ratio between the voidage volume and the total volume:

---

[1] Note that the effective thermal conductivity is commonly used to describe structures such as sintered heat pipe wicks containing a liquid – not unlike a foam containing a PCM in liquid (or solid) form. See for example Maxwell, J.C. [ ] A treatise on electricity and magnetism, Third Edition, Vol. 1, OUP, 1054. Reprinted by Dover, New York, NY, 1981, and Reay et al [ ]. Kew, P.A. and McGlen, R. Heat Pipes, 6th Edition, pp.78-81, Butterworth-Heinemann, Oxford, 2014.

$$Porosity, \varepsilon = \frac{voidage\ volume}{total\ volume} x100\%$$

Equation 2-5

The porosities of common metal foam/PCM composite are generally >90%, in order to maximize the latent storage capacity [52]. The common foam materials are copper, aluminium, stainless steel, and nickel [53]. The choice of material is a balance between the material thermal conductivity (e.g. copper ~400 W/m.K, stainless steel ~17 W/m.K) and its compatibility with the PCM to avoid chemical degradation or corrosion complications. The cost of the foam is also an important factor. Most works found in the literature present the enhancement due to foams by presenting: 1) the *'effective thermal conductivity'* increase e.g. Siahpush *et* al. [54] measured a 95% porosity copper foam/eicosane composite conductivity to be 3.06 W/m.K, a significant increase from the baseline eicosane 0.423 W/m.K value, and 2) the reduction in melting/solidification time relative to the baseline PCM e.g. in the previous example, the melting was reduced from 500 min to 250 min (i.e. -50%).
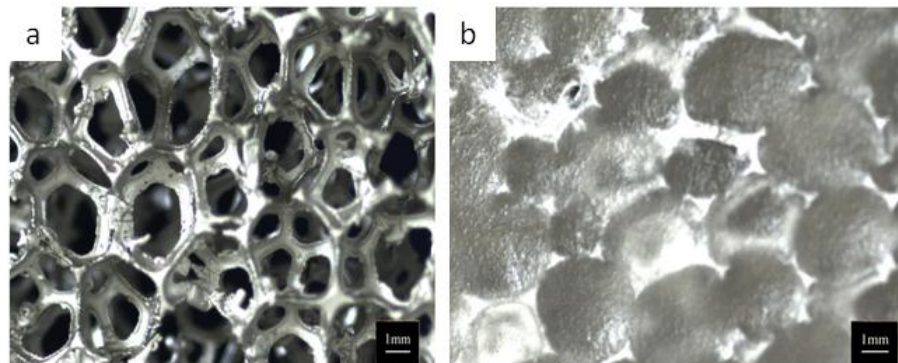
Figure 2-15 (**a**) The structure of an open-cell aluminium foam, (**b**) the foam filled (impregnated) with paraffin wax PCM [55].

- **Metal meshes**

Inspired by the metal foam performance, a novel use of the common metal mesh (which is used for a variety of applications as shown in Figure 2-16 and referred to by some manufacturers as expanded metal – Expamet being one trade name) is to enhance the heat transfer performance of PCM. Advantages of the mesh against metal foam are in its competitive cost and ready availability. Mustaffar *et* al. [8] reported that the metal mesh is generally significantly cheaper than metal foam per unit volume, up to 96%, for certain types. Shuja *et* al. [56] pioneered this research by investigating the melt

behaviour of n-octadecane impregnated with aluminium mesh of different geometries: triangular, square, and hexagonal – see Figure 2-17. The results showed a preference toward the triangular geometry, which resulted in the shortest time taken to melt the PCM. The experimental results conformed to direct 2D numerical simulations [8].
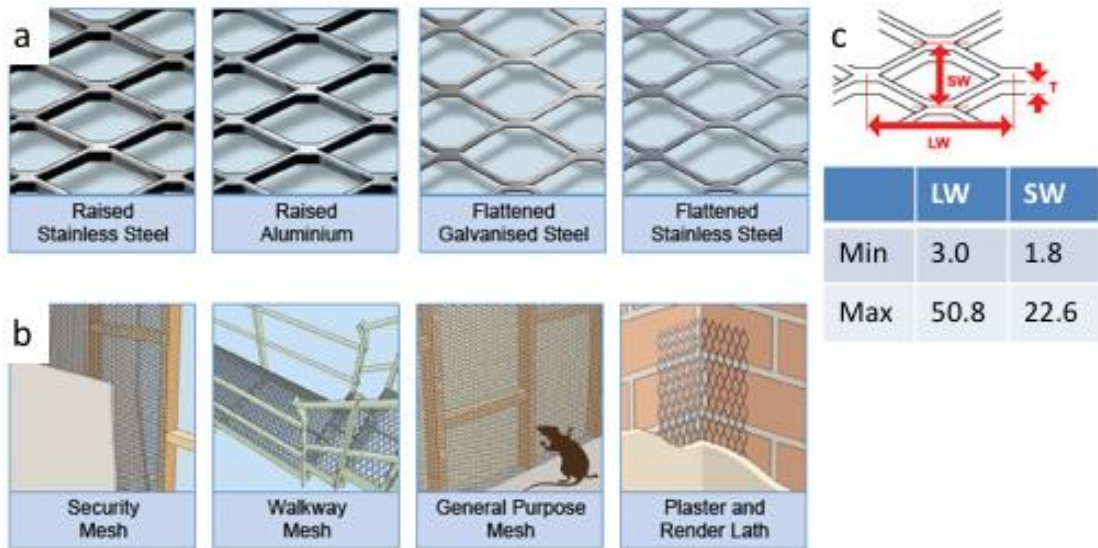
Figure 2-16 **Metal mesh from *Expam*et *Building Products* (a)** commercial variance, (**b**) common applications, (**c**) the range of mesh size (in mm) for the raised aluminium mesh type.
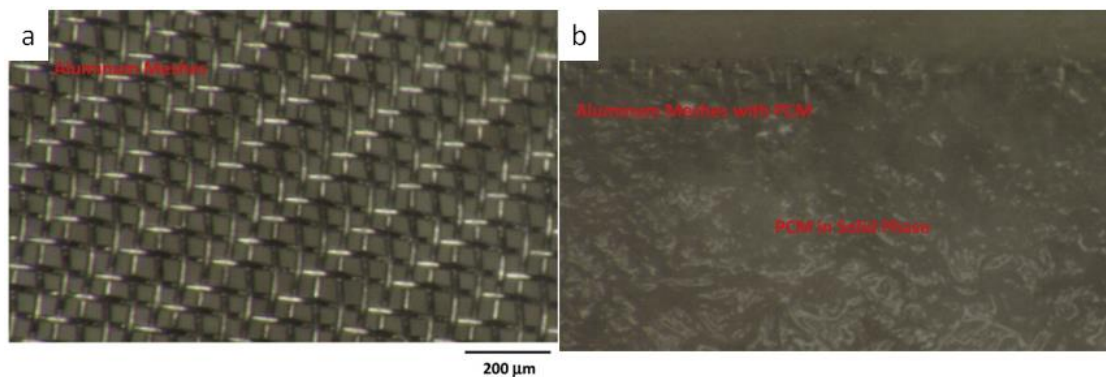
Figure 2-17 (**a**) Aluminium square mesh (**b**) the PCM melt progress. An investigation by Shuja *et* al. [56].

The link between the metal foam, the subject of the research in this thesis, and the metal mesh (expanded metal) is that the latter was found to be a lower cost alternative as a result of ongoing literature studies throughout the research programme.   It was therefore decided to highlight it as a potential alternative for applications in heat exchangers and in PCM storage.

As introduced below, the use of graphite cloth (see Figure 2-14(C)) in Section 2.4.2.1 above) is another alternative good thermal conductor for use in PCM mixes – however it lacks the rigidity of the metallic mesh and the foam. In 'Advances in Thermal Energy Storage Systems – Methods and Applications', by Luisa F. Cabeza [57], it is pointed out that the poor mechanical strength is a drawback, although some graphites have been mixed with metal additives (aluminium nitride is mentioned) to enhance thermal conductivity and, the reference implies, rigidity. 'Expanded graphite' is a form of graphite (not a mesh) that can be bound with PCM under compression to enhance conductivity, but the structure is essentially random – see Xiao *et* al. (2015).

- **Graphite composites**

Graphite composite can be made by dispersing graphite flakes in the PCM. This can be achieved above the melting temperature by mechanical dispersion within the molten PCM or at room temperature by mixing the two components. Pincemin *et* al. [58] investigated the composite of graphite flakes with several high temperature PCMs (nitrate salts). The thermal conductivity of the composites with 20 wt% graphite effectively increased to 3.5-9.0 W/m.K from the baseline of ~0.5 W/m.K (Figure 2-18).
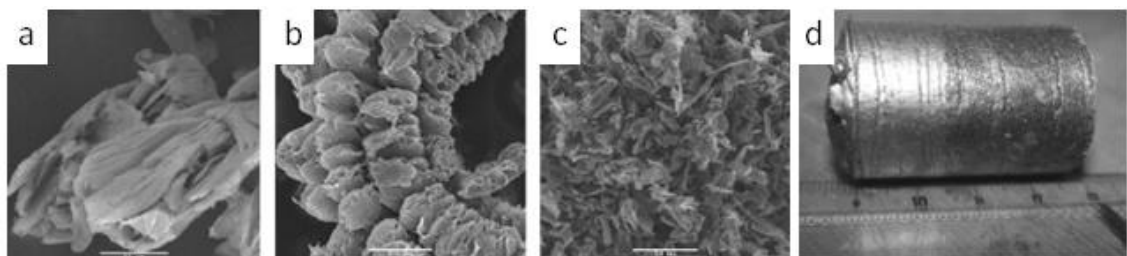
Figure 2-18 (**a**) Natural graphite flakes, (**b**) expanded natural graphite, (**c**) grounded expanded natural graphite, (**d**) graphite/PCM composite formed after being poured into a stainless steel mould [58].

2.4.2.3 Discussion and analysis

Table 2-5 on page 33 analyses the pros and cons of the enhancement techniques. It is not easy to pinpoint the best enhancement technique for any application as each depends upon circumstances. For example, although the metal foam technique is arguably the most superior as attested by the vigorous research upon it compared to the other techniques [59], in the Thermac® project [60], on which the author worked,

aluminium fins were carefully designed to time 7 hour PCM charging and 4 hour energy discharging periods instead of the metal foam solution – see Figure 2.19. In essence, when a PCM storage application has been selected, the heat transfer solution must take into account economic and technical considerations. In this PhD project, the transient heat sink employed the metal foam solution because rapid energy charge and discharge from the salt hydrate PCM was a requirement. In addition, a high degree of fluid retention was important as it was expected that the viscosity of the salt hydrate to decrease greatly as it changed phase from solid to liquid, which could be made possible by using metal foam due to its tortuous paths [61].
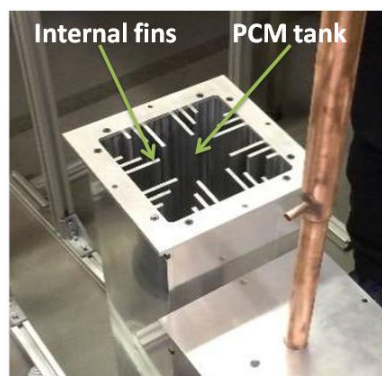
Figure 2-19 The internal and external fins were carefully designed to provide overnight charging and daytime discharging of PCM in the Thermac® project [60].

2.5 Phase change material/metal foam composite

The ensuing discussion concerns the fundamentals of phase change material/metal foam composite analyses.

2.5.1 Effective thermal conductivity

Effective thermal conductivity, k_{eff} is an essential parameter for any PCM/metal foam composite in order to design and model/simulate the TES system. There exist experimental and numerical methods for the measurement. The main reason for using the composite is associated with the need to overcome the poor thermal conductivity of PCMs, in both their solid and liquid states, so that the stored heat can be transferred out of the store at the rate desired by the application, and charging – the flow of heat in the reverse direction to melt the PCM – can be made equally effective in terms of cycle time.

As discussed in Section 2.4.2.2, the analysis of heat transfer within a structure involving a solid and liquid or two different solids can be complex, but equations describing the *'effective thermal conductivity'* have been established, particularly in areas such as heat pipe wick thermal conductivity analyses. Examples are given below.

Unless the PCM or any fluid has a low viscosity, the mode of heat transfer between the solid and liquid (molten PCM) is essentially by conduction. So if one has a low thermal conductivity PCM liquid the rate at which latent heat can be taken to the container wall on solidification (or, in the continuous molten state, sensible heat), will be by conduction. Thus the use of a composite that gives high thermal conductivity paths within the PCM – metal strands – should aid thermal conduction and speed up charge and discharge. Models for this are discussed below in Section 2.5.1.2.

2.5.1.1   Experimental methods

There are two methods for measuring effective thermal conductivity – these are the transient and steady-state methods. Transient methods include the laser flash method [62] and the transient plane heat source method [63]. However, Xiao *et* al. [64] argued that these methods carry large uncertainties as well as deviations in many cases due to the thermal contact resistance (TCR) between the specimen and the sensors. However, the steady state conventional method is also plagued with TCR problems. In this relatively simple method, temperature difference across a sample is measured in response to a heating power applied (Figure 2-20a) in a rig as shown in Figure 2-20b. The conductivity can be determined from this correlation:

$$q = -A\text{k}_{\text{eff}}\frac{dT}{dx}$$
Equation 2-6

Where: q = heat flow (W), A = cross sectional surface area (m^2), dT/dx = unidirectional temperature gradient (K/m), and k_{eff} = effective thermal conductivity (W/m.K). The authors modified this basic equation to include the TCR correction factor. The k_{eff} values of copper/paraffin composites obtained from their test rig showed a good agreement with theoretical predictions.

Table 2-5 Comparative analysis of PCM heat transfer enhancement techniques.

Technique	Advantage	Disadvantage
Microencapsulation	- Leakage prevention. - Prevention of reactivity with outside environment e.g. container. - Volume change containment. - High heat transfer area per unit volume.	- Low conductive shell materials. - Low PCM mass fractions i.e. low energy density. - Most publications concern on capsule synthesis: lacking heat transfer performance data.
Metallic structures e.g. fin, and heat pipe	- Easy to fabricate. - Inexpensive option.	- Compatibility of metals/PCMs must be considered. - Performance/metallic volume balance consideration. - Performance is less superior to porous matrices per unit metal volume.
Particle dispersion	Simple method.	- Particle fraction must be minimized to maximize energy density. - High density causes particles to settle at the bottom container. - Compatibility of metallic particles/PCMs.
High conductivity, low density materials e.g. carbon fibre, brush, and cloth	- Resistant to corrosion/chemical attacks. - Lightweight.	- Fibre/PCM volume balance for energy density consideration. - Commercial carbon fibres may not be available easily. - Lacking experimental data: only investigated by a few researchers.
Metal foam	- Excellent conduction due to interconnecting network of metallic ligaments. - High heat transfer surface area/volume. - Superior heat transfer performance. - Lightweight/commercially available.	- Thin ligaments can be brittle after multiple thermal cycling. - Reportedly corrosive with nitrate salt PCMs under high temperature operations [65]. - Heat transfer via convection could be suppressed due to ligaments, but research suggests superior conduction offsets this drawback.
Metal mesh	- Relatively inexpensive compared to foams. - Commercially available.	Lacking research data: a novel technique.
Graphite composite	Chemically stable - resist corrosion by PCMs.	Dispersion of graphite flakes in PCMs can be very difficult.
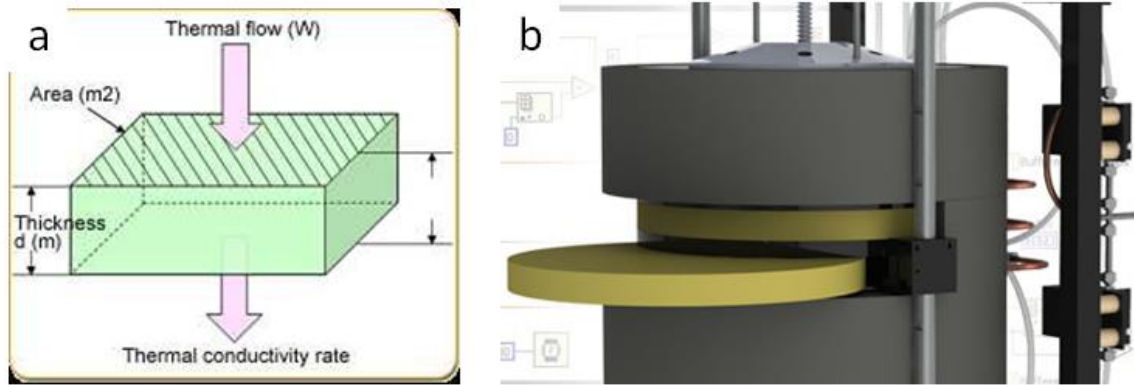
Figure 2-20 **Steady state thermal conductivity measurement** (**a**) the basic theory, (**b**) an example of laboratory-scale conductivity rig [66].

2.5.1.2 Theoretical models

The fundamental theory to predict the thermal conductivity of a solid and fluid composite phase can be based upon two models: series and parallel models (referring to the heat flow direction – Equation 2-7, 8). The models are functions of porosity, ε and both phases' thermal conductivity, k. The models represent the lower and upper bounds of the thermal conductivity range as these are based solely on the conductive heat transfer, neglecting the effects of convection [62], therefore more precise models were subsequently developed to predict more accurate effective thermal conductivity values.

$$k_{eff-series} = \cfrac{1}{\left[\cfrac{\varepsilon}{k_{fluid}} + \cfrac{(1-\varepsilon)}{k_{solid}}\right]}$$ Equation 2-7

$$k_{eff-parallel} = \varepsilon k_{fluid} + (1-\varepsilon)k_{solid}$$ Equation 2-8

Researchers generally built idealized cell models considering the geometric parameters of the foams and calculated the thermal conductivity based on thermal resistance analyses. The solid phase properties are those of the metal foam skeleton whereas the saturated fluid phase is either air or water properties, which can be substituted by the PCM properties. Ranut *et* al. [67] presented an excellent analysis of the available empirical and theoretical correlations whereas Xiao *et* al. [64] attempted to validate the prominent models with paraffin/high porosity (>90%) metal foam composites. From these and other similar works, some conclusions can be made:

- Among the models available in literature, the older, more established empirical models are popular because they have been experimentally validated numerous

times (to a varying degree of success). This includes the models of Calmidi and Mahajan [68], Dul'nev [69], as well as Boomsba and Poulikakos [70]. The newer, more complex theoretical models do not lead to better results in most cases [71].

- So far, all models assume the density of the liquid phase to be constant with its solid phase, which is untrue in the case of PCMs, as they undergo volume change whilst melting/solidifying. The conductivity of the solid phase has also assumed to be equal to that of the liquid phase. Recently, Xu *et al.* [63] established a model that considered the shrinkage of the PCM, which was validated only for very high porosity foams (97-98%) by Xiao *et* al. [64].

- Most of the models so far have been experimentally validated solely with high porosity foams, in the range of 89-98% and generally utilizing paraffin PCMs [71]. Therefore, there exists a gap in this subset of PCM research that needs to be addressed, which is the applicability of these models to the lower porosity foams (<80%) and to other foam material/PCM combinations.

2.5.1.3   Realistic model method/homogenization

The previously discussed models were derived solely from idealized foam structures. Another method is to realistically produce the foam structure to be examined via X-ray microtomography (μCT) scan. A μCT scan produces a series of 2D images by making recordings during a 360° rotation of the sample around its vertical axis (Figure 2-21). The 2D images are then stacked to produce a 3D volume, in which the elemental digital units are called 'voxels'. This method is non-invasive and ideal for use here as the integrity of the sample must be maintained. The 3D volume can be manipulated for various analyses e.g. direct visualization for anomaly detection in organic samples (medical sciences) and for solid modelling, which can be used in computational fluid dynamics (CFD) simulations, one of which is the heat transfer simulation to calculate the effective thermal conductivity. In this method, a cubic domain derived from the reconstructed 3D volume is assigned boundary conditions as shown in Figure 2-22. A thermal gradient is established between the opposite boundary faces of the cube model and the peripheral surfaces are considered adiabatic. The fluid phase is considered stagnant/motionless therefore, momentum equations are not solved, only the energy equation is involved:

$$k_{eff} = \frac{-\int q.dA}{\frac{\delta T}{\delta x}.A} = \frac{-\left(\int_s q.dA_s + \int_s q.dA_f\right)}{\frac{\delta T}{\delta x}(A_s + A_f)}$$

<div align="right">Equation 2-9</div>

Where subscripts s and f refer to the solid and liquid phase, respectively. This equation is a rearrangement of Equation 2-6. Ranut *et* al. [72] compared this method with experimental values available in literature based on foam porosities (88-98%) and water/air as the fluid phase, with a good agreement. Zafari *et* al. [61] also validated this method for 85-95% porosity aluminium/copper foams but observed a small discrepancy, which was attributed to the impurity of the foam samples. Their results indicate that: 1) the k_{eff} value decreased from ~10.0 to 2.5 W/m.K as the porosity increased from 85 to 95% (aluminium, air composites), 2) the models presented in Calmidi and Mahajan [68] and Boomsba and Poulikakos [70] agreed well with the realistic model method in this porosity range, and 3) a high degree of anisotropy observed within the samples as the k_{eff} values obtained from different directions i.e. x,y,z-axes varied considerably.
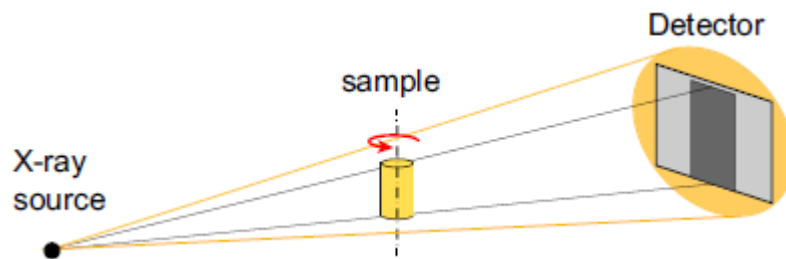
Figure 2-21 The working principle of an X-ray μCT (cone beam type) [72].
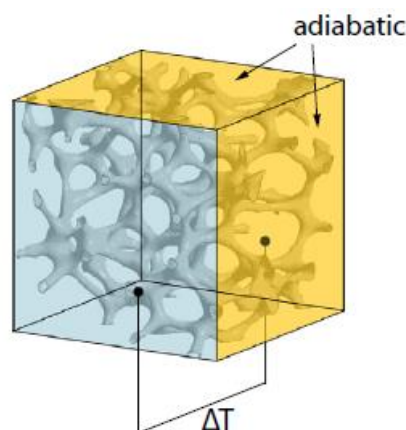
Figure 2-22 The domain and its boundary conditions for the calculation of effective thermal conductivity [72].

2.5.2   Numerical simulation techniques

Numerical simulation is an important subset of PCM research as it enables the understanding of the phase change process as well as being the basis for rapid prototyping of PCM-based devices through modelling and simulation. The fundamental problem to be solved is the identification of the position of the solid/liquid phase boundary, which moves with time (transient). This interface is non-linear in nature and is controlled by the latent heat lost or absorbed at the boundary. Currently, the 'enthalpy method' is commonly used to track the interface albeit implicitly, through the formation of a mushy zone or 'melt front' (Figure 2-23). A sharp interface can be tracked via the 'temperature method'. However, this method has proved to be too complex to solve as it utilizes discrete energy equations for both phases, compared to a single energy equation in the former method [73]. The equations for the enthalpy method (also called 'enthalpy porosity technique') can be found in Al-abidi *et* al. [74] or in Section ??? (Chapter 5). To numerically solve these equations, researchers utilized various software e.g. Matlab or Fortran (for direct, line-by-line coding), COMSOL Multiphysics, Star-CMM+, and Ansys FLUENT. It is relatively easy to simulate heat transfer in simple PCM heat exchangers e.g. shell and tube and plates. However, the same cannot be said for the complex geometry of metal foams. Broadly speaking, to simulate thermal fluid flow in porous media, two methods can be employed: *microscopic* (pore scale) and *macroscopic* (volume average) procedures.
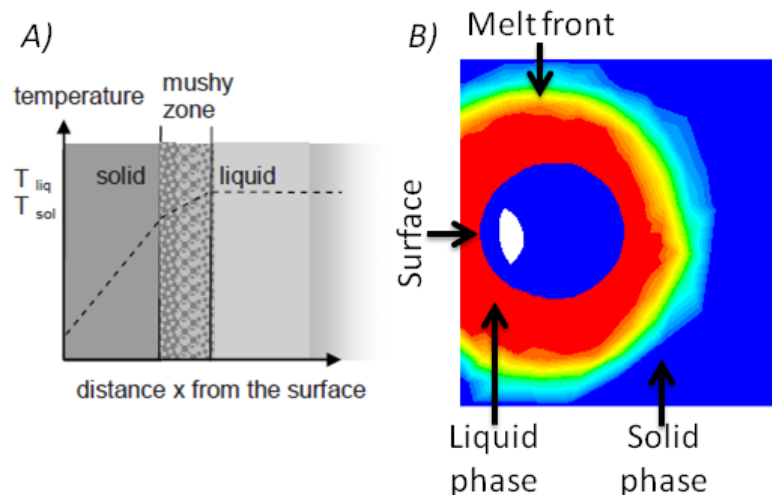
Figure 2-23 **Mushy zone or 'melt front'** (**A**) during PCM cooling process [1], (**B**) during heating process (simulated with Ansys FLUENT).

2.5.2.1 Pore scale

The pore scale method involves accounting for the actual foam geometry through idealized (a model developed from scratch) or realistic (a model formed from microtomography) approaches (Figure 2-24a). This method directly couples the heat transfer and fluid flow between the foam matrix and PCM. Pore scale simulation unfortunately requires a huge amount of computational power and is therefore limited to small scale studies i.e. a few foam cells. Relatively few researchers have employed this method e.g. Sundarram *et* al. [75] and Chen *et* al. [76]. The latter used a lattice Boltzmann model to study two dimensional pore scale melting and obtained good agreement with experimental results.

2.5.2.2 Volume average

In the volume average method (Figure 2-24b), in spite of the pore-scale distribution, only global thermal fluid flow in the domain is solved via the volume-averaged governing equations. Based on local thermal equilibrium or non-equilibrium assumptions, the volume average method may employ either the one or two temperature model as the energy equation. The one temperature model utilizes an identical energy equation for the two phases (solid/liquid) of the domain whereas the two temperature model employs a distinct energy equation for each phase. So far, most researchers employed the volume average method with the two temperature model – however, a recent thorough investigation by Feng *et* al. [77] has revealed that it is unnecessary to use the two temperature model as it could potentially produce numerical errors, in addition to being more complicated to implement.
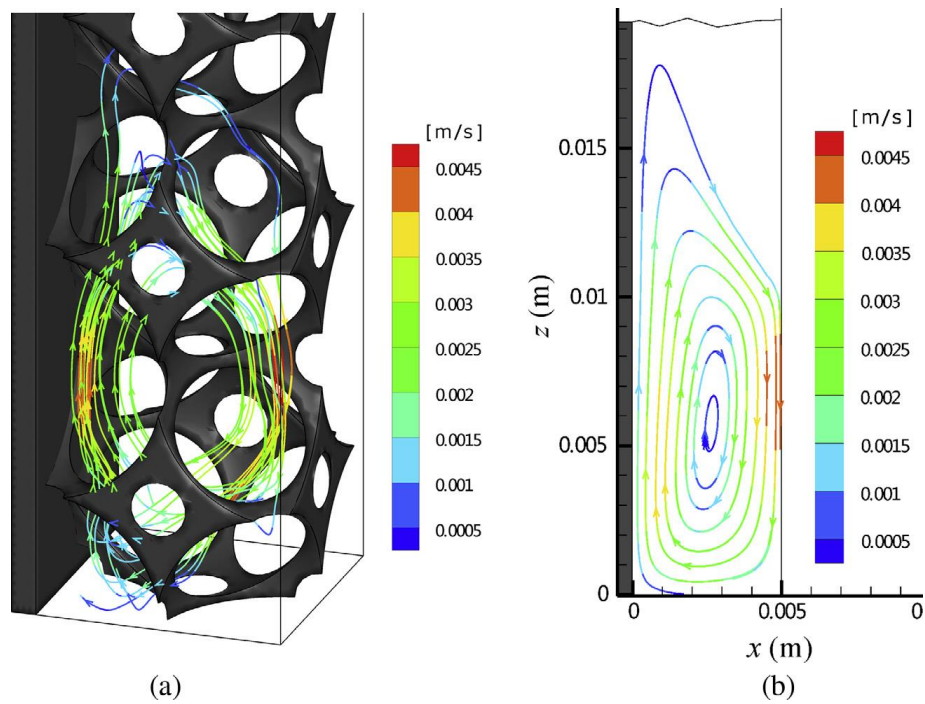
Figure 2-24 **Side-by-side comparison of PCM melting simulation between** (**a**) pore scale, (**b**) volume average approaches. Note: liquid fraction at 50% and contours showing flow streamlines (from Feng *et* al. [77]).

2.5.3 Discussion and analysis

Due to the nature of the metal foam prototype being highly irregular (Figure 2-25B) with unpredictable and random geometries, an accurate model must be realized through the CT scanning route as opposed to common metal foams, which can be idealized to estimate the properties (Figure 2-25A). As argued by Ranut *et* al. [71], properties such as effective thermal conductivity and porosity obtained through the CT scanning route are more accurate. However, given that it is time and resource consuming, it is not always cost effective and is justifiable only for special cases. As mentioned in Section 2.5.1.2, the empirical models were derived from idealized foams and are limited in their experimental validation within the high porosity range of >85%, which are therefore not necessarily applicable to the prototype as its porosity is unknown. Prediction of PCM thermal performance within the prototype could not be represented by pore scale simulation because of its random nature. It was therefore decided that the simulation effort would employ the volume averaging method with the singular temperature model to strike a balance between accuracy and complexity, (Figure 2.25B).
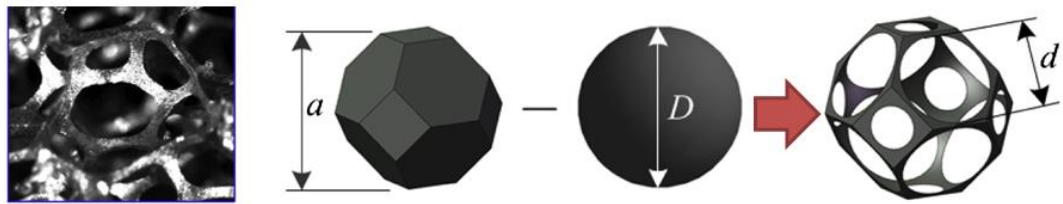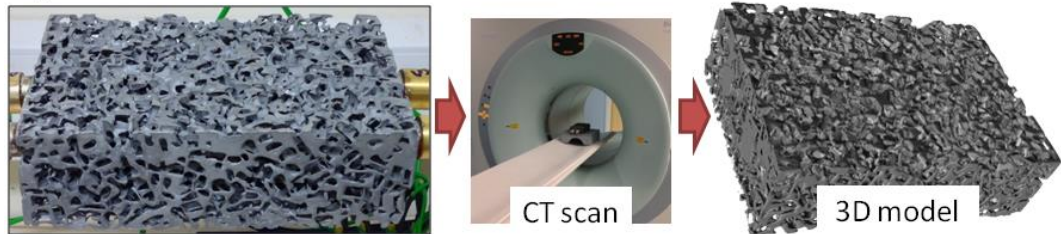
Figure 2-25 (**A**) Idealized modelling route for common metal foams [77], (**B**) realistic route suitable for highly unpredictable foam geometries.

2.5.4 Preparing a PCM/metal foam composite

The ensuing discussion relates to the established techniques to prepare the PCM/metal foam composite in the laboratory and its characterisation.

2.5.4.1 Impregnation procedure

Figure 2-26 shows the basic procedure to 'impregnate' metal foam with PCM. The steps are as follows: 1) a closed container is prepared, which contains the PCM in its solid form with the foam placed on top. The air in the container can be evacuated using a vacuum pump (or not; this is an option). The initial temperature is the room temperature. 2) The heating starts and the PCM slowly melts. The foam therefore slowly sinks into the molten PCM under its own weight. 3) The heating process carries on until the foam is fully immersed. Afterward, the set-up is allowed to cool to solidify the PCM. Steps 2 and 3 are time-dependent i.e. the duration is an important consideration to ensure an effective impregnation process whilst minimizing energy usage. 4) After the solidification is complete, the container wall is carefully heated to aid the composite removal (good care to not melt the already infiltrated PCM). PCM residues on the foam surface are then cleaned off.

Nomura *et* al. [78] impregnated expanded perlite with erythritol (a sugar alcohol PCM). Xiao *et* al. [55] impregnated nickel and copper foams with paraffins. These studies

concluded that the best impregnation process is achieved under vacuum conditions because otherwise, any air trapped in the metal foam matrix could hamper the PCM infiltration process. Nomura *et* al. established that time is indeed an important parameter. In their experiments, the longest duration procedure (1800s) impregnated 10% more PCM mass compared to the shortest duration one (600s). To assess the impregnation process effectiveness, a dimensionless ratio, α can be used:

$$\alpha = \frac{m_{actual}}{m_{ideal}} = \frac{m_{PCM}}{\varepsilon V_b \rho_{PCM-S}} \; (in \; \%)$$

<div align="right">Equation 2-10</div>

Where: m = mass (kg), ε = porosity (fraction), ρ = density (kg/m^3), and V = volume (m^3). Where subscript: actual, ideal = actual, ideal impregnation, b = bulk property, and PCM-S = solid phase PCM. This dimensionless parameter reflects the actual mass of PCM impregnated into the metal foam to the ideal mass able to be impregnated. The value is 100% if all porous voids are perfectly impregnated. Under 60 minutes of heating, Xiao *et* al. [55] were able to achieve 93-96% impregnation ratios for paraffin/copper foam composites. Jiang *et* al. [79] was able to achieve 86-90% ratios impregnating aluminium foams with paraffins (under vacuum, 0.3-1.5h).
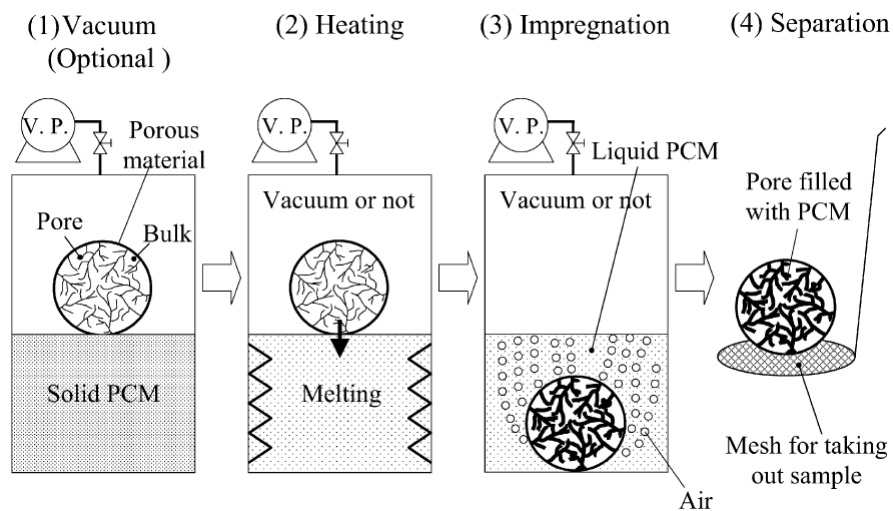
Figure 2-26 The basis of the PCM impregnation procedure [78].

2.5.4.2 Composite latent heat capacity

Once a good composite is prepared (as a consensus, α > 80%), the latent heat property is augmented by both components. Assuming a perfect impregnation, theoretically the composite latent heat, Q$_{comp}$ can be calculated as follows:

$$Q_{comp} = \frac{m_1 Q_{PCM} + m_2 Cp_S \Delta T}{m_1 + m_2}$$
<div align="right">Equation 2-11</div>

Where Q$_{comp}$ = the latent heat of the composite (kJ/kg), Q$_{PCM}$ = the latent heat of the PCM (kJ/kg), Cp$_S$ = specific heat capacity of the foam (kJ/kg.K), ΔT = temperature lift (K), and m$_1$, m$_2$ are the mass fractions of the PCM and foam, respectively [79]. The mass fractions can be measured directly with laboratory scales by using before and after impregnation mass differences.

2.5.4.3 Discussion and analysis

It is established that a vacuum condition during impregnation is essential to ensure an effective process. The duration of heating is relative to the size of the foam e.g. the sample in Jiang *et* al. [79] was 10 x 10 x 24 mm (2.4 x 10^3 mm^3) and it took 1.5h at most to achieve a 90% impregnation ratio. The dimension of the foam prototype to be used in this project is 50 x 114 x 165 mm (9.4 x 10^5 mm^3), which is significantly larger. Hence, the heating must be carried for significantly longer irrespective of the ensuing energy usage. Different foam materials could affect the impregnation process; as evident in Xiao *et* al. [55], where it was shown that copper, a higher conductivity material performed better than nickel. Similar effects were observed between PCM materials – paraffin performed better than stearic acid in aluminium foams as reported by Jiang *et* al. [79]. Impregnation of salt hydrate in any foam material has never been attempted. This would be challenging to handle in particular due to its hard solid texture, which is different than the waxy texture of the paraffins.

2.6   Metal foam as a steady state heat sink

Open cell metal foams have been considered to be one of the most promising enhanced surfaces due to their characteristics, the most prominent being: high heat transfer area to volume ratio, excellent stiffness and strength, and enhanced flow mixing capability. Such features are beneficial in numerous applications e.g. heat exchangers, combustion chambers, cladding on buildings, catalytic beds, air cooled condensers, petroleum reservoirs, and compact heat sinks [80]. Figure 2-27 shows some examples.
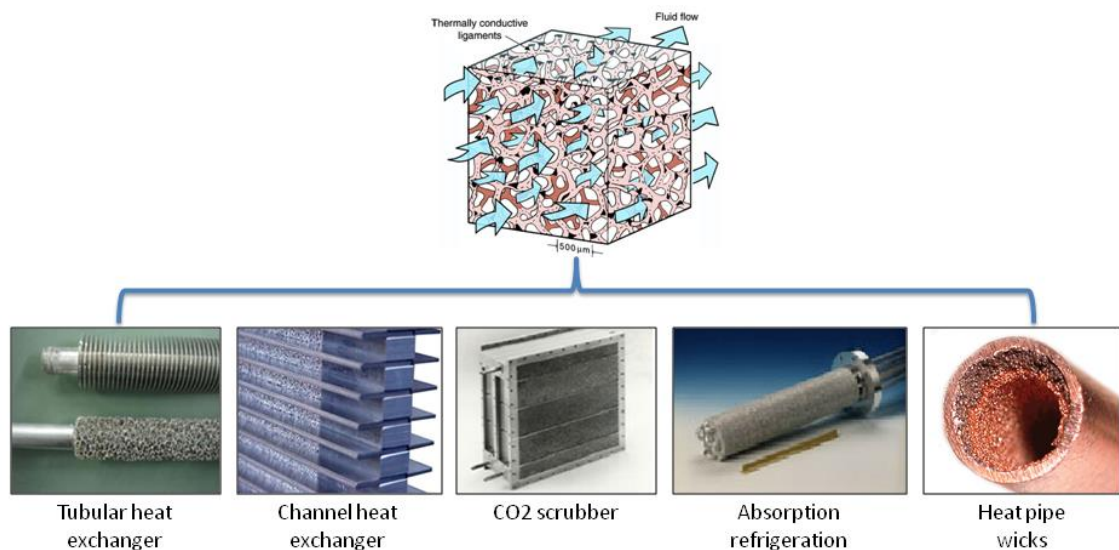
Figure 2-27 Example of heat transfer applications of metal foams (adapted from [81]).

2.6.1   Manufacturing routes

To start, a brief discussion on the manufacturing processes of metal foam would be beneficial. Banhart *et* al. [82] presented an excellent review on this subject. There are several established methods, which include:

- **Replication**

Metal foam can be made by casting (infiltrating) molten metal around space holders (preforms) to retain voids in the melt. By removing these space holders via chemical or thermal methods, a porous metal structure can be produced. An example would be aluminium metal foam made from sodium chloride (salt) preforms. This method has the advantage of being inexpensive. The salts are non-toxic and easily leached by water. The

pore size and porosity are flexible by varying the preform quantity, size and shape (Figure 2-28) as well as changing the infiltration methods and pressures [83].
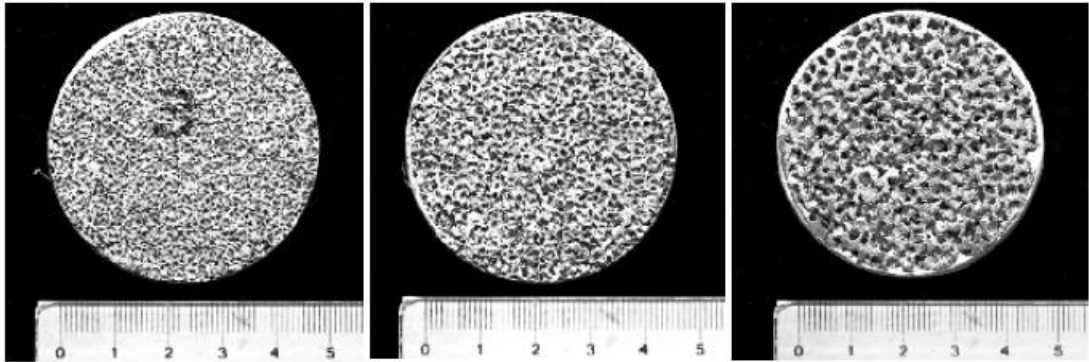
Figure 2-28 Small, medium, and large (left to right) pore sizes made from different preform sizes, an example of work by Barari, 2013 [84].

- **Direct foaming**

Molten metal can be foamed directly by creating gas bubbles in the melt. Normally, due to the buoyancy forces in high density melts, the bubbles tend to rise quickly to the surface. This can be hampered by increasing the viscosity of the melts via the addition of ceramic powders or alloys. There are two ways to directly introduce bubbles: via direct gas injection from an external source or via in-situ gas formation by premixing the melt with gas-releasing blowing agents [85]. An example is described in the patent for the use of zirconium hydride (ZrH_2) as the blowing agent for aluminium melt [86].

- **Electro-deposition**

By using the ionic state of metal as the starting material (i.e. ion solution in an electrolyte), the metal is electrically deposited onto a polymeric foam with open cells, which is subsequently removed. Electro-deposition on polymer foam requires some electrical conductivity of the initial polymer foam. After electroplating, the polymer can be removed from the metal/polymer composite via thermal treatment [82]. An example is shown in the following Figure 2-29.
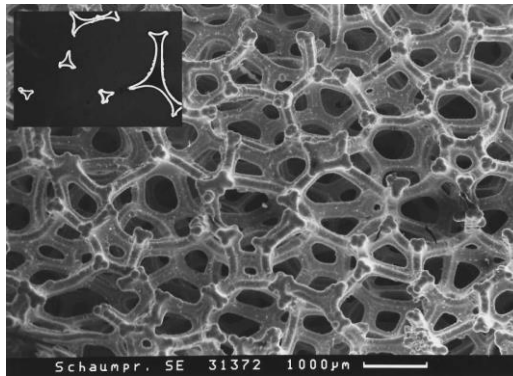
Figure 2-29 Nickel foam prepared by electro-deposition [82].

These and other methods are available for commercial manufacturing of metal foam. The production costs are coming down due to the metal foam's growing applicability and customer base. However, this does not infer a halt to research activities – an example can be found in Alantum Corporation alloy foams, which are sprayed with alloy powders to create bumpy surface along the foam struts, creating foams with a much larger specific surface area compared to traditional ones (Figure 2-30) [87].
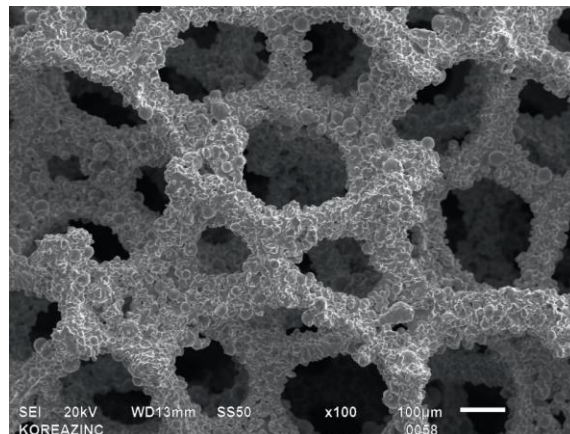
Figure 2-30 SEM micrograph of an Alantum Corp. alloy foam with bumpy surface struts [87].

2.6.2 Characterization methods

There are many avenues to characterize metal foam in order to obtain its physical/structural or mechanical data. The most important physical data are: pore and strut sizes, pore density (pore per inch; PPI), porosity, and surface area. Of these, specific surface area (SSA) is considered as the most important structural property because it is fundamental for momentum, heat, and mass transfer correlations. Mechanical data include Young's modulus, yield strength, and corrosion, among others. The available methods can be categorized as: 1) non-destructive and destructive, and 2) theoretical and experimental. Some prominent methods are concisely described here:

2.6.2.1 Mathematical models

This is the fundamental, easiest route and is derived from idealized geometric models, e.g. cubic cell, tetrakaidecahedra, 'cherry-pit' [88], and pentagonal dodecahedra models. These models are utilized to predict the SSA by using measured parameters such as pore/strut sizes and porosity. So far, numerous researchers have reported that the tetrakaidecahedra model (Figure 2-31) best matches experimental measurements [89]. This model was proposed more than a century ago by Lord Kelvin, and the model consists of six square and eight hexagonal faces in a cell [90]. As examples, Buciuman *et* al. [91] and Richardson *et* al. [92] used this model as the basis for the derivation of SSA correlations for foam with triangular strut morphology. Recently, Inayat *et* al. [89] improved the correlations with a good experimental validation. Researchers agree that these models only approximate the complex geometry of metal foams; as an example, the strut morphology (cross section, d_s; Figure 2-31c) could be a cylinder, triangle, or triangle-concave (cavity) [93].
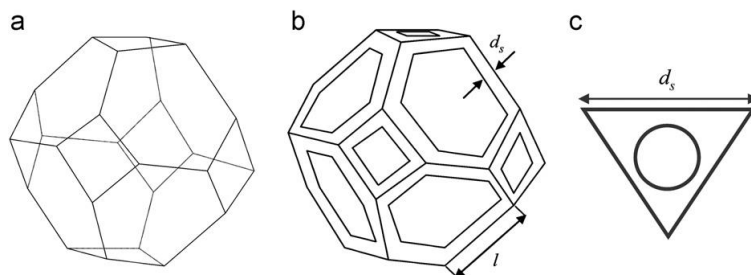
Figure 2-31 (**a**) Tetrakaidecahedron geometry, (**b**) representative cell unit model with triangular struts, (**c**) cross section of the triangular strut with an internal cavity [89].

2.6.2.2   X-ray microtomography (CT scan)

To relieve the limitations of the idealized geometry models, the X-ray microtomography method provides a solution. A primer of microtomography has been presented in Section 2.5.1.3. The complexity of this method is the acquisition of an accurate final model of the scanned sample, which is determined by CT scanner beam intensity, voxel size, X-ray focal spot size, sample material, image segmentation threshold, and more. Therefore, there is interplay between equipment, sample, and analytical parameters, which must be addressed in order to gain a high confidence level in the reconstructed 3D model. Equipment-wise, researchers often use high resolution 'desktop-size' microCT (µCT) scanners, which can provide resolutions at the micrometer (µm) scale. However, there is still a limitation in using µCT scanners – as a rule of thumb, for high resolution imaging, the sample size must be reduced to a minimum. The dimensions should not exceed 500-1000 times the resolution limit required [94]. Therefore an area of research has been concentrating on increasing the sample size limit whilst maintaining a high resolution. Recently, the Centre of X-ray Tomography at the University of Ghent (the UGCT), Belgium has developed a µCT scanner called *Nanowood*, which allows sample dimensions of up to 35cm with resolutions down to 0.4µm [95]. For now, the solution to scanning samples larger than the limits of µCT scanners is via conventional scanners with lower resolutions. To increase the accuracy of 3D models from these scanners, users can employ software solutions; a recent algorithm development by Simpleware in their ScanIP software package allows the creation of smooth surface models (Figure 2-32), which circumvents the traditional voxel-based models. This software algorithm refines the surface of models scanned from low resolution scanners [96].
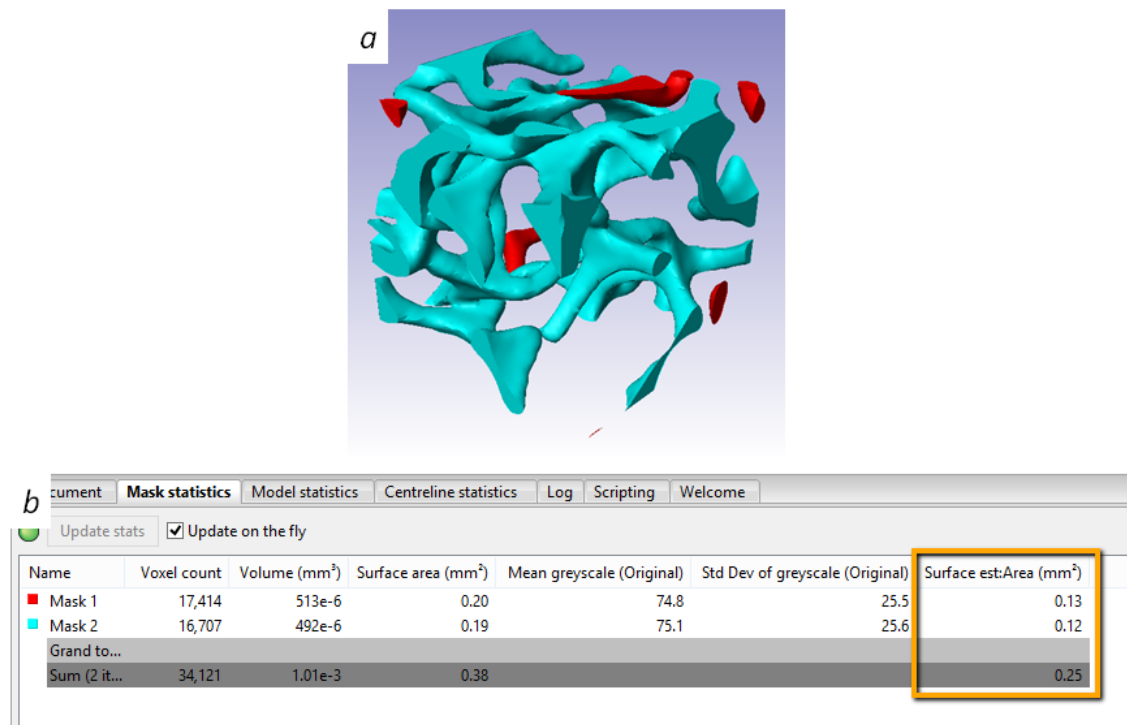
Figure 2-32 **Measuring structural properties of a scanned metal foam section via ScanIP software** (**a**) the reconstructed 3D model, (**b**) screenshot of the model statistics, with the surface area values highlighted.

2.6.2.3 Displacement method

This is a simplistic experimental method for the measurement of sample porosity. In volumetric displacement, the measurement of any two of the three volumes allows for the determination of porosity:

$$V_b = V_s + V_p$$

Equation 2-12

Where: V_b = bulk (total) volume, V_s = solid volume, and V_p = pore volume. The bulk volume can be measured by immersing the sample in liquid with any means of coverage e.g. adhesive tape or a paraffin coating to prevent seepage of liquid into the pores. The solid volume is the volume measured without covering the pores. The difference between these two volumes is adequate to calculate the sample porosity. This method is common in characterizing internal rock morphology, which can be applied for metal foam, and is simple, inexpensive, and non-destructive.

2.6.2.4   Gas adsorption (BET technique)

In physical gas adsorption, an inert gas (usually nitrogen) is adsorbed onto the surface of a solid material. In the case of porous materials, this happens on the surface of pores. Most popular is the determination of the BET (Brunauer–Emmett–Teller) surface area by gas adsorption. Adsorption of nitrogen at a temperature of 77K leads to a so-called adsorption isotherm, sometimes referred to as the BET isotherm, which is mostly measured over porous materials. Samples with low surface area can adequately be characterized by Krypton gas adsorption. In those cases, only a part of the BET isotherm can be measured, but this still provides a BET area with high accuracy. ERG Aerospace Corp. used the krypton gas adsorption to measure the SSA of their Duocel® metal foam products [97]. A bench scale BET analyzer is shown in the following Figure 2-33.
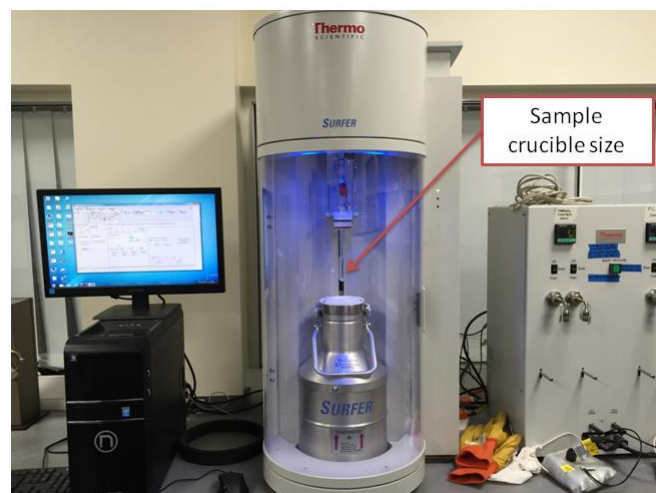
Figure 2-33 Thermo Scientific *Surfer* BET surface analyzer in Newcastle University. Marked is the crucible size for sampling.

2.6.2.5   Discussion and analysis

The discussion on some methods for characterizing metal foams/porous materials has been presented. The most important parameter for determining the heat transfer coefficient is the specific surface area. For the foam prototype to be examined (Figure 2-25B), the morphology completely deviates from the established models discussed, therefore they will not provide accurate SSA values. The only option is via a CT scan but given its dimensions, it does not fit in any μCT scanners. It was therefore decided to use a medical (conventional) CT scanner coupled with software augmentation for an

accurate 3D model development. There are many manipulations possible upon the reconstructed model such as the measurement of porosity and pore/strut sizes as well as internal structural assessment, which otherwise would require physical dissection of the prototype. CT scanning is still a complex and expensive route that uses an enormous amount of resource for equipment access, software analysis, and manpower. Therefore it is uneconomical for common foam samples. The porosity measured from the model can be validated via the displacement method. BET surface analysis cannot be applied to the prototype because it requires small size sampling, which also would imply destroying the prototype. Because BET is designed for nanoscale analysis, it can result in too large surface areas being reported, more than the apparent area for heat transfer [98].

2.6.3   Heat transfer coefficient

The heat transfer coefficient quantifies the heat transfer by means of convection between a flowing fluid and a solid surface. It is universally determined by indirect methods using an energy balance [99]. By using this principle, researchers such as Calmidi *et* al. [100] and Mancin *et* al. [101] have developed experimental test rigs based on the single blow method as in Figure 2-35. In this simple setup, a wind tunnel was constructed and foam samples were inserted. The base of the foam was heated and air is blown as coolant. The interchangeable nature of the foam samples allowed the study of heat transfer characteristics for different parameters, e.g. inlet air velocity, foam porosity, and pore density. As a guideline, the mean heat transfer coefficient, $\bar{h}$ is given by,

$$\bar{h} = \frac{q}{A_{base}(\bar{t}_w - t_{air,in})}$$
Equation 2-13

Where: $\bar{h}$ = mean heat transfer coefficient (W/m^{2}K), q = heat flow rate (W), A_{base} = foam base (cross sectional) area (m^2), $\bar{t}_w$ = mean wall temperature (K), and $t_{air,in}$ = inlet air temperature (K). The mean value, $\bar{h}$ is considered due to the difficulty of calculating local i.e. pore level heat transfer coefficients. The mean wall temperature, $\bar{t}_w$ is averaged over numerous thermocouple readings in the foam. It is important to note that the area parameter involved is only the surface area of the foam base, which indicates the $\bar{h}$

values calculated are not representative of the actual foam surface area. This method of accounting only the heat transferring surface was beneficial when researchers wanted to compare the thermal performance of foam heat sinks to common heat sinks such as the parallel plate heat sinks. An example is given in the following Figure 2-34 in the works of Seo Young *et* al. [102]. A recent work by Barari *et* al. [103] approximated the total surface area of their foam samples indirectly by measuring the surface area of ball bearings they used to fabricate their samples. They also suggested the use of computed tomography (CT) scan to accurately measure the surface area metal foams.
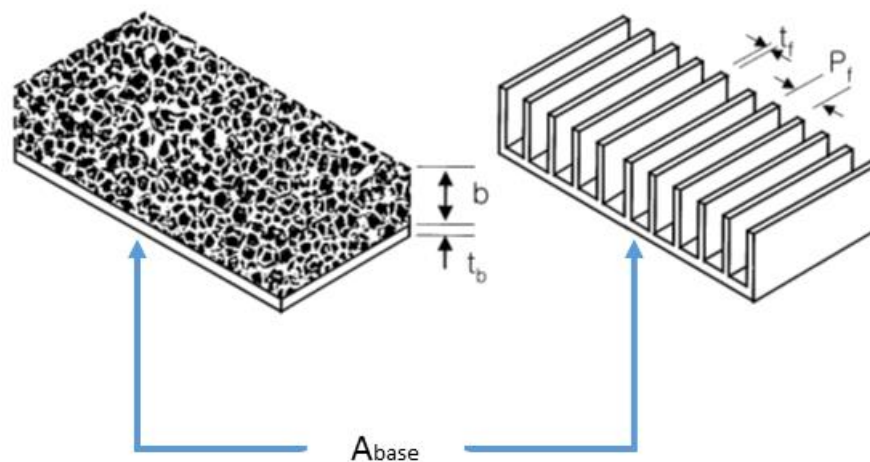
Figure 2-34 Like many other metal foam researchers, Seo Young *et* al. [102] employed the heat transferring surface, A_{base}, in their heat transfer coefficient calculations. In this figure, the base area is 30 x 90 mm for both the foam and parallel plate heat sink test units.

By employing pressure transducers upstream and downstream of the sample, pressure drop can be measured, which allows one to derive more important properties such as Nusselt number and permeability [80]. The work on metal foams so far mostly involved air as coolant, given its viability for applications ranging from air conditioning to electronics cooling. From the literature review (e.g. Hsieh *et* al. [104], Kim *et* al. [105], and Giani *et* al. [106]) several deductions can be made:

- Heat transfer coefficient increases with inlet air velocity raised to the power of 0.40-96, essentially <1.00 (refer to Figure 2-37 for an example of profile plot).
- Heat transfer coefficient is independent of the power supplied (heat flux, q) to the foam.

- At constant porosity, heat transfer is better at high pore density (PPI).

- At constant pore density, the heat transfer coefficient increases as porosity decreases.

- Heat transfer is dependent on the foam material e.g. copper exhibited better thermal performance than aluminium at constant porosity and pore density.
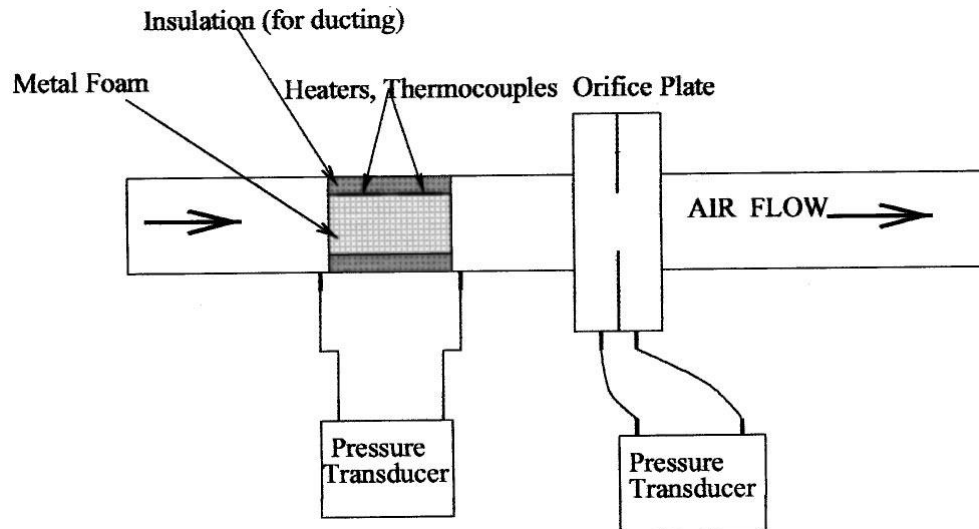
Figure 2-35 Experimental setup for forced convection tests in Calmidi *et* al. [100].

2.6.4 Flow field analysis

The three dimensional, complex solid structure of metal foams results in very complicated flow phenomena. In order to investigate heat transfer in metal foams, the details of both flow and temperature fields within the foam must be known.

2.6.4.1 Pressure drop

Pressure drop through a porous matrix can be represented by,

$$\frac{\Delta P}{L} = \frac{\mu}{K} v$$

Equation 2-14

Where: ΔP = pressure drop across the foam (Pa), L = length of the foam in the flow direction (m), μ = dynamic viscosity of the fluid (kg/m.s), K = permeability of the foam (m^2), v = Darcian velocity of the fluid (m/s).

This correlation was developed by Darcy in 1856 [107], which states that for slow moving fluids pressure drop per unit length (i.e. normalized pressure drop) of a porous medium is proportional to the dynamic viscosity and velocity of the fluid, and inversely proportional to the permeability of the porous medium. This correlation however, is only valid for low Reynolds number (Re < 2000) [108]. For higher velocities, Dupuit [109] and Forchheimer [110] suggested a quadratic velocity term to extend the original Darcy law to accommodate the impact of form drag at higher velocities. The model is as follows:

$$\frac{\Delta P}{L} = \frac{\mu}{K} v + \rho C v^2$$

Equation 2-15

Where: ΔP = pressure drop across the foam (Pa), L = length of the foam in the flow direction (m), μ = dynamic viscosity of the fluid (kg/m.s), K = permeability of the foam (m^2), v = Darcian velocity of the fluid (m/s), C = form drag coefficient of the foam (m^{-1}) and ρ = density of the fluid (kg/m³).

For flow with higher Reynolds number (Re > 2000), the pressure drop varies with velocity squared. As an example, tests performed by Barari [84] revealed pressure profiles as in Figure 2-36. It also shows that the largest pore sizes had smaller pressure drops. To present the complete picture, the heat transfer coefficients are plotted in Figure 2-37, which shows the increase of heat transfer coefficient with increasing Reynolds number. The largest pore size however, had the smallest heat transfer coefficient. An example of analyses via the microtomography method is presented in Figure 2-38 by the work of Zafari *et* al. [61].

In typical wind tunnel tests, an additional pressure drop is caused by inlet contraction and exit expansion that are usually taken as 1 dynamic head each, by heat exchanger designer. For foam samples, this value should be sufficient [111].
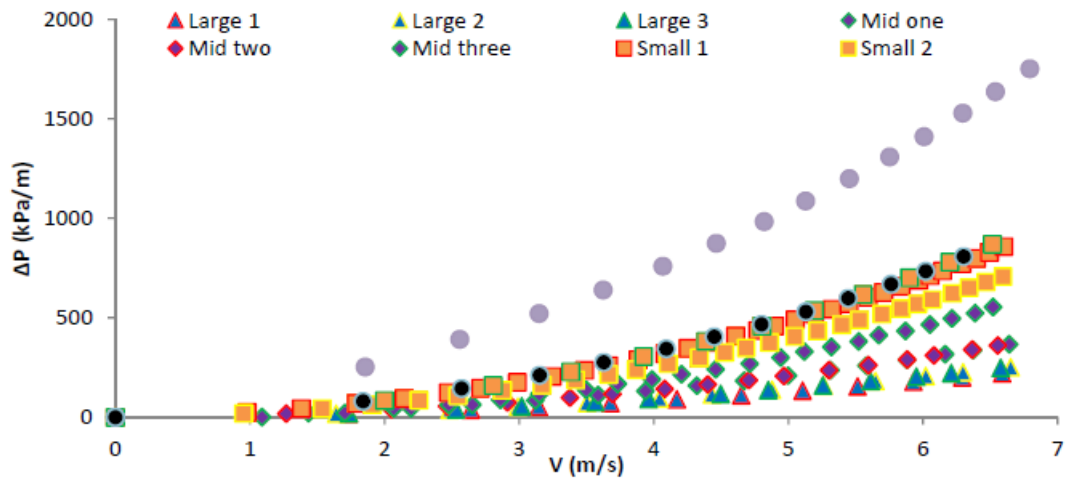
Figure 2-36 Normalized pressure drop (ΔP/L) of metal foam with three different pore sizes (three samples each) (refer Figure 2-28 for the foam pictures) [84].
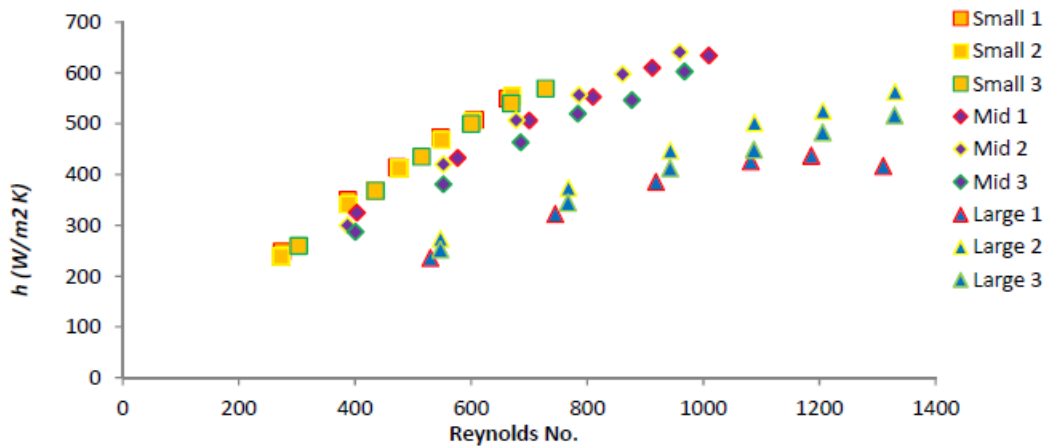
Figure 2-37 Heat transfer coefficient results for the samples in Figure 2-36 [84].
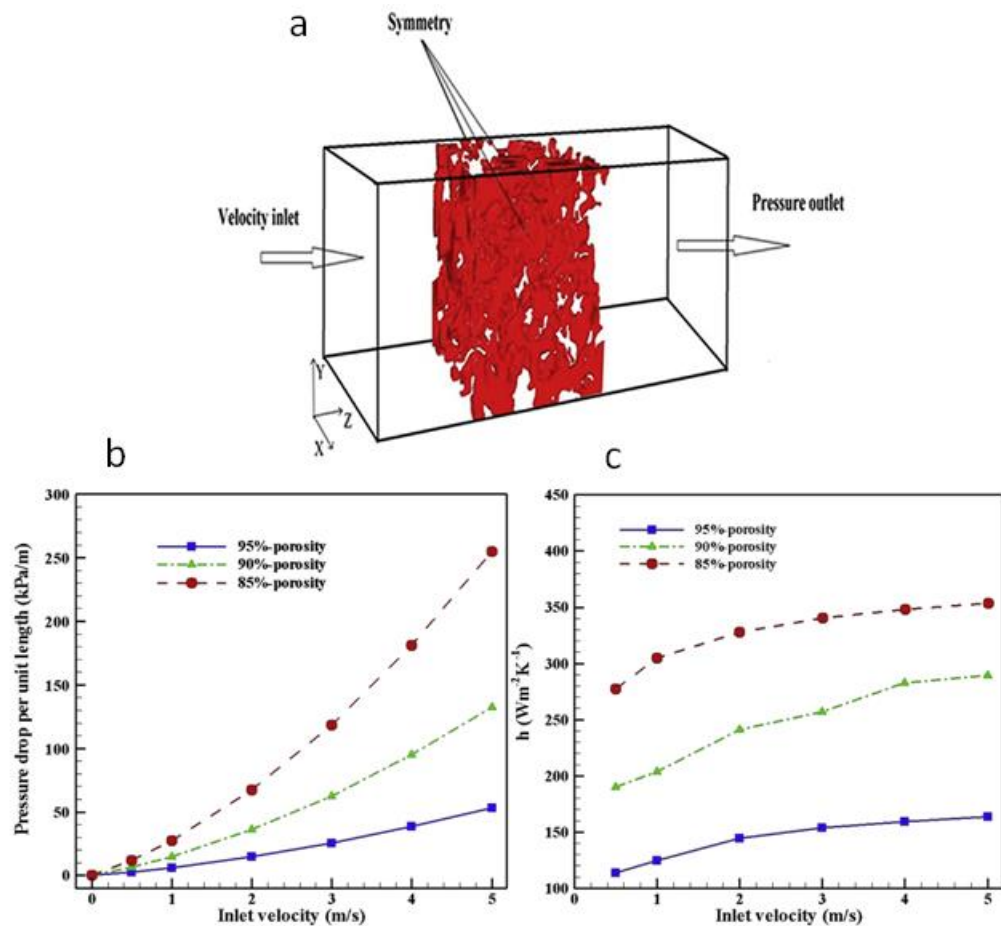
Figure 2-38 Microtomography-based analyses of Zafari *et* al. [61] for 85-95% porosity aluminium foams (a) the foam domain and boundary conditions, (b) normalized pressure drop, (c) heat transfer coefficient.

2.6.4.2   Permeability

Permeability, K is essentially the measure of ease of fluid flow through the metal foam. The common method of determining K or C (form drag coefficient) is by curve fitting the profile of normalized pressure drop as a function of Darcian velocity. In most cases, the flow is in the Forchheimer regime i.e. pressure drop is proportional to the square of velocity, in which the curve fitting equation is compared with Equation 2-15. K and C can therefore be easily determined [112]. The K values are usually in the power of 10^{-7} (m^2). A few are listed in Table 2-6, but an extensive list is available in Ranut *et* al. [72].

Table 2-6 Permeability for 20 PPI metal foams.

Porosity	$K \times 10^7$ (m^2)	Type	Reference
0.87	1.25	Experimental	Liu *et* al. [113]
0.90	2.18	Experimental	Kamath *et* al. [114]
0.91	1.61	Numerical	Bodla *et* al. [115]
0.98	1.42	Experimental	Bhattacharya *et* al. [68]

2.6.4.3 Tortuosity and thermal dispersion

The inherent random strut structure of foams creates at least two identifiable effects: tortuosity and thermal dispersion. The former refers to the solid strut whereas the latter refers to the flowing fluid.

- **Tortuosity**

Tortuosity, τ is simply the measure of a curve's deviation from being straight, which can be therefore be defined as:

$$\tau = \frac{s}{L_{ref}}$$

Equation 2-16

Where: s = length of the curve and L_{ref} = reference length, usually the scalar distance between the two endpoints (Figure 2-39). It is an indication of the degree of anisotropy in foams: if struts are more tortuous in the x-direction than in the y-direction, a higher thermal conductivity is exhibited in the y-direction due to the additional conductive resistance exhibited in the x-direction. Bodla *et* al. [115] measured tortuosity by creating nodal networks on µCT scan images, which yielded τ = 2.15 to 3.31, showing a considerable degree of anisotropy in their scanned foam sample. Brun, 2009 [116] measured tortuosity in a similar way, which yielded an average value of 1.33.
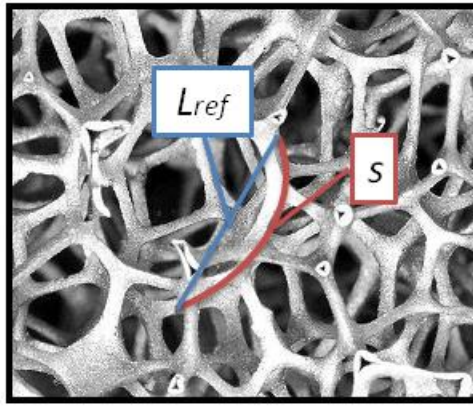
Figure 2-39 Parameters for the manual calculation of tortuosity.

- **Thermal dispersion**

Thermal dispersion is the spreading of heat caused by variations in flow velocity about the mean velocity. In addition to the molecular thermal diffusion, there is a mechanical dispersion of heat and fluid flow within metal foams due to the hydrodynamic mixing of fluid particles passing through foams. This effect causes an additional mode of heat transfer. A correlation applied by Calmidi and Mahajan [117] in their 95% porosity foams indicated that for a low air velocity (3m/s), the dispersion thermal conductivity was merely 3% of the stagnant (base) conductivity. This value rose to 27% when the flow was increased to 20m/s. This is a relatively scarce part of foam flow research, which needs further investigations [112]. Section 6.4.2.3 investigates this effect.

2.6.5 Foam-fin efficiency

As an extended surface for heat transfer enhancement, fin efficiency in metal foam heat exchangers is an important subject from the point of view of design considerations. Ironically, there are very few publications on it. Via a modelling approach, Mancin *et* al. [118] indicated that fin efficiency is a function of foam material, height, pore density (at constant porosity), and flow velocity. Some of the results are plotted in Figure 2-40, which indicate that lower conductivity material (aluminium < copper), increasing foam height and inlet air velocity have the effect of decreasing foam efficiency. Although not shown in the figure, increasing pore density also decreases efficiency. This part of foam flow research needs to proliferate further, especially, it needs to be experimentally investigated.
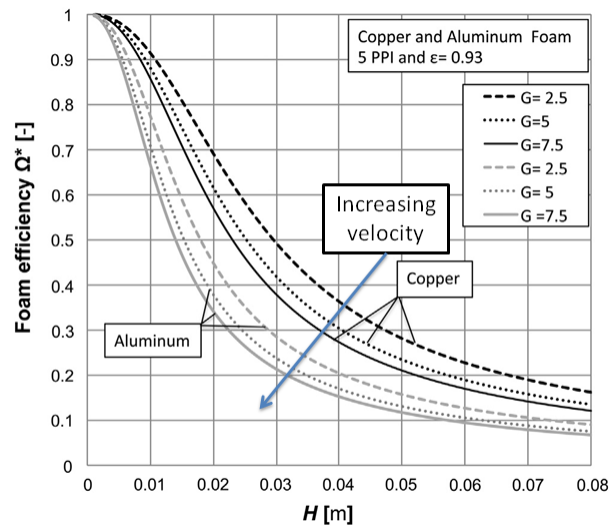
Figure 2-40 The effects of air velocity, G (in kg/m^2.s), foam material, and foam height, H (in m) on foam-fin efficiency (at constant porosity and pore density) modelled by Mancin *et* al. [118].

2.7 Future prospects and barriers for growth

A practical way to forecast the future prospect of any research subject is by looking at the history of publications related to it (Figure 2-41). For both PCM and foam-related research, there is a healthy trend with a significant rise since 2010. For PCMs, this could be due to the growing awareness of energy efficiency, fuelled by the necessity of mitigating the effects of global warming. Thermal storage, in particular using PCMs, contribute by overcoming the mismatch between thermal supply and demand as well as energy recovery. The forecasts of future PCM research points toward the development of bio- and nano-based materials. The self-recovery property of biological agents could be adapted in producing self-repairing PCM materials, which in theory could sustain themselves chemically to become long-life thermal batteries. Nanomaterials offer vast possibilities in the design of novel advanced composites with far superior properties to those of conventional materials [104]. In the *Arup* forecast of buildings in smart cities [105], it infers that in 2050 buildings would include PCMs as interior wall components, which act as heat recovery devices (Figure 2-42).

Some threats to the technology include:

- The critical lack of international technical standards for testing PCMs. This has led to research groups employing their own methods for characterizing energy

storage materials, which makes it difficult to directly compare thermophysical properties. This renders repetition of experiments rather than focusing on the development of advanced storage materials [104].

- The proliferation of thermochemical storage is expected to overtake the share of PCMs. Although it is still a complex technology, its advantages of very high energy density and negligible or zero thermal losses when reactions are not taking place are motivations for its extensive development.

Metal foams have been researched extensively by many research institutions and companies. Replacing conventional finned heat sinks with foams can be seen as a high potential application [106]. However, in the words of Schaffler, 2013 [107], the breakthrough has not yet happened. These are some of the reasons:

- There are so many types of foam material and manufacturing methods in the market without any clear standardized classifications. This issue creates confusion among customers.

- The lack of real knowledge in automotive and transportation industries, which is one of the target markets. Foam materials are relatively new to be in their internal database for comparative analysis with established materials.

- Cost is always seen as a major barrier for foam implementation in industry. The bulk price (per volume) is still high compared to competing materials. However, this is expected to be lowered over the next few years, when metal foams may well become competitive economically.
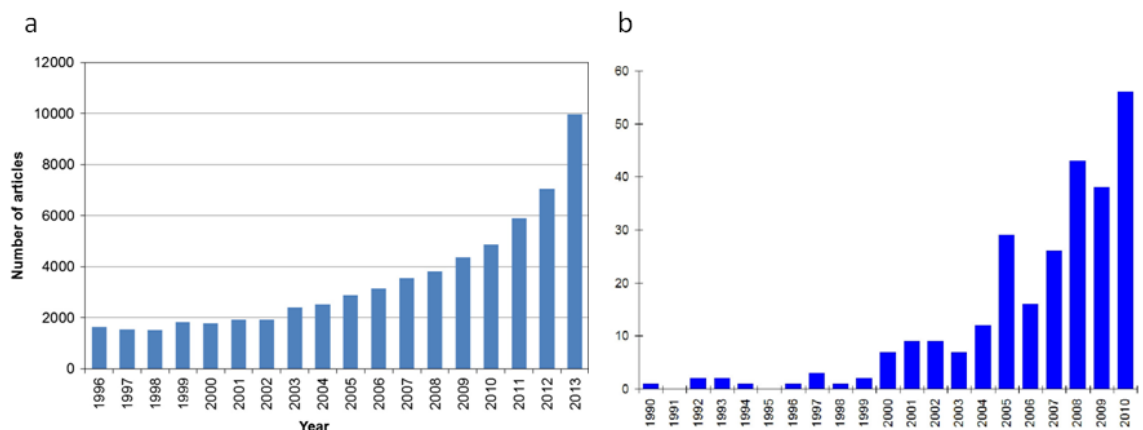
Figure 2-41 **Trends of publication (1990s-2010s) on** (**a**) PCM-related subjects [119], (**b**) metal foam-related subjects [98].

Figure 2-42 2050 outlook: the ubiquity of PCM as material for green buildings [120].

2.8   Conclusions and the next stage of the work

In establishing a transient heat sink based on phase change material, a holistic review on the subject matter has been carried out. To enhance its thermal conductivity, a novel irregular aluminium foam 'prototype' is to be used, performance of which as a steady state heat sink is also to be analysed.

- Salt hydrate PCM that melts at 46°C is selected due to its appropriate melting temperature for power electronics cooling. Its other advantages include high energy density and thermal conductivity, and acceptable volume expansion. It is sourced locally and has been treated by the supplier for melt congruency. Its robust corrosion data are readily available. However, it may suffer from supercooling and this must be confirmed experimentally.

- Discounting costs, metal foam is fundamentally the best method to enhance the very poor PCM thermal performance due its high specific surface area, light weight, extensive strut network, high conductivity material choices, and the ability to retain fluid within its tortuous strut paths. However, when economics and practicality are considered, simpler methods like fins and microencapsulation are preferred, depending on applications.

- The aluminium foam to be used was manufactured using a novel process, which gave its characteristic pore irregularity. Its departure from idealized geometries,

for which proven empirical models have been derived, prompted the use of a CT scanner for characterization of structural and thermal properties via 3D model reconstruction. Only the low resolution, conventional CT scanners can be used due to the sample exceeding the size limit for microCT scanners. Recent software development could refine the accuracy of the models created from low resolution scanning by the 'smoothing surface' approach.

- Numerical simulation of the thermal fluid flow of the PCM/metal foam composite will employ the 'volume averaging' approach because pore scale approach would not represent its inherent irregularity. The latter approach is also impractical for full scale modelling and would require massive computing resources.

- To ensure an effective impregnation process, the vacuum method is chosen. There is no precedence for salt hydrate/metal foam operation in literature. Therefore, the duration of the heating process is extended beyond those reported i.e. >3h, regardless of the energy penalty.

- Heat transfer coefficient measurement of metal foams is usually based on the energy balance principle without involving the actual surface area value. By using the accurate surface area from a CT scan-derived model, characterization of steady state thermal and fluid flow performance of the foam prototype would be considered precise, and truly representative of the actual heat sink. This would also allow direct experimental investigation of the foam-fin efficiency, which has never been attempted.

- Cost has always been judged as the barrier for metal foam industrial implementations and it will take more years for engineers and architects to become familiar with it, despite current volume industrial production. An economic alternative in the form of 'metal mesh' has been introduced in the Literature Review for PCM applications.

With regard to the next stage of the research, it was necessary to establish the precise form of the metal foam sample so that its morphology and performance could be characterised.

This was carried out, as reported in Chapter 3, by:

- Measuring the surface area of the foam sample, which has random pore and strut morphology.
- Detecting any defect(s) due to manufacturing issues.
- Creating a 3D model of the foam to characterize it i.e. porosity and manipulating the model for CFD (flow) modelling.

This was done by scanning the foam in a medical CT scanner and then using software to allow an analysis of the internal structure for modelling purposes and to aid understanding of later experimental data.

Chapter 3   Three-dimensional reconstruction of the irregular foam

3.1   Abstract

In Chapter 2, it was decided that in order to effectively accelerate the energy charging and discharging processes of phase change material, metallic foam must be embedded into it. The metal foam selected is a novel aluminium foam consisting of irregular pores: rectangular pore size 8.41±2.09 mm and oval pore size 6.69±1.00 mm. It must be characterized in terms of its structural parameters i.e. porosity and specific surface area. Its extreme physical deviation from common metal foams prevented the use of common metal foam characterization techniques i.e. established numerical and empirical models. Instead, it was scanned by using a medical CT scanner, generating a 3D model, from which crucial information were acquired. The following data were derived: 1) porosity: 67% and 2) specific surface area: $1495 m^2/m^3$. In addition, its pores were found to be rectangular and oval shapes with a high degree of heterogeneity. A manufacturing defect was detected in the form of a ring-shaped dense region at the lower bottom of the foam. For the normal region of the foam, it exhibited a uniform porosity and specific surface area despite of the apparent pore irregularity. The data extracted were used for heat transfer and fluid flow analyses, as the foam was intended to be used as a heat sink. The confidence level of the 3D model accuracy was very high as the model porosity was validated experimentally (model porosity: 67 % whereas experimental porosity: 67±3 %). Recent software development enabled the creation of model with smooth surface, bypassing traditional voxel-based analysis. This negated the necessity for high resolution microCT scanners, which were limited in sample size. Larger sample could therefore be scanned by using lower resolution CT scanners and the model reconstruction accuracy would be enhanced software-side.

Keywords: irregular metal foam; heat sink; X-ray computed tomography; non-invasive evaluation; porosity; specific surface area

3.2 Introduction

In Chapter 2, an extensive literature review was carried out in order to develop a transient power electronics cooling concept for traction systems. The review specified a heat sink based on phase change material, which is to be embedded with metal foam in order to accelerate the energy charging and discharging processes.

Metal foam is a cellular structure made up of solid metal with a large volume fraction of pores. These pores can either be sealed (closed cell foam) or they can form an interconnected network (open cell foam). Open cell metal foams possess high surface area to volume ratios (specific surface area), tortuous flow paths, and high stiffness and strength. These features of open cell metal foams make them attractive to be applied as heat exchangers, electronic heat sinks, energy absorbers, air-oil separators, etc. [121]. Metal foam base material is usually aluminium. However copper, nickel, and metal alloys are also common. Carbon and ceramic foams are also feasible. Most commercially available metal foams have homogeneous open cell size and shape [80] (Figure 3-1d). Because metal foams have been around for many decades, they are well described in the literature. In this study, the aluminium metal foam studied is uniquely heterogeneous with regard to its pore and strut morphology, which is henceforth termed as the 'irregular aluminium foam prototype' or 'irregular foam'. It is primarily intended to be a forced convection heat sink, an alternative to the common fin stack heat sink.

3.2.1 The irregular aluminium foam prototype
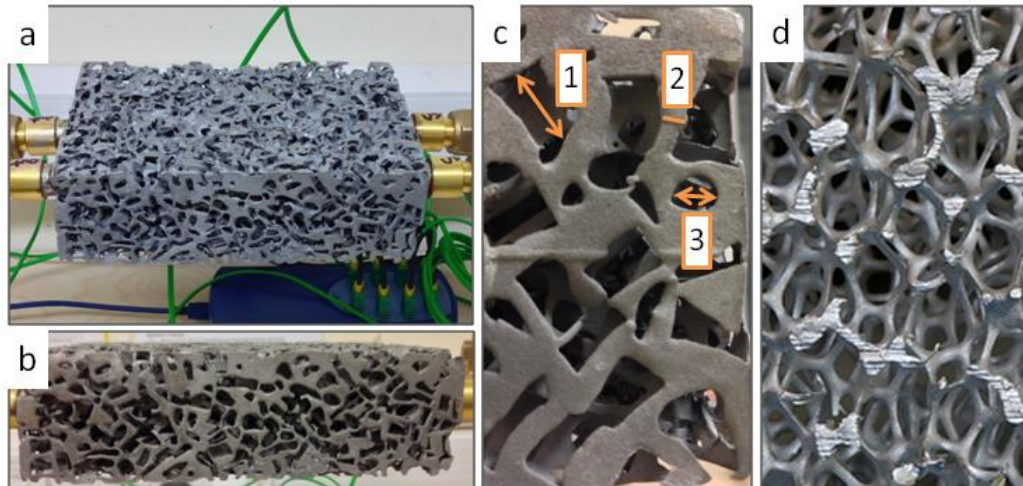
Figure 3-1 **The irregular, open cell aluminium foam** (**a**) overview. Note the pipes embedded through the foam as liquid coolant conduits, (**b**) the profile view, (**c**) a close up view of the pores and struts. The definition of size for (1) rectangular pore, (2) strut thickness, and (3) oval pore, (**d**) a close up view of a common metal foam.

The foam prototype is shown in Figure 3-1. It is clear (Figure 3-1c vs. d) that the pore and strut morphology is not similar to conventional metal foams. The foam was supplied by Thermacore Europe Ltd., Ashington, UK. The company sourced the foam from a classified manufacturer. The foam was made via the 'replication' route (see Conde *et* al. [83] and Banhart [85]) by using multi-shape salts as the preformer. The preformer could then be compressed to give a flexible solid strut size, which was a novel approach for foam manufacturing. The manufacturer hypothesized that this heterogeneous morphology would induce greater air flow mixing than common metal foams. This could cause thermal dispersion effects. This is examined in Chapter 6.

Upon receipt of the prototype, the manufacturer supplied only the foam specifications below (Table 3-1), hence the exact specifications of this prototype had to be independently determined. Cellular materials are typically characterised by pore and strut size, pore density (PPI), and porosity, ε, among others [80]. Because the foam was primarily intended to be a heat sink, its actual heat transfer surface area was of a particular interest for a precise heat transfer coefficient calculation. Due to the irregular structural characteristic of the foam prototype, it was difficult to estimate the surface area through mathematical models (refer Elsner *et* al. [88] and Druma *et* al. [122]), hence direct measurement of the surface area was necessary. Therefore in this study,

the foam prototype surface area was measured through an accurate three dimensional (3D) model constructed from an X-ray computed tomography (CT) scan. The porosity (the ratio of voidage volume to total volume) was also determined from this model. Furthermore, the model was used to assess and quantify any manufacturing faults through an internal topology analysis, which would have been impossible from visual observation alone. In Chapter 5 and 6, the model was used for finite element (FE)-based and computational fluid dynamics (CFD)-based simulations.

The work described here is an important contribution to the analysis of an unusual form of heat exchanger – one for which it would not be possible to characterise accurately using methods other than an internal topographical analysis using CT scanning and computer analysis.

Table 3-1 Manufacturer specifications. The structural data were imprecise for use in thermal and fluid flow calculations. This study aimed to provide accurate data.

Pore size (diameter)	>1mm
Porosity (% void)	50-80%
Young's modulus	5-1GPa (65-80% porosity)
Yield strength	17-7MPa (65-80% porosity)

3.2.2   X-ray computed tomography

X-ray computed tomography (CT) involves taking a number of X-ray radiographs at different angles by projecting an X-ray beam through a specimen. CT images are formed on a detector by the X-rays that attenuate in energy as they passed through the specimen via scattering and absorption. The attenuation depends principally on the thickness and density of the specimen in the beam direction. The attenuation is exponential to the specimen thickness and is represented by Beer's Law,

$$I = I_0. \exp(-\mu t)$$

<div align="right">Equation 3-1</div>

Where: I = X-ray beam intensity after passing through the specimen (keV), I_0 = X-ray source beam intensity (keV), t = thickness of the specimen in the beam direction (mm), and μ = X-ray linear attenuation coefficient of the specimen material (mm^{-1}).

The grey level value of each pixel in each two dimensional (2D) CT image is an indication of the net intensity, I, of the X-ray beam emerging from the object in the direction along the line connecting the X-ray source to the image pixel. The 2D CT images produced from different directions are then stacked to form a 3D volume reconstruction of the specimen with a finite thickness equal to the voxel (volumetric-pixel) resolution [123].

The I and I_0 are described in terms of peak X-ray energy in keV unit, which is determined by numerous factors such as the X-ray energy source, beam hardening, autofiltration, and beam detector efficiency [124].

3.2.3   CT scanner classifications

CT scanners are generally classified based on their voxel resolution (Figure 3-2a) and specimen size limit. The lowest resolution, conventional CT scanners (e.g. medical CT scanners) (Figure 3-3a) can scan specimens at metre scale with millimetre scale resolution whereas the highest resolution CT scanners (microtomography or microCT scanners) (Figure 3-3b) can scan specimens in millimetre scale with the resulting micrometre resolution. Several parameters contribute to the resolution such as the spot size, the distance between beam source/specimen/detector, and the X-ray beam source energy. The interplay between these parameters and the resolution is well described in Richard *et* al., 2001 [124] and therefore will not be repeated here. Essentially, higher resolution CT scanners produce higher quality i.e. more detailed images, therefore microCT scanners are preferred. However, the resolution of microCT systems rapidly degrades with increasing specimen size. For example, Carl Zeiss' XRADIA Versa XRM 500 microCT scanner resolution decreases from 0.7 - 20.0µm for sample size 20 - 100mm [125]. Recently, a team at Ghent University (UGCT), Belgium developed a novel microCT scanner that could scan specimens of up to 350mm with a 5µm resolution [126]. This equipment however, was in the research stage. The foam prototype size was beyond the limit of any available microCT scanners, which was 165mm at its maximum dimension. Therefore only medical CT scanners could be used despite their low

resolution. The prototype had also to be returned to the owners in its original form i.e. physical segmentation, which would imply destruction, for thorough analysis was not allowed.
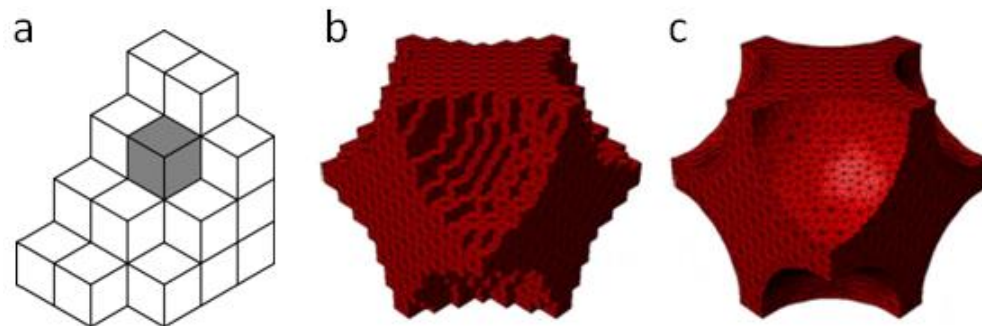
Figure 3-2(**a**) A voxel finite unit (i.e. the scanner resolution) shaded within an array of voxels, (**b**) the model with a stepped voxel surface, (**c**) the model with a smoothed surface [96].
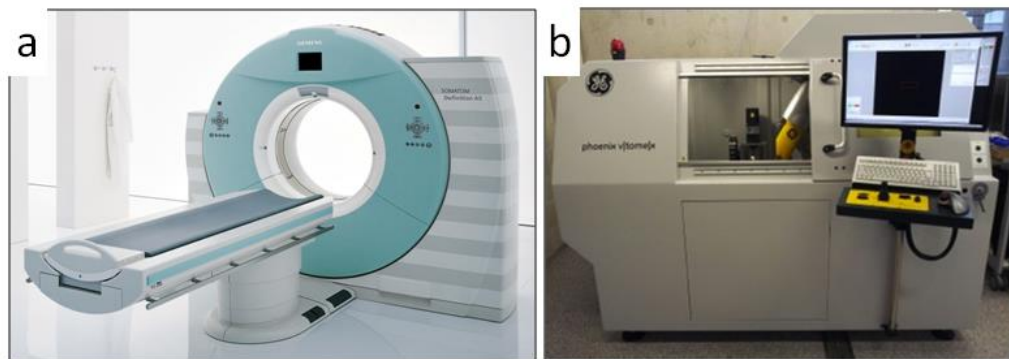
Figure 3-3 **An example of** (**a**) medical CT scanner, (**b**) microCT scanner [127].

3.2.4   Software

Figure 3-2b shows a 3D model constructed with a conventional stepped voxel surface from which the surface area could be measured. Accuracy of the measurement is therefore a function of the voxel size (Figure 3-2a). A smaller voxel size from a higher resolution scanner creates a more refined model. This is why microCT scanners are preferred over conventional CT scanners. A recent software development from Simpleware [96] enabled the creation of a smoothed surface model (Figure 3-2c) whilst preserving its volume and topology. This 'smart mask smoothing' algorithm circumvents the conventional method of surface area measurement based on voxels. This is an important development making a substantial contribution to the author's research, as voxel-based surface area measurements often overestimate the actual surface area. For

example, the surface area of the stepped voxel model in Figure 3-2b is $6\pi r^2$ whereas its correct analytical value is $4\pi r^2$, a 50% overestimation.

3.2.5 Objectives

The primary aim of this study was to evaluate the foam prototype accurately through a non-destructive means via a 3D model constructed from data obtained using a medical CT scanner.

- The foam irregularity, characterized by its pore and strut morphology, was quantified.
- The effects of scanning and analysis parameters on the surface area and porosity measurements were examined.
- The data from the stepped voxel and smoothed surface models were compared.
- The finalized 3D model accuracy was verified experimentally.
- Internal morphology assessment of the foam was carried out to qualify and quantify any manufacturing defects.

This study was the first to use the actual heat transfer surface area of a full size metal foam to solve heat transfer and fluid flow formulations.

3.3   Materials and methods
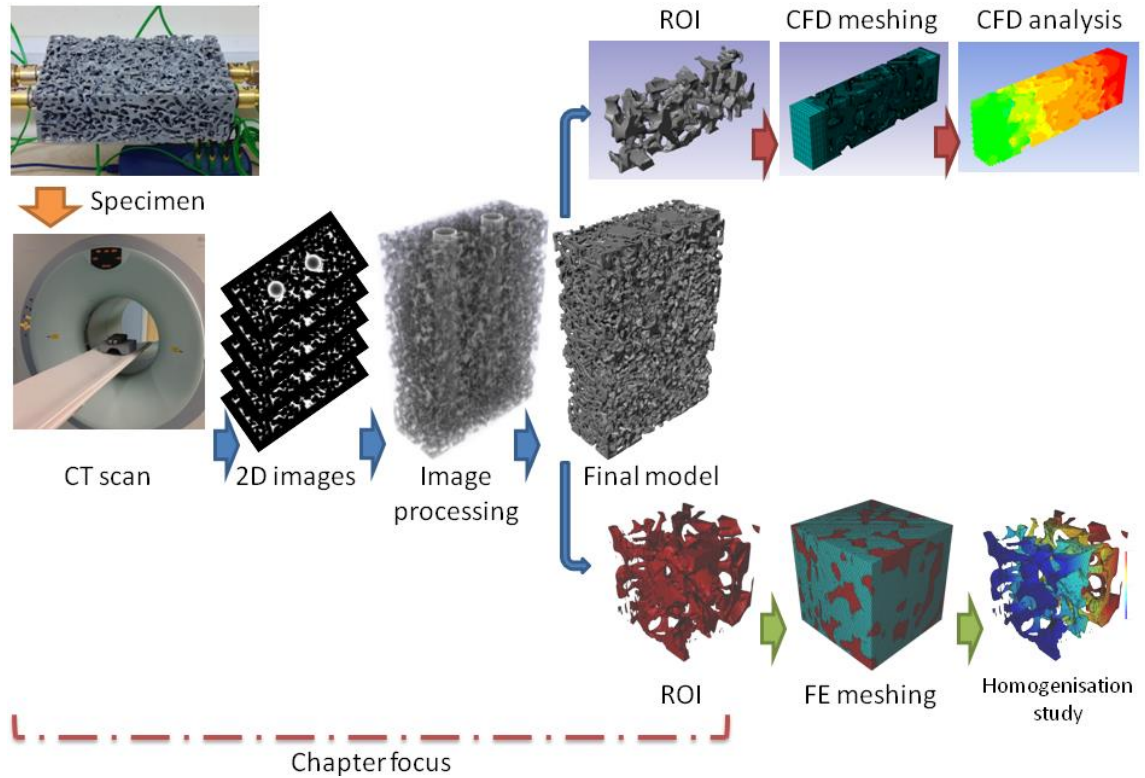
Figure 3-4 Overview of the methodology.

Figure 3-4 shows the irregular foam evaluation methodology (Chapters 3 to 6). The focus of this chapter was the CT image processing that produced the final 3D model, the porosity of which was then verified experimentally. Two software packages were involved, OsiriX and ScanIP.

3.3.1   Specimen detail

The foam prototype was initially supplied with a pair of embedded copper heat pipes with screen wicks (pipe OD = 18mm, ID = 15mm), which were cast into the foam. However, the endcaps and the screen wicks were removed to allow integration into a custom made rig for hot water flow for liquid cooling tests. The schematic is shown in Figure 3-5. The dimension of the foam is 165 x 50 x 114 mm (z-y-x axis). The foam was made from $AlSi_7Mg_{0.6}$ alloy with a thermal conductivity range of 150-180 W/m.K at 20°C. The scan specimen therefore was a metal foam with two protruding pipes.
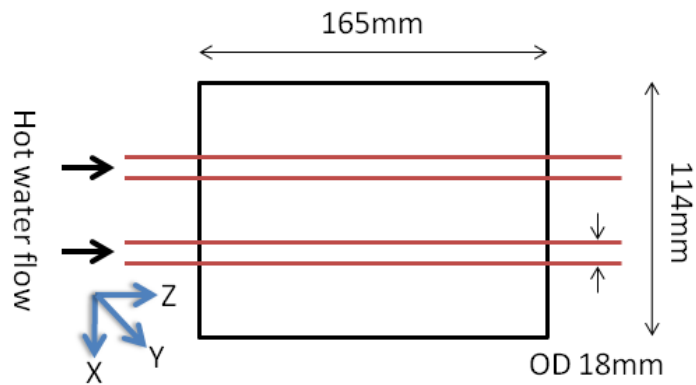
Figure 3-5 Schematic (plan view) of the supplied foam prototype with the embedded pipes (2D plan view, x-z plane).

3.3.2 The CT scanner specifications

The Siemens Biograph TruePoint 40 PET-CT Scanner at Positron Emission Tomography (PET) Centre of Newcastle University (http://www.ncl.ac.uk/pet/facilities/pet/) was used to scan the specimen (Figure 3-6). It was one of the latest generation medical CT scanners consisting of a fixed complete ring of detectors and a single X-ray source that rotated around the specimen being scanned. The detector material was Lutetium oxyorthosilicate (LSO). The scanning parameters include: 1) X-ray current = 1330mA (a fixed value), 2) X-ray voltage = 80-140kV in steps of 20kV, and 3) spot size = 0.75mm. These parameters result in a 0.3-0.6mm scanner resolution. The effect of the X-ray voltage on the image quality/3D model reconstruction is explored in Section 3.4.2.1. The raw data from any scan is called the "DICOM" file, which for the foam, was a series of 275 2D images (275 x 0.6mm = 165mm: the dimension of the specimen in the z-axis, the longest dimension).
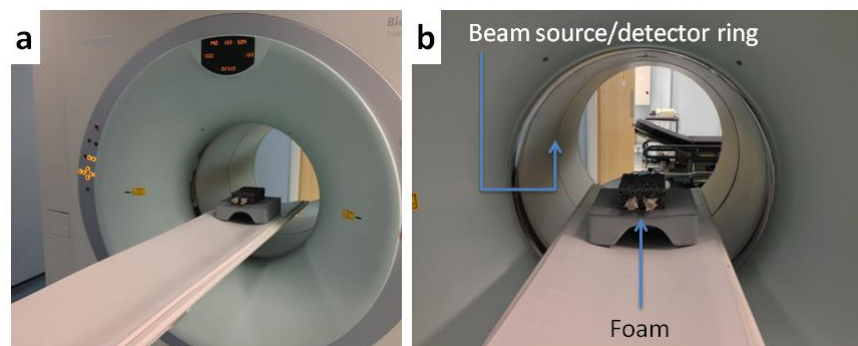
Figure 3-6 **The medical CT scanner at PET Centre, Newcastle University** (**a**) overview, (**b**) the scanning process with the foam inside the scanning field.

3.3.3 Image processing

The DICOM files were then exported to several software packages, OsiriX [128] for pore and strut size measurements and Simpleware ScanIP [96] for image processing.

3.3.3.1 OsiriX

OsiriX works only on the Mac OS platform and it is DICOM-dedicated image processing software. In this study, it was solely used for the size measurements (for definitions, see Figure 3-1c). The measuring process was carried out for both vertical and horizontal 2D images (Figure 3-7). This method was verified as shown in Figure 3-8 because the length measured by the software was precise to the actual length (z axis, 16.4mm). Figure 3-9 demonstrates how measurements were carried out on a vertical 2D image slice.
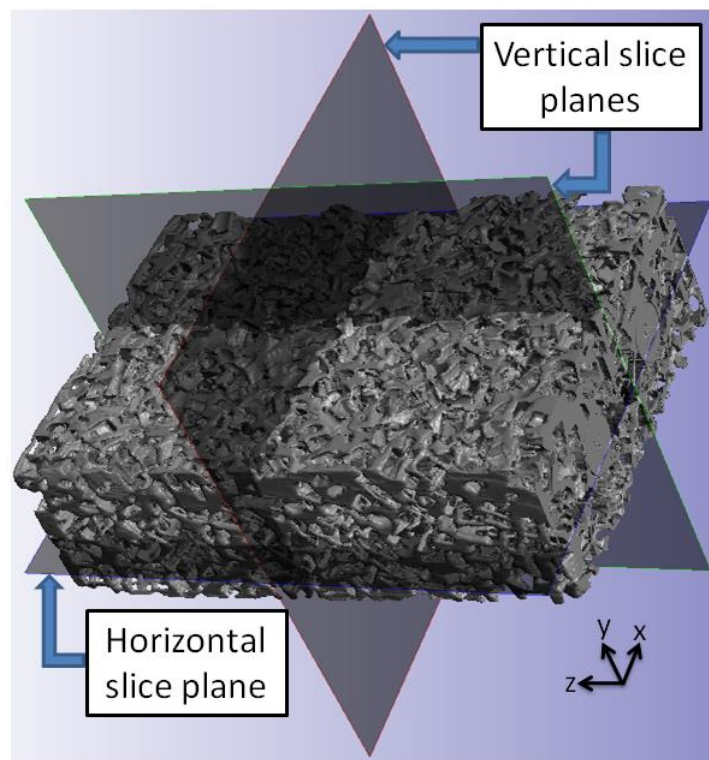
Figure 3-7 2D image planes.
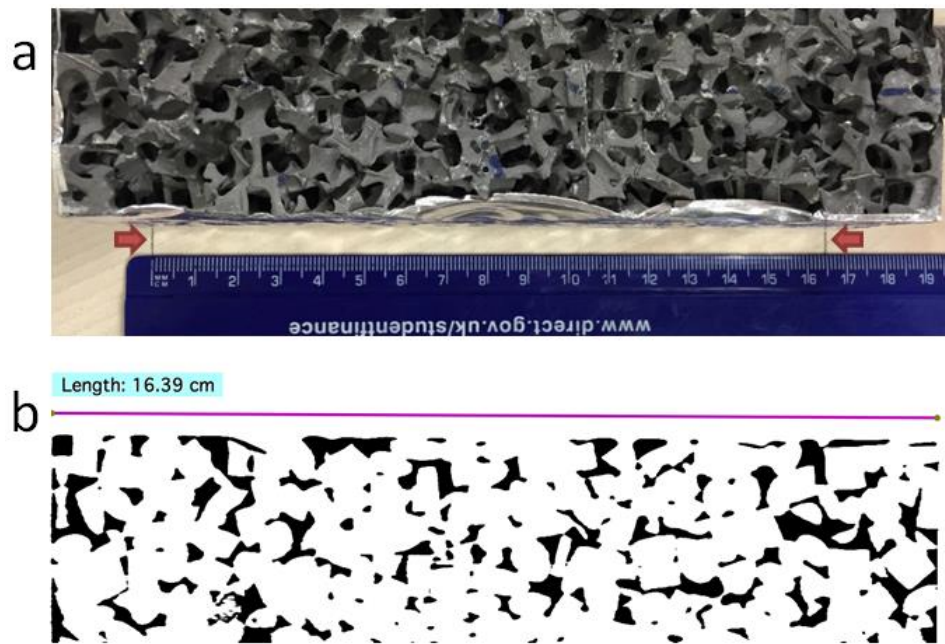
Figure 3-8 **OsiriX verification** (**a**) actual foam showing 16.4cm length (arrows mark the edges), (**b**) OsiriX linear measurement showing a similar value of 16.4cm.
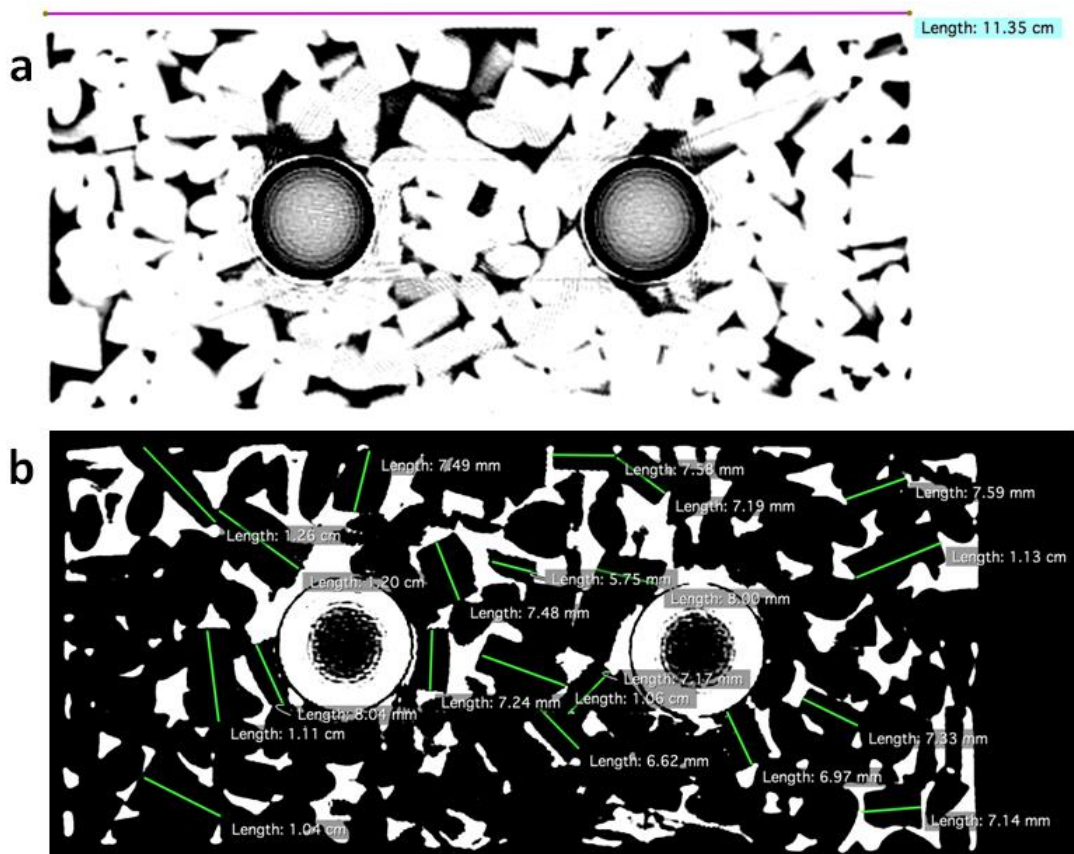
Figure 3-9 A vertical 2D slice showing the measurement method of the pore and strut size.

3.3.3.2 Simpleware package

Simpleware provides the world-leading software solution for the conversion of 3D images into CAD, Rapid Prototyped, and Finite Element models. Simpleware offers four software options for processing and meshing 3D image data.

The software is based on a core image processing platform, ScanIP, with optional bolt-on modules for mesh generation and CAD integration. The relationship between these products is shown in Figure 3-10 [96]. The modules important for this project are the ScanIP, +FE, and +LaPlace.

- **ScanIP**

ScanIP offers an extensive selection of image processing tools to assist you in visualising and segmenting Regions of interest (ROIs) from any volumetric 3D data (e.g. MRI, CT, Micro-CT, etc.). Segmented images can be exported as STL files for rapid prototyping or manufacturing, or as a starting point for volume meshing in another package.

- **+FE module – mesh generation module**

The +FE module provides a robust approach for the conversion of segmented 3D image data into multi-part volumetric and/or surface meshes. The high quality meshes generated can be directly imported into a range of commercial FE and CFD packages. +FE is available as a bolt on module fully integrated within the ScanIP interface.

- **+LaPlace – Laplace equation simulation module**

The +LAPLACE module calculates the effective properties of materials whose behaviour is governed by the Laplace equation, including electrical conductivity/permittivity, thermal conductivity and molecular diffusivity. Perform numerical homogenisation with a built-in FE solver or derive quick semi-analytical estimates from segmented images.
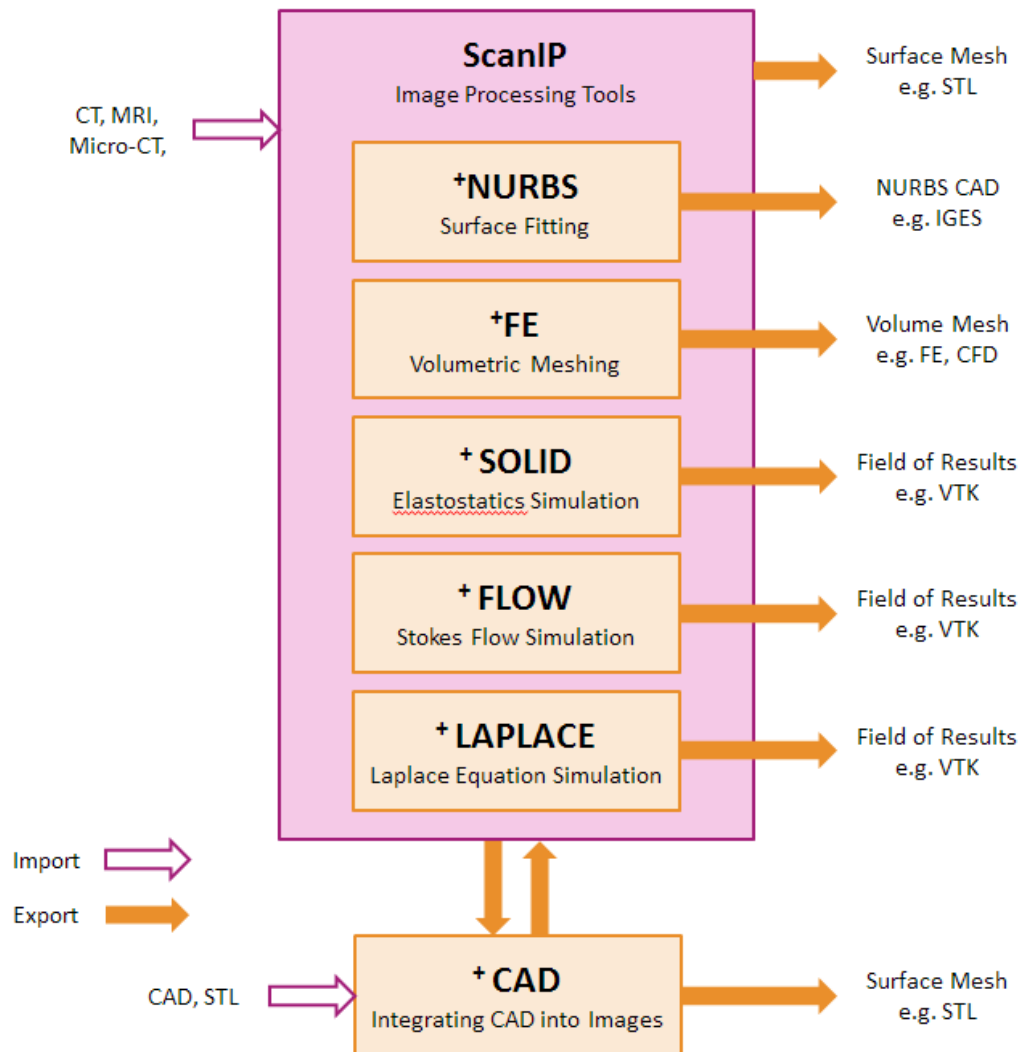
Figure 3-10 Simpleware software products (www.simpleware.com). The important modules for this project are: ScanIP, +FE, and +Laplace. Note: NURBS: Non-Uniform Rational B-Splines, VTK (Visualization ToolKit) and STL (STereoLithography) are surface export file types.

The image processing involves the following steps: 1) smoothing and 2) segmentation, prior to a 3D model construction.

- **Image smoothing**

Once imported, the DICOM image series was rendered automatically into a 'background' image volume with a certain noise level. The noise had to be be filtered prior to image segmentation. The Recursive Gaussian filter was used as a typical smoothing filter. The Gaussian sigma value (in mm) is a spatial parameter that defined the number of neighbouring pixels that contributed to the smoothing operation of each pixel. The larger the kernel sigma, the stronger was the smoothing effect. In Section 3.4.2.2, this

sigma value was varied from 0 to 2 mm and the consequences for the model were investigated.

- **Image segmentation**

Once the background was filtered accordingly, segmentation was carried out. For CT images, only the greyscale thresholding technique was needed [96]. This technique segments an image based on its greyscale intensities. The aim was to distinguish the different parts in a 3D space. This was an important step and it is investigated in Section 3.4.2.3.

The product of a processed background image volume is a 'mask', which represents objects of interest within the volume. The mask can be further worked on and filtered until the final version is satisfied. Often for complex structures like metal foams, many non-contiguous masks are contained within a volume, these are then combined into a 3D model. The software can subsequently assess the statistics of the model such as the voxel count, volume fraction, mean greyscale, and surface area.

In Chapter 5 and 6 the finalized model were meshed for export into heat transfer (finite element, FE) and fluid flow (computational fluid dynamics, CFD) simulations.

3.3.4 Experimental validation

It was important to validate the scanning and analysis parameters that produced the final model through any experimental means. Specific surface area can be measured via the BET (Brunauer-Emmett-Tellar) method [129] however it is limited in sample size. Porosity can be measured by the volumetric displacement method, which measures the change in volume when a specimen is immersed in a fluid. Figure 3-11 shows the set up for the test. The foam plus the protruding pipe ends were immersed in a rectangular container where the change in height (h_2-h_1) equals to the solid phase (foam plus pipe) volume, V_s (Equation 3-3). The bulk volume, V_b was measured linearly. By rearranging Equation 3-2, the voidage volume, V_v was calculated. The porosity could then be directly calculated using Equation 3-4. Uncertainty from the random error was reduced by carrying out five replicate tests (n=5).
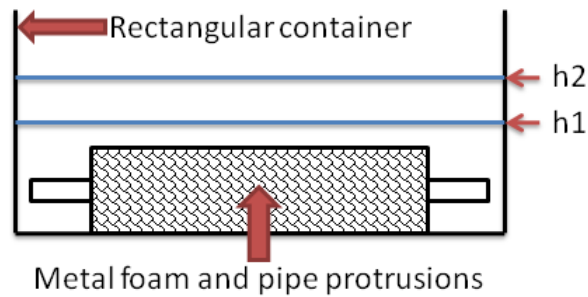
Figure 3-11 Volumetric displacement test set up.

$$V_b = V_s + V_v \qquad\qquad \text{Equation 3-2}$$

$$V_s = L * W * (h_2 - h_1) \qquad\qquad \text{Equation 3-3}$$

$$\varepsilon = \frac{V_b - V_s}{V_b} = \frac{V_v}{V_b} \qquad\qquad \text{Equation 3-4}$$

Where: V_b = bulk volume, V_s = solid (foam and pipes) volume, V_v = voidage volume (all in mm^3), L = length of container, W = width of container, h_1 and h_2 = height of fluid (all in mm), and ε = porosity (fraction).

Appendix A2 discusses the description of error propagation analysis used throughout the thesis.

3.4   Results and discussion

3.4.1   Pores and struts

As shown in Figure 3-1c, generally the foam prototype pores were of rectangular and oval shapes. Some pores were circular but significantly smaller in size and number, thereby they were not considered for measurement. The definition of pore and strut size was explained in Figure 3-1c. Figure 3-12 shows the measurements from both vertical and horizontal images. The mean values are: 1) rectangular pore = 8.41±2.09mm, 2) oval pore = 6.69±1.00mm, and 3) strut thickness = 1.67±0.52mm. The large standard deviations characterize the foam inherent irregularity. The values here are necessary for classifying the air flow in terms of turbulence or laminar flow in Chapter 6. Reynolds number (Re) for flow through the foam is a function of pore diameter. As an example, the following Figure 3-13 shows the variation of Reynolds number with pore diameter (5 - 10 mm, based on the range in Figure 3-12) at constant velocity (3.00 m/s). Pore-based Re is based upon a formula by Boomsba *et* al. [108],

$$Re = \frac{\rho v d_p}{\mu}$$

Where ρ = density (kg/m3), v = velocity (m/s), d_p = pore diameter (m), and µ = dynamic viscosity (kg/m.s) of the inlet air.
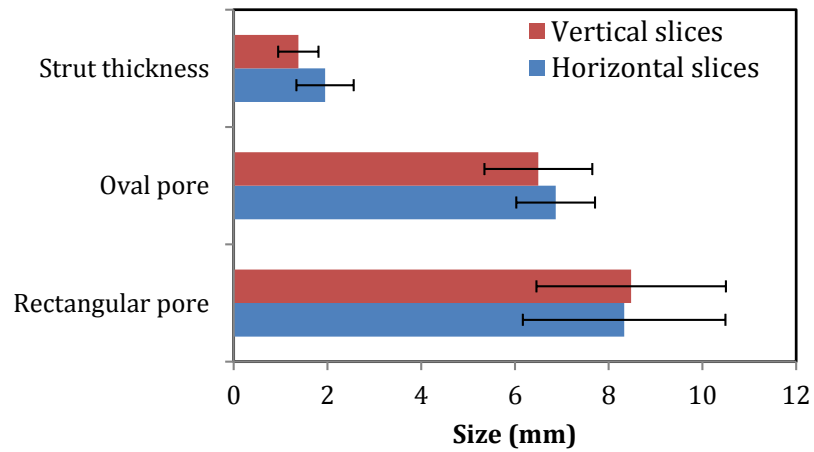
Figure 3-12 Pore and strut size. Error bars show mean ± standard deviation.
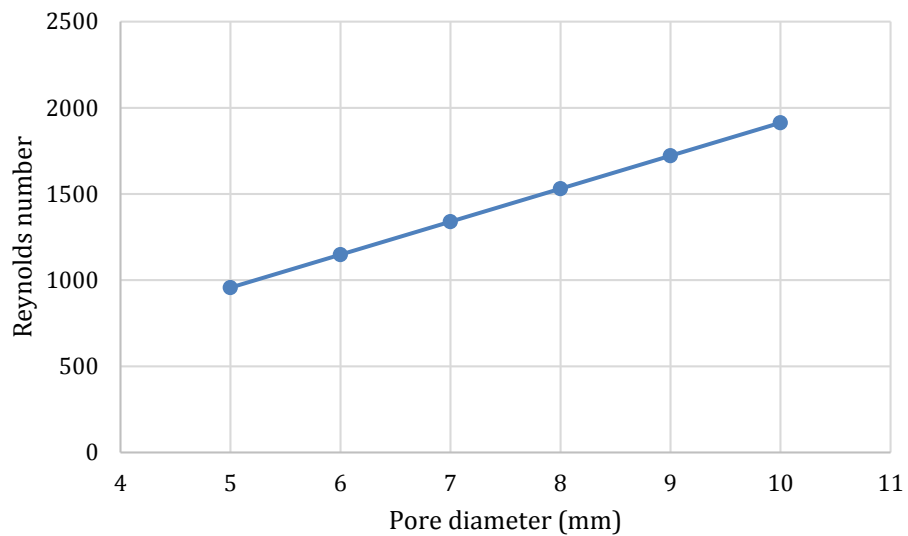
Figure 3-13 The variation of Reynolds number with pore diameter (5 – 10 mm) at constant velocity (3 m/s), based upon inlet air properties at 300 K.

It can be seen from the figure above that the Reynolds number range is 956 to 1913 for pore diameter range of 5 to 10 mm. This barely crosses the turbulent threshold (Re > 2000).

3.4.2 Porosity and surface area

3.4.2.1 Effect of the X-ray source voltage

The X-ray source voltage is an important consideration when the specimen is biological as a step increase in voltage exposes a higher dose of harmful radiation to the specimen. Often the focus of the latest generation medical CT scanners is to lower the radiation dose while maintaining image quality via various methods. It was interesting to test the voltage effect upon the 3D model quality of the foam prototype as it was of a different material (metal vs. biological) and of different density. The X-ray current was fixed at 1330mA. The voltage was varied from 80 to 140kV in steps of 20kV. The background data from all voltages were processed with similar smoothing and segmentation factors (smoothing, Gaussian sigma = 0mm and segmentation, greyscale range = -484 to 3041). Smoothed surface models were then constructed and the porosity and surface area were measured and compared (Figure 3-15). At the lowest voltage of 80kV, the porosity was the lowest at 49% while its surface area was the largest at 1.49m^2. There was a huge leap in values from 80 to 100kV, but from then a steady and slow trend in porosity rise until 140kV. The values at the maximum voltage of 140kV were: 1) porosity = 67% and 2) surface area = 0.54m^2. Figure 3-14 shows a processed image from all the voltages. At 80kV, the presence of noise was very significant. The noise was reduced gradually until 140kV was reached. The highest voxel count of 1.03x10^7 at 80kV shows that the noise was included in reconstructing the 3D model, which effectively increased the solid fraction and hence, decreased the porosity and increased the surface area. It was therefore concluded that the highest X-ray voltage setting for any medical CT scanner must be selected to maximize the model measurement precision.
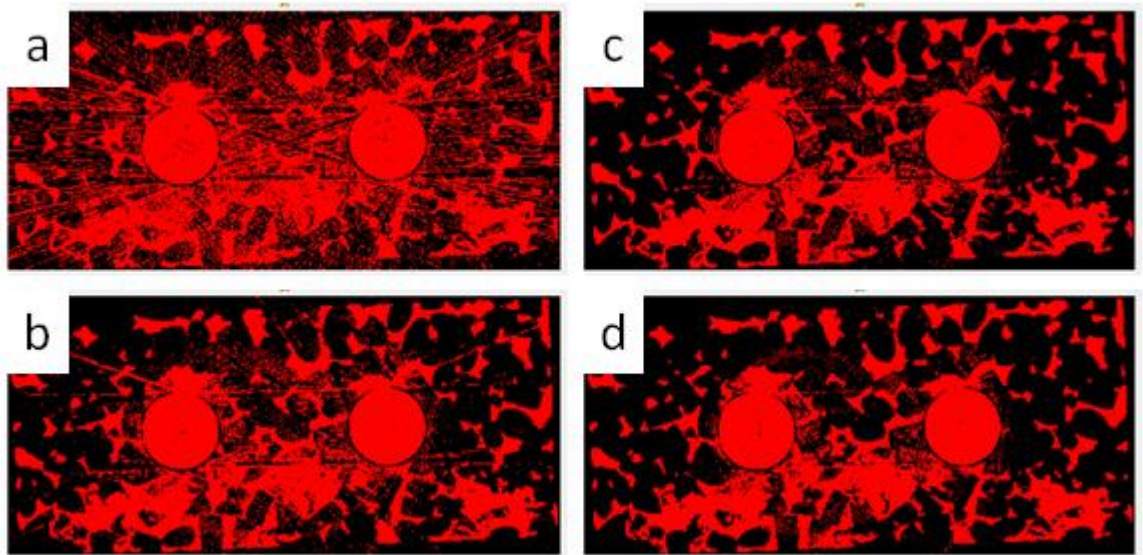
Figure 3-14 **A processed scan image for** (**a**) 80kV, (**b**) 100kV, (**c**) 120kV, (**d**) 140kV.
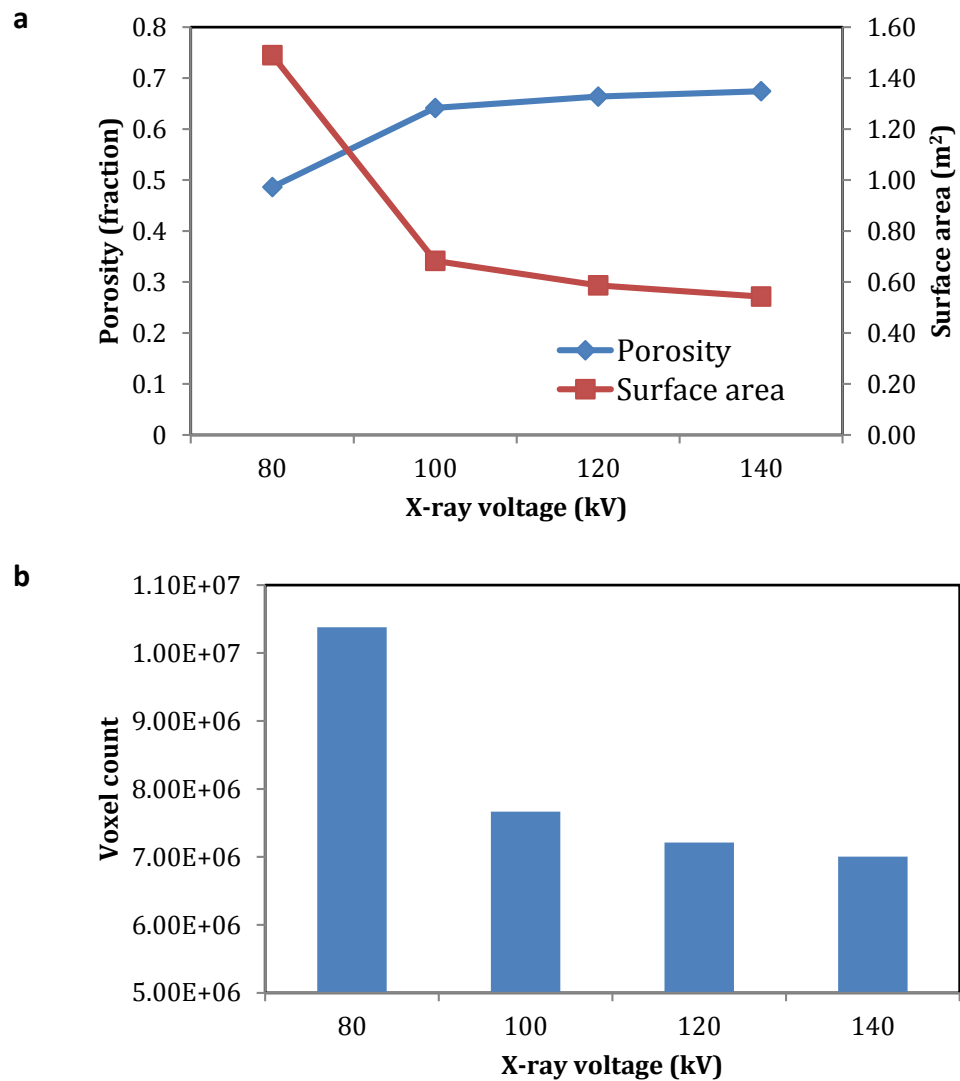
Figure 3-15 **Effect of the X-ray voltage on the** (**a**) apparent porosity and surface area, (**b**) total voxel count.

3.4.2.2 Effect of smoothing (Recursive Gaussian)

Figure 3-16 is a qualitative analysis on the effect of varying the Recursive Gaussian filter sigma value during the image smoothing process. The X-ray voltage was fixed at the highest setting of 140kV. The segmentation factor was similar as in the voltage studies i.e. fixed at a greyscale range of -484 to 3041. With the sigma = 0mm, i.e. no smoothing factor, the 3D model was visibly similar to the actual foam whereas at sigma = 2mm, the 2D image was not well-defined with the resulting model observed to be 'bubbly' and deviating greatly from the actual foam appearance. Porosity and surface area vs. the sigma values are plotted in Figure 3-17. Both stepped voxel and smoothed surface models were constructed for comparison. The continuing discussion concerns the smoothed surface model only. For the sigma = 0 model, the porosity was 67% and its surface area was $0.54m^2$ whereas for the sigma = 2, its porosity and surface area were 47% and $0.26m^2$, respectively. The correlation between porosity and surface area was reversed compared to the previous voltage studies. This was because porosity is calculated based on the total solid fractions in the 3D volume. For the low voltage 80kV model (Figure 3-14a), the solid fractions included the contribution from the foam and the noise elements that the 3D model was constructed from. Small solid volumes due to the noise elements increased the total surface area of the model. Here, the noise was significantly reduced, as the data were obtained at the highest voltage (140kV) setting (Figure 3-14d). The porosity for the sigma = 2 model was very low at 47% as the foam solid was relatively large due to the bubbly solid struts, which inadvertently closed the gaps between pores and hence, gave the very low surface area value.
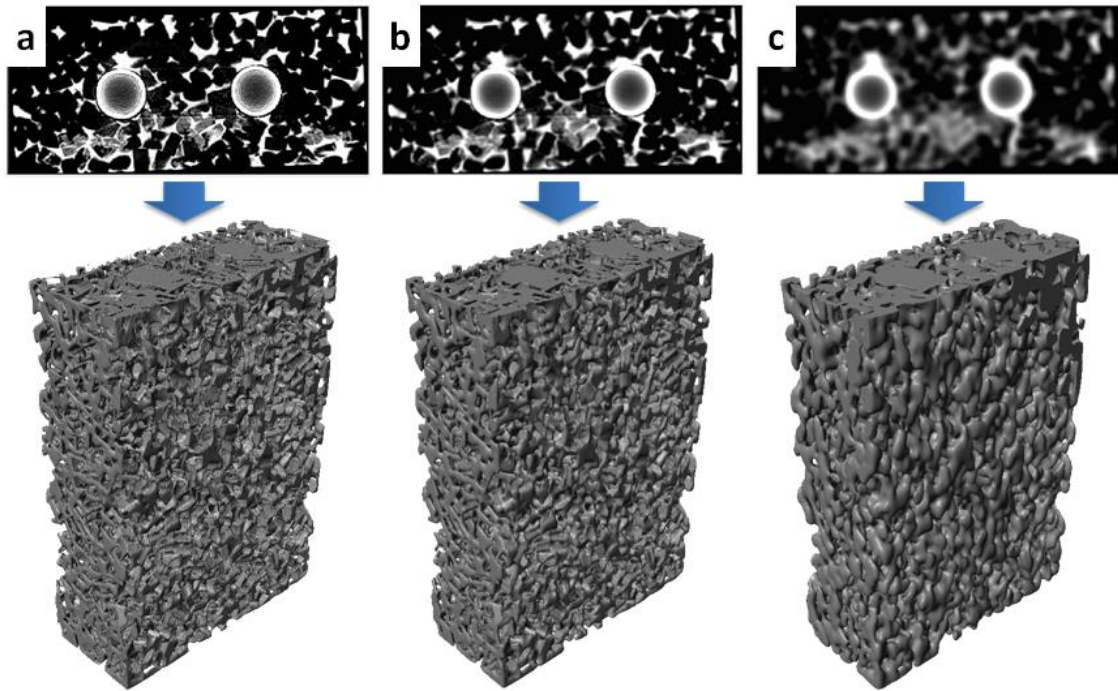
Figure 3-16 **Effect of the Recursive Gaussian filter sigma value on the 3D model reconstruction** (**a**) 0, (**b**) 1, (**c**) 2 (all in mm).
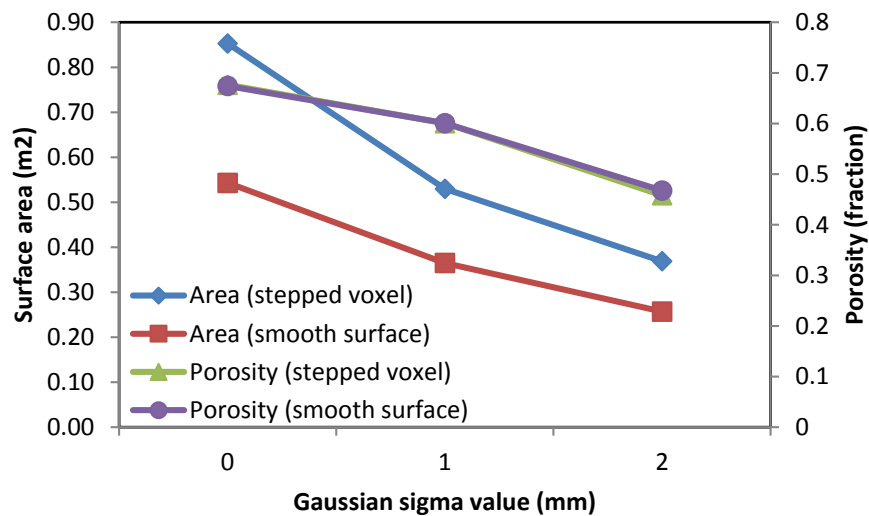
Figure 3-17 Effect of the Recursive Gaussian filter sigma value on the porosity and surface area for both stepped voxel and smoothed surface models.

3.4.2.3   Effect of segmentation (greyscale threshold)

Segmentation is an important step as it determines the object each pixel belongs to i.e. background (air) or solid (foam). For CT images, only greyscale thresholding is necessary. For magnetic resonance images (MRI), the objects are differentiated by their texture [96]. The voltage and smoothing studies used a fixed greyscale threshold of -484 to 3041

for all cases, which is termed as the 'default values' to simplify discussions. The lower bound refers to the most white and the upper bound, the most black. For image data types with bit depths of 16 bit or higher, the lower value is often a negative value, such as with the foam scan images. Segmentation must be done manually to visually identify the different parts of the model. To study the effect of the greyscale range (Table 3-2), the default bound (range no. 2) was fixed at its higher value and two more lower bounds were set at ±76. The voltage was set at 140kV and smoothing at the Gaussian sigma = 0. Figure 3-18 shows the results for the porosity and surface area values. Comparing range no. 1 and 3, the deviations in porosity and surface area values were 6% and 12%, respectively. The effect was therefore as equally large as the voltage and smoothing factors as the deviations were caused from a mere ±2% change from the default range size. The default range was selected from a visual assessment, which consumed most of the image processing time. Unfortunately, this feature had yet to be automated (autothresholding) by Simpleware.

Table 3-2 The greyscale range with varied lower bounds. Range 2 is the default.

Range	Lower values	Higher values
1	-560	3041
2	-484	3041
3	-408	3041
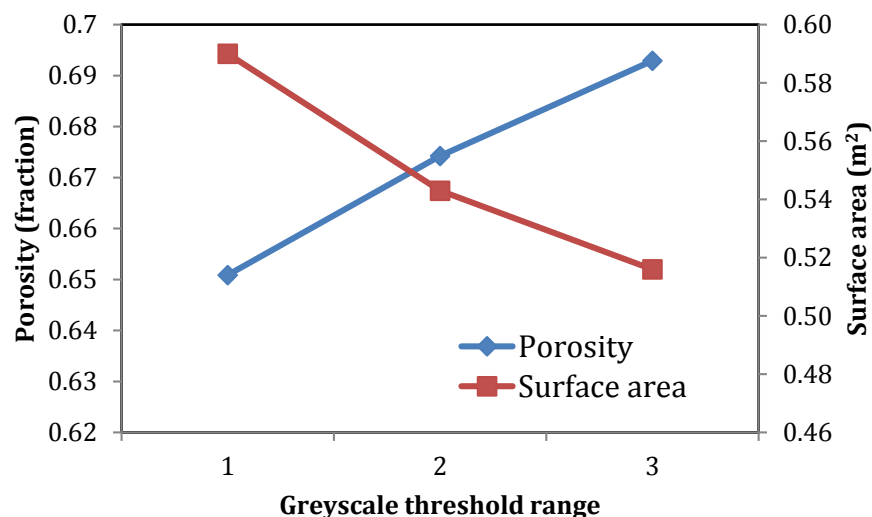
Figure 3-18 Effect of varying the greyscale range on the porosity and surface area.

3.4.3 The finalized model

The volumetric displacement tests yielded the foam porosity to be 67 ± 3%. The result is shown in the following Equation 3-6 (V_b and V_v are the mean values). The included 3% uncertainty was due to the systematic error from the linear measurements used to measure the bulk volume, V_b plus the random error, which was significantly reduced from the multiple replicates (n = 5).

$$\varepsilon = \frac{V_v}{V_b} = \frac{6.68 \ x \ 10^{-4} m^3}{9.97 \ x \ 10^{-4} m^3} = 0.67 \qquad\qquad \text{Equation 3-6}$$

Figure 3-19 below shows the finalized model compared to the actual foam, both are visually similar. Table 3-3 lists the scanning and analysis parameters that created the finalized model. The basis of comparison was the porosity, as presented in Figure 3-20.
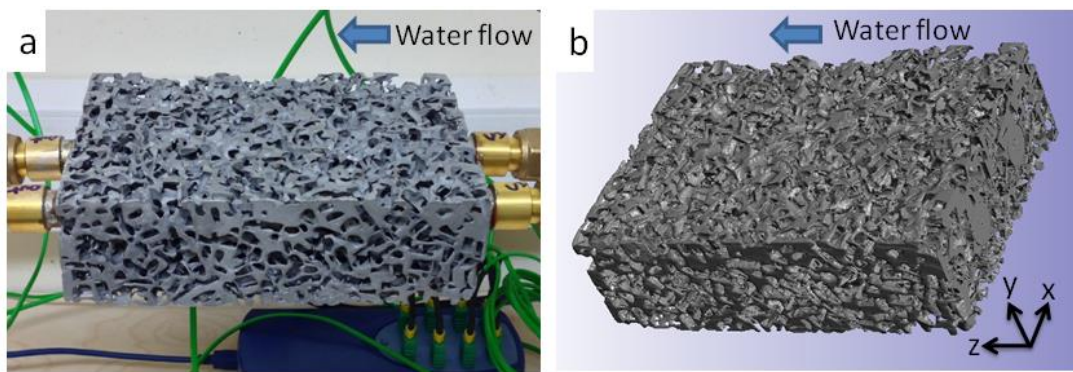
Figure 3-19 (**a**) The actual foam, (**b**) the finalized model.

An important outcome from the comparison was the level of confidence in the accuracy of the finalized model. Figure 3-21 compares its porosity and surface area in terms of smoothed vs. stepped voxel surfaces. As expected, the porosity was similar whilst the surface area of the latter overestimated by 60% (similar to the case presented in Figure 3-2b vs. c). This confirmed the volume and topology preserving algorithm of the smart mask smoothing used to create the smooth surface model. Similar porosity for two different model types meant that the model can be validated by the porosity alone. This may set a precedence in allowing the use of low resolution scanners combined with software enhancements to produce accurate 3D models, from which a confident surface area measurement can be extracted as the method circumvents the voxel approach.

This enables scanning of large specimens without the need for physical segmentation, which would be an undesirable, destructive approach.

Table 3-3 Parameters of the finalized 3D model.

Scan/analysis	X-ray voltage (kV)	140
	Smoothing (Recursive Gaussian sigma, mm)	0
	Segmentation (greyscale threshold range)	-484 to 3041
Model	Voxel resolution (mm)	0.60 x 0.29 x 0.29 (z-y-x)
	Dimension (mm)	165 x 54 x 116 (z-y-x)
Measurement	Porosity (% void)	67
	Surface area (m^2)	0.54
	Specific surface area (m^2/m^3)	1495
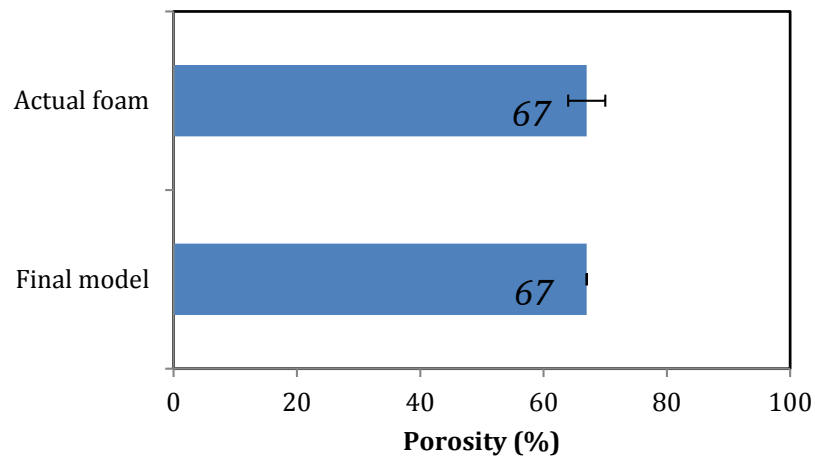
Figure 3-20 Porosity of the actual foam and the finalized model. Error bar shows mean ± standard deviation, n=5.
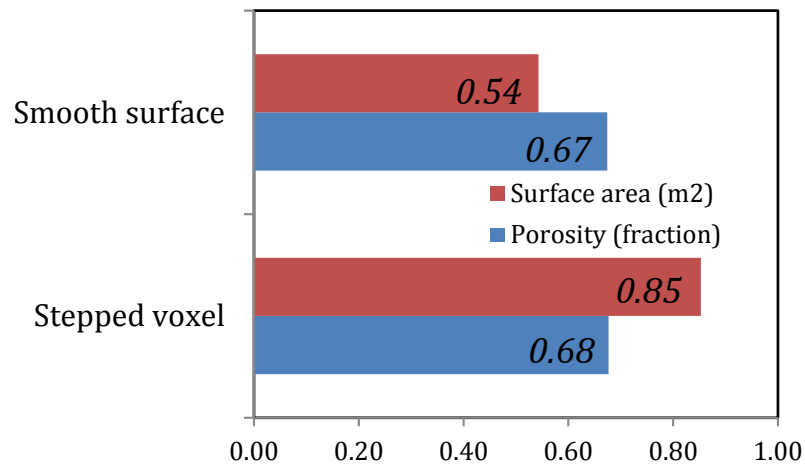
Figure 3-21 Porosity and surface area of the finalized model of both stepped voxel and smoothed surfaces. Similar porosity for two different model types meant that the model can be validated by the porosity alone.

3.4.4 The presence of an inhomogeneity

Horizontal image slices (Figure 3-22) and vertical ones (Figure 3-23) enabled the examination of the internal morphology, which revealed a manufacturing defect in the form of a ring-shaped dense solid region within the foam volume under the pipes, approximately 20mm from the foam bottom (Figure 3-24). This would affect the air flow through the foam (discussed in Chapter 6). In this chapter, this defect region effect on the foam porosity was quantified.
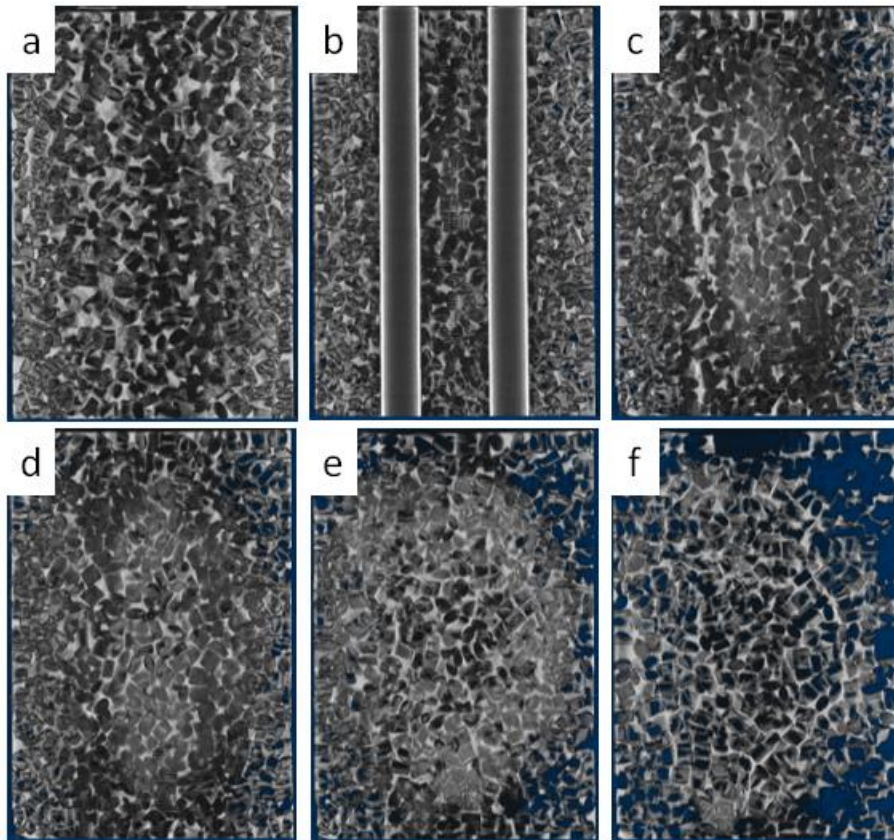
Figure 3-22 Horizontal slice images (x-z plane) of the foam from (**a**) the topmost slice to, (**f**) the bottommost slice. The defect region is clearly visible in **e** and **f**.
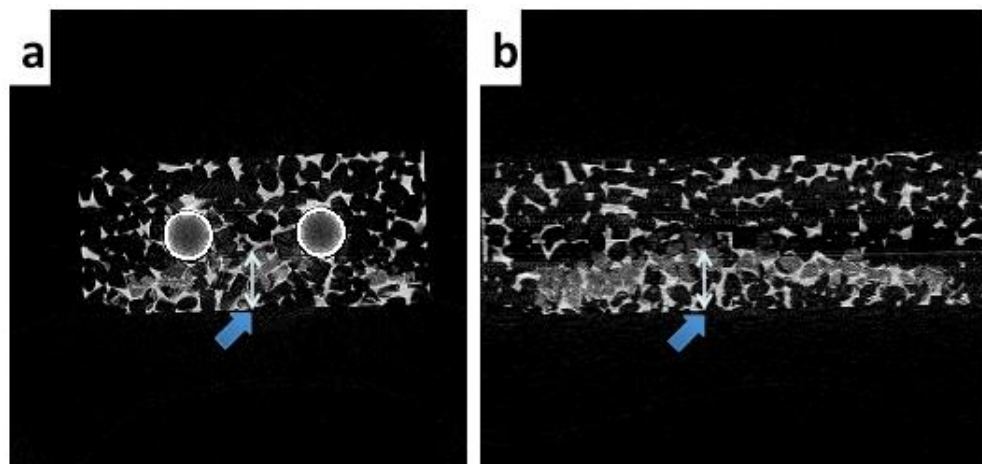
Figure 3-23 **CT image showing the extent of the defect region from base** (**a**) x-y plane, (**b**) y-z plane.
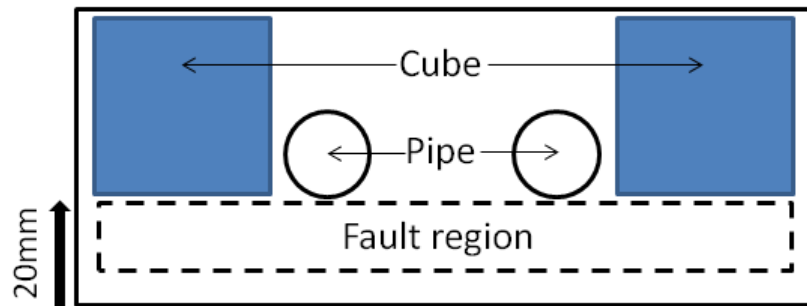
Figure 3-24 Location of the defect region and the segmented cubes' relative size and position within the foam (x-y plane).

Six equivalent-size cubes were segmented from the full model and they avoided the defect region (Figure 3-24). The cubes are shown in Figure 3-25. Interestingly, when the porosity and specific surface area (SSA) were measured (Table 3-4), despite the irregularity in terms of pore and strut morphology, the porosity was uniform at 80 % (specifically 79±1 %) and the specific surface areas only deviated by ±2.5 % from the mean of 2188 m^2/m^3. This analysis showed that a similar foam if manufactured without the defect, would have a porosity of 80%. With the defect included, the foam porosity therefore was reduced by 16% and the specific surface area by 32%. Two deductions were made:

- Equations as a function of porosity and surface area (e.g. effective thermal conductivity) could be used confidently because of their uniformity in the foam, disregarding the defect volume.
- The specific surface area for heat transfer was reduced by 32%, which meant that the thermal performance as a forced convection heat sink would not be optimal, irrespective of the dense region effect upon the pressure drop (refer Chapter 6). New, defect-free irregular foam must be used.
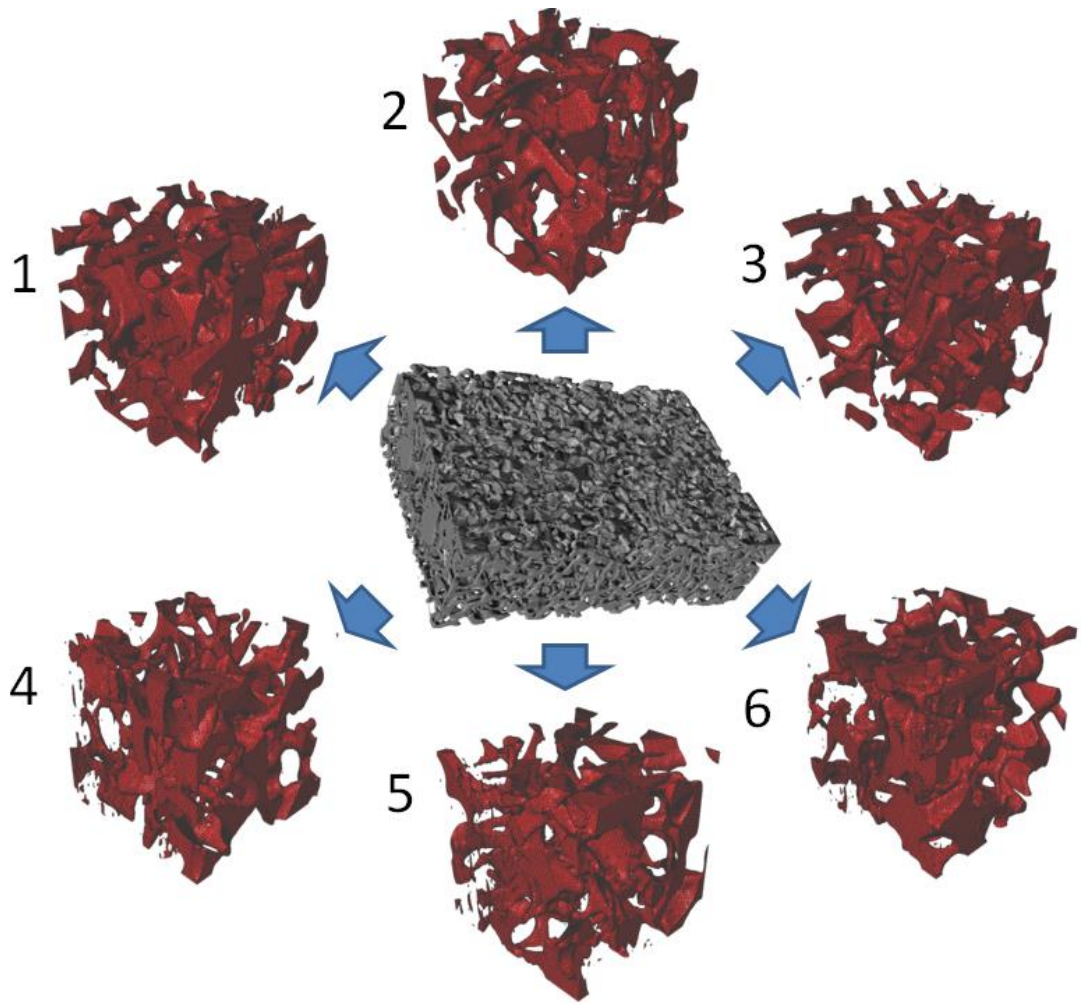
Figure 3-25 The physical model of the segmented cubes (isometric).

Table 3-4 The porosity and specific surface area of the segmented cubes, discounting the dense, ring-shaped region.

Cube	Porosity (% void)	Specific surface area (m^2/m^3)
1	76	2081
2	79	2198
3	80	2196
4	79	2223
5	80	2241
6	79	2190
Average	79	2188
Std. dev.	1	56

3.5   Conclusions

A metal foam prototype was successfully, non-invasively assessed via a construction of an accurate 3D model. This is the first time a low resolution, medical CT scanner was used to create an accurate 3D model, made possible by software enhancement.

The main findings of the study are as follows:

- The pores were found to be predominantly rectangular and oval in shape. The sizes were 8.41 ± 2.09mm and 6.69 ± 1.00mm, respectively. The strut thicknesses were 1.67 ± 0.52mm. The large standard deviations represented the irregularity of the foam.
- The highest voltage setting in the CT scanner must be used to minimize noise.
- The image smoothing and segmentation were carried out with care as small changes would have created inconsistent 3D models from the real foam.
- Volumetric displacement tests were carried out to measure the foam porosity and to verify the finalized 3D model porosity. The experimental porosity was $67\pm3\%$ whereas that of the model was 67%. The total and specific surface areas acquired from the model were $0.54m^2$ and 1495 m^2/m^3, respectively.
- The smoothed surface model circumvented the traditional method of voxel based measurements (especially the surface area). Because higher resolution microCT scanners were used to provide more refined voxels and hence, to increase accuracy at the expense of specimen size, this would be no longer necessary as the combination of medicalCT scanners and software enhancements would provide precise models.
- Internal morphology assessment revealed a manufacturing defect that caused the porosity and specific surface area to be reduced by 16 and 32%, respectively from its intended form.
- Despite of the irregular morphology, the foam was actually uniform in its porosity and specific surface area.

A validated, high resolution 3D model was constructed that enabled a variety of parameters to be acquired. The characterization values acquired, especially the porosity of the foam is crucial in the calculations within Chapter 4. The segments of the model were meshed for use in heat transfer and fluid flow simulations in Chapter 5 and 6.

Chapter 4   Phase change material melting in the irregular foam

4.1   Abstract

To cope with the increasing cooling loads in power electronics especially in traction, a new heat sink based on the irregular aluminium foam/salt hydrate phase change material composite was proposed for integration into liquid cooling or heat pipe systems to provide transient cooling during the traction stationary phase. The coolant was water, heated up to 60°C, similar to the inlet condition in traction liquid cooling systems. The vacuum impregnation method used to create the composite resulted in a 96% impregnation ratio. The heat sink absorbed a thermal load of 0.079 – 0.092 kWh (corresponded to 55 - 60°C charge temperature) in less than an hour of heating, in which the PCM was fully melted. This was a combination of latent and sensible heat storage methods. The thermal capacity value matched the preliminary calculations first presented in Chapter 1 (Introduction). An hour of complete melting would match the stopping period of intercity trains at the terminus, and the sink would be able to cool a group of 4 - 5 IGBTs, rated at 20W power dissipation each, during this stopping period. The heat balance carried out was commendable due to the small (~7%) imbalance and therefore, could be used to further optimise the design with alternative PCMs, foam porosities, operational conditions, thermal masses, heat exchanger configurations, and so on.

Keywords: transient heat sink; IGBT; irregular metal foam; phase change material; vacuum impregnation; heat balance

4.2 Introduction

Chapter 1 has introduced the concept of transient cooling of power electronics in traction systems during its stationary phase. Power electronic devices such as MOSFET, GTO, IGBT, and IGCT are now widely used to efficiently deliver electrical power in home electronics, industrial drives, telecommunications, wind power generation, transport, the electricity grid, and numerous other applications. Thermal management of these devices especially for heat removal and junction temperature control is vital to achieve efficiency, cost, and reliability objectives. Current technologies include heat pipes and thermosyphons in natural or forced convection air cooling and liquid cold plates, which offer cooling of high heat loads and fluxes [130].

4.2.1 PCM-based transient cooling for power electronics in traction systems

Most mass transit systems such as subways use electricity. Crude electricity supplied to the locomotive and rolling stock must be conditioned to provide propulsion, lighting, and air conditioning. Power semiconductors are utilized to condition the electricity. The removal of heat as efficiently as possible is critical to their operation [131]. These days, heat loads continue to increase, which means more and more OEMs are turning to liquid cooling to remove high power density loads via cold plates, heat exchangers, and ambient air sinks. To aid in removing heat loads during the traction stationary phase e.g. in stations or during abrupt stops, a new transient cooling solution is proposed based on a phase change material (PCM)/metal foam composite heat sink. This concept is intended for integration into existing heat pipe or liquid cooling systems. The operational sequence is as follows (Figure 4-1): 1) the heat load is channelled via heat pipes or coolant to the sink during the stationary phase when the PCM absorbs the heat and melts, and 2) during the movement phase, the PCM is cooled and solidified by forced air convection through the connected fin stacks. This would allow the PCM to be reused during the next stationary phase. Should heat pipes be used, this would be a fully passive system. Avoiding liquid coolant would also greatly reduce system weight and avoid the associated pressure drop/performance complications.
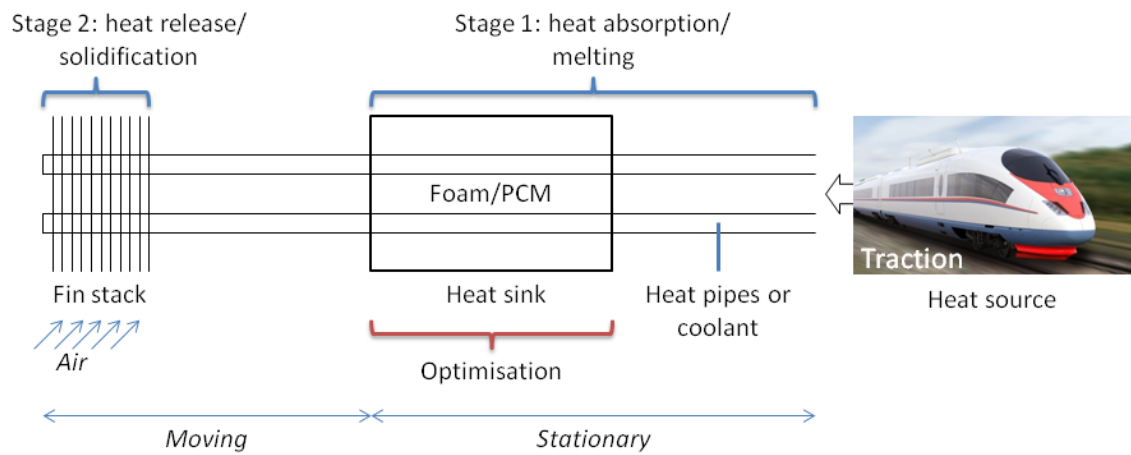
Figure 4-1 Transient heat sink concept based on metal foam/PCM composite for power electronics cooling esp. traction systems.

4.2.2 Phase change material and metal foams

Phase change material provides an efficient method for thermal storage because it can absorb an enormous amount of heat during melting. Because generally a PCM has a high latent heat density (kJ/kg), it provides a compact alternative to sensible storage materials such as water, rocks, and metals. The melting phase that occurs isothermally provides an efficient heat absorption/release process compared to thermal gradients in sensible storage [132]. These and many other factors push forward the PCM as a promising 'thermal battery' candidate.

Commercial PCMs, which come in a variety of melting temperatures are hindered performance-wise by their inherent low thermal conductivities at around 0.45W/m.K [133]. For the traction cooling device, this would mean the PCM alone would not absorb the heat efficiently within the time frame of short stops. However, if the PCM is embedded in high conductivity matrices such as metal foams, this could solve the problem. In addition to increasing the effective thermal conductivity of PCMs, metal foams would increase the thermal mass for heat uptake, thereby increasing thermal capacitance of the composite.

4.2.3 The rationale behind the experimental design and conditions

In Section 1.2 in Chapter 1 – the conditions, power dissipations, and stopping periods of traction systems during the stationary phase were reviewed from literature sources. Table 4-1 below summarizes these data. These provided the rationale behind the experimental design and conditions. From preliminary calculations, the heat sink of PCM within an aluminium foam of 70% porosity would provide roughly 270 kJ of thermal capacity or 0.075 kWh, adequate to cool a group 3 to 4 IGBT rated at 20W within an hour during the train stopping period (for intercity trains at the terminus) [3]. Water-based coolant was to be used, with an inlet temperature of 60°C – this is a common inlet condition for tractions [2]. The PCM chosen was a salt hydrate PCM that melted at 46°C with a latent energy density of 210 kJ/kg (Figure 4-2b).

Table 4-1 The conditions, power dissipations, and stopping periods of traction systems during the stationary phase. These provided the rationale behind the choice of experimental design and conditions.

	Value	Traction type	Reference	Experimental condition
Total load (power dissipation) per IGBT module	20W	Commuter/ common trains	[3]	Heat sink energy capacity is 0.075kWh*. IGBT power dissipation is 0.02kW in 1h (0.02kWh). Enough capacity to cool 3-4 modules.
	~ a few Watts	Trains equipped with high efficiency (98%) IGBT modules	[6]	
Operating temperature	70 - 85°C (within 60 seconds)	Metro trains	[7]	
	60°C	Common trains	[2]	Charging at 60°C maximum with water as coolant.
Coolant flow rate	50 LPM			
Stopping period	~ 60 seconds	Metro trains	[3, 7]	

	200 – 3000 seconds	Intercity trains		Target application is 1 h i.e. PCM to complete charging within 1 h.
	~ 1 hour or more	Long distance trains		

*Based on preliminary calculations (refer Chapter 1 – Introduction, Section 1.2).
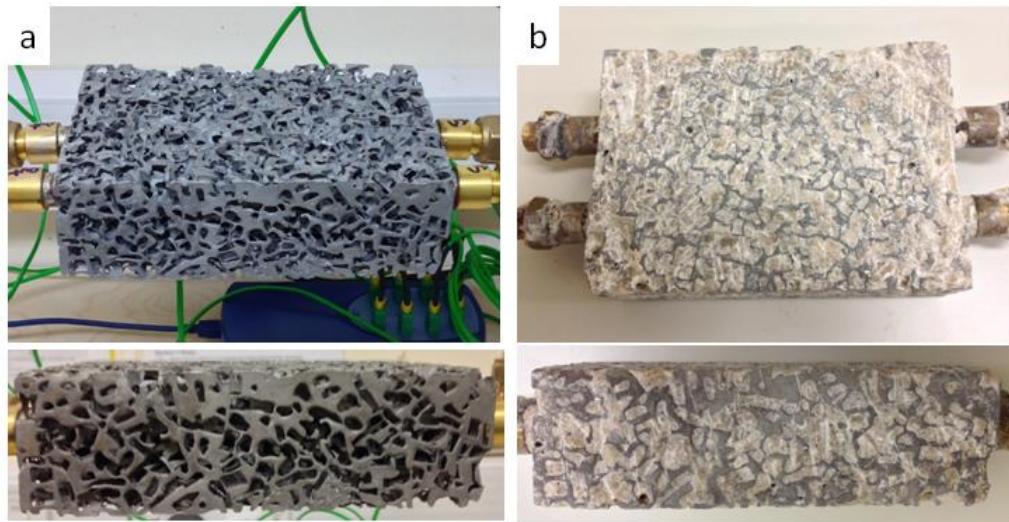
Figure 4-2(**a**) The irregular aluminium foam prototype, (**b**) the aluminium foam/salt hydrate S46 PCM composite.

4.2.4 Objectives

The aim of the chapter was to establish the basis for the foam/PCM composite as a heat sink specifically for transient cooling applications in traction systems.

- The process of impregnating the salt hydrate into the foam via the vacuum method was investigated and its efficacy assessed.
- The thermal capacity of the composite under current design specifications and operational conditions was measured through heat balance equations. This was to be compared with preliminary capacity calculations in Chapter 1.
- The PCM melting behaviour under different inlet temperatures was investigated.

These experimental works were complemented with modelling and simulation in Chapter 5 to create the basis for design optimisation, with the aim of producing a test prototype with heat pipes.

4.3   Materials and methods

4.3.1   PCM specifications

The phase change material used was a salt hydrate 'S46' supplied by PCM Products Ltd. [22], which melted at 46°C. Figure 4-3 shows it in its supplied form as chunks of hard solid. Table 4-2 shows its thermophysical data. It was selected primarily on the basis of its melting temperature and secondarily, on its relatively high latent energy density of 210kJ/kg. Its differential scanning calorimetry (DSC) data are shown in Figure 4-4, which tested its melting temperature range and energy density. Its chemical composition was $Na_2S_2O_3.5H_2O$ plus sepiolite and fumed silica additives for chemical stability [134].

Figure 4-3 The salt hydrate S46 was supplied as solid chunks.

Table 4-2 Salt hydrate S46 thermophysical data.

Density (solid)	1587 kg/m^3
Specific heat	2410 J/kg.K
Latent heat	2.10 x 10^5 J/kg
Thermal conductivity	0.45 W/m.K
Viscosity	10^{-5} kg/m.s
Melting temperature	46°C
Maximum exposure temperature (chemical denaturation limit)	60°C
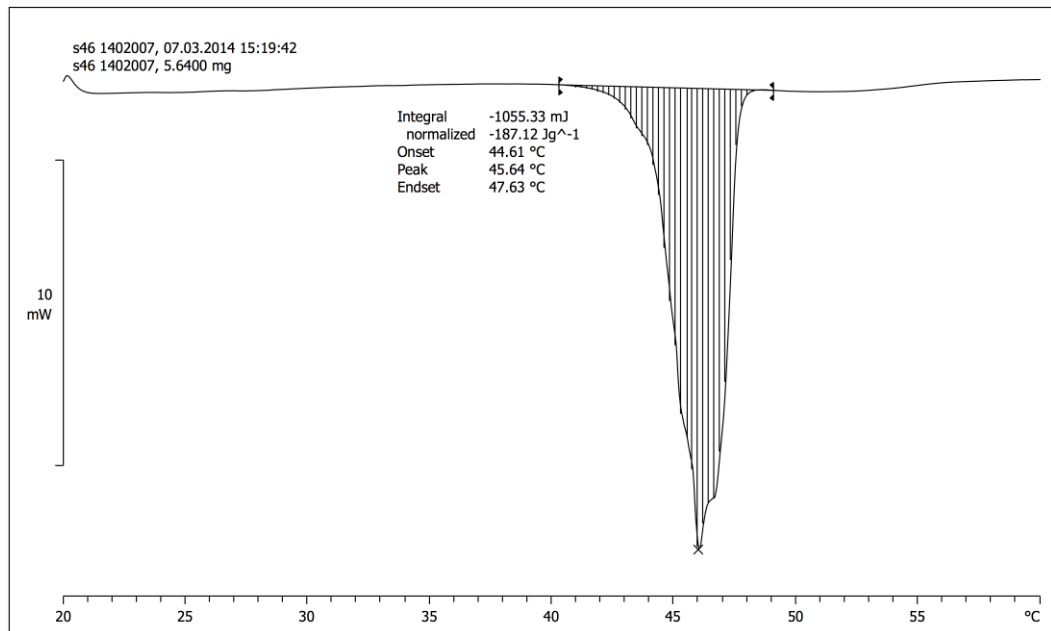
Figure 4-4 DSC data from the supplier (PCM Products Ltd. [22]), which shows that the melting temperature range was 44.61-47.63°C (45 - 48°C), peaked at 46°C.

4.3.2 Metal foam specifications

The metal foam used was an irregular aluminium metal foam, characterized by its deviations in pore and strut morphology compared to common metal foams. Figure 4-5 shows the actual foam and its three-dimensional model. Figure 4-6 shows its schematic. The process of transforming the foam into a model has been explored in Chapter 3. The model enabled the measurements of porosity, total surface area, and pore/strut size. Its specifications are listed in Table 4-3. Copper pipes were expanded into drilled holes in the foam, ensuring an excellent thermal contact between the two. The pipes provided a flow conduit of hot water from a heater circulator located upstream.
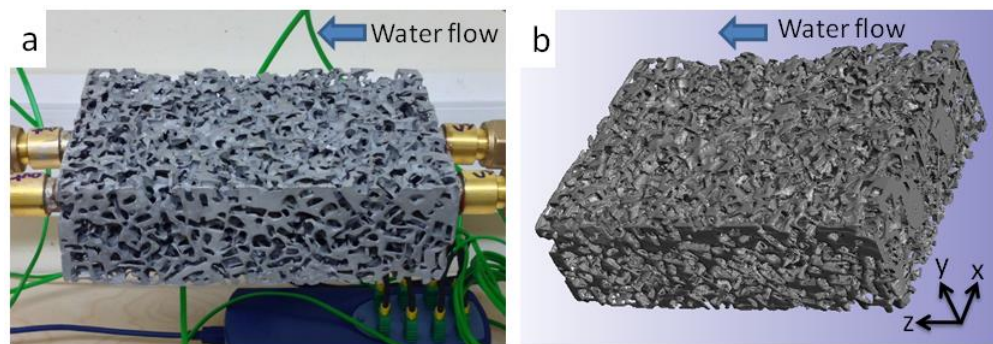
Figure 4-5 (**a**) The irregular metal foam. The copper pipes are visible, (**b**) its 3D model.
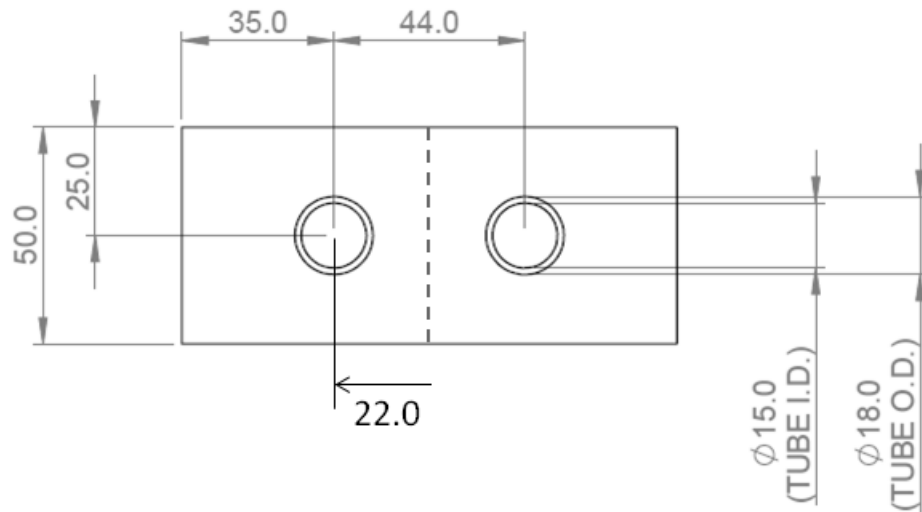
Figure 4-6 Schematic of the metal foam heat exchanger (x-y plane). Dimensions in mm. Dashes indicate the imaginary symmetrical division. Courtesy Thermacore Ltd.

Table 4-3 Metal foam specifications [135]. *Standard deviation indicates irregularity.

Dimension (foam)	165x50x114 mm (z-y-x axis)
Dimension (pipes)	15 mm (ID)
	18 mm (OD)
Material	AlSi7Mg0.6
Density	2680 kg/m^3
Thermal conductivity (at 20°C)	150-180 W/m.K
Porosity	67 %
Total surface area	0.54 m^2
Specific surface area	1495 m^2/m^3
Pore size – rectangular pores	8.41±2.09 mm*
Pore size – oval pores	6.69±1.00 mm*
Strut thickness	1.67±0.52 mm*

4.3.3 PCM impregnation procedure

The PCM was firstly crushed into small chunks and melted in a vacuum oven (Gallenkamp – see Appendix A3) at 56°C for 5 hours in a metal container (Figure 4-7A). The vacuum oven helped in removing air from the pores [78] as well as impurities from the air. The foam pores were cleaned via compressed air blasts and the pipe ends were covered with tapes to prevent the PCM melt from seeping into the pipes. The melted PCM was then cooled under ambient temperature (Figure 4-7B). The foam was then placed on top of it (Figure 4-7C). It was melted again (56°C, 7h). The foam slowly submerged into the melting PCM under its own weight and gravity as the melt phase gradually filled the pores (Figure 4-7D). While this was carried out, the container was

periodically tapped and shaken to agitate the melt PCM/foam composite to aid in air pockets removal. The composite was then left to cool (ambient, 3h) to allow for PCM solidification. Once cooled, the composite was extracted from the container via melting (from the container walls), followed by crushing, and chiselling until a final composite form was achieved (Figure 4-7E). PCM residues were cleaned off the pipe surfaces and thermocouple holes were drilled. Finally, the composite was integrated into the test rig (Figure 4-7F).
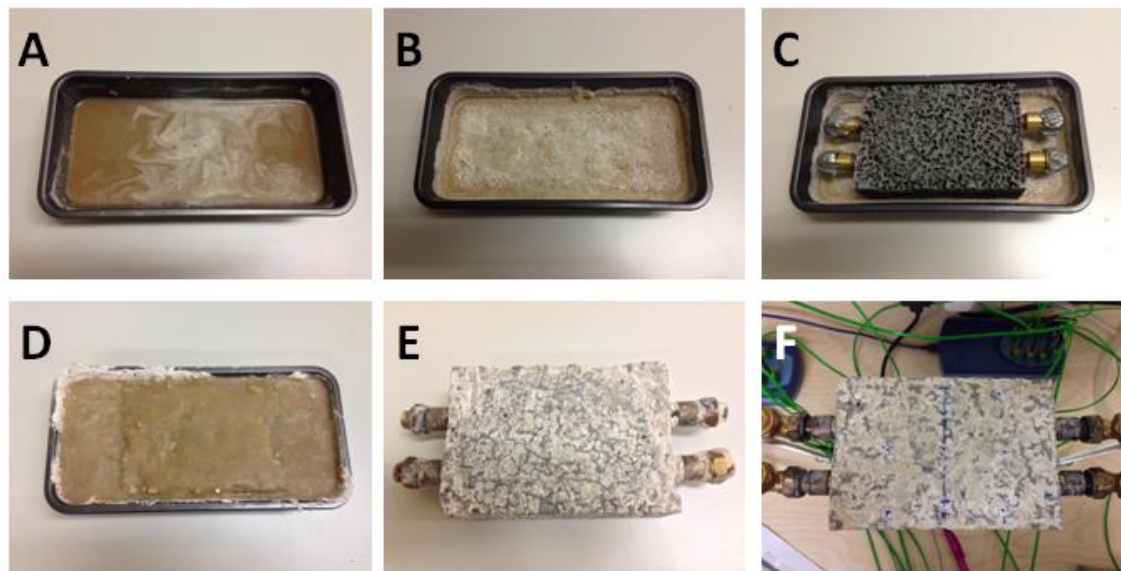
Figure 4-7 PCM impregnation procedure (adapted from Xiao *et* al. [136]).

4.3.4 PCM impregnation ratio

To measure the effectiveness of the impregnation procedure, a dimensionless parameter called impregnation ratio, α, was used to define the ratio of actual mass of PCM impregnated into the porous foam to the ideal mass able to be impregnated. The value was 100% if all the pore spaces were perfectly impregnated with PCM [136]. The scale used for weighing masses was a Mettler PM4800.

$$\alpha = \frac{m_{actual}}{m_{ideal}} = \frac{m_{PCM}}{\varepsilon V_b \rho_{PCM-S}} = 95.8\% \qquad \text{Equation 4-1}$$

Where: m=mass (kg), ε=porosity (fraction), ρ=density (kg/m³), and V=volume (m³).
Where subscript: actual=actual impregnation, ideal=ideal impregnation, b=bulk property minus the pipes, and PCM-S=solid phase PCM.

4.3.5   Test rig design

The heat source was from a heater circulator (Haake analogue C10, 5L capacity, 25-100°C supply range, 0.01-0.04°C temperature stability, flow at 12.5L/min). The fluid used was from the laboratory mains water. The circulator had a singular fluid output, which was branched into two, allowing fluid flow into the two pipes. This had the effect of reducing the flow to 4L/min. Munson *et* al. [137] provided the necessary equation to calculate the minimum hydrodynamic entrance length, L_{min} to ensure a fully developed flow under these supply conditions (4L/min, 60°C maximum). Flow measurement was via Rotameters.

$$L_{min} = 4.4Re^{1/6}D$$ Equation 4-2

Where: Re=flow Reynolds number and D=pipe diameter (m). The minimum length calculated was 330mm. The length constructed was 540mm (Figure 4-8 below).
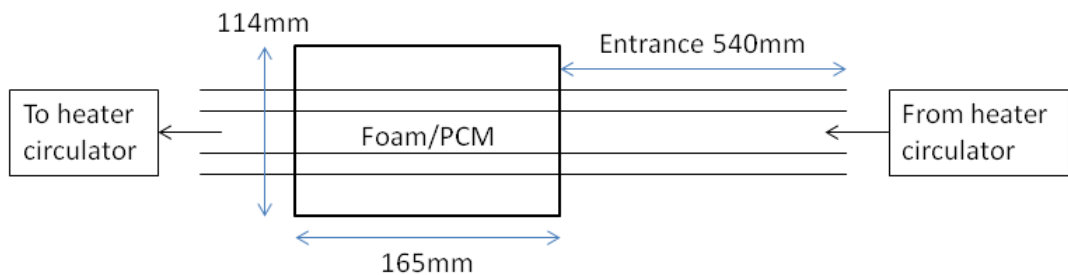
Figure 4-8 Schematic of the test rig (plan view: x-z plane).

All equipment involved in all experimentations are catalogued in detail in Appendix A3.

4.3.5.1   Temperature measurement

Temperature measurement involved the following equipment:

- Type K thermocouples, 1.5mm diameter, and manufacturer stated accuracy of ±0.75% (manufacturer: TC Direct). A total of 16 thermocouples was used. Numbering format was TC*XX* (i.e. TC01 – TC16).
- Data logger, manufacturer stated accuracy ±0.25% (manufacturer: PicoLog). A total of two data loggers were used as each data logger could only accommodate 8 active thermocouple channels.

The measurements taken were the differential water temperature, dT_W, ambient temperature, T_a, and PCM temperatures (Figure 4-10).

Thermocouple operation is based on the "Seebeck effect", in which when two wires composed of dissimilar metals are joined at both ends and one of the ends is heated, a continuous current flows in the "thermoelectric" circuit (Figure 4-9a). If this circuit is broken at the centre, as shown in Figure 4-9b, the new open-circuit voltage is a function of the junction temperature and the compositions of the two metals [138].
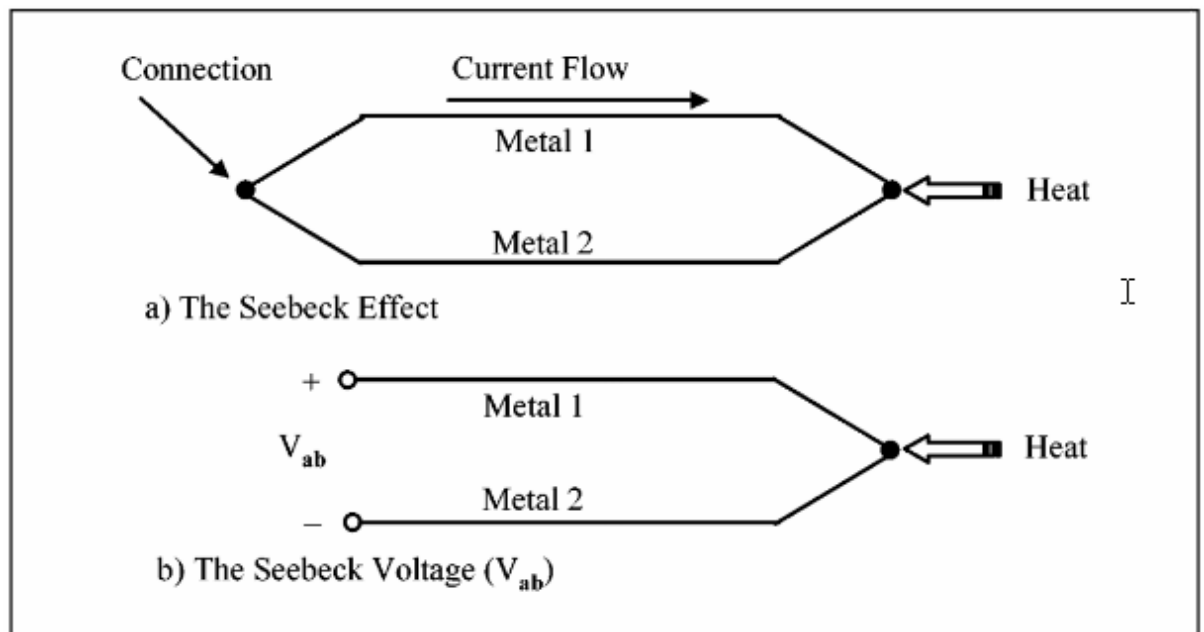
Figure 4-9 The thermoelectric circuit, in which thermocouple principle is based upon [138].

The two metal combinations for the type K thermocouples are: 1) Nickel-chromium (Chromel) and 2) Nickel-aluminium (Alumel). Based on guidance from the British Standard BS 1041: Part 4 (1992) [139], Type K thermocouple is suitable for use in an oxidizing atmosphere. It has a wide temperature range, from -250 to 1100°C. It is the most commonly used type in industry today [140].

According to BS1041: Part 4 and the manual document from the manufacturer, TC Direct [141], for the following temperature cut-offs, these problems could occur:

- At 250 - 600°C, temperature cycling hysteresis could occur, which results in errors of several degrees.

- Above 800°C, oxidation increasingly causes drift and decalibration.

The temperature range involved in the experiments here was: ambient (20°C) to 60°C maximum, therefore these issues were not anticipated.

The following Figure 4-10 shows the locations of the thermocouple within the sink. Holes were drilled after the PCM impregnation procedure was completed, and solidified. Thermocouples were carefully inserted to avoid contact with the metal phase, therefore the temperature recorded was representative of the PCM temperature. This avoided the thermocouples acting as "pin fins".

For the purchased thermocouples, the tolerance on output was guaranteed to be 0.75% (For example, 1000±7.5°C). The manual specifically states that the tolerance is expressed as either as a deviation in degrees Celsius or as a function of the actual temperature [139, 141]. The thermocouples were pre-calibrated by the manufacturer. However, an ice bath test was carried out on the thermocouples to examine the accuracy (Appendix A4) and this was carried out post-experimentation to assess the presence of any drift issue.

4.3.5.2 All other equipment

The major items of equipment are shown in Figure 4-11. Operational conditions were:

1. A singular flow of 4L/min, and
2. Inlet temperatures of 50, 55, and 60°C as the PCM was limited to 60°C exposure.

To contain the PCM whilst melting within the foam domain, a tight fit stainless steel container was constructed and a clear plastic top cover provided an unobstructed view of the melt progress (Figure 4-10b). The cover also helped in securing the thermocouples in place as well as to contain any evaporated water vapour (the PCM was a hydrate). Insulation was not applied to enable melt observation, and therefore heat loss due to natural convection was considered in the heat balance equations (Equation 4-1 to 11).
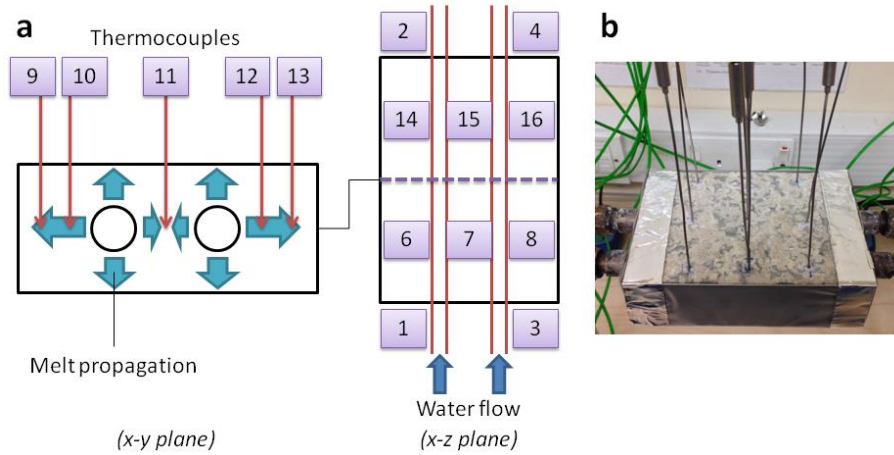
Figure 4-10 (**a**) Schematic of thermocouple locations. All thermocouples were placed midway from the bottom. X-y plane shows that the PCM melt propagates outward from the pipe surfaces, (**b**) the completed setup showing the metal container, plastic top cover, and thermocouples in place. TC09-13 provided a mean to study the melt propagation, discussed later in Chapter 5.
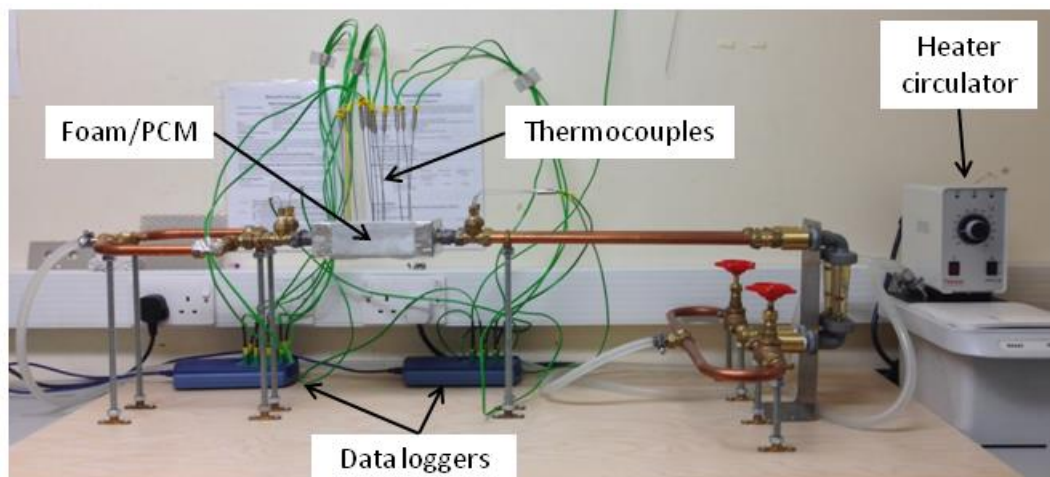
Figure 4-11 The test rig showing all the major equipment.

4.3.6   Heat balance governing equations

To measure the cooling capacity of the PCM under current heat exchanger design and operational conditions, a heat balance between the supply-side (heat release) and the PCM-side (heat absorption) was calculated. Heat absorption included the contributions from solid phase of PCM and aluminium i.e. sensible heating. The mass of PCM, m_{PCM} was measured after the impregnation process completion (m_{PCM} = 616g). Mass of aluminium (foam), m_{AL} was calculated via a correlation of its density, porosity, and the

bulk volume. Ambient temperature, T_a was 23°C averaged during the period of experiments (TC05, indoor lab, August 2014). Initial and ending temperatures, T_i and T_e were based on the temperature profiles in Figure 4-18a-c. Several simplifications and assumptions were made:

- Heat uptake by the copper pipes was ignored (thickness = 3mm) because of their relatively small mass compared to the aluminium foam and PCM.
- Differential temperatures, dT were similar for both solid aluminium and PCM.
- Differential water temperatures, dT_W were averaged between the subtractions of TC02-01 and TC04-03 pairs (Figure 4-10a, x-z plane) over t_i to t_e (start to end time).
- In terms of radiative heat transfer, it was assumed that the sink acted as a black body, in which it was an ideal radiator and absorber of energy at all electromagnetic wavelengths. Therefore, the effect of radiation was neglected.

Thermal images were taken of the foam when it was heated without the presence of the PCM (Figure 4-12), and exposed to the environment. It clearly shows that the metal struts were at uniform temperature. This meant that the efficiency of the foam was assumed to be unity (~1). This was the driver behind the heat exchange between the PCM and the foam because the PCM phase would need to achieve a thermal equilibrium with the metal struts, this process therefore increased the PCM temperature, and it undergoes melting as a result.
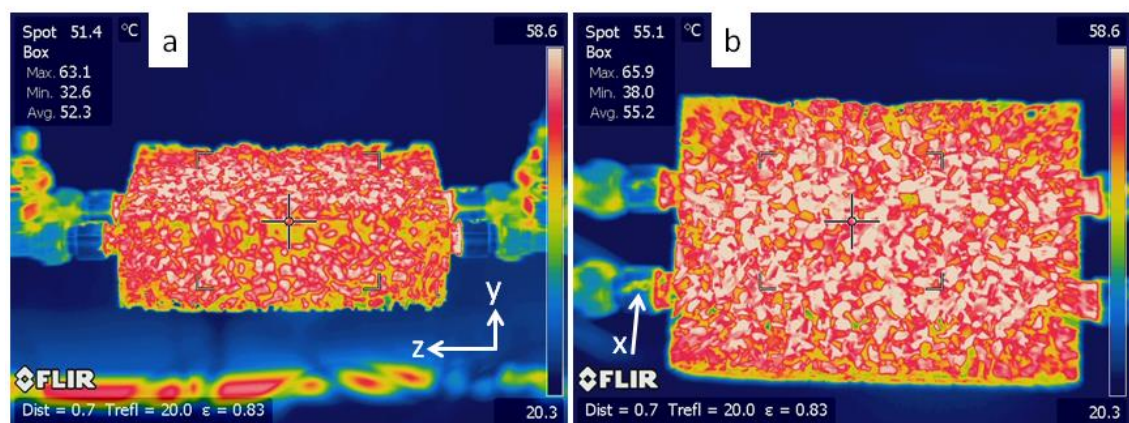
Figure 4-12 FLIR images of the foam, heated to 60°C, without the presence of the PCM, and exposed to the environment (a) overview, (b) top view.

The temperature profiles in Figure 4-17and Figure 4-18a-c showed that the starting temperature for all three cases were within 20-30°C. All experiments ended at t=3600s. The proceeding Equation 4-3 - 10 are the governing equations. The heat balance results in Figure 4-20 are also presented in terms of normalized energy capacity, kWh/m^3 (the cubic metre here is the foam/PCM volume i.e. the heat sink volume).

$$Q_W = Q_{PCM-S} + Q_{PCM-L} + Q_{AL-S} + Q_{LOSS}$$ Equation 4-3

$$Q_W = m_W * Cp_W * dT_W$$ Equation 4-4

$$Q_{PCM-S} = m_{PCM} * Cp_{PCM} * dT$$ Equation 4-5

$$Q_{PCM-L} = m_{PCM} * L_{PCM}$$ Equation 4-6

$$Q_{AL-S} = m_{AL} * Cp_{AL} * dT$$ Equation 4-7

$$m_{AL} = \rho_{AL} * (1 - \varepsilon) * V_b$$ Equation 4-8

$$Q_{LOSS} = U_{LOSS} * A * (T_{avg} - T_a)$$ Equation 4-9

$$T_{avg} = \frac{T_i + T_e}{2}$$ Equation 4-10

Where: Q=thermal energy capacity (kJ), Cp=specific heat (kJ/kg.K), m=mass (kg), dT=differential temperature (°C), T=temperature (°C), L=latent heat (J/kg), ρ=density (kg/m^3), V=volume (m^3), U=heat transfer coefficient (W/m^2.K), and A=area (m^2).

Where subscript: W=water, PCM=phase change material, AL=aluminium, S/L=solid/liquid phase, LOSS=heat loss, i/e=initial/ending, a=ambient, and avg=average.

The heat exchanger was not insulated during tests and the convective heat loss coefficient, U$_{LOSS}$ was assigned to the exposed surfaces (stainless steel, natural convection, ambient temperature, T$_a$ = 23°C), unique to each orientation (Figure 4-13) [142].

$$U_{LOSS} = constant. (\Delta T/l)^{0.25}$$ Equation 4-11

Where: U_{LOSS}=heat loss coefficient (in kW/m^2.K) and ΔT=PCM temperature – ambient. The constants and characteristic lengths, l, are given in Table 4-4. The unique coefficient values were calculated accordingly and are given in Table 4-5.
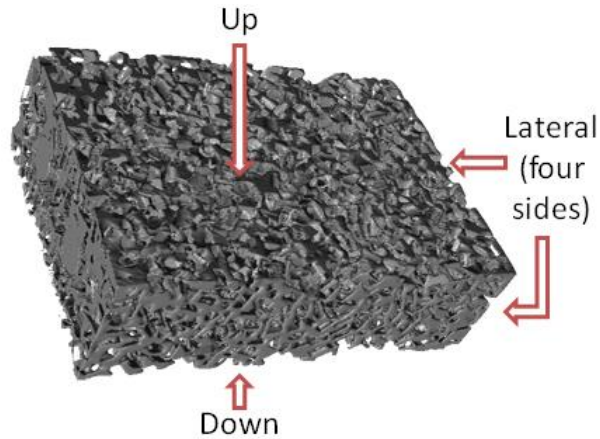
Figure 4-13 Surface orientations. The foam/PCM was enclosed within a stainless steel container during tests.

Table 4-4 Relevant values for calculating the convective heat loss coefficients.

Orientation	Constant	Characteristic length, l	
Vertical plane	0.00245	Height	0.05 m
Horizontal up	0.00235	Mean side length	0.165 m
Horizontal down	0.00107	Mean side length	0.165 m

Table 4-5 Heat loss coefficient values, unique to surface orientation.

Orientation	Value
Up	8.770 W/m^2.K
Down	3.993 W/m^2.K
Lateral (four sides)	12.323 W/m^2.K

4.4 Results and discussion

4.4.1 PCM impregnation

Based on the results in Table 4-6, the impregnation ratio, α was calculated as follows,

$$\alpha = \frac{0.616 kg}{0.67 \ x \ 6.045 x 10^{-4} m^3 \ x \ 1587 kg/m^3} \ x \ 100\% = 95.8\%$$

The ratio of 95.8% could be considered a success and was comparable to the works by Jiang *et* al. [79] (paraffin/copper foam/95% porosity, 89.7%) and Xiao *et* al. [136] (paraffin/nickel foam/97% porosity, 98.6%). In these works, the vacuum method was compared with the constant pressure method and the former was proven to give superior impregnation as it aided in removing air from the foam pores. Impregnation could never reach 100% because the PCM inside the metal foam inevitably shrank during the freezing process, which was attributed to the difference in the PCM density between its solid and liquid states (solid density is larger). The shrinkage led to small cavities inside the composite foam/PCM [143]. In this study, the impregnation was carried out only once to limit the risk of damaging the foam struts. After all experiments were completed, the PCM was leached out carefully in three stages e.g. heating, washing, and slow air blasts. The mass of the cleaned foam was measured and the mass loss was calculated to be 3.2%. This could be attributed to mechanical handling, PCM expansion/shrinkage cycles within the foam, and corrosion.

Table 4-6 The results from the vacuum PCM impregnation.

Foam+pipe protrusions (dry) mass	858.7 g
Foam+pipe protrusions+PCM mass	1474.2 g
Impregnated PCM mass	615.5 g
Impregnation ratio (in %)	95.8 %
Post-experiments foam+pipe protrusions (dry) mass	831.4 g
Foam+pipe protrusions mass loss (% over original)	3.2 %

4.4.2 Effect of inlet temperature on the PCM melting behaviour
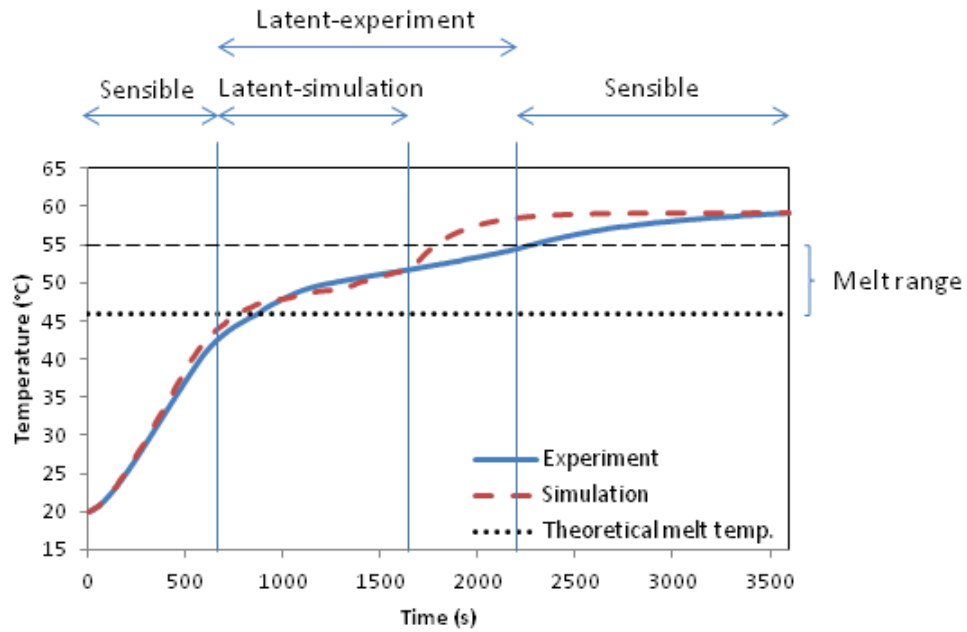
Figure 4-14 The definition of PCM heating phases. Inlet temperature 60°C. Included is the simulated profile (discussed in Chapter 5).

The PCM heating phases were defined in Figure 4-14. It shows the PCM temperature profile at the inlet 60°C. Two phases are visible: sensible and latent heating. The melting process was within the 46 - 55°C range. This was slightly bigger than the range indicated in the DSC data from the manufacturer (Figure 4-4), which was 45 - 48°C. This could be due to the differences in the heating condition of the PCM or other experimental parameters – as in Figure 4-15 (inlet at 50°C), it shows that the melt range matched the DSC range i.e. 44 - 48°C. Melting within a range is normal for PCMs. To determine the basis of comparison between the inlet temperatures, the heating profile using the lowest inlet temperature i.e. 50°C was studied in Figure 4-15. Visual inspection revealed the melt started at t ~1500s and ended at t ~3000s. The temperature at the melt end was 48°C. The melt behaviour therefore followed the prediction as shown in Figure 4-10a, which led to the conclusion that to assess the melt completion, the perimeter temperatures took precedence i.e. those temperatures recorded by TC09 and 13 as in Figure 4-16. The profiles here showed that TC13 lagged behind compared to TC09 in all cases (0.5-1.0°C maximum), therefore TC13 took precedence between both. Figure 4-17 plots the TC13 profiles for all three inlet temperatures, and the melt was considered complete once the profile finished the latent stage heating. It revealed the melt completion time to be: 1) 50°C: 3000s, 2) 55°C: 1900s, and 3) 60°C: 1600s (all rounded

values). The inlet temperature therefore had a significant effect as evidently, a 10°C increase from the baseline 50°C, the melt was completed 46% quicker. The 60°C inlet limit was due to the PCM safety limit. Above this, it would have triggered a chemical decomposition of the salt hydrate. It was also the common inlet temperature of power electronics [144]. Although the melt completed within 1600s for the expected inlet condition in traction of 60°C, the heating continued in the sensible heating mode until equilibrium is reached, therefore the sink could still uptake the heat if the stopping period is estimated to be 1 hour (for intercity trains).

In terms of obtaining the fastest melting, a large temperature difference between the charging (inlet) temperature and the PCM melting point is recommended, subject to equipment and PCM limitations.
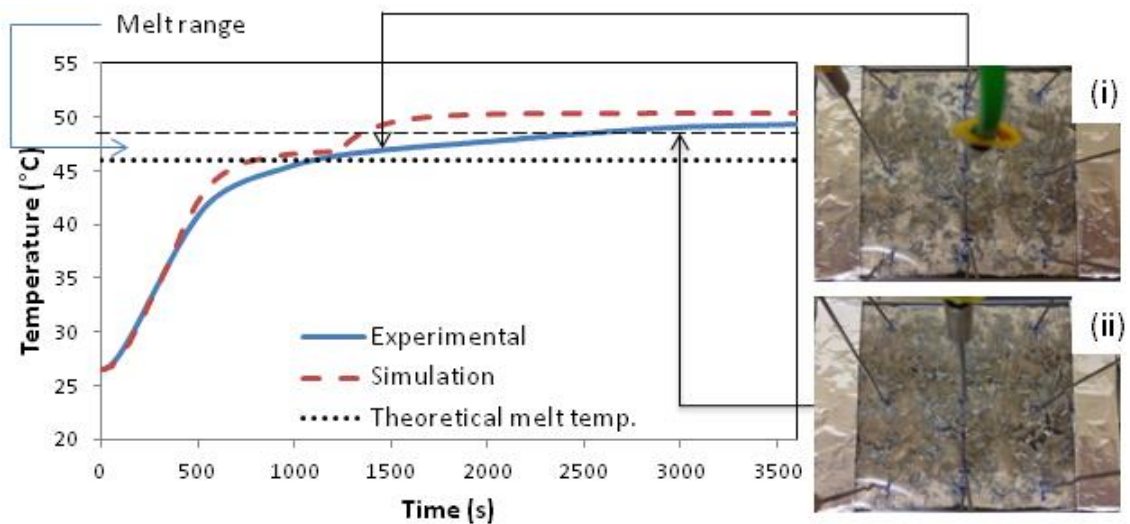
Figure 4-15 **Visual inspection of the PCM melt progress**. Inlet temperature 50°C (**i**) start of melt: t = 1490s, T = 46°C, (**ii**) end of melt: t = 2920s, T = 48°C.
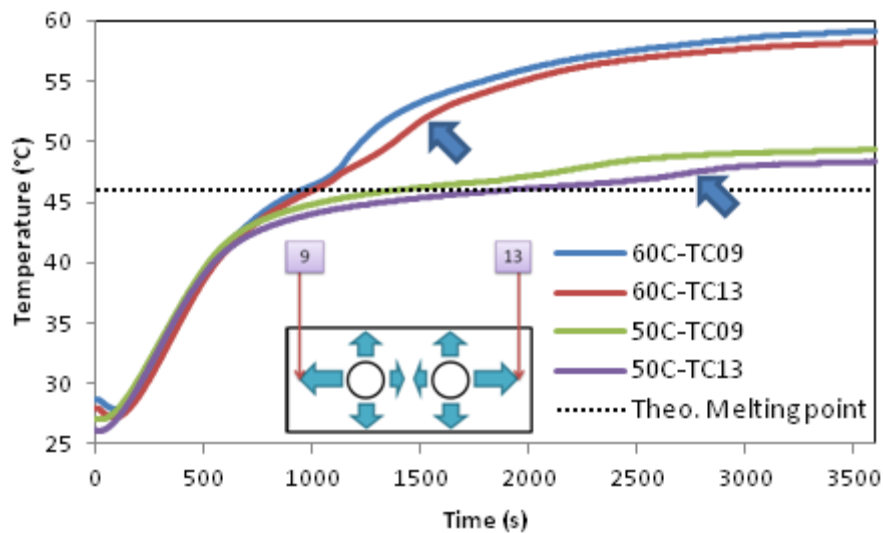
Figure 4-16 Perimeter temperature profiles: TC09 and 13 for inlet temperatures 50 and 60°C. TC13 are lagged behind, relative to TC09 in all cases (blue arrows).
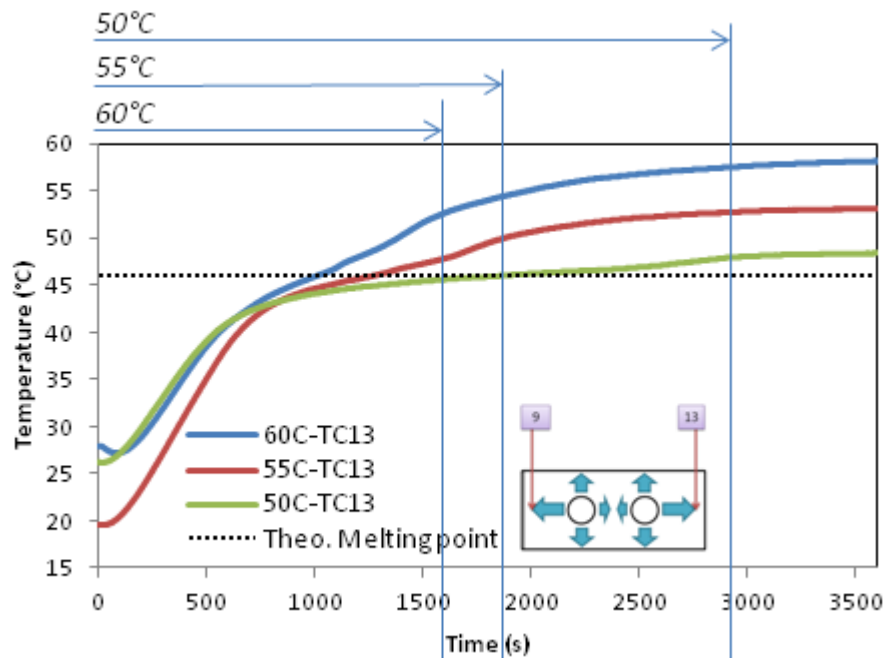
Figure 4-17 TC13 profiles plotted for all three inlet temperatures: 50, 55, and 60°C. The melt completion is defined as the end of the latent stage.

4.4.3   Heat balance

Figure 4-18 shows the PCM temperature profiles with the heater inlet profiles and water dT_W. It was noted that at t = 0s, the heater started to heat up steadily until it reached its setting within ±2.0°C, typically within a t = 500-800s period (refer Figure 4-19). Correspondingly, the PCM heated up as well. The dT_W followed the trend of the heater profile and peaked at the onset of the heater stabilisation before it set on its own stable value. The overall positive dT_W values signified that the foam/PCM composite absorbed heat from the hot water as it underwent latent and sensible heating.

The heat balance under all inlet temperatures was plotted in Figure 4-20. Generally, the released heat (mean values) were approximately 7% higher in value compared to the absorbed heat. This could be attributed to some simplifications imposed on the calculation (Section 4.3.6).

The heat sink thermal capacity was calculated to be 0.079 ± 0.009 kWh (for 50°C inlet) and 0.092 ± 0.007 kWh (for 60°C inlet). These correlated with the preliminary calculation firstly presented in Chapter 1, Section 1.2, which was 0.075 kWh. The values in this Chapter were calculated in more detail, hence are more accurate. In terms of applicability in traction transient cooling during the stopping period, the sink would be able to cool a group of 4 to 5 IGBT modules, should each module is rated at 20W dissipation rate, within a stopping period of 1h (hence, 0.02 kWh) for intercity trains, based on the data by Perpina *et* al. [3]. Because the PCM completed the melting by 1600s for 60°C inlet, it would also be applicable for a much shorter stopping period – as indicated in Table 4-1, the stopping period for intercity trains was estimated to be in the range of 200 – 3000s.
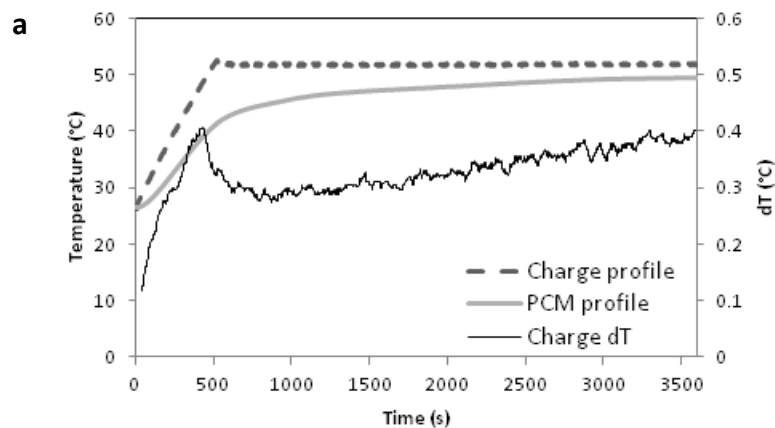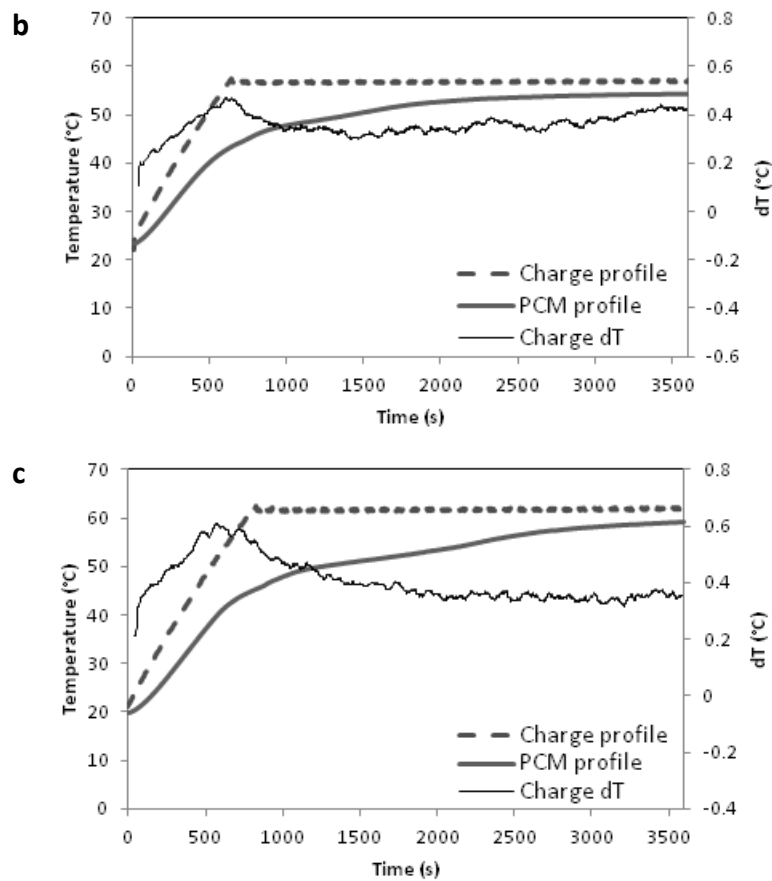
Figure 4-18 Experimental heater, PCM, and dT_W profiles for the inlet temperature of (**a**) 50°C, (**b**) 55°C, (**c**) 60°C.
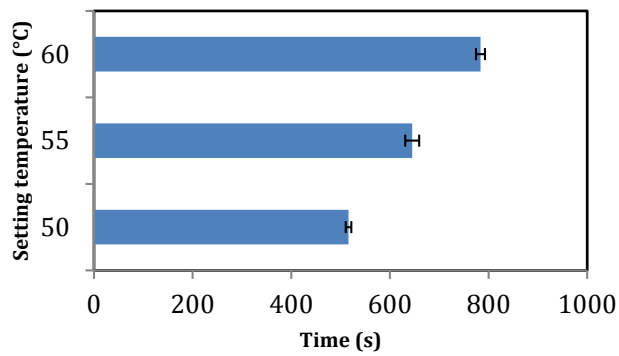
Figure 4-19 Time taken for the heater to stabilize to its temperature setting. Error bars show mean ± standard deviation, n = 3.
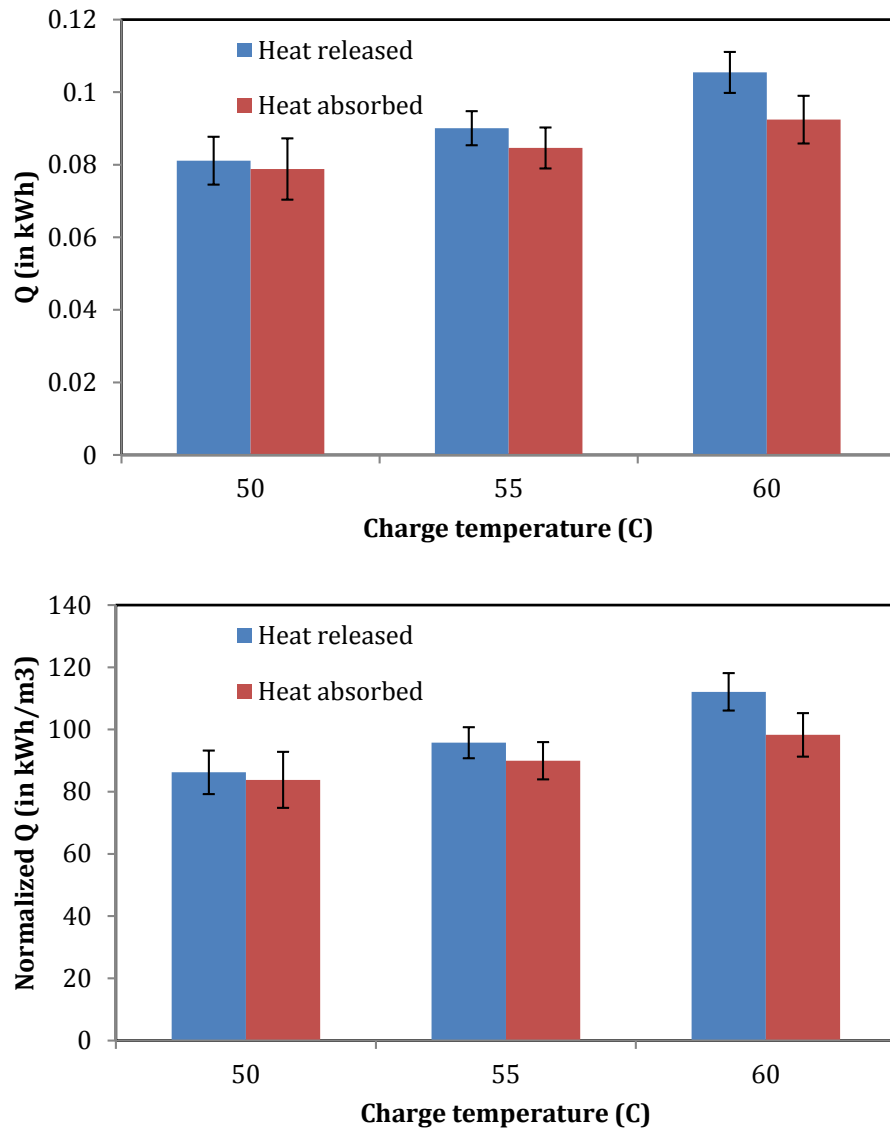
Figure 4-20 The results from the heat balance calculations. Thermal capacity i.e. uptake of energy by the sink (aluminium and PCM) in terms of kWh and normalized kWh (per cubic metre of the sink) under current design and operational conditions. Note: the conversion factor is 1 kWh = 3600kJ. Error bars show mean ± s.d., n = 3.

4.4.4 Heat transfer rate

The delta T data from the water-side enabled the calculation of heat transfer rate by using the previously mentioned Equation 4-4 ($Q_w = m_w * Cp_w * dT_w$). The heat transfer rate is plotted in Figure 4-21 for all three charging temperatures; 60, 55, and 50 °C. The heat transfer profiles show that the heat transfer peaked at 140 W (for 60°C charge), 130 W (for 55°C charge), and 110 W (for 50°C charge). The rates then reduced and increased steadily during the sensible/latent heating processes of the PCM. These were generally observed for all charge temperatures.
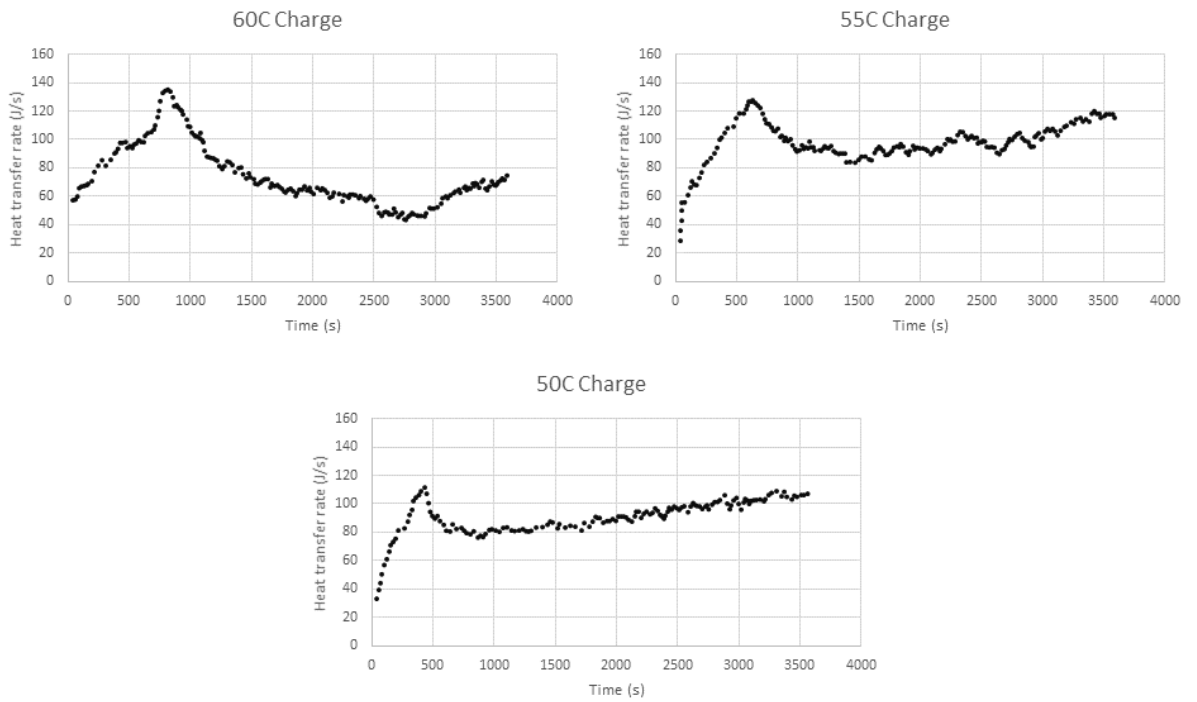
Figure 4-21 Heat transfer rate, based on delta T data from the water circulator for all charge temperatures.

4.4.5 Localized melting rates

Localized melt fronts were investigate with the aid of the thermocouple placements (Figure 4-22b). Figure 4-22a shows the temperature did not vary significantly along the pipe length (z-axis) i.e. TC07-15 and TC08-16, but it varied greatly in the x-axis i.e. when comparing the TC07-15 and TC08-16 sets.

Three observations were made:

- The melting range followed the range estimate indicated by the DSC data (Figure 4-4), between 45 - 50°C.

- The heat concentration in the middle of the foam (Figure 4-22b) rendered temperature variations across the heat exchanger – the melting at this region was quicker than the rest of the foam zones – to alleviate this effect, a redesign of the heat exchanger was proposed in Figure 4-22c to give a more symmetrical profile. This redesign was modelled and presented in the next Chapter 5.

- There was a temperature difference between the inlet and outlet of hot water feed, which indicated thermal energy uptake by the sink as it melted the PCM. The copper wall temperature however, could be considered constant – this

enabled the modelling of constant copper wall temperature in the next Chapter 5 to simplify the modelling process.
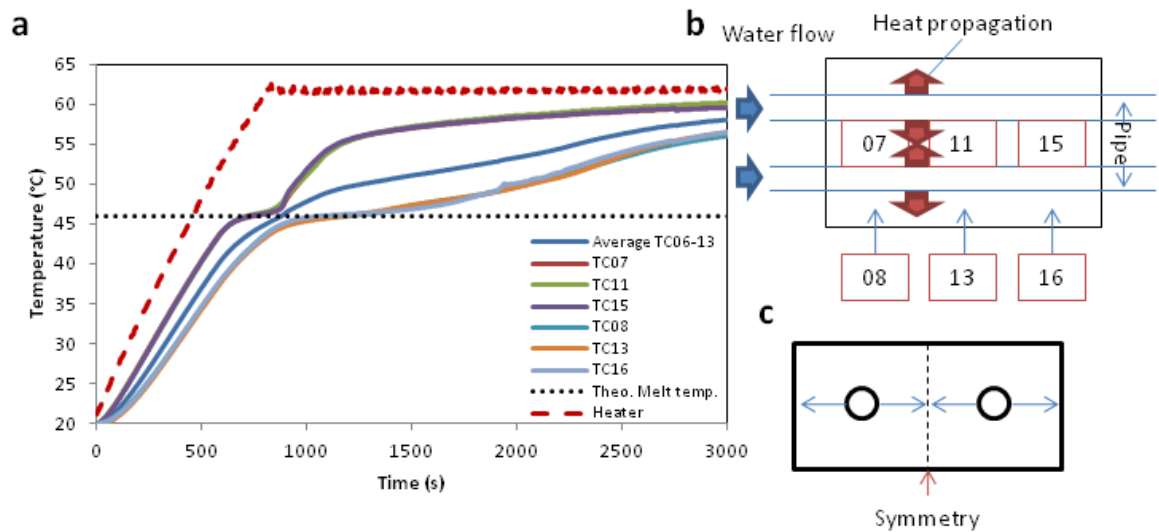
Figure 4-22 **Melt front tracking** (**a**) temperature profiles, (**b**) x-z plane showing the heat propagation and concentration in the middle foam section, (**c**) proposed simple improvement of current design giving a more symmetrical feature (x-y plane).

4.4.6   Subcooling during solidification

Solidification is to be carried out via forced convection cooling through a fin stack as in Figure 4-1. This test rig was planned to be constructed in the near future at Thermacore Ltd. The current rig was customized for temperature-variable melting only. However, solidification experiments were carried out to understand the PCM cooling behaviour. Immediately after the end of 60°C charge, the water in the heater circulator was quickly replaced with cool water at 20°C and flowed into the piping (4LPM). The water temperature increased by ~10°C as the residual heat from the piping, valves, and other thermal masses from the rig was released into the stream as it was pumped through. The PCM temperature profile is shown in Figure 4-23. The solidification showed subcooling (labelled 'B') as expected (refer Section 2.4.1.3), which was 10°C lower (i.e. 36°C) than the theoretical solidification temperature. This discouraged simulation of the cooling process as software generally could not include the subcooling phenomenon. One of the aims in PCM research was to mitigate the subcooling effect by adding nucleating agents, etc [145]. As discussed in the earlier Section 4.4.5, a design issue that created differential melting rates was also evident during solidification (labelled 'A').
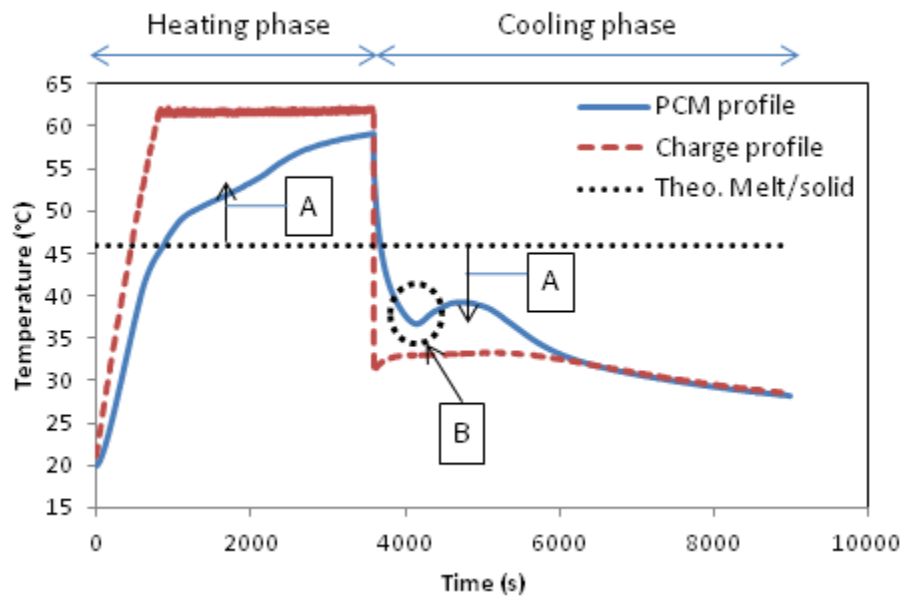
Figure 4-23 **Heating and cooling profiles** (**A**) deviation from theoretical values due to a design issue (**B**) 10°C subcooling. Note: heating at 60°C, cooling at 20°C.

4.5 Conclusions

The aluminium foam/salt hydrate PCM was composited via a vacuum impregnation method and heated with water at 4LPM and at 50, 55, and 60°C inlets. This was the first study to attempt to create a metal foam and salt hydrate composite.

The main outcomes of the study were as follows:

- The vacuum impregnation method yielded a 95.8% impregnation ratio. The cavity volume ratio therefore did not exceed 5.0%.

- The melting time was dependent on the inlet temperature: the larger the differential temperature (positive dT) between the melting point and the inlet temperature, the quicker it melted.

- At the highest inlet temperature of 60°C, the latent heating period spanned 1500s and it melted the PCM 46% quicker than the 50°C inlet temperature.

- At inlet of 60°C (common to traction inlet conditions), the composite absorbed 0.092 kWh of thermal energy within 3500s, inclusive of the sensible and latent heating. The melt was also completed within 1600s. This meant that the sink would be able to cool 4-5 IGBT modules rated at 20W dissipation during stopping periods of less than an hour (for intercity trains). The thermal capacity

calculations here, albeit done in more detail, matched the preliminary calculations (prediction) in Chapter 1.

- Localized melt fronts propagated at different rates, due to the original heat exchanger design. A slight modification (pipes relocation) was proposed to give a more symmetrical feature of the heat exchanger.

In the next Chapter 5, the experimental data obtained here were used for validating the numerical simulation.

Chapter 5   Numerical simulation of phase change material melting in the irregular foam

5.1   Abstract

Chapter 1 and 2 have established the bases of the transient heat sink idea during traction stopping at terminus, which was decided to be based on a novel irregular metal foam and phase change material. Chapter 3 formed a crucial step in characterizing the metal foam via CT scanning. In Chapter 4, experimentation was carried out to assess the performance of the sink. Thereby in this Chapter 5, numerical simulation was developed to model the experimentation. Developing a robust numerical simulation was intended to ensure a high confidence in applying the methodology for redesign and scaling-up of the irregular metal foam/phase change material-based heat sink prototype. A full-scale heat exchanger model was constructed, mimicking the actual dimensions and boundary conditions. The foam/phase change material (PCM) phases were treated as a homogeneous fluid phase with the effective thermal conductivity, K_{eff}, calculated via the homogenization analysis from the computed tomography (CT) scan to be 10.83 ± 1.00 W/m.K. This value also meant that the foam increased the thermal conductivity of the PCM by 24 times (from 0.45 W/m.K baseline). The phase change process was simulated by employing slightly modified enthalpy porosity equations. The simulated temperature profiles were verified experimentally. Examination of the temperature contours revealed that the current design adversely affected the isothermal charging characteristic due to hot spot proliferation in the middle foam zone, creating varied heating rates. A slight design modification (pipes relocation) managed to relieve this hot spot by 8°C. A simpler, more economical numerical approach was proposed by using the established Boomsba and Poulikakos model in calculating the K_{eff} instead of the homogenization, which required a CT scan step.

Keywords: irregular metal foam, phase change material, homogenization, effective thermal conductivity, numerical simulation.

5.2   Introduction

Harnessing the thermal storage potential of phase change materials (PCM) often requires their inherently low thermal conductivity of 0.2 - 0.5W/m.K [146] to be increased in some way, for most commercial PCMs. To increase the energy charging and discharging rates, many techniques have been theorized and tested such as passive techniques: finned tubes [42], macro and microencapsulation [147], and active techniques: ultrasonic vibrations [148]. An excellent review on such techniques could be found in Fernandes *et* al. [59], which also concluded that porous metal matrices (such as metal foam) impregnated with PCM was the most attractive solution. Metal foam matrix conducts heat throughout the PCM volume passively, effectively enhancing the heat transfer rates. Characteristically it is lightweight, possesses high surface area/volume ratio, and is in some instances commercially viable.

Numerical simulation is an important subset of PCM research as it provides an economical method for rapid prototyping, heat exchanger optimization, and general understanding of the PCM systems. The essence of PCM is the phase change process: melting and solidification, typically solved through the enthalpy-porosity (EP) theory [73], the basic form of which is currently an option in commercial computational fluid dynamics (CFD) software such as Ansys Fluent [149] and Comsol Multiphysics [150].

To simulate the PCM phase change process, the heat exchanger model (2D or 3D) is created and the PCM domain subsequently formed. Depending on the researchers, a volume of fluid (VOF) algorithm would be incorporated to accommodate PCM expansion during melting [151]. The thermal source was simulated and the PCM heating phases studied through temperature and liquid fraction profiles. It is important to note that model domain size was often minimized to optimize the simulation grid size and computational power relationship. Time step size was also optimized as PCM simulation is dominantly transient. Numerical results must be independent of these two parameters for accuracy and confidence.

If the heat exchanger configuration is simplistic e.g. finned tubes, the aforementioned procedure is easy. However for random and complex structures like metal foam/PCM

composite, the modelling approach was often carried out through 'volume averaging' i.e. treating the metal matrix and PCM phases as homogeneous. Modelling realistic porous structures could be achieved via CT scanning foam samples and transforming them into models but this method is currently limited to small-scale analyses such as measuring effective thermal conductivity and flow permeability [152].

5.2.1 Objectives

To further optimize/scale-up the irregular metal foam/PCM transient heat sink design, a simplistic but accurate numerical approach had to be established.

- Calculation of the effective thermal conductivity through Homogenization.
- Validation of the phase change process simulated via the enthalpy porosity technique with experimental results in Chapter 4.
- Development of a simpler numerical approach without homogenization, which would avoid the CT scanning step.

### 5.3 Numerical methodology

5.3.1 Method summary
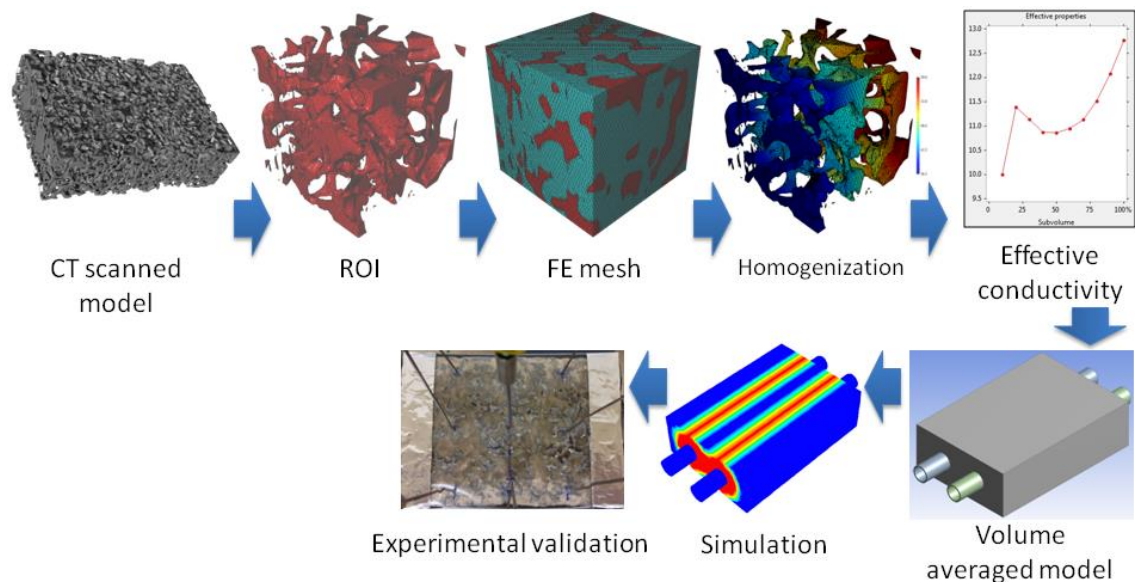
Figure 5-1 The numerical simulation methodology.

The numerical approach is shown in Figure 5-1. The irregular foam was firstly scanned via a CT scanner, which was then transformed into a 3D model. Six cubic regions of interest (ROI) were meshed (finite element, FE, mesh) and a Homogenization analysis revealed the effective thermal conductivity, Keff values of the metal/PCM composite. A 3D model with dimensions and boundary conditions mimicking the actual heat exchanger was drawn and meshed (CFD mesh). The PCM phase change process was then simulated through the EP (enthalpy porosity) technique and the temperature profiles were fitted to the experimental results for validation.

5.3.2 Governing equations

The numerical model employed the enthalpy porosity theory to predict the phase change process. This technique does not track the melt interface between solid/liquid explicitly but instead, liquid fraction, β, is associated with each grid cell in the domain. Liquid fraction indicates the fraction of grid cell volume that is liquid. It is computed at each iteration based on the enthalpy balance. The region where the liquid fraction is between 0-1, it is called the "mushy zone" or "melt front". The fluid is considered unsteady, laminar, incompressible, and three dimensional. The continuity, momentum and energy equations are expressed in Equation 5-1, 5-2 and 5-3, respectively.

$$\partial_t(\rho) + \partial_i(\rho u_i) = 0 \qquad\qquad \text{Equation 5-1}$$

$$\partial_t(\rho u_i) + \partial_j(\rho\, \partial_i\, \partial_j) = \mu\, \partial_{ij} u_i - \partial_i p + \rho g_i + S_i \qquad \text{Equation 5-2}$$

$$\partial_t(\rho h) + \partial_t(\rho \Delta H) + \partial_i(\rho u_i h) = \partial_i(k\, \partial_i T) \qquad \text{Equation 5-3}$$

Where: ρ=fluid density, u=fluid velocity, μ=dynamic viscosity, p=pressure, g=gravitational acceleration, S=source term, h=sensible enthalpy, H=latent enthalpy, k=thermal conductivity, and T=temperature.

Where subscript: t=time and i,j=vector indicating x, y, and z directions (three dimensional flow).

In the continuity equation, the fluid density, ρ, followed the Boussinesq model to correlate the change of density with temperature [153]. This model accommodated many natural convection problems.

$$\rho = \rho_0[1 - \gamma(T - T_0)]$$

<div align="right">Equation 5-4</div>

Where: ϒ=fluid expansion factor. For the PCM, it is 0.1.

Where subscript: 0=reference value.

In the momentum equation, the flow pressure loss due to the presence of solid PCM phase and metal struts was contributed by the source term, S, as introduced by Voller and Prakash [154] and modified by Liu *et al.* [155].

$$S_i = \frac{C(1 - \beta)^2}{\beta^3 + \omega}u_i + \frac{\mu}{a}u_i + \frac{1}{2}I\rho u_i|u_i|$$

<div align="right">Equation 5-5</div>

Where: C=mushy zone coefficient. In this study, it is 10^5 kg/m^3.s, β=liquid fraction, and ω=a small constant to avoid divisions by 0. Here, it is 0.00001, a=permeability, and I=inertial coefficient.

Gravitational acceleration is also taken into account. A buoyancy effect is included in the y-axis component of Equation 5-6.

$$S_y = \frac{C(1 - \beta)^2}{\beta^3 + \omega}u_y + \frac{\mu}{a}u_y + \frac{1}{2}I\rho u_y|u_y| - \rho g\gamma(T - T_0)$$

<div align="right">Equation 5-6</div>

Permeability, a, and inertial coefficient, I, are functions of porosity, ε, foam ligament size, d_f, and pore size, d_p, as formulated by Calmidi and Mahajan [117]. These values were successfully measured from the CT scan.

$$a = 0.00073(1 - \varepsilon)^{-0.224}d_f^{-1.11}d_p^{0.89}$$

<div align="right">Equation 5-7</div>

$$I = 0.00212(1 - \varepsilon)^{-0.132}\left(\frac{d_f}{d_p}\right)^{-1.63}$$

<div align="right">Equation 5-8</div>

Where porosity, ε=0.80, ligament size, d_f=0.00167m, and pore size, d_p=0.00755m.

In this work, a local thermal equilibrium between the PCM melt (liquid) phase and the metal struts was considered for simplicity – this infers that heat exchange was completed between the PCM and metal. For solid PCM phase, thermal non-equilibrium was considered, hence enabling heat transfer between both phases (this was first explained by the aid of Figure 4-12 in Chapter 4). The energy equation involved the following terms.

$$h = h_0 + \int_{T_0}^{T} C_p dT \qquad\qquad \text{Equation 5-9}$$

$$H = h + \Delta H \qquad\qquad \text{Equation 5-10}$$

$$\Delta H = \beta L \qquad\qquad \text{Equation 5-11}$$

$$\beta = 0 \qquad \text{if} \quad T < T_s$$

$$\beta = 1 \qquad \text{if} \quad T > T_l \qquad\qquad \text{Equation 5-12}$$

$$\beta = \frac{T - T_s}{T_l - T_s} \qquad \text{if} \quad T_s < T < T_l$$

Where: C_p=specific heat (at constant pressure) and L=latent heat.

Where subscript: s=solidus and l=liquidus.

The thermal conductivity, k is the focus of the next section as the value was taken as the effective term, K_{eff} contributed to by both the PCM and metal strut phases.

5.3.3 Homogenization analysis

High conductivity metal foam matrix such as aluminium and copper within low conductivity fluid such as water, air, and PCM increases the composite effective thermal conductivity, K_{eff}. It is common to consider the foam/fluid composite as homogeneous for design purposes to enable the estimation of K_{eff}. The complexity is derived from the fact that: 1) foam ligament normal to the flow direction may induce disruptions to the flow boundary layers, 2) conduction from the solid phase is expected to augment axial and radial heat transfer, and 3) for the PCM case, conduction is prominent during its solid phase and deteriorates as it melts, in which convection starts to proliferate. These and other factors enabled the deduction that K_{eff} depends (to varying degrees) on conduction in the solid/liquid, convection, and radiation (for high temperatures – for

simplification in the modelling, the sink in its entirety was considered a black body - an ideal radiator and absorber of energy at all electromagnetic wavelengths, thereby neglecting radiative heat transfer). Based on many studies, it was found that conduction in the solid phase was the principal heat transfer mode even in the case of less conductive metal matrices. So far, K_{eff} was often predicted through empirical and theoretical correlations, or deduced after numerical simulations. These established models (reviewed by Ranut and Nobile [71]) were derived from idealized foam geometries, which were therefore not applicable to the irregular foam. To solve this problem, an homogenization analysis was carried out.

The aim of homogenization was to approximate a heterogeneous material, for example a porous medium or a composite made up of several homogeneous phases, to a homogeneous material whose response to external stimuli (depending on the physics, e.g. applied stress or potential difference) resembled as closely as possible the original material. This helped to simplify the analysis. The properties of the homogeneous material approximating the original heterogeneous medium were called its "effective properties" (Figure 5-2).
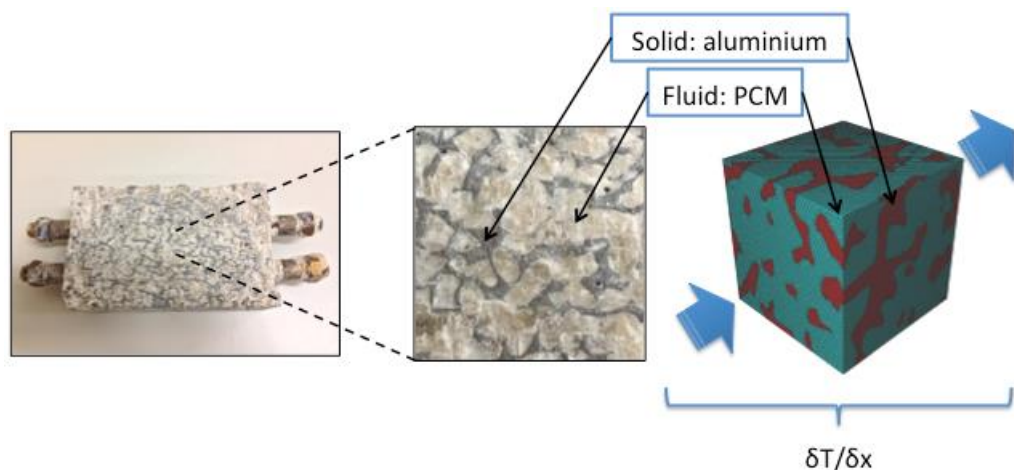

Figure 5-2 Homogenization analysis in calculating K_{eff} for the foam/PCM composite. The external stimuli was the temperature differential, $\delta T/\delta x$, unidirectectional but, applied to all axes (x, y, z).

The irregular foam was scanned with the CT scanner and cubic samples were segmented from the full model. The size of each cube model was 80x80x40 voxel, corresponding to 24x24x24 mm, x-y-z axes (the resolution is 0.3x0.3x0.6 mm, x-y-z). Six cubes were

segmented (Figure 5-3). These cube models were discretized into finite element meshes to the highest resolution possible to ensure the highest accuracy. Effective thermal conductivity was calculated based on Fourier's law [156].

$$K_{eff} = \frac{-\int q.\,dA}{\frac{\delta T}{\delta x}.A} = \frac{-\left(\int_s q.\,dA_s + \int_s q.\,dA_f\right)}{\frac{\delta T}{\delta x}(A_s + A_f)} \qquad \text{Equation 5-13}$$

Where: q=heat flux vector. A = cross sectional area (m^2), and δT/δx=axial thermal gradient along the cube. Where subscripts: s and f refers to the solid and fluid phases, respectively.
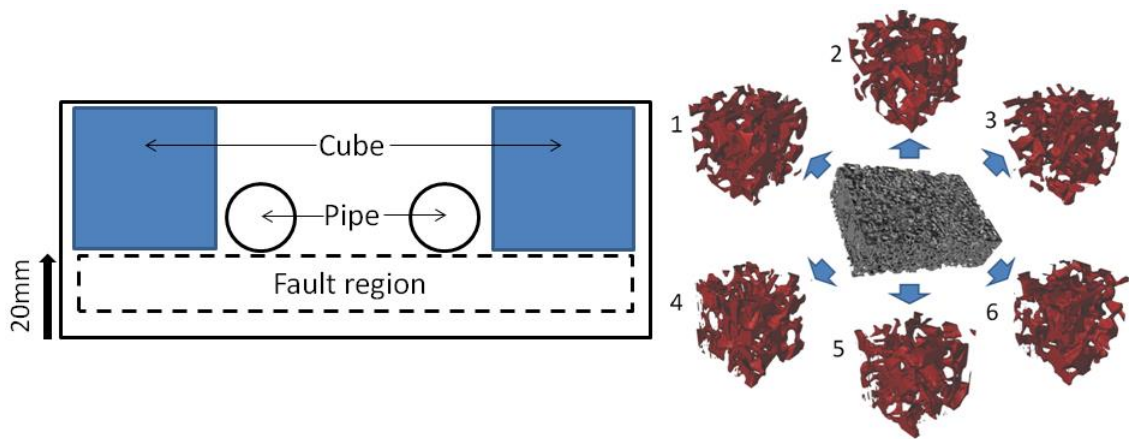

Figure 5-3 Six segmented cubes from the full 3D model. The cubes avoided the fault zone (ring-shaped dense region) within the foam. All cubes were 24x24x24 mm (x-y-z).

A thermal gradient was applied between two opposite boundary faces on an axial vector (x, y, or z) whilst all other faces were set to be adiabatic [157]. The heat flux, q was the result of steady-state finite element analysis and was obtained by summing up all nodal heat fluxes on one surface where the temperature was applied. The K_{eff} was calculated in uniaxial directions (x, y, or z) by changing appropriately the constant temperature planes and adiabatic conditions from which isotropic approximations were derived. This was why only cuboidal models were suitable.

The influence of boundary effects on the results of FE-based homogenization could be reduced by calculating the K_{eff} from field averages taken over a domain smaller than the ROI (Region of Interest) used in simulations. Appropriate domains were obtained by

scaling down the ROI proportionally, with the centre kept fixed. The yellow box in Figure 5-4b shows the size and position of the domain whose volume was 50% of the ROI volume (blue box). The graph of the 'effective properties vs. subvolume' (Figure 5-4a) shows the dependence of the calculated effective properties on the volume of the domain over which field averages were taken. The volume was expressed as a fraction of the ROI volume. If the ROI was large enough to cover a representative sample of the material, the curve was expected to reach a plateau at the intermediate averaging volumes. Absence of a plateau would have indicated that the chosen ROI was too small to be representative [96].
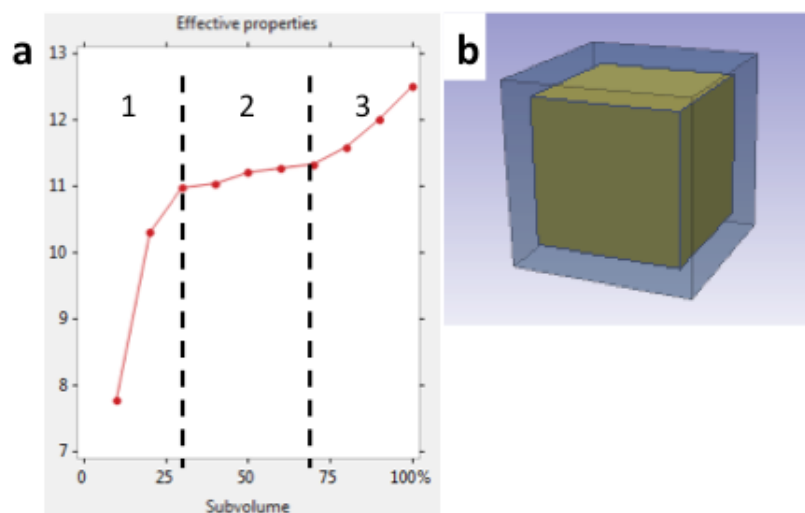

Figure 5-4 **The mitigation of boundary effects on the K$_{eff}$ calculations** (**a**) effective properties vs. subvolume graph showing the presence of plateau (cube 3 is shown as an example), (**b**) the scaled down domain (50%) from the ROI.

### 5.3.4 The physical model
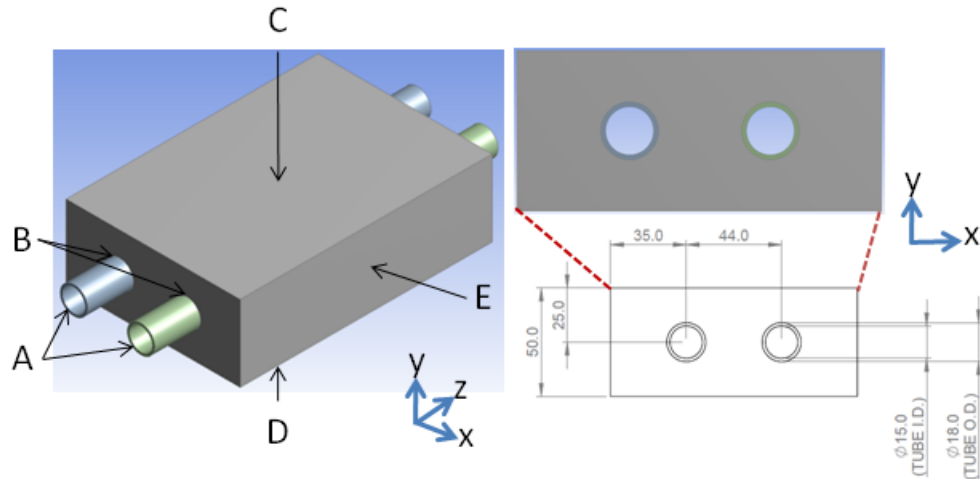
Figure 5-5 The physical model: dimensions and boundary conditions (A-E).

Figure 5-5 showed the 3D model that was drawn. Its dimensions were accurate to the actual foam heat exchanger. For the experiment, the thermal source was hot water. Differential temperatures between the inlet and outlet, dT, were measured to calculate heat uptake by the heat sink. Temperature profiles showed dT=0.1-0.5°C between inlet/outlet (Figure 5-6), hence the heat was simulated as a wall with constant temperature. The heat exchanger was not insulated during tests and convective loss coefficient, U_{LOSS} was assigned to the exposed boundary layers (stainless steel, natural convection, free stream temperature, T_∞=23°C), unique to each surface orientation [142],

$$U_{LOSS} = constant.(\Delta T/l)^{0.25}$$ Equation 5-14

Where: U_{LOSS}=heat loss coefficient (in kW/m^2.K) and ΔT=PCM temperature – ambient. The constants and characteristic lengths, l, are given in Table 5-1. The fluid phase i.e. homogeneous PCM/foam phase was enclosed within the boundary walls. Details of the boundary conditions are tabulated in Table 5-2 Heat loss from pipe surfaces were considered negligible i.e. adiabatic.
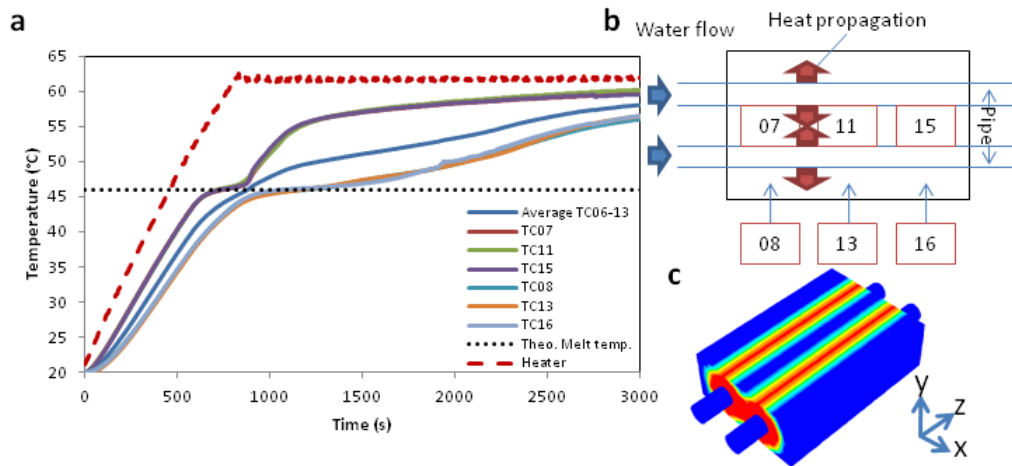
Figure 5-6 **Temperature variations along the x and z-axes, experimental** (**a**) Temperature profiles showing negligible dT along the pipe axis (z-axis) and significant dT perpendicular to the pipe axis (x-axis), (**b**) thermocouple placements, (**c**) simulated melt contour.

Table 5-1 Relevant values for calculating the convective loss coefficients.

Orientation	Constant	Characteristic length, l	
Vertical plane	0.00245	Height	0.05 m
Horizontal up	0.00235	Mean side length	0.165 m
Horizontal down	0.00107	Mean side length	0.165 m

Table 5-2 Boundary conditions. (*) Refers to plane orientation.

	Description	Value
A	Charging wall	50, 55, 60°C
B	Coupled wall interface for heat transfer	-
C	Convective loss surface: up*	8.770 W/m^2.K
D	Convective loss surface: down*	3.993 W/m^2.K
E	Convective loss surface: lateral* (four sides)	12.323 W/m^2.K

5.3.5 Grid and temporal independence analysis

Two types of computational grid were involved: 1) FE for homogenization analysis and 2) CFD for phase change simulations. The FE meshes were generated at the highest resolution possible at approximately 1.6 million elements per cube model, therefore no grid validation was necessary (Table 5-5). Tetrahedral meshes were used with refinements based on necessity e.g. at metal/PCM phase interfaces and curves. The meshes were less refined elsewhere to minimize the element number (Figure 5-7). The CFD meshes were a mixture of tetrahedral and hexahedral meshes with the fluid zone incorporating software controlled inflation at 1.2 growth rate factor (Figure 5-8). To

check for grid independence, the phase change process was simulated: charge at $T_W=60°C$, t=0-2000s, and time step size=1.0s. The melting time was compared for five different grid sizes. At the optimized grid size, temporal independence was carried out at three different time step sizes. The results are tabulated in Table 5-3. Considering the finest grid size 5 as reference, in which no further increase in size could be made, grid size 4 showed only a 0.27% deviation in the numerical result, hence it was selected. For the time step size, 1.0s was selected to reduce the amount of computational time as well as to simplify the root mean square ($RSQ = R^2$) fitting i.e. comparison with experimental data as thermocouple samplings were all 1.0s resolution.
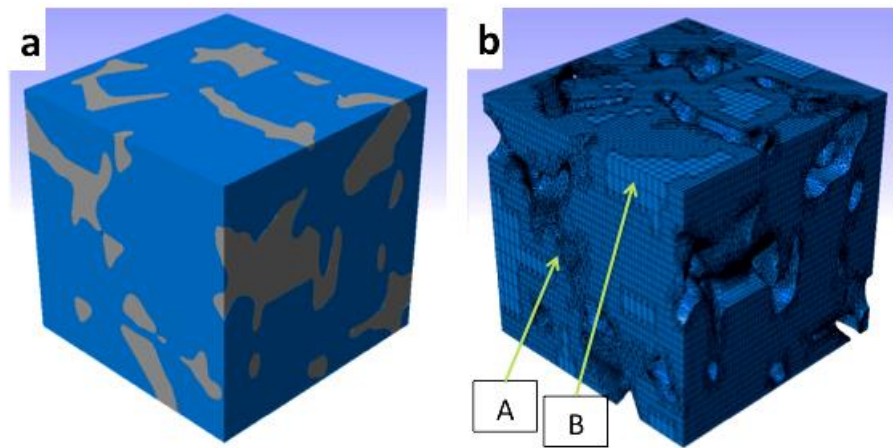
Figure 5-7 (**a**) A cube model showing solid metal (gray) and PCM (blue) composite, (**b**) generated FE tetrahedral meshes (only the PCM phase shown for clarity). (A) Refinement at interfaces and (B) less refined mesh area.
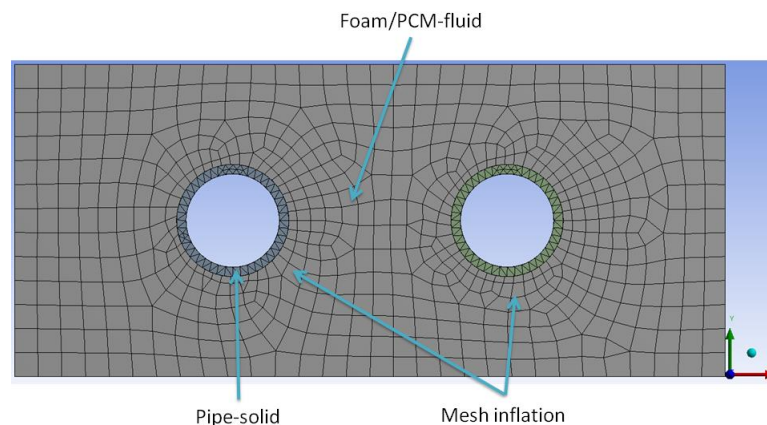
Figure 5-8 Computational grids for the CFD simulation showing mesh inflation in the fluid zone, growing from the pipe surface.

Table 5-3 Grid and temporal independence analysis. (*) Denotes the reference case.

Grid size	Element number	Melting time (s)	Difference (%)	Time step size (s)	Melting time (s)	Difference (%)
1	62585	1508	3.22	0.1*	1484	-
2	80341	1491	2.05	0.5	1478	0.40
3	109909	1478	1.16	1.0	1465	1.28
4	147858	1465	0.27			
5*	223574	1461	-			

5.3.6 Numerical procedure

Homogenization analyses were carried out by using Simpleware ScanIP software. All numerical calculations were performed by Ansys Fluent Release 14 (R14) with modifications to the momentum equations via user-defined functions (UDF). The governing equations were discretized by the finite volume methodology. Pressure and velocity were coupled by the Second Order Implicit Method for Pressure-Linked Equations algorithm (SIMPLE). The PRESTO scheme was used for the pressure correcting equation. The solution convergences were checked to satisfy the residuals criteria of the continuity equation, velocity components, and energy equation as 10^{-5}, 10^{-5}, and 10^{-6}, respectively [158]. Thermophysical data of the PCM and metal foam are listed in Table 5-4.

Table 5-4 PCM and metal foam thermophysical data.

PCM type/name	Salt hydrate/S46
Density, ρ	1587 kg/m^3
Specific heat, C_p	2410 J/kg.K
Thermal conductivity: PCM	0.45 W/m.K
Thermal conductivity: metal foam (AlSi7Mg0.6)	160 W/m.K
Viscosity, μ	10^{-5} kg/m.s
Latent heat, L	2.10×10^5 J/kg
Solidus temperature, $T_{solidus}$	46°C
Liquidus temperature, $T_{liquidus}$	46°C

5.4 Results and discussion

5.4.1 Effective thermal conductivity

The results from homogenization are tabulated in Table 5-5 for all six cubes. The effective thermal conductivity, K_{eff} was found to be 10.83±1.00 W/m.K. Coincidentally, the studies provided the opportunity to calculate the porosity and specific surface area of the foam without the manufacturing fault zone: 79±1% and 2189±56 m^2/m^3, respectively. The less than 3% standard deviation in these parameters showed that despite the pore and strut irregularity, the foam was characteristically uniform with regard to porosity and surface area. This information was important for further analyses e.g. the actual surface area enabled an accurate calculation of heat transfer coefficient for the forced convection mode. This K_{eff} value was therefore exported to the simulation parameter as the homogeneous phase thermal conductivity.

Table 5-5 Homogenization results.

Cube	No of FE elements	Porosity (fraction)	Specific surface area (m^2/m^3)	K_{eff} subvolume (% of ROI)	K_{eff} (W/m.K)
1	1626104	0.76	2081	40	12.50
2	1614790	0.79	2198	40	11.00
3	1580531	0.80	2197	60	10.25
4	1612091	0.79	2223	50	11.00
5	1612001	0.80	2242	50	10.75
6	1601927	0.79	2191	25	9.50
Average	1607907	0.79	2189	44.17	10.83
Standard deviation	15479 (0.96%)	0.01 (1.27%)	56 (2.57%)	12.01 (27.19%)	1.00 (9.23%)

5.4.2 Experimental validation: temperature profiles

Experimental temperature measurements enabled a validation method for the simulation results. Figure 5-9a shows the typical PCM heating phases, which included the sensible stages and a latent stage. The key observations were: 1) the simulated latent phase completed earlier than experimental and 2) the simulated latent phase showed a more prominent isothermal profile. The former (no. 1) could be due to inaccurate latent heat data provided by the supplier. The latter (no. 2) was explained in Chapter 4: because of the current design, there were different PCM heating rates within the foam (Figure 5-6 above). In the middle zone between the pipes, the isothermal

phase was shorter compared to the other zones due to the localized heat concentration. The profiles shown in Figure 5-9 were averaged over all thermocouple readings, hence the profiles tend to skew upwards instead of being horizontal and straight (isothermal). The simulated temperatures were taken as volume-averaged, this was not achievable experimentally. To quantify the validation, both data points were fitted with the RSQ (R^2) function. The RSQ value could be interpreted as the proportion of the variance in simulation profile attributable to the variance in experimental profile. Because it was only suitable for linear trends, the RSQ was unique for each of the heating phases. The values are tabulated in Table 5-6. RSQ1 and 2 were generally excellent for all profiles with values close to 1.00. RSQ3 was generally weaker because the simulated latent phases ended significantly earlier. The RSQ average value of 0.86 (mean) showed that the simulations were sufficiently accurate. This validated the numerical approach.
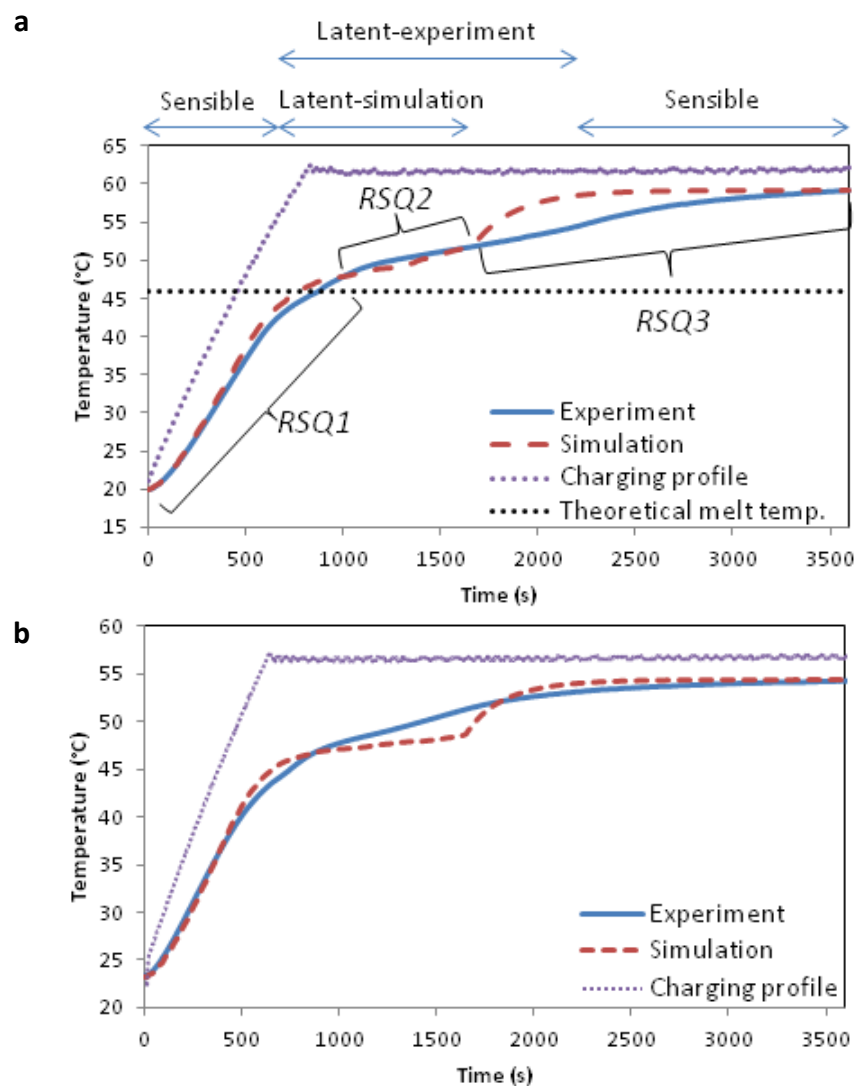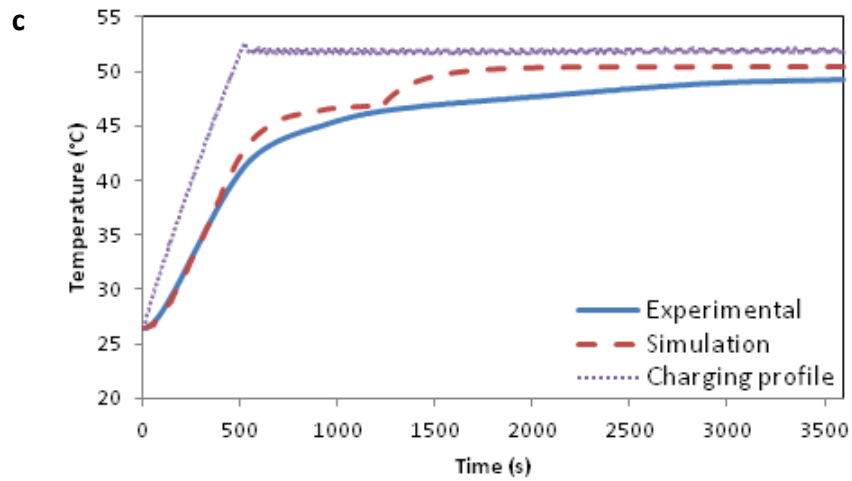
Figure 5-9 PCM temperature profiles for the charge temperature of (**a**) 60°C, (**b**) 55°C, (**c**) 50°C. Shown in (**a**) are the heating phases and the RSQ1-3 sections.

Table 5-6 Root mean square (RSQ) analysis for the profiles in Figure 5-9.

	Charge temperature (°C)		
	60	55	50
RSQ1	0.9996	0.9975	0.9963
RSQ2	0.9014	0.9778	0.9426
RSQ3	0.6545	0.8035	0.5155
RSQ average	0.8519	0.9263	0.8181

5.4.3   Experimental validation: temperature contours
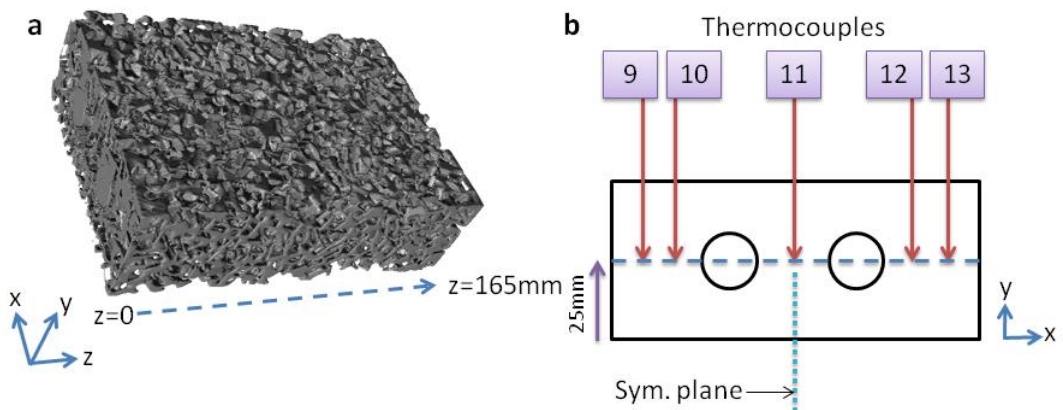
Figure 5-10(**a**) Isometric view of the foam, (**b**) thermocouple locations at coordinate y=50.0, z=82.5 (mm). Imaginary symmetrical plane is shown.

The PCM temperature varied negligibly along the pipe axis (z-axis) therefore the contour studies were limited to one-dimension, the x-axis. Figure 5-10b showed the positions of the thermocouples involved. The placements enabled two studies: 1) temperature front validation and 2) symmetrical heating assessment.
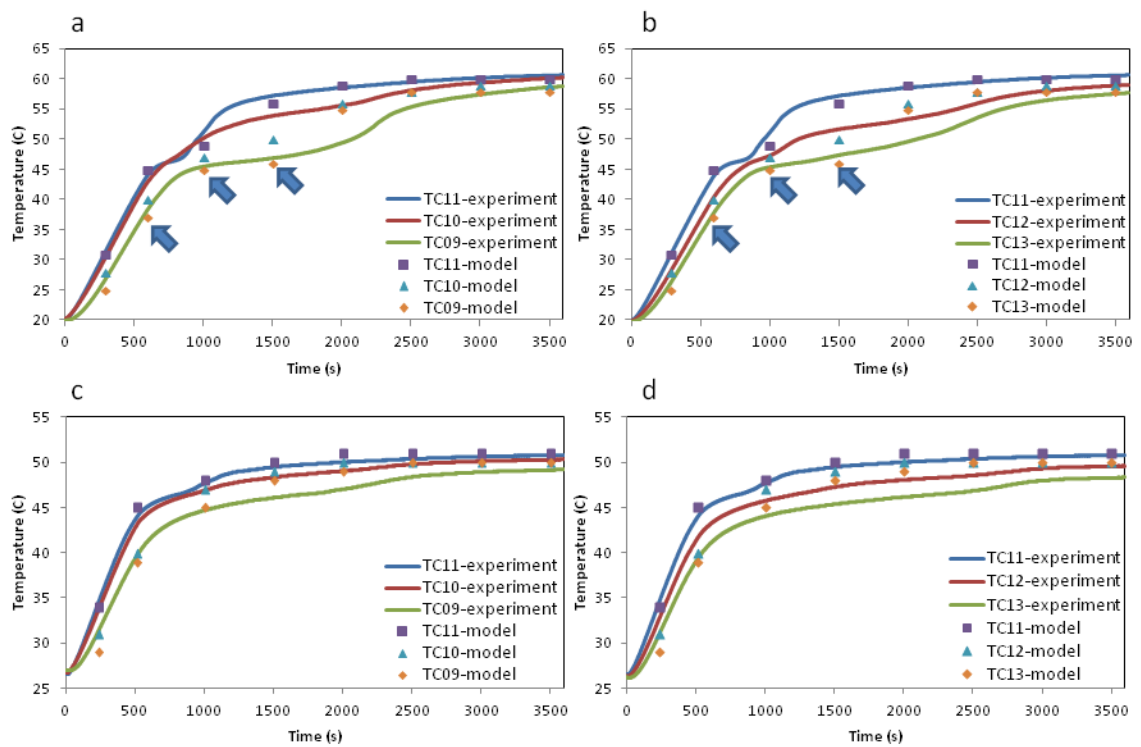
Figure 5-11 One-dimensional temperature profiles (x-axis) for the charge temperature of (**a-b**) 60°C, (**c-d**) 50°C. Arrows in **a-b** shows the temperatures of interest (Table 5-7).

Figure 5-11 showed the temperature profiles perpendicular to the pipe axis. The simulation and experimental profiles were in excellent agreement for both charge temperatures: 50 and 60°C. Experimental setup with a clear plastic top cover allowed for a visual inspection of the melt front, which is shown below in Figure 5-12. This was also agreed well by the simulated temperature profiles.
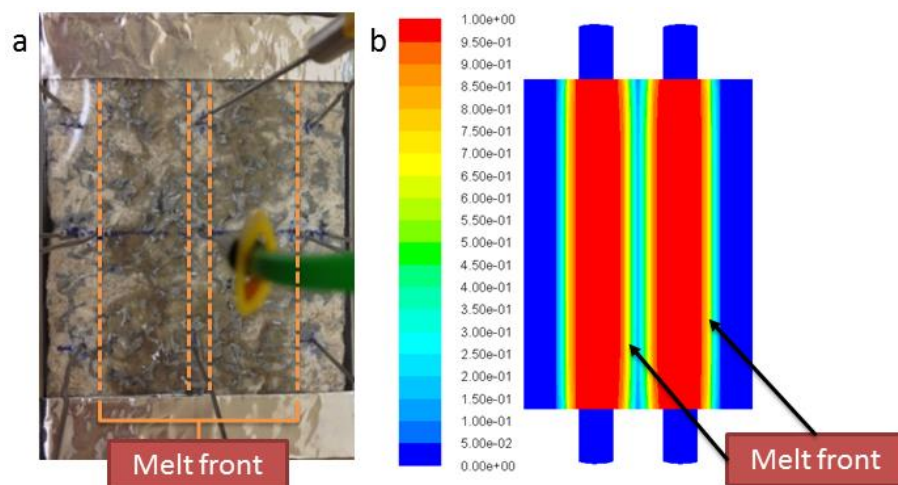
Figure 5-12 **Melt front at t ~1000s, charged at 60°C** (**a**) experimental, (**b**) simulation.

The experimental profiles showed small devations in the heating rate at both sides of the imaginary symmetrical plane (the plane is shown in Figure 5-10b). For example, at the perimeters of the foam domain i.e. TC09 and 13, at t=1000 for the 60°C charge temperature, the TC09 and TC13 readings were 45.5°C and 45.4°C, respectively. Whereas for the 50°C charge temperature, the TC09 and TC13 were 44.8°C and 44.1°C, respectively. A similar trend was observed for all charge temperatures in which the TC13 lagged behind TC09. It was therefore concluded that in defining the experimental melt completion, TC13 took precedence – this was considered to be caused by non-symmetrical melting rate of the PCM on both sides of the symmetrical plane. The time for melt completions are shown in Figure 5-13a. Based on this definition, the charge temperature influenced greatly the melt behaviour as charging at 60°C halved the melting time required by 50°C. The simulated liquid fraction also agrees with this definition (Figure 5-13c).
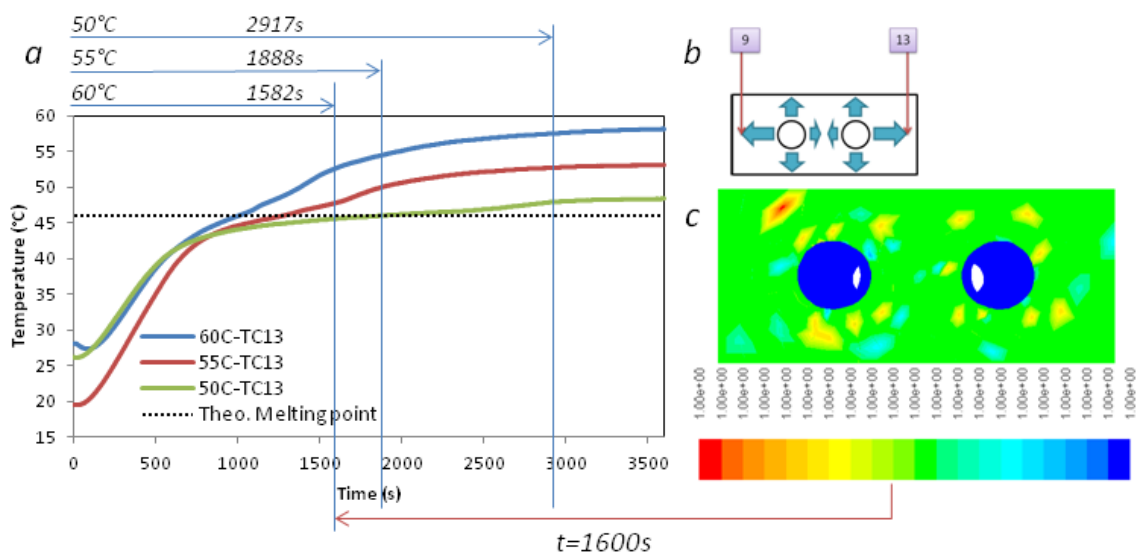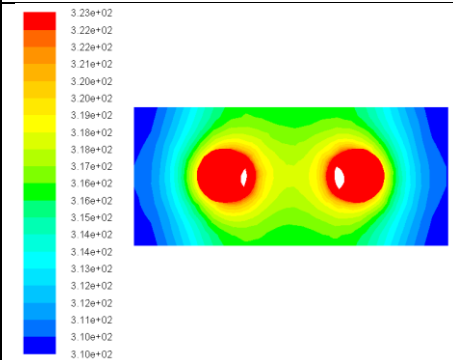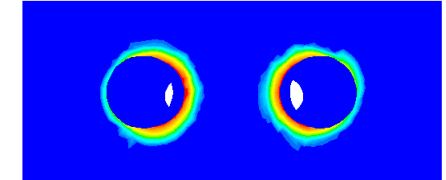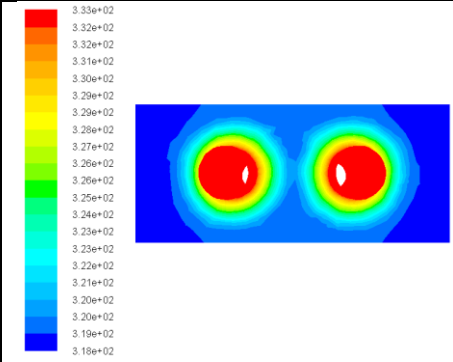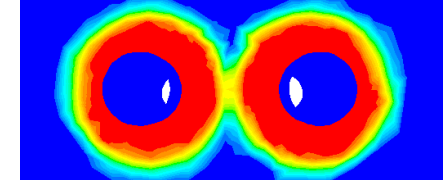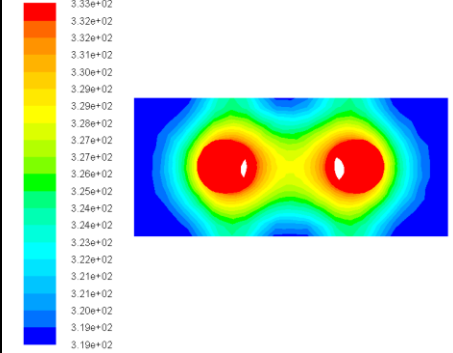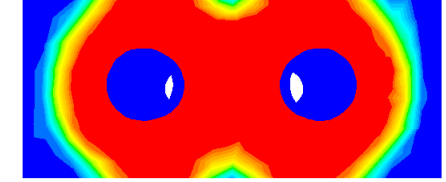
Figure 5-13 **Melt completion** (**a**) temperature profiles, (**b**) TC09/13 location, (**c**) liquid fraction at t=1600s, showing a complete melting (60°C charge temperature).

The heat exchanger design caused differing heating rates within the foam domain. As evident in Figure 5-11a-b, the middle zone (represented by TC11) only experienced a brief period of latent phase of approx. 200s, which was contrasted by the other zones: the perimeter (TC13) experienced a 1300s latent phase. Table 5-7 shows the simulated temperature and melt fronts at different times: t=600, 1000, and 1500s. The heat and melt propagations were uniform, propagating outward from the pipe surfaces, prior to t=1000s. After this point of time, the intensity of heat in the middle zone started to

proliferate, whilst the perimeters remained relatively cooler. Ideally, this hot spot needed to be eliminated to provide the best possible isothermal charging and discharging characteristic.

From here, it can be seen that the design of the heat exchanger for the PCM must be done correctly to ensure an optimal performance. The separation between the heat source (the pipes) must be specified carefully. This was investigated in Section 5.4.5 via a numerical method.

Table 5-7 Temperature and liquid fraction contours for a charge temperature of 60°C.

Time (s)	Temperature (K)	Liquid fraction
600		
1000		
1500		

5.4.4 Development of a simpler numerical methodology

As mentioned in Chapter 3 (foam characterization chapter), It would be economically desirable to remove the CT scanning step as it involves a significant access fee plus extra fees for manpower subcontracting and/or software purchase for analysis. A good model for K_{eff} calculation was formulated by Boomsba and Poulikakos [159] and was verified by many researchers such as Tian *et* al. [133] and Zhang *et* al. [160]. The model was so far verified only for foam porosities of 88-98%. Verification was never attempted for the lower porosity values. The model was based on a 3D tetrakaidecahedron structure, which was made up of six squares and eight hexagons. This model accounted for the convective heat transfer, instead of solely taking into account the conductive heat transfer, which formed most of the classical models. The model is given in the following Equation 5-15-21.

$$K_{eff} = \frac{\sqrt{2}}{2(R_A + R_B + R_C + R_D)}$$

Equation 5-15

$$R_A = \frac{4\text{y}}{\left(2e^2 + \pi\text{y}(1-e)\right)k_s + (4 - 2e^2 - \pi\text{y}(1-e))k_f}$$

Equation 5-16

$$R_B = \frac{(e - 2\text{y})^2}{(e - 2\text{y})e^2 k_s + (2e - 4\text{y} - (e - 2\text{y})e^2)k_f}$$

Equation 5-17

$$R_C = \frac{(\sqrt{2} - 2e)^2}{2\pi\text{y}^2\left(1 - 2e\sqrt{2}\right)k_s + 2(\sqrt{2} - 2e - \pi\text{y}^2\left(1 - 2e\sqrt{2}\right))k_f}$$

Equation 5-18

$$R_D = \frac{2e}{e^2 k_s + (4 - e^2)k_f}$$

Equation 5-19

$$\text{y} = \sqrt{\frac{\sqrt{2}(2 - (5/8)e^3\sqrt{2} - 2\varepsilon)}{\pi(3 - 4e\sqrt{2} - e)}}$$

Equation 5-20

$$e = 0.339$$

Equation 5-21

$$K_{eff} = 10.49 \, W/m.$$

By inputting the values of: porosity, ε = 0.80, PCM conductivity, k_f = 0.45 W/m.K, and foam conductivity, k_s = 160W/m.K, the K_{eff} was calculated to be 10.49 W/m.K, which was similar to the value calculated from the homogenization analysis, 10.83±1.00 W/m.K. This could be due to the uniformity of porosity discovered via the 3D model (Table 5-5) because the model was a function of porosity. If this model would be applicable to 80%

porosity foams and to the irregular foams, a simpler methodology could therefore be proposed, as in Figure 5-14. This conjecture however must be validated accordingly, via further testing.

Figure 5-14 A simpler numerical methodology (BP: Boomsba and Poulikakos).

5.4.5 A modified heat exchanger design

A slight modification to the current design by shifting the location of the pipes closer to the edges resulted in fully symmetrical features (Figure 5-15). The objective was to eliminate the hot spot in the middle zone during heating. To test this modification, a heating simulation was carried out until a 0.6 liquid fraction was achieved. As shown in Figure 5-16b, the middle zone temperature for the modified design was 46°C compared to the current design, which was 54°C. This was a reduction of 8°C, which was significant. It is recommended that this modification be incorporated in any future test prototypes.
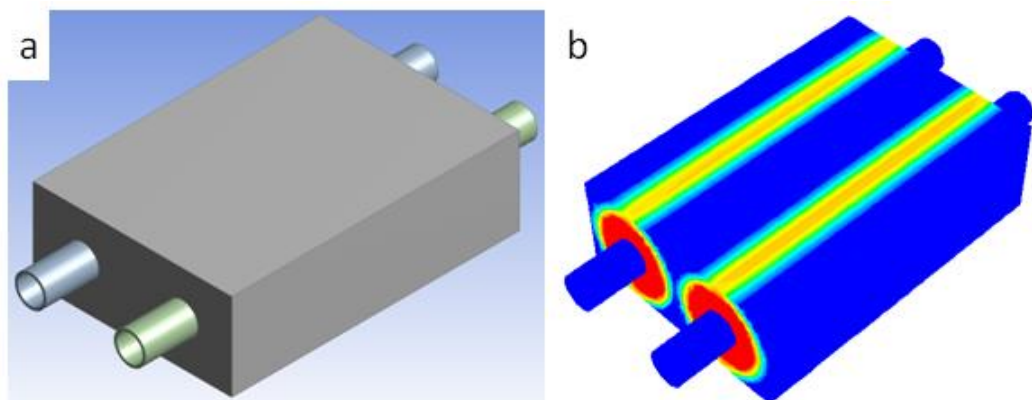
Figure 5-15 **The modified design** (**a**) the model, (**b**) melt contour at liquid fraction=0.6.
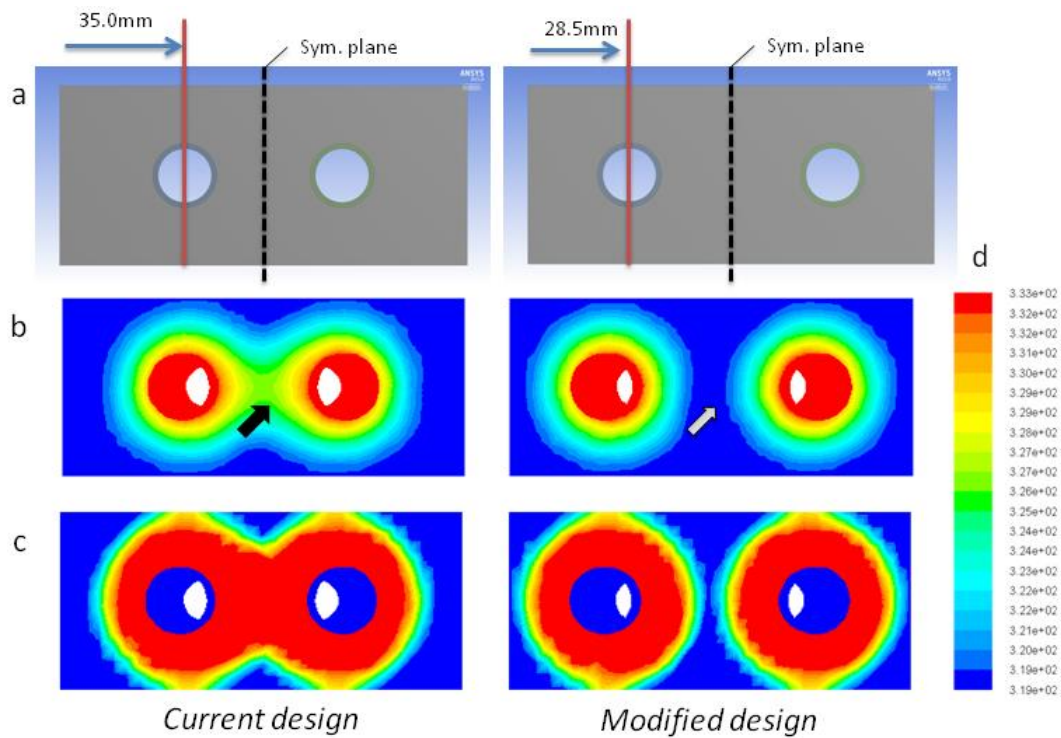
Figure 5-16 **The modified design to eliminate the middle zone hot spot** (**a**) the geometries, shown are the shifting of the pipe locations, and the imaginary symmetry plane, (**b**) temperature contours, arrows show the middle zone, (**c**) melt front contours at liquid fraction=0.6, (**d**) temperature scale for **b**.

If the water cooling system was to be applied in practice, it would have been worth examining a different scenario – a larger number of smaller diameter tubes. However, as the ultimate solution will use heat pipes, this would have increased the cost substantially as several more heat pipes would be needed for each foam block.

5.4.6   Effective thermal conductivity

To measure the effectiveness of metal foam or any porous material in enhancing phase change material performance, ratios of K_{eff}/K_{PCM} are given in Table 5-8. This formed the basis of comparison with other works in the literature. One cannot compare different PCM/foam combinations, hence the present work is incomparable as it is unique with respect to this combination. The main parameter for comparison is porosity. The thermal conductivity ratio has been shown to increase with decreasing porosity, essentially due to the quantity of the higher conductivity phase (metal or graphite). With similar porosities, a higher specific surface area increased the ratio [161]. A higher conductivity material (copper > nickel) also increased the ratio [64]. Some researchers measured the K_{eff} value at different temperatures. At higher temperature, the ratio was

generally higher because metal conductivity increased with temperature and the contact between PCM/metal struts was better as it liquefied [161]. This work showed an impressive ratio of 24. However, it should be noted that this could be a function of the PCM used.

Table 5-8 Effective thermal conductivity of PCM/foam composites from literature.
Note: Ratio = K_{eff}/K_{PCM}, Exp = experimental, Num = numerical.

PCM/foam composite	Porosity (%)	Base, K_{PCM} (W/m.K)	Effective, K_{eff} (W/m.K)	Ratio	Method	Reference
Paraffin/ copper	97	0.39	5.04	13	Exp/ Num	[64]
	89		16.01	41		
Paraffin/ nickel	98		1.24	3		
	90		2.33	5		
Cyclohexane/ graphite	75	0.13	30 (at 20°C)	230	Exp/ Num	[162]
			25 (at 90°C)	192		
NaNO₃/KNO₃/ graphite	90	0.5	2.0	4	Exp	[58]
	70		8.0	16		
Eicosane/ copper	95	0.42	3.06	8	Exp/ Num	[54]
Paraffin/ aluminium	92 (796 m²/m³)	0.52	10.4 (at 37°C)	20	Exp	[161]
			15.6 (at 67°C)	30		
	93 (2615 m²/m³)		63.5 (at 37°C)	33		
			78.8 (at 67°C)	41		

Salt hydrate/ aluminium (irregular)	80 (2190 m²/m³)	0.45	10.8	24	Num	Present work

5.5   Conclusions

This work established the fundamentals for the next phase in the transient heat sink design by providing an accurate numerical simulation technique for scale-up and redesign.

- The homogenization analysis revealed the effective thermal conductivity of the metal foam/salt hydrate PCM composite to be 10.83±1.00 W/m.K, which was 24 times higher than pure salt hydrate conductivity of 0.45 W/m.K.
- The homogenization analysis also revealed the uniformity with regards to the foam porosity and surface areas despite the irregularity in pore and strut morphology.
- The phase change process, which was simulated using a slightly modified enthalpy porosity theory, was validated by the experimental data. This implied that the irregular foam/PCM composite could be represented by a homogeneous phase within a 3D model.
- To simplify and economize the numerical approach, the effective thermal conductivity could be alternatively calculated with the established BP model, subject to further experimental validations.
- A simple redesign of the heat exchanger was modelled to eliminate a hot spot during heating. This is recommended for adoption in the next test prototypes.

Chapter 6   The irregular foam as a steady state heat sink

6.1   Abstract

As a steady state heat sink, metal foams have been demonstrated to offer greater thermal performance compared to common parallel fin stacks due to the higher specific surface area and random geometry. The work here tested the irregular foam prototype in terms of its steady state performance: heat transfer and fluid flow. The novelty of this work was the use of the actual surface area, derived from the 3D model obtained from a CT scan (Chapter 3) for calculations. The mean heat transfer coefficient was found to be independent of the imposed heat flux but, highly dependent on the coolant (air) flow rate. Numerical simulation allowed for a detailed examination of the dense region detected during the initial morphological analysis (Chapter 3). Two models were created: 1) the worst case scenario (defect) and 2) the best case scenario (normal), in terms of pressure drop. The defect model imposed a 20 times higher pressure drop at the highest air velocity, whereas the permeability of the normal model was 4 times higher. Flow analysis revealed a localized flow constriction, which caused a Venturi effect. Surprisingly, experimental pressure drop revealed the foam fitted the normal model pressure drop profile. The dense region therefore did not exert an adverse effect upon the pressure field, but it caused a significant reduction in the specific surface area for heat transfer by 30%. The foam therefore was still not optimal for heat sink operation.

Keywords: Irregular metal foam; parallel fin stack; steady state cooling; heat transfer coefficient; fin efficiency; pressure drop; permeability; thermal dispersion

6.2 Introduction

The heat generation per unit volume by power electronics is always increasing. This heat must be removed for efficient operation. Two ways to deal with this increasing cooling load are via: 1) extended surface (parallel plate fins are common) and 2) increasing coolant flow rate. Metal foam has been reported as a promising extended surface candidate. Seo Young *et* al. [163] performed an experimental comparison between aluminium foams (90%, 10-40 PPI) and a parallel plate sink. Their results showed a 28% higher thermal performance using the foams (in terms of Nusselt number and convective thermal resistance). As a compliment to the use of the irregular metal foam in enhancing the heat transfer rate in PCM (Chapter 4 and 5) - in this Chapter, the foam was tested in its steady-state performance.

6.2.1 Objectives

The objectives of this part of the project were:

1) Experimental measurement of the mean heat transfer coefficient.
2) Experimental measurement of the pressure drop.
3) Numerical investigation of the defective region effect upon pressure drop and permeability, and validation with the experimental pressure drop.

The actual surface area value from the accurate foam model (Chapter 3) was used for the heat transfer coefficient calculation in objective no. 1.

6.3 Materials and methods

6.3.1 Rig setups

Two rigs were constructed, a heat transfer rig and a wind tunnel.

6.3.1.1 Heat transfer rig
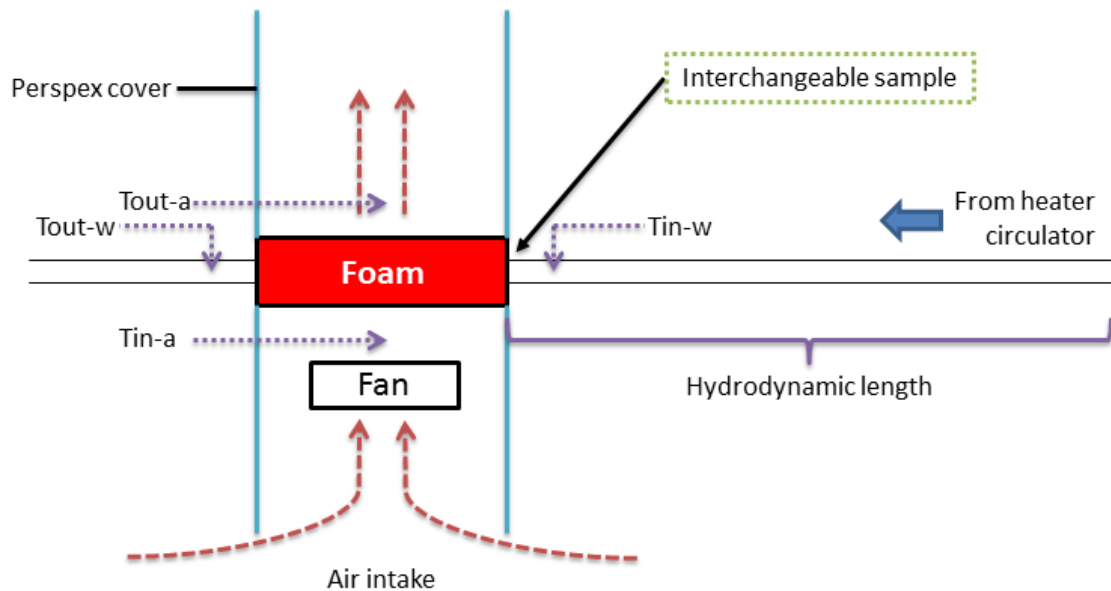
Figure 6-1 Schematic of the rig, designed for flexibility in sample interchangeability. Shown are the thermocouple sets: $T_{in/out-a}$ for air side and $T_{in/out-w}$ for water side.

The rig (Figure 6-1) was a similar setup to that used during the foam/phase change material tests (Chapter 4) with an addition of a Perspex enclosure to direct air flow. The rig was designed for the foam to be replaceable with any sink of similar dimensions via removable pipe fittings. The heat source was hot liquid from an upstream heater circulator (Haake analogue C10, flow 2–4L/min, temperature <100°C, mainswater). Hydrodynamic entrance length was 540mm to ensure a fully developed flow under the maximum conditions of 4L/min, 80°C. Thermocouples used were 1.5mm, Type K, uncertainty ±0.75% (TC Direct). They were used for measuring the inlet and outlet temperatures for both water and air. The data logger used was a PicoLog, TC-08, uncertainty ±0.25%. A fan was customized to fit into the rig. Its speed was controlled by a voltage controller. The voltage range was 0 to 12V maximum, resulting in 0.00 – 4.58 m/s or 0.000 – 0.018 kg/s air mass flow rate (tested with a hot wire anemometer, TESTO, 405). A thermal imaging camera was used (FLIR Instruments, T1K, emissivity (e) = 0.83:

calibrated for aluminium) to map the heat distribution of the foam. The experimental parameters are summarized in Table 6-1 below.

Table 6-1 Experimental parameters for the heat transfer rig. *Based on the pipe area and inlet conditions, **Null value = natural convection.

Water temperature	80°C
Water flow rate	2 and 4 L/min (LPM)
Water mass flow rate	0.0324 and 0.0648 kg/s
Water heat flux*	1800 and 3600 W/m^2
Fan voltage range**	0 to 12V
Air velocity**	0.00 to 4.58 m/s
Air mass flow rate**	0.000 to 0.018 kg/s
Heat transfer area i.e. foam total area	0.54 m^2

For each run, the period of experimentation was approximately 3600s. Once the heater circulator was switched on, water temperature increased steadily until it reached a steady state (Figure 6-2). From temperature profile examinations, the values used for thermal calculations were averaged after a steady state condition was achieved, usually at t>1300s.
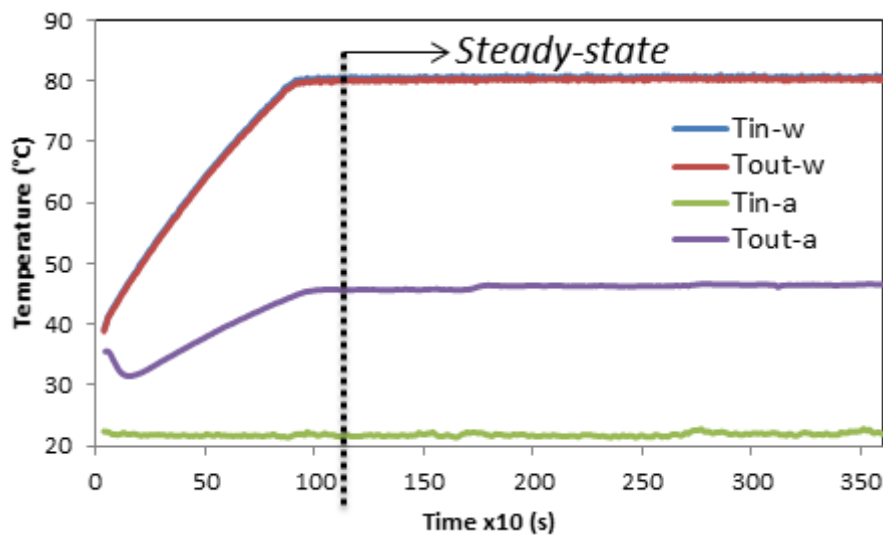
Figure 6-2 Steady state condition was usually achieved after t > 1300s.

6.3.1.2 Wind tunnel
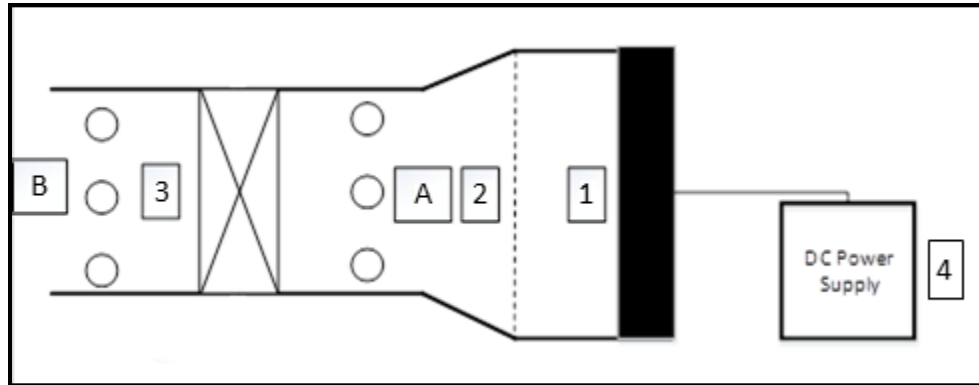
Figure 6-3 **Schematic of the wind tunnel** (1) Fan, (2) Porous mesh, (3) Foam sample, (4) DC power supply, (A) Inserts for measurement probe before sample, (B) Inserts for measurement probe after sample. Probe inserts are in C: centre line, -40mm, and +40mm relative to C position.
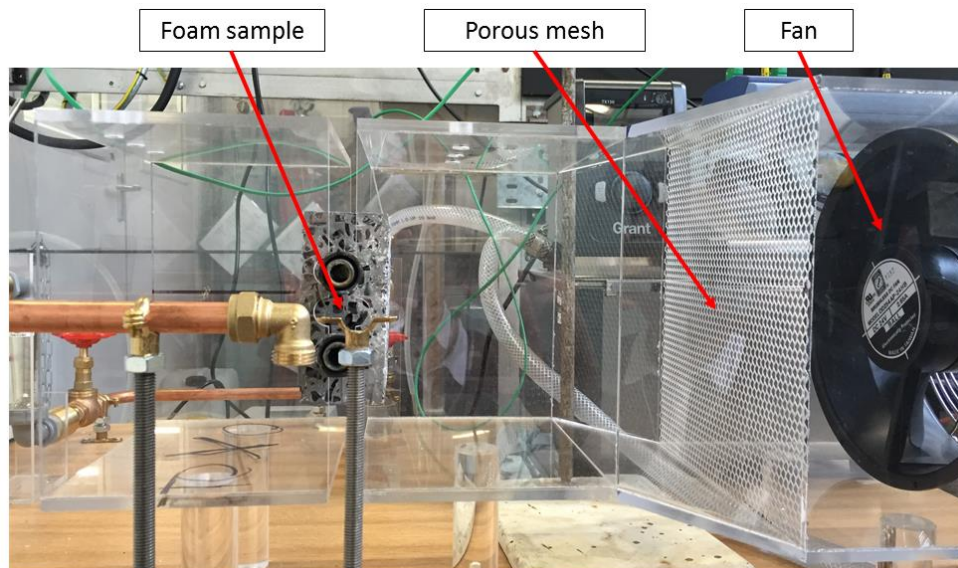
Figure 6-4 Photograph of the rig with the foam sample prior to tightening of the Perspex enclosure.

A wind tunnel was designed with rigid Perspex as the main structural material (Figure 6-3) with a dimension of 525 mm (L) x 250mm (W) x 300mm (H).

A fan was used to blow air (standard atmospheric pressure, room temperature) through the foam sample. To ensure the uniformity of the air velocity, an upstream metal mesh

(porous) screen was inserted. Tests were carried out and it showed a uniform cross-sectional velocity profile was achieved:

The results are shown below in Figure 6-5. The results show a significant variation in velocities between the centre line (C), 40mm below (-40), and 40mm above (40), as depicted in Figure 6-3. Figure 6-5 (top) shows that the air velocity near the walls of the wind tunnel was higher in comparison to the centre. The likely cause of this was that the sample being fixed in position too close to the fan, with the fan having a large solid casing section at the centre. The mesh was inserted and the air velocities measured, with results shown in Figure 6-5 (bottom). These results show improved air velocity distribution with reduced average velocities at each voltage caused by the mesh restricting air flow.
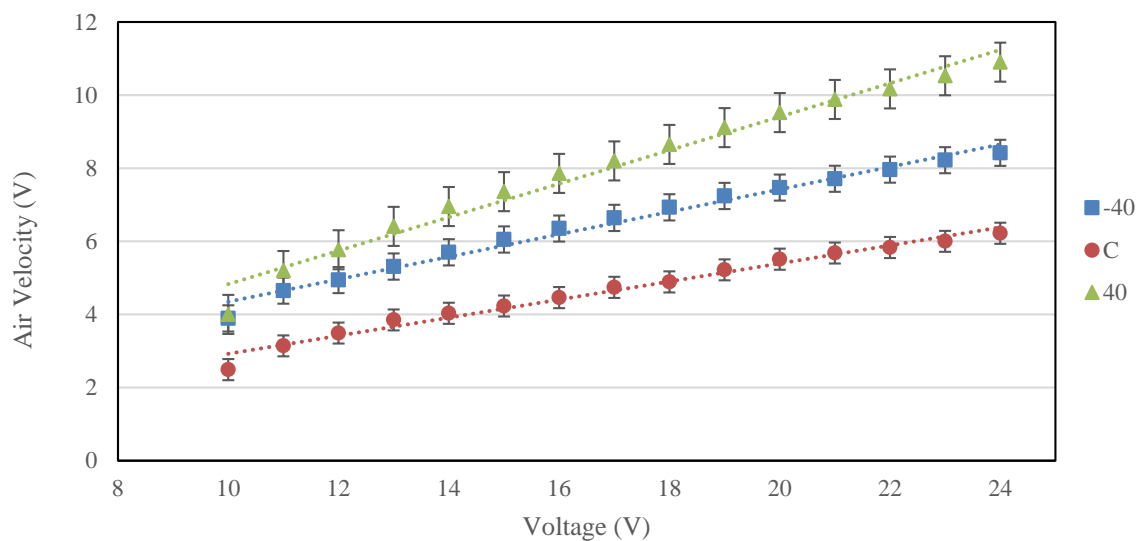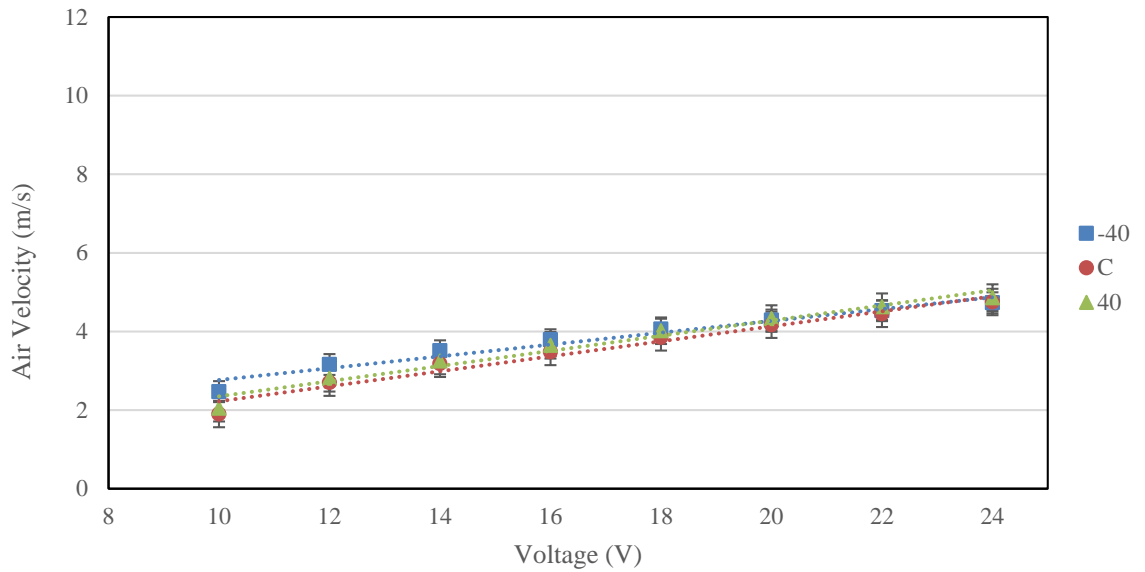
Figure 6-5 **Wind tunnel air velocity distribution** (top) without mesh screen, (bottom) with mesh screen. Note: these characterization tests used the maximum fan voltage (24V) whereas in the actual tests, only 20V maximum was used for safety reasons.

Upstream and downstream ports (points A and B, respectively in Figure 6-3) enabled the pressure differential measurements. Pressure was measured by using a Pitot-static probe (Testo, 512, uncertainty ±0.5%), the measurement was based on Equation 6-1, which was derived from Bernoulli's equation [164],

$$P = \frac{1}{2}\rho v^2$$
<div align="right">Equation 6-1</div>

Where: v = inlet velocity (m/s), ρ = inlet density (kg/m³), and P = dynamic pressure (Pa). Dynamic pressure is the differential between static pressure and total pressure.

It was assumed that because temperature did not change across the wind tunnel, static pressure did not change, therefore the dynamic head from the probe was the only one considered.

Testing parameters are tabulated in the following Table 6-2:

Table 6-2 Experimental parameters for the wind tunnel.

Fan voltage range	10 – 20 V
	(24V fan design maximum)
Inlet air velocity	1.90 – 4.00 m/s
Pressure	Atmospheric = 101325 Pa

Pressure drop measurement procedure:

1. Inlet pressure measurements are taken at the inserts at point A, Figure 6-3.

2. Measurements were taken at the centre insert, with the L-bend of the Pitot tube being placed 15mm above the bottom of the wind tunnel and facing against the direction of air flow.

3. Results were recorded for each of the voltages. Pressure values were recorded every 10 seconds over the course of 1 minute and averaged.

4. As shown in Figure 6-3, to measure the outlet pressure with a sample connected, the Pitot tube took measurements from the centre point at the inserts points B.

5. Steps 2 and 3 were repeated.

6.3.2 Energy balance

A critical step in determining the veracity of data is the energy balance between the air side and the coolant side in the heat transfer rig. Thermal equations in Equation 6-2 and 3 were used to measure the energy balance.

$$Q_w = m_w * Cp_w * (T_{in-w} - T_{out-w})$$

Equation 6-2

$$Q_a = m_a * Cp_a * (T_{out-a} - T_{in-a})$$

Equation 6-3

Where: Q = heat transfer rate (J/s, Watt), m = mass flow rate (kg/s), Cp = temperature dependent specific heat (J/kg.K), and T = temperature (K).

Where subscripts: a = air-side, w = water side, in = inlet, and out = outlet.

A series of rig adjustments resulted in the energy imbalance to be at most 10% (at the highest air velocity). A thermal image taken during one of the runs is shown in Figure 6-6. It indicates heat loss from the pipe areas downstream and upstream of the thermocouples (label 'A'). The lagging used and the Perspex cover were crucial to prevent heat loss from the foam (label 'B').
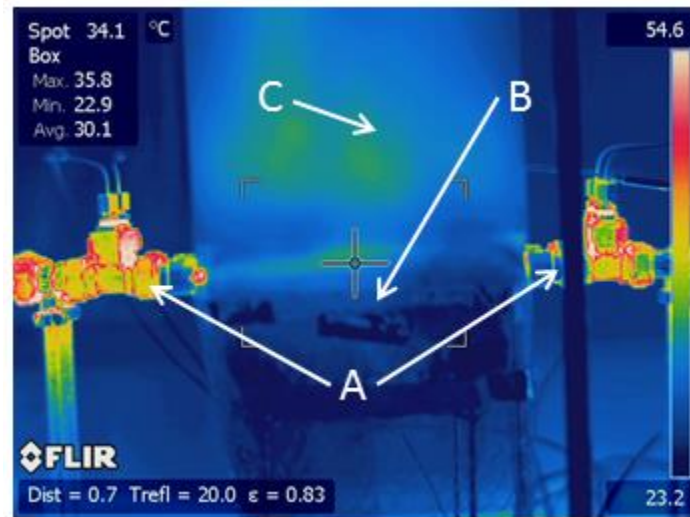
Figure 6-6 **Thermal image of the rig during experimentation** (**A**) shows heat loss from the pipes, (**B**) shows no detectable heat loss from the foam (lagged and covered with Perspex), (**C**) minimal heat loss from the air side.

Experimental uncertainties were applied as exemplified in Appendix A2 and the list of equipment used in this Chapter is in Appendix A3.

6.3.3 Experimental governing equations

6.3.3.1 Mean heat transfer coefficient

By using the principle of cross flow heat exchange from the water and air sides, the heat balance and logarithmic mean temperature difference (LMTD) were calculated by using general heat transfer equations. Neither fluid changed phase, therefore the LMTD method was valid [165]. The mean (or global) heat transfer coefficient, $\bar{h}$ was a composite of conductive and convective coefficients and representative of the foam as a whole (hence 'mean'), instead of the localized values. The following Equation 6-5 and 6 concern this parameter. The value 'A' refers to the actual surface area of the foam, obtained from the CT scanned model. The heat transfer, Q was averaged between the air and water sides.

$$Q = \frac{Q_w + Q_a}{2} \qquad \text{Equation 6-4}$$

$$\bar{h} = \frac{Q}{A * LMTD} \qquad \text{Equation 6-5}$$

$$LMTD = \frac{(T_{in-w} - T_{in-a}) - (T_{out-w} - T_{out-a})}{Ln \dfrac{T_{in-w} - T_{in-a}}{T_{out-w} - T_{out-a}}} \qquad \text{Equation 6-6}$$

6.3.3.2 Dimensionless parameters

A practical measure of the performance of a heat exchanging device is the dimensionless Nusselt number, which was calculated by using the following equation (based on Boomsba *et* al. [166]):

$$Nu = \frac{\bar{h}D_h}{k_a} \qquad \text{Equation 6-7}$$

Where Dh = hydraulic diameter (4*cross sectional area of flow channel/wetted perimeter) and k_a = thermal conductivity of air (0.0271 W/m.K). The heat transfer coefficients used were functions of the actual surface area from the CT scan (Chapter 3).

For the Reynolds number, the correlation is given as in Equation 6-8 below.

6.3.4 Numerical simulation

Here, the aim of numerical simulation was to understand the effect of the defect region upon the nature of fluid flow. Typical parameters for this purpose are pressure drop and permeability. The flow simulation allowed for pore scale examination, which would be impossible to do experimentally. It was also to be validated by experimental pressure drop data.

6.3.4.1 Governing equations

The nature of the flow must be set first. The flow range was limited to v = 0.73 − 4.58 m/s (4 − 12V), within the heat transfer experimental range. It did not start at 0 m/s as it would imply no flow to simulate. To characterize the flow, the pore-based Reynolds number formulated by Boomsba *et* al. [108] specific for metal foams was applied,

$$Re = \frac{\rho v d_p}{\mu}$$

<div align="right">Equation 6-8</div>

Where ρ = density (kg/m^3), v = velocity (m/s), d_p = pore diameter (m), the value of which was measured as 0.00755m (the mean between oval and rectangular pores), and μ = dynamic viscosity (kg/m.s) of the inlet air. The Re range was calculated to be 335 – 2101 (under ambient conditions), therefore barely crossing the turbulence threshold. The flow was solved by using the laminar model. Only continuity and momentum equations were solved as in the Equation 6-9 and 17, respectively.

$$\frac{\partial}{\partial x_i} \rho v_i = 0$$

<div align="right">Equation 6-9</div>

$$\frac{\partial}{\partial x_i}(\rho v_i v_j) = -\frac{\partial P}{\partial x_i} + \frac{\partial}{\partial x_i}\left(\mu \frac{\partial v_i}{\partial x_i}\right)$$

<div align="right">Equation 6-10</div>

Subscripts i and j refer to the directional vectors. The flow model was solved by using Ansys FLUENT software, employing the second order upwind difference scheme for increased computational accuracy. SIMPLE scheme was used for pressure-velocity coupling. Numerical convergence was satisfied once the collective residuals fell below 10^{-4}, which usually occurred after 140 – 160 iterations.

6.3.4.2 Model development

It was not be possible for the flow to be simulated through the main foam model (Figure 6-7a) due to computational limitations. After a series of analyses, a sub-model with dimension of 10 x 50 x 20mm (x,y,z-axes) was created, for the ROI (region of interest). Two models of the ROI were created: 1) 'normal', which represented the foam without any defect (Figure 6-7d) or the best case scenario and 2) 'defect', which represented the foam with the defect region (Figure 6-7e) or the worst case scenario.
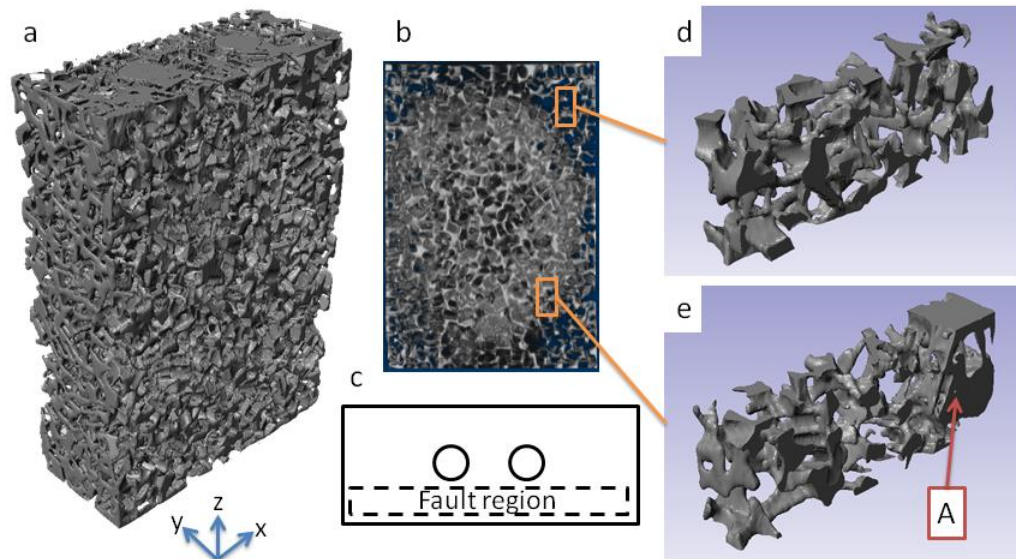
Figure 6-7 **Model development** (**a**) the main model, (**b**) top view, (**c**) profile view, (**d**) the 'normal' model: 2290 m^2/m^3, (**e**) the 'defect' model: 1850 m^2/m^3 showing the constricted flow region (A).

Table 6-3 compared the specific surface area (SSA) of the ROI and the main model i.e. the model of the entire foam. The normal ROI SSA was comparable to its main model property whereas the defect ROI SSA overestimated slightly from its main model property. This indicated that the ROI models were considered representative.

Table 6-3 Specific surface area in m^2/m^3.

	Main model	ROI model
Normal	2190	2290
Defect	1495	1850

The selection of the defect model was initially difficult as the dense solid often caused a fluid domain discontinuity (Figure 6-8b), which rendered the flow simulation impossible. The boundary conditions are shown in Figure 6-8a. The direction of air flow followed the experimental setup (through the y-axis). Symmetry (non-slip) boundaries were assigned to the lateral surfaces.
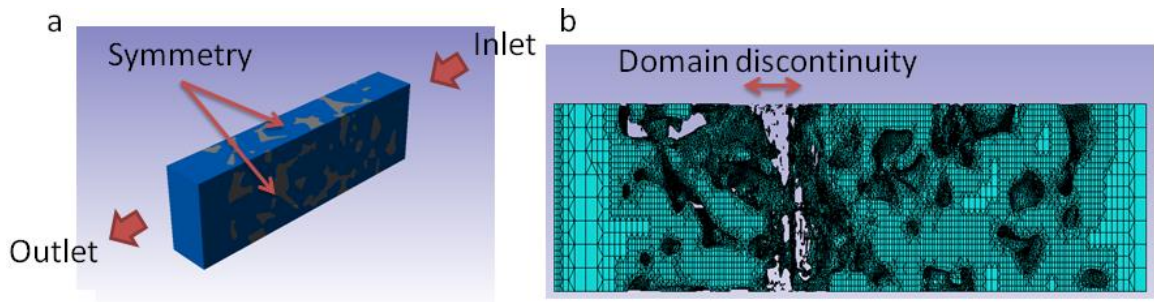
Figure 6-8 (**a**) The fluid domain (extended in the flow direction) and the boundary conditions, (**b**) the fluid domain discontinuity issue during early trials.

The models were generated by using Simpleware ScanIP software using the raw DICOM images from the CT scan. The software also featured in-house mesh generation algorithms: +FE Free and +FE Grid. Two grid sizes from the +FE Free algorithm were created: 1) coarse: 156554 grids and 2) refined: 769344 grids (Figure 6-9a and b, respectively). For the +FE Grid, the automated generation was used, resulting in 278893 grids (Figure 6-9c). The +FE Free generated only tetrahedral meshes whereas the +FE Grid generated a mixture of tetrahedral and hexahedral meshes. The +FE Grid was based on an algorithm that allowed clustering of hexahedral cells in regions where structured grids i.e. tetrahedral cells, were not needed.
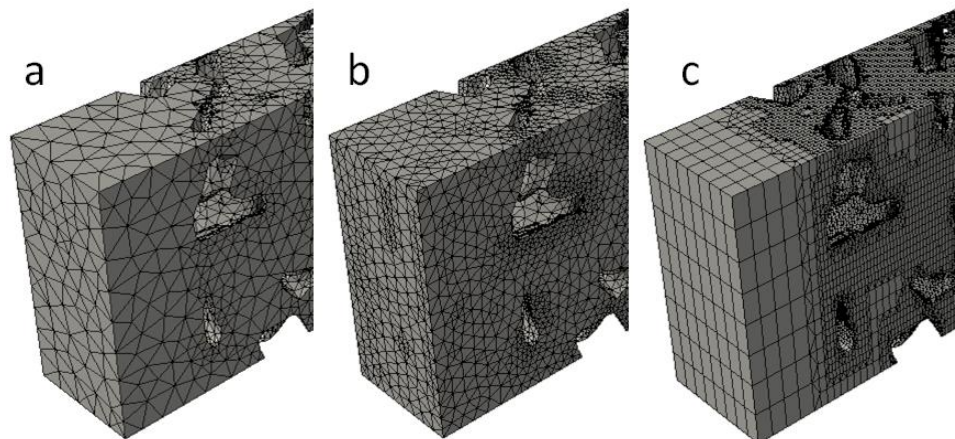
Figure 6-9 **Mesh generation and topology** (**a**) +FE Free: coarse, (**b**) +FE Free: refined, (**c**) +FE Grid showing a mixture of tetrahedral and hexahedral mesh clusters.

To test these grids, pressure drop profiles (for 0.7 – 4.6 m/s inlet velocity) were plotted in Figure 6-10 below, for the ROI defect model. It showed that generally, the solutions depended very little on the grid size. Close examination showed that the results from

the +FE Grid fitted very closely to that of the +FE Free: refined mesh size. Because of this, the +FE Grid was chosen over the +FE Free options due to its minimal grid size.
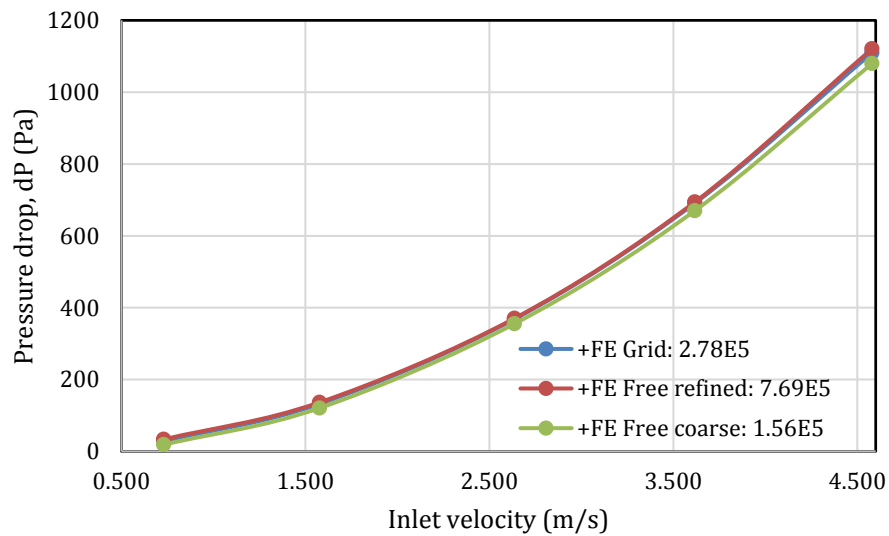
Figure 6-10 Influence of the mesh size on the simulated results (pressure drop, for the ROI defect model).

6.4   Results and discussion

6.4.1   Experimental results

6.4.1.1   Heat transfer

Figure 6-11a and b show the heat transfer and mean heat transfer coefficient profiles, respectively. The two flow rates, 2 and 4 LPM corresponded to two heat fluxes: 1800 and 3600 W/m², respectively (calculated based on water properties at the inlet conditions and pipe surface areas). Both parameters increased with increasing air flow rate. Both parameters changed very slightly with the imposed heat flux even though the increase was one fold from 1800 to 3600 W/m². This correlated with observations in other works e.g. Mancin *et* al. [80] and Hsieh *et* al. [104], which concluded that the global heat transfer coefficient is independent of the imposed heat flux but highly dependent on the coolant (air) flow rate. The $\bar{h}$ values calculated were small because of the division with the actual foam surface area, A = 0.54m² [$\bar{h}$ = Q/(A.LMTD)]. If the heat flux area was considered instead i.e. A = 0.038m² (surface area of the pipes: 14 times smaller value), the values were significantly larger. This is plotted in Figure 6-11c. It was not possible to compare with results from literature due to the differences in experimental setup. Most

of them used electrically heated foams, which could provide very high heat fluxes. The setup in this study used a water heater at relatively low flow rates hence, low heat fluxes. In addition, the heat transfer performance of the foam was not representative of the irregular foam due to the reduction of the specific surface area by 30%, compared to the ideal irregular foam. For future work, once the new, defect free prototypes are available, comparison with literature will be valid.

c
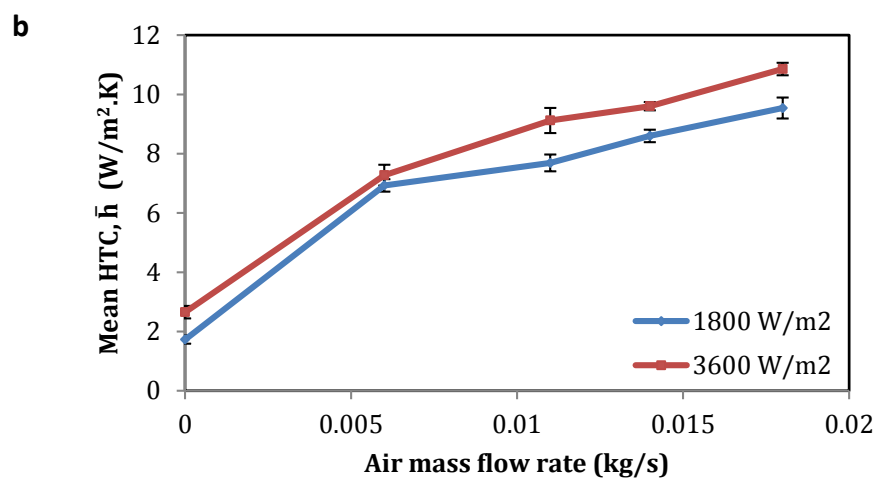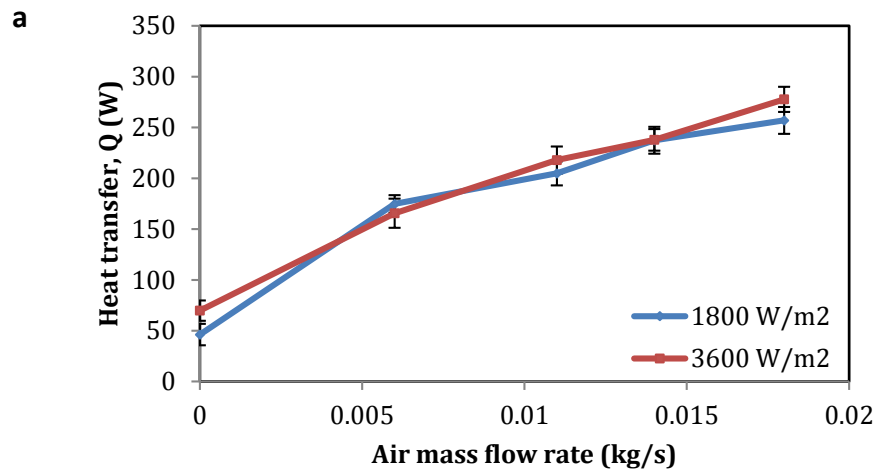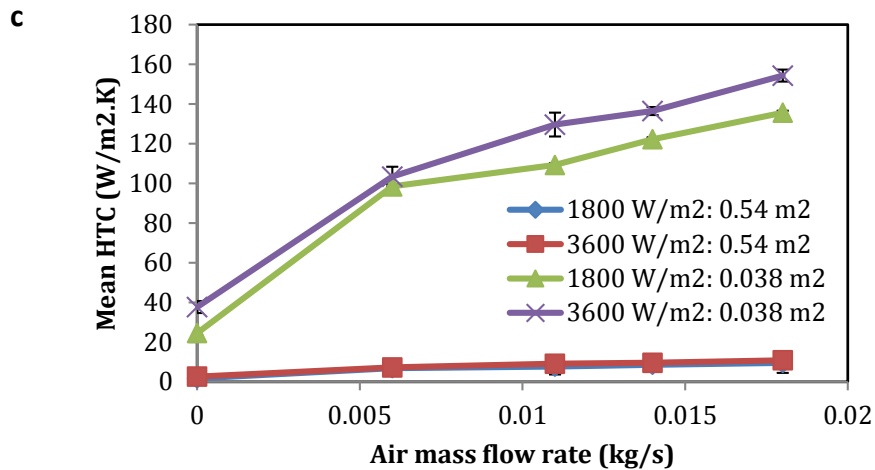
Figure 6-11 **Thermal performance plotted against air mass flow rate for two heat fluxes** (**a**) heat transfer rate, (**b**) mean heat transfer coefficient, $\bar{h}$ (**c**) $\bar{h}$ calculated by using the heat flux area (0.038 m²). Mean ± standard deviation, n = 3.

The resulting Nusselt number is plotted in Figure 6-12 below. The Nu values substantially increased with the increase of Re. To compare with other works, the plot from Seo Young *et* al. [102] (aluminium foam, 92% porosity, 10-30 PPI, characteristic length was flow channel height) is in Figure 6-13, and from Boomsba *et* al. [166] (aluminium, 67-88% porosity, characteristic length was hydraulic diameter) is in Figure 6-14. The values were comparable considering within similar Re range for Seo Young *et* al. albeit their higher porosity foams. For both of these works, the trends of Nu/Re correlation were similar to the trend in our work.
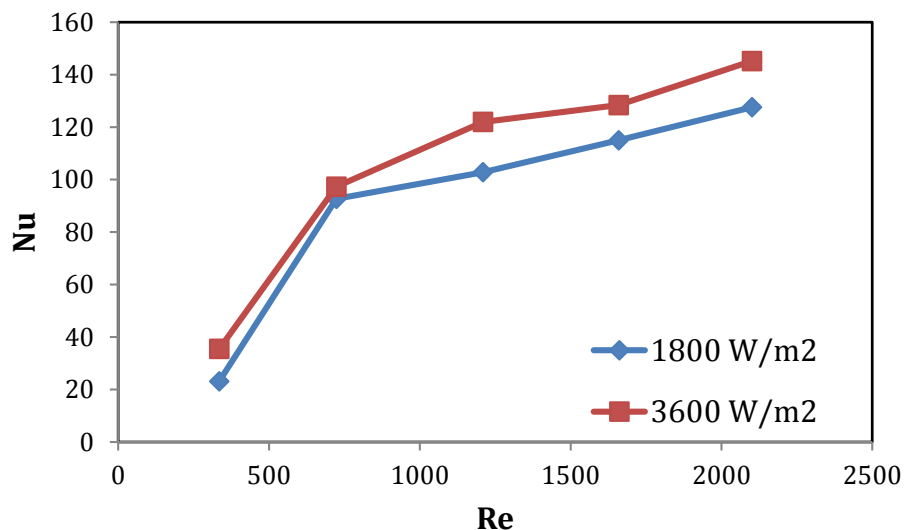
Figure 6-12 The Nusselt (Nu) number plotted against Reynolds (Re) number.
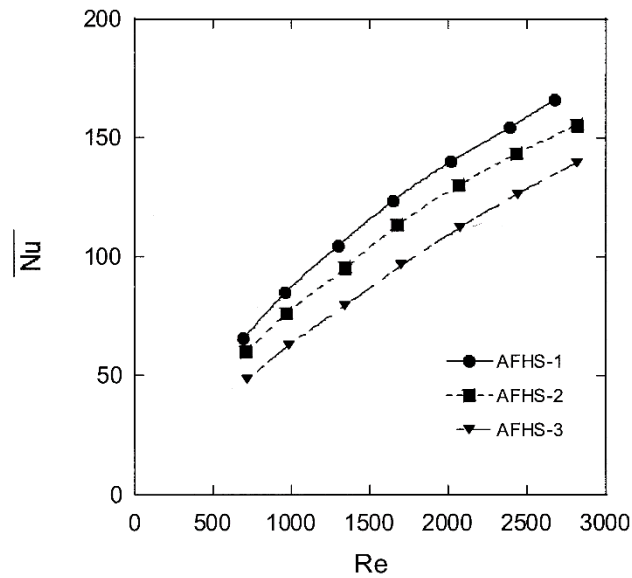
Figure 6-13 Nu/Re correlation for Seo Young *et* al.
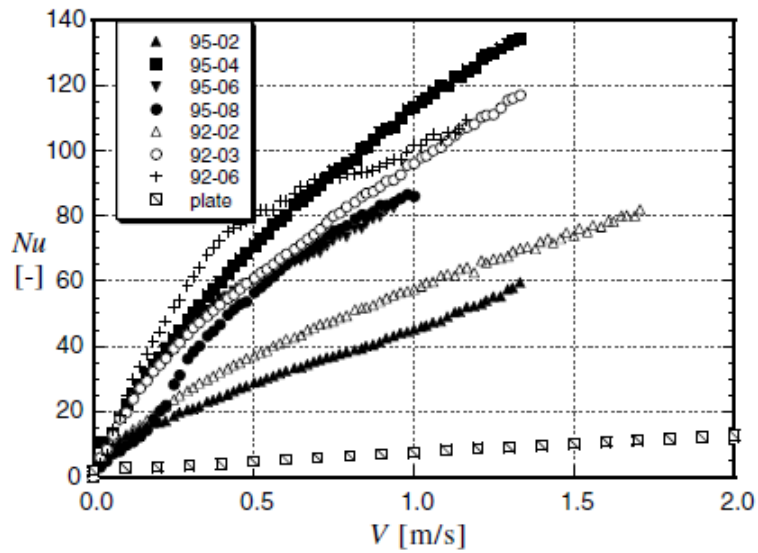
Figure 6-14 Nu/Re correlation for Boomsba *et* al.

6.4.1.2 Pressure drop

Figure 6-15 shows the pressure drop across the foam. Within the range of air velocity in the wind tunnel i.e. 1.90 – 4.00 m/s (corresponding to the minimum and maximum fan voltage), the pressure drop apparently increased linearly with increasing air velocity. This could be very well due to the laminar flow in the experimental range as explained in the following correlations:

$$\Delta P = 4g \frac{L}{D} \frac{\rho v^2}{2}$$

$$g = \frac{64}{Re} = \frac{64}{\rho v D / \mu}$$

$$\Delta P \propto v$$

Which shows that under low velocities (laminar flow), the pressure drop is proportional to the velocity.

A regression analysis in Table 6-4 showed that the trend was either linear or polynomial (similar R-squared value). This experimental profile was compared with the model profiles in Figure 6-16, the range of which was extended from 0.00 to 4.58 m/s (the range of the heat transfer experiments).
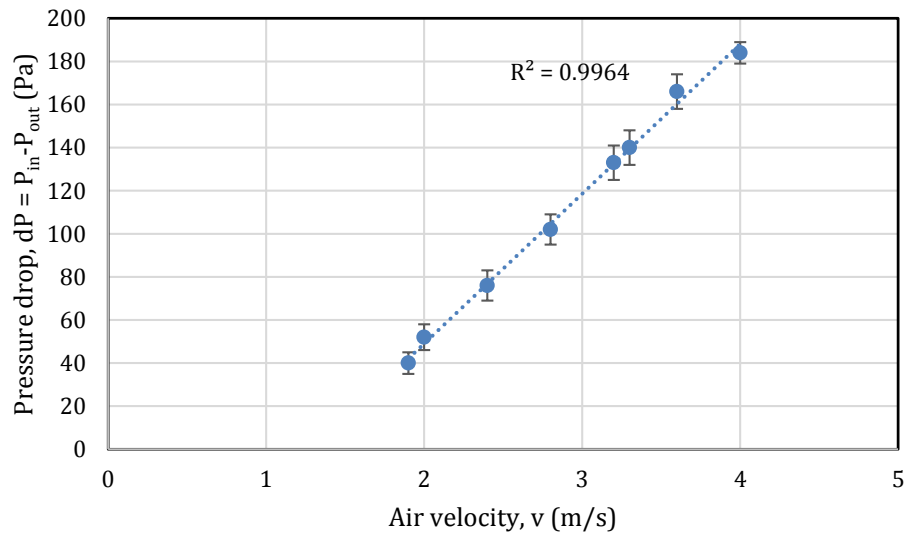
Figure 6-15 Measured pressure drop plotted against inlet air velocity. Error bars show mean ± standard deviation, n = 3.

Table 6-4 Regression analysis for the experimental pressure drop data.

Linear	0.9964
Polynomial	0.9965

6.4.2 Numerical results

6.4.2.1 Pressure drop and permeability

The pressure drop was also determined by modelling. The P_{out} value was taken as an area-weighted average of the pressure outlet boundary. P_{in} was atmospheric (1.01×10^5 Pa) as in the experiment. The velocity range used in the simulation was $0.00 - 4.58$ m/s, similar to the heat transfer rig. The pressure data is plotted in Figure 6-16. It shows that the experimental pressure drop, representative of the entire foam, fitted well with the normal ROI (the best case scenario) pressure drop. All series fitted polynomial trendlines. These data show that the defect region did not impact upon pressure drop adversely. The models employed non slip lateral boundaries with conserved continuity. This meant that all fluid needed to flow through the flow restricted domain without any chance of flowing laterally as in the actual foam. This resulted in the high pressure drop value for the defect ROI (the worst case scenario). The defect region reduced the specific surface area from 2200 to 1500 m^2/m^3 (minus 30%). This implies low efficiency in terms of available surface area for heat transfer. Defect-free foams must be used for an optimal heat transfer performance.
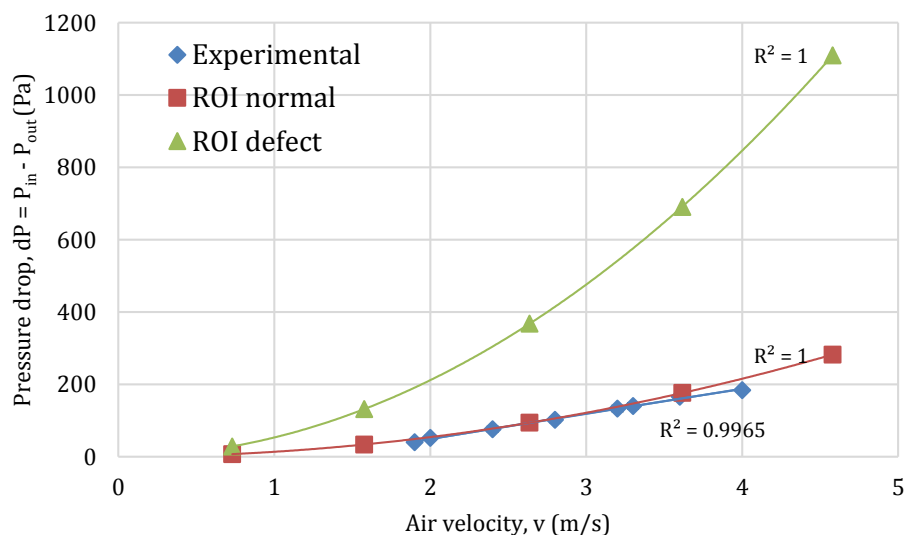
Figure 6-16 Pressure drop plotted against inlet air velocity for the experimental and numerical models. All series are fitted into the polynomial regression.

The normal ROI results can be considered to be representative of the foam. To measure the permeability, the flow through the ROI models had to be converted into Darcian

velocity first. Darcian velocity, V, can simply be calculated by dividing the volumetric flowrate, $\dot{V}$ (m³/s) by the cross sectional area, A_c, normal to the flow (m²) [112].

$$V = \frac{\dot{V}}{A_c}$$

The pressure drop data is presented in terms of per unit length, dP/L (Pa/m). The important dimensions of the model can be observed in Figure 6-17 below.
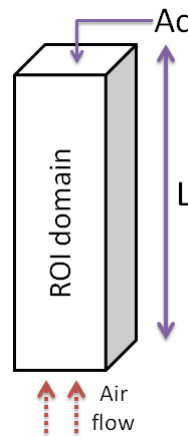
Figure 6-17 Properties of the ROI important for calculations. Length, L = 0.05m, cross sectional surface area, A_c = 2 x 10⁻⁴ m².

The pressure drop data are plotted in Figure 6-18. They clearly show that the defect region inflicted a substantially high pressure drop compared to the normal region. At the highest Darcian velocity of 75 m/s, the defect model pressure drop was 22195 Pa/m whereas for the normal region, it was 1109 Pa/m i.e. a factor of 20 higher. The pressure drop trends were correlated in a polynomial with the velocity values by the 2nd order. The regression trendlines showed a good fit ($R^2 > 0.99$). These data imply that the flow range investigated was no longer in the Darcian regime (linear trend) but was now in the Forchheimer regime (2nd order polynomial). The flow in this regime can be described by this correlation,

$$\frac{\Delta P}{L} = \frac{\mu}{K}V + \rho C V^2$$

Equation 6-12

By using proper values for the inlet air: dynamic viscosity, $\mu = 1.980 \times 10^{-5}$ kg/m.s and density, $\rho = 1.205$ kg/m³, the permeability, K (m²) and drag coefficient, C (m⁻¹) were calculated. These are tabulated in Table 6-5. It was evident that the normal ROI was four times more permeable than the defect ROI. The values here are consistent with values found in literature, which are typically $K \times 10^{-7}$ m² (refer to Table 2-6 in Chapter 2). Because the normal ROI pressure drop agreed well with the experiment, its permeability value of 1.85×10^{-6} m² was considered representative of the foam.
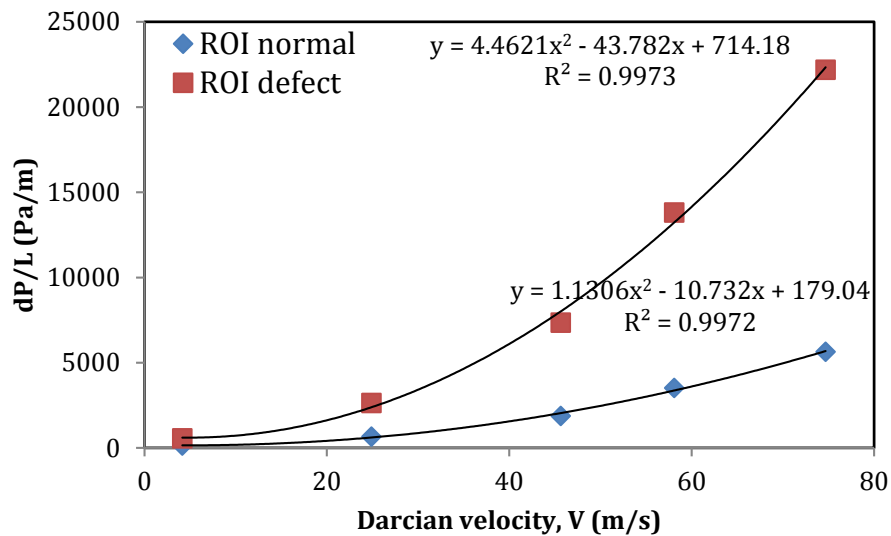
Figure 6-18 Pressure drop per unit length (Pa/m) plotted against the Darcian velocity (m/s).

Table 6-5 Permeability and drag coefficient.

ROI	Permeability, $K \times 10^7$ (m²)	Drag coefficient, C (m⁻¹)
Normal	18.45	0.938
Defect	4.52	3.703

6.4.2.2 Analysis on the flow and pressure fields

The defect region caused a 20 times higher pressure drop than the normal region at the highest inlet velocity (v = 4.58 m/s or in Darcian, V = 75 m/s). A detailed examination of the flow at this velocity is shown in Figure 6-19. Here, the streamlines clearly show the presence of a restricted flow, which caused a 'Venturi effect' (label 'A'). At this constriction, the velocity spiked to 25 m/s (Figure 6-21a). Consequently the pressure dropped (Figure 6-20 and Figure 6-21b). From the flow streamlines, it is apparent that

the air flowed laterally through the tortuous flow paths after the Venturi event (label 'B') made possible by the open cell structure. On a grander scale of the foam, this would mean the flow stabilized quickly after flowing through these restrictions, which was evident in the experimental pressure drop data. The flow streamlines and pressure field of the normal region are shown in Figure 6-22. In this case, the pressure dropped steadily along the domain length. This would model the behaviour of the flow if the foam was manufactured without the defect.
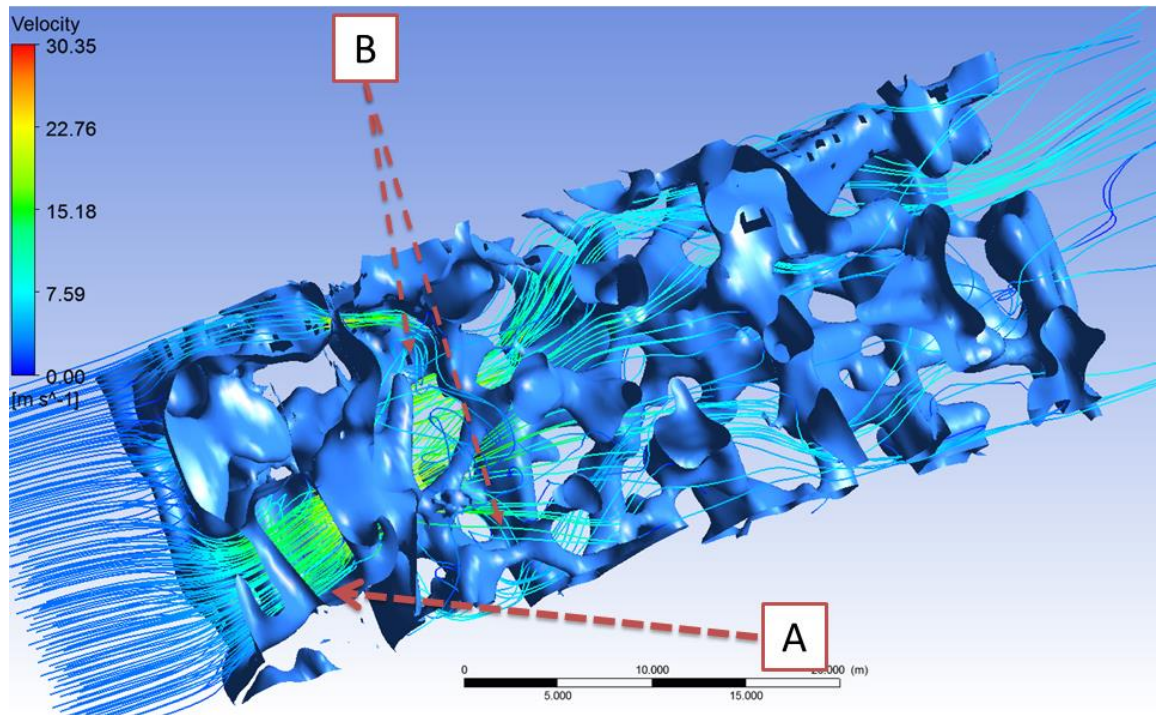
Figure 6-19 **ROI defect: flow streamlines (inlet air velocity = 4.58 m/s)** (**A**) indicates the Venturi effect, (**B**) indicates the lateral flow of fluid after the constriction.
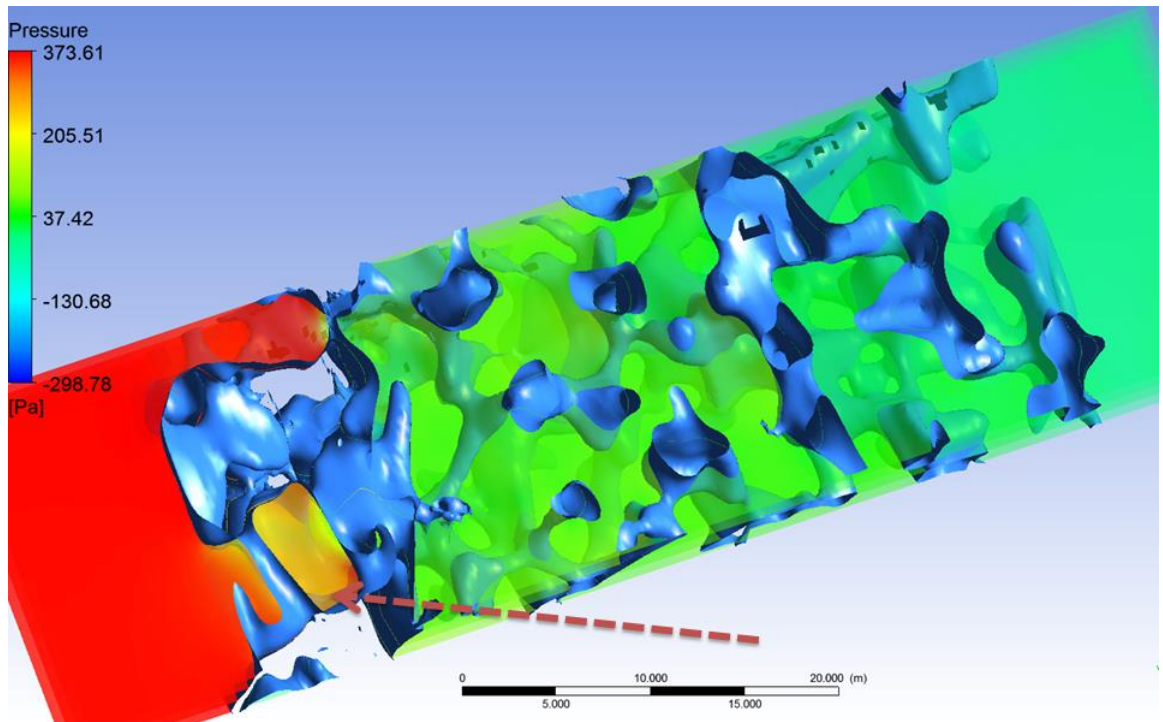
Figure 6-20 ROI defect: pressure field (inlet air v = 4.58 m/s). Arrow indicates the constricted flow.
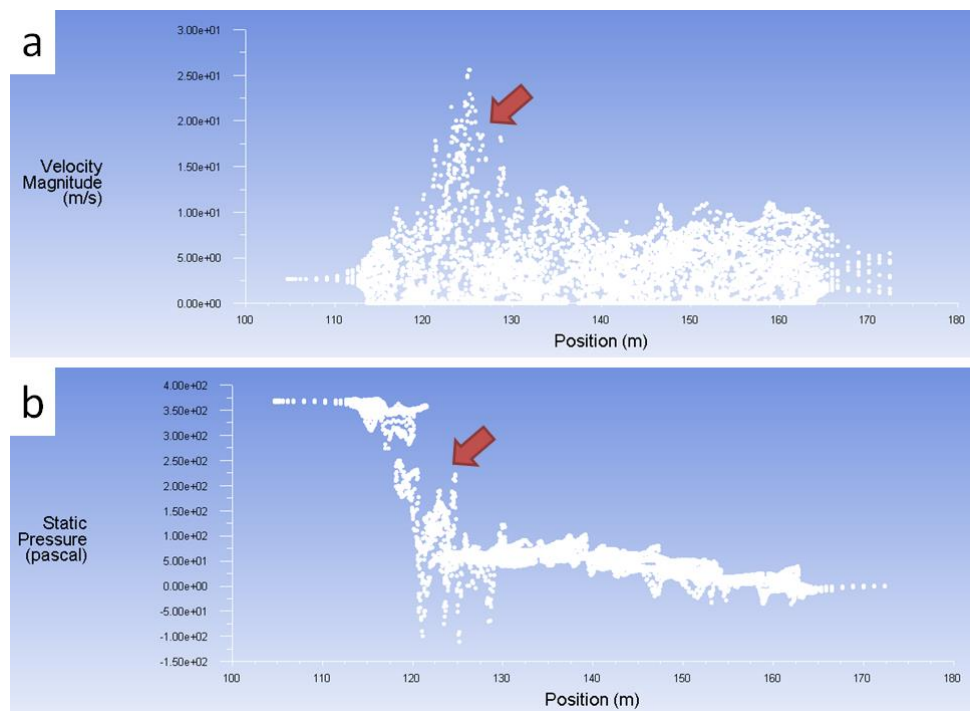
Figure 6-21 **ROI defect (at inlet v = 4.58 m/s)** (**a**) velocity magnitude, (**b**) static pressure. Y-axis refers to the length, L of the domain (refer to Figure 6-17). Arrows show the Venturi event.
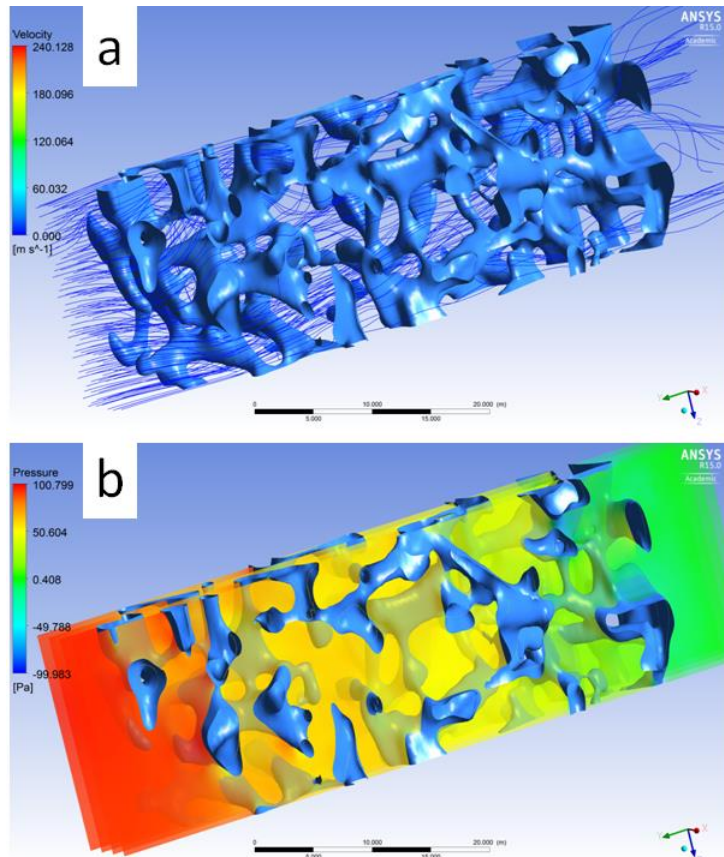
Figure 6-22 **ROI normal (at inlet v = 4.58 m/s)** (**a**) flow streamlines, (**b**) pressure field.

6.5 Conclusions

In this Chapter, the irregular foam prototype was evaluated in its steady state performance: heat transfer and fluid flow. Numerical simulation allowed for pore scale flow examinations. This work complemented the work on the transient heat sink using the similar foam as in Chapters 4 and 5.

The main conclusions are:

- For the first time for metal foams, the global heat transfer coefficient calculation employed the actual surface area value obtained from the 3D model (developed in Chapter 3).

- The global heat transfer coefficient was independent of the imposed heat flux but highly dependent on the coolant flow rate.

- Within the wind tunnel air velocity range (laminar flow), the pressure drop increased linearly with increasing inlet air velocity. Pressure drop data for the normal region model (best case scenario) fitted very well with the experimental data.

- The defect region therefore did not impose a significant effect upon the pressure drop. However, it was still not an optimal heat sink due to the 30% reduction of specific surface area for heat transfer from 2200 to 1500 m^2/m^3.

- Flow simulation for the worst case scenario (defect region) showed a 20 times higher pressure drop compared to the best case scenario (normal region) at the highest air velocity. A detailed examination revealed the intense pressure drop was caused by a localized flow restriction, which created a Venturi effect.

Chapter 7   Conclusions and future work

This thesis has presented a new concept in cooling power electronics (IGBTs) for locomotives during stopping periods at station. The "transient" heat sink consisted of a salt hydrate PCM and a novel irregular aluminium foam. During these stops, the sink would absorb heat from the IGBTs and therefore the PCM melted, a process accelerated by the metal foam. The PCM would then be re-solidified once the trains moved via forced convection. Once heat pipe is to be used as heat conduit, the system would be completely passive.

The sink with its current specifications (with liquid cooling) was able to absorb a thermal load consistent from a group of 4-5 IGBTs, which dissipated a low power of 20W per module during stops. The heating period of 1600-3500s per cycle meant the sink could be fitted to intercity locomotives.

Analytical methodologies employed during the project have validated the use of low resolution medical CT scanners (which allowed the use of large size samples) to create accurate 3D models. This was made possible by the use of the ScanIP software. In Chapter 3, a detailed guidance on the procedure was presented, this would be useful for researchers in modelling (and hence, characterizing) large samples without the need to cut their samples to fit into micro CT scanners, which is the current employed method. Models from the scanner could also be used into modelling systems for heat, flow, or mechanical simulations - just as demonstrated in Chapter 6, in which fluid flow was simulated through some models of the scanned foam.

Numerical simulation of the sink in Chapter 5 provided tools for design, redesign, scale-up, and development of porous metal/PCM heat sink.

The project was deemed successful in terms of its holistic approach to engineering design: the concept was constructed, analytical methods were presented, and the platform for redesign and scale-up was developed.

The next step in the transient sink development is to employ heat pipe as the heat conduit, replacing the liquid cooling (please refer to Appendix A1). This would create a fully passive system. This would also allow the full cycle of melting and solidifying of the PCM (based on the original concept) to be tested.

List of References

1. Mehling, H., Cabeza, L., *Heat and Cold Storage with PCM: An up to date introduction into basics and applications*. 2008: Springer.
2. Bauckhage, C. and T. Barber. *CASE STUDY: Six Cool IGBT's*. 2015 [cited 2015 20 November]; Available from: http://www.lytron.com/Tools-and-Technical-Reference/Application-Notes/Electronics-Cooling-Case-Study.
3. Perpiñà, X., et al., *Local thermal cycles determination in thermosyphon-cooled traction IGBT modules reproducing mission profiles.* Microelectronics Reliability, 2007. **47**(9–11): p. 1701-1706.
4. Weng, Y.-C., et al., *Heat pipe with PCM for electronic cooling.* Applied Energy, 2011. **88**(5): p. 1825-1833.
5. Gernert, N., *Heat-Pipe/Heat-Sink Technology Improves 6-kW Cooling.* Power Electronics Technology, 2009: p. 32-34.
6. Widmer, J., *High efficiency IGBT cooling load*, D. Reay, Editor. 2016.
7. Fratelli, L., et al., *Long term reliability testing of HV-IGBT modules in worst case traction operation.* Microelectronics Reliability, 1999. **39**(6–7): p. 1137-1142.
8. Mustaffar, A., A. Harvey, and D. Reay, *Melting of phase change material assisted by expanded metal mesh.* Applied Thermal Engineering, 2015. **90**: p. 1052-1060.
9. Romm, J. *World's Largest Solar Power Plants With Thermal Storage To Be Built In Arizona*. 2009 [cited 2015 22 October]; Available from: http://www.worldchanging.com/archives/009788.html.
10. Gil, A., et al., *State of the art on high temperature thermal energy storage for power generation. Part 1—Concepts, materials and modellization.* Renewable and Sustainable Energy Reviews, 2010. **14**(1): p. 31-55.
11. Cabeza, L.F., *3.07 - Thermal Energy Storage*, in *Comprehensive Renewable Energy*, A. Sayigh, Editor. 2012, Elsevier: Oxford. p. 211-253.
12. Koene, F. *Thermochemical storage - testing prototype reactors at TNO*. 2015 [cited 2016 26 April]; Available from: http://www.e-hub.org/thermochemical-storage-ECN.html.
13. Yu, N., R.Z. Wang, and L.W. Wang, *Sorption thermal storage for solar energy.* Progress in Energy and Combustion Science, 2013. **39**(5): p. 489-514.
14. Ristić, A. and S.K. Henninger, *Sorption Composite Materials for Solar Thermal Energy Storage.* Energy Procedia, 2014. **48**: p. 977-981.
15. Pardo, P., et al., *A review on high temperature thermochemical heat energy storage.* Renewable and Sustainable Energy Reviews, 2014. **32**: p. 591-610.
16. N'Tsoukpoe, K.E., et al., *A review on long-term sorption solar energy storage.* Renewable and Sustainable Energy Reviews, 2009. **13**(9): p. 2385-2396.
17. Shukla, A., D. Buddhi, and R.L. Sawhney, *Thermal cycling test of few selected inorganic and organic phase change materials.* Renewable Energy, 2008. **33**(12): p. 2606-2614.
18. Zhou, D., C.Y. Zhao, and Y. Tian, *Review on thermal energy storage with phase change materials (PCMs) in building applications.* Applied Energy, 2012. **92**: p. 593-605.
19. Rathod, M.K. and J. Banerjee, *Thermal stability of phase change materials used in latent heat energy storage systems: A review.* Renewable and Sustainable Energy Reviews, 2013. **18**(0): p. 246-258.

20. Abhat, A., *Low temperature latent heat thermal energy storage: Heat storage materials.* Solar Energy, 1983. **30**(4): p. 313-332.

21. Sugo, H., E. Kisi, and D. Cuskelly, *Miscibility gap alloys with inverse microstructures and high thermal conductivity for high energy density thermal storage applications.* Applied Thermal Engineering, 2013. **51**(1–2): p. 1345-1350.

22. PCMProducts. *Phase Change Materials: Thermal Management Solutions*. 2009; Available from: http://www.pcmproducts.net/.

23. Moreno, P., et al., *Corrosion of metal and metal alloy containers in contact with phase change materials (PCM) for potential heating and cooling applications.* Applied Energy, 2014. **125**: p. 238-245.

24. Ltd., W.X.C.I.C. *Magnesium Chloride White Flake*. 2015 [cited 2015 20 October]; Available from: http://www.xiangkunchem.com/en/zhsh.asp?id=270&menu=read.

25. Cabeza, L.F., et al., *Immersion corrosion tests on metal-salt hydrate pairs used for latent heat storage in the 32 to 36°C temperature range.* Materials and Corrosion, 2001. **52**(2): p. 140-146.

26. Cabeza, L.F., et al., *Middle term immersion corrosion tests on metal-salt hydrate pairs used for latent heat storage in the 32 to 36°C temperature range.* Materials and Corrosion, 2001. **52**(10): p. 748-754.

27. Kenisarin, M. and K. Mahkamov, *Solar energy storage using phase change materials.* Renewable and Sustainable Energy Reviews, 2007. **11**(9): p. 1913-1965.

28. Risueño, E., et al., *Mg-Zn-Al Eutectic Alloys as Phase Change Material for Latent Heat Thermal Energy Storage.* Energy Procedia, 2015. **69**: p. 1006-1013.

29. Sharma, S.D., D. Buddhi, and R.L. Sawhney, *Accelerated thermal cycle test of latent heat-storage materials.* Solar Energy, 1999. **66**(6): p. 483-490.

30. Porisini, F.C., *Salt hydrates used for latent heat storage: Corrosion of metals and reliability of thermal performance.* Solar Energy, 1988. **41**(2): p. 193-197.

31. Sun, J.Q., et al., *Thermal reliability test of Al–34%Mg–6%Zn alloy as latent heat storage material and corrosion of metal with respect to thermal cycling.* Energy Conversion and Management, 2007. **48**(2): p. 619-624.

32. Oh, Y.K., S.H. Park, and Y.I. Cho, *A study of the effect of ultrasonic vibrations on phase-change heat transfer.* International Journal of Heat and Mass Transfer, 2002. **45**(23): p. 4631-4641.

33. Legay, M., et al., *Enhancement of Heat Transfer by Ultrasound: Review and Recent Advances.* International Journal of Chemical Engineering, 2011. **2011**: p. 17.

34. Agyenim, F., et al., *A review of materials, heat transfer and phase change problem formulation for latent heat thermal energy storage systems (LHTESS).* Renewable and Sustainable Energy Reviews, 2010. **14**(2): p. 615-628.

35. Xu, B., P. Li, and C. Chan, *Application of phase change materials for thermal energy storage in concentrated solar thermal power plants: A review to recent developments.* Applied Energy, 2015. **160**: p. 286-307.

36. Alam, T.E., et al., *Macroencapsulation and characterization of phase change materials for latent heat thermal energy storage systems.* Applied Energy, 2015. **154**: p. 92-101.

37. Jamekhorshid, A., S.M. Sadrameli, and M. Farid, *A review of microencapsulation methods of phase change materials (PCMs) as a thermal energy storage (TES) medium.* Renewable and Sustainable Energy Reviews, 2014. **31**: p. 531-542.

38. Huang, H.J., X.D. Chen, and W.K. Yuan, *Microencapsulation based on emulsification for producing pharmaceutical products: A literature review.* Developments in Chemical Engineering and Mineral Processing, 2006. **14**(3-4): p. 515-544.

39. Borreguero, A.M., et al., *Synthesis and characterization of microcapsules containing Rubitherm®RT27 obtained by spray drying.* Chemical Engineering Journal, 2011. **166**(1): p. 384-390.

40. Agyenim, F., P. Eames, and M. Smyth, *A comparison of heat transfer enhancement in a medium temperature thermal energy storage heat exchanger using fins.* Solar Energy, 2009. **83**(9): p. 1509-1520.

41. Pakrouh, R., et al., *A numerical method for PCM-based pin fin heat sinks optimization.* Energy Conversion and Management, 2015. **103**: p. 542-552.

42. Al-Abidi, A.A., et al., *Internal and external fin heat transfer enhancement technique for latent heat thermal energy storage in triplex tube heat exchangers.* Applied Thermal Engineering, 2013. **53**(1): p. 147-156.

43. Shabgard, H., et al., *High temperature latent heat thermal energy storage using heat pipes.* International Journal of Heat and Mass Transfer, 2010. **53**(15–16): p. 2979-2988.

44. Sharifi, N., et al., *Simulation of heat pipe-assisted latent heat thermal energy storage with simultaneous charging and discharging.* International Journal of Heat and Mass Transfer, 2015. **80**: p. 170-179.

45. Zeng, J.L., et al., *Study of a PCM based energy storage system containing Ag nanoparticles.* Journal of Thermal Analysis and Calorimetry, 2007. **87**(2): p. 371-375.

46. Elgafy, A. and K. Lafdi, *Effect of carbon nanofiber additives on thermal behavior of phase change materials.* Carbon, 2005. **43**(15): p. 3067-3074.

47. Fukai, J., et al., *Thermal conductivity enhancement of energy storage media using carbon fibers.* Energy Conversion and Management, 2000. **41**(14): p. 1543-1556.

48. Fukai, J., et al., *Effect of carbon-fiber brushes on conductive heat transfer in phase change materials.* International Journal of Heat and Mass Transfer, 2002. **45**(24): p. 4781-4792.

49. Nakaso, K., et al., *Extension of heat transfer area using carbon fiber cloths in latent heat thermal energy storage tanks.* Chemical Engineering and Processing: Process Intensification, 2008. **47**(5): p. 879-885.

50. Abdollahzadeh, M. and M. Esmaeilpour, *Enhancement of phase change material (PCM) based latent heat storage system with nano fluid and wavy surface.* International Journal of Heat and Mass Transfer, 2015. **80**: p. 376-385.

51. Fauzi, H., et al., *Sodium laurate enhancements the thermal properties and thermal conductivity of eutectic fatty acid as phase change material (PCM).* Solar Energy, 2014. **102**: p. 333-337.

52. Wu, Z.G. and C.Y. Zhao, *Experimental investigations of porous materials in high temperature thermal energy storage systems.* Solar Energy, 2011. **85**(7): p. 1371-1380.

53. Chen, J., et al., *Research Progress of Phase Change Materials (PCMs) Embedded with Metal Foam (a Review).* Procedia Materials Science, 2014. **4**: p. 389-394.

54. Siahpush, A., J. O'Brien, and J. Crepeau, *Phase Change Heat Transfer Enhancement Using Copper Porous Foam.* Journal of Heat Transfer, 2008. **130**(8): p. 082301-082301.

55. Xiao, X., P. Zhang, and M. Li, *Preparation and thermal characterization of paraffin/metal foam composite phase change material.* Applied Energy, 2013. **112**: p. 1357-1366.

56. Shuja, S.Z., B.S. Yilbas, and M.M. Shaukat, *Melting enhancement of a phase change material with presence of a metallic mesh.* Applied Thermal Engineering, 2015. **79**: p. 163-173.

57. Cabeza, L.F., *Advances in Thermal Energy Storage Systems - Methods and Applications.* Woodhead Publishing.

58. Pincemin, S., et al., *Highly conductive composites made of phase change materials and graphite for thermal storage.* Solar Energy Materials and Solar Cells, 2008. **92**(6): p. 603-613.

59. Fernandes, D., et al., *Thermal energy storage: "How previous findings determine current research priorities".* Energy, 2012. **39**(1): p. 246-257.

60. Reay, D. *Thermal management controller for domestic micro-generation systems.* 2015 [cited 2015 25 October]; Available from: http://www.hexag.org/publications.html.

61. Zafari, M., et al., *Microtomography-based numerical simulation of fluid flow and heat transfer in open cell metal foams.* Applied Thermal Engineering, 2015. **80**: p. 347-354.

62. Oya, T., et al., *Phase change composite based on porous nickel and erythritol.* Applied Thermal Engineering, 2012. **40**: p. 373-377.

63. Xu, W.Q., X.G. Yuan, and Z. Li, *Study on effective thermal conductivity of metal foam matrix composite phase change materials.* Gongneng Cailiao/Journal of Functional Materials, 2009. **40**(8): p. 1329-1332+1337.

64. Xiao, X., P. Zhang, and M. Li, *Effective thermal conductivity of open-cell metal foams impregnated with pure paraffin for latent heat storage.* International Journal of Thermal Sciences, 2014. **81**: p. 94-105.

65. Zhou, D. and C.Y. Zhao, *Experimental investigations on heat transfer in phase change materials (PCMs) embedded in porous materials.* Applied Thermal Engineering, 2011. **31**(5): p. 970-977.

66. Consulting, R.C. *Thermal conductivity testing.* 2014 [cited 2015 20 October]; Available from: http://www.redcore.ca/en_thermal.html.

67. Ranut, P., *On the effective thermal conductivity of aluminum metal foams: Review and improvement of the available empirical and analytical models.* Applied Thermal Engineering.

68. Bhattacharya, A., V.V. Calmidi, and R.L. Mahajan, *Thermophysical properties of high porosity metal foams.* International Journal of Heat and Mass Transfer, 2002. **45**(5): p. 1017-1031.

69. Dul'nev, G.N., *Heat transfer through solid disperse systems.* Journal of engineering physics, 1965. **9**(3): p. 275-279.

70. K. Boomsba, D.P., *On the effective thermal conductivity of a three-dimensionally structured fluid-saturated metal foam.* International Journal of Heat and Mass Transfer, 2001. **44**: p. 827-836.

71. Ranut, P. and E. Nobile, *On the effective thermal conductivity of metal foams*, in *32nd UIT (Italian Union of Thermo-fluid-dynamics) Heat Transfer Conference.* 2014, IOP Publishing.

72. Ranut, P., E. Nobile, and L. Mancini, *High resolution X-ray microtomography-based CFD simulation for the characterization of flow permeability and effective*

thermal conductivity of aluminum metal foams. Experimental Thermal and Fluid Science, 2015. **67**: p. 30-36.

73.   Dutil, Y., et al., *A review on phase-change materials: Mathematical modeling and simulations.* Renewable and Sustainable Energy Reviews, 2011. **15**(1): p. 112-130.

74.   Al-abidi, A.A., et al., *CFD applications for latent heat thermal energy storage: a review.* Renewable and Sustainable Energy Reviews, 2013. **20**(0): p. 353-363.

75.   Sundarram, S.S. and W. Li, *The effect of pore size and porosity on thermal management performance of phase change material infiltrated microcellular metal foams.* Applied Thermal Engineering, 2014. **64**(1–2): p. 147-154.

76.   Chen, Z., D. Gao, and J. Shi, *Experimental and numerical study on melting of phase change materials in metal foams at pore scale.* International Journal of Heat and Mass Transfer, 2014. **72**: p. 646-655.

77.   Feng, S., et al., *Pore-scale and volume-averaged numerical simulations of melting phase change heat transfer in finned metal foam.* International Journal of Heat and Mass Transfer, 2015. **90**: p. 838-847.

78.   Nomura, T., N. Okinaka, and T. Akiyama, *Impregnation of porous material with phase change material for thermal energy storage.* Materials Chemistry and Physics, 2009. **115**(2–3): p. 846-850.

79.   Jiang, J., et al., *Preparation and performances of bulk porous Al foams impregnated with phase-change-materials for thermal storage.* Progress in Natural Science: Materials International, 2012. **22**(5): p. 440-444.

80.   Mancin, S., et al., *Heat transfer during air flow in aluminum foams.* International Journal of Heat and Mass Transfer, 2010. **53**(21–22): p. 4976-4984.

81.   Zhao, C.Y., *Review on thermal transport in high porosity cellular metal foams with open cells.* International Journal of Heat and Mass Transfer, 2012. **55**(13–14): p. 3618-3632.

82.   Banhart, J., *Manufacture, characterisation and application of cellular metals and metal foams.* Progress in Materials Science, 2001. **46**(6): p. 559-632.

83.   Conde, Y., et al., *Replication Processing of Highly Porous Materials.* Advanced Engineering Materials, 2006. **8**(9): p. 795-803.

84.   Barari, F., *Metal foam regenerators; heat transfer and pressure drop in porous metals*, in *Department of Mechanical Engineering*. 2013, The University of Sheffield: Sheffield, United Kingdom.

85.   Banhart, J., *Manufacturing routes for metallic foams.* JOM, 2000. **52**(12): p. 22-27.

86.   Jarema, C., T. Lee, and L. Niebyski, *Preparation of metal foams with viscosity increasing gases*. 1974, Google Patents.

87.   Kim, S. and C.-W. Lee, *A Review on Manufacturing and Application of Open-cell Metal Foam.* Procedia Materials Science, 2014. **4**: p. 305-309.

88.   Elsner, A., et al., *Specific Surface Area and Volume Fraction of the Cherry-Pit Model with Packed Pits.* The Journal of Physical Chemistry B, 2009. **113**(22): p. 7780-7784.

89.   Inayat, A., et al., *Determining the specific surface area of ceramic foams: The tetrakaidecahedra model revisited.* Chemical Engineering Science, 2011. **66**(6): p. 1179-1188.

90.   Bock, J. and A.M. Jacobi, *Geometric classification of open-cell metal foams using X-ray micro-computed tomography.* Materials Characterization, 2013. **75**: p. 35-43.

91.   Buciuman, F.C. and B. Kraushaar-Czarnetzki, *Ceramic Foam Monoliths as Catalyst Carriers. 1. Adjustment and Description of the Morphology.* Industrial & Engineering Chemistry Research, 2003. **42**(9): p. 1863-1869.

92.   Richardson, J.T., Y. Peng, and D. Remue, *Properties of ceramic foam catalyst supports: pressure drop.* Applied Catalysis A: General, 2000. **204**(1): p. 19-32.

93.   Calmidi, V.V. and R.L. Mahajan, *The Effective Thermal Conductivity of High Porosity Fibrous Metal Foams.* Journal of Heat Transfer, 1999. **121**(2): p. 466-471.

94.   Gregor, T., P. Kochova, and L. Eberlova, *Correlating Micro-CT Imaging with Quantitative Histology, Injury and Skeletal Biomechanics*, T. Goswami, Editor. 2012.

95.   Dierick, M., et al., *Recent micro-CT scanner developments at UGCT.* Nuclear Instruments and Methods in Physics Research Section B: Beam Interactions with Materials and Atoms, 2014. **324**: p. 35-40.

96.   Simpleware. *Converting 3D images into models*. [cited 2015 24 June]; Available from: https://www.simpleware.com/.

97.   ERG. *Surface Area of Duocel® Foam*. 2011 [cited 2015 18 October]; Available from: http://www.ergaerospace.com/surface-area.html.

98.   De Paepe, M., et al., *The use of open cell metal foams in heat exchangers: possibilities and limitations*, in *8th International Conference on Heat Transfer, Fluid Mechanics, and Thermodynamics*. 2011: Mauritius.

99.   Fraunhofer. *Characterisation of Cellular Materials*. 2015 [cited 2015 18 October]; Available from: http://www.ifam.fraunhofer.de/en/Dresden/Energy_and_thermal_management/Charakterisierung_zellularer_Werkstoffe.html.

100.   Calmidi, V.V. and R.L. Mahajan, *Forced Convection in High Porosity Metal Foams.* Journal of Heat Transfer, 2000. **122**(3): p. 557-565.

101.   Mancin, S., et al., *Air forced convection through metal foams: Experimental results and modeling.* International Journal of Heat and Mass Transfer, 2013. **62**(0): p. 112-123.

102.   Seo Young, K., P. Jin Wook, and K. Byung Ha, *Thermal performance of aluminum-foam heat sinks by forced air cooling.* IEEE Transactions on Components and Packaging Technologies, 2003. **26**(1): p. 262-267.

103.   Barari, F., et al., *Metal foam regenerators; heat transfer and storage in porous metals.* Journal of Materials Research, 2013. **28**(17): p. 2474-2482.

104.   Hsieh, W.H., et al., *Experimental investigation of heat-transfer characteristics of aluminum-foam heat sinks.* International Journal of Heat and Mass Transfer, 2004. **47**(23): p. 5149-5157.

105.   Kim, S.Y., J.W. Paek, and B.H. Kang, *Flow and Heat Transfer Correlations for Porous Fin in a Plate-Fin Heat Exchanger.* Journal of Heat Transfer, 2000. **122**(3): p. 572-578.

106.   Giani, L., G. Groppi, and E. Tronconi, *Heat Transfer Characterization of Metallic Foams.* Industrial & Engineering Chemistry Research, 2005. **44**(24): p. 9078-9085.

107.   Darcy, H., *Les Fontaines Publiques de la ville de Dijon.* 1856, Paris: Dalmont.

108.   Boomsma, K., D. Poulikakos, and Y. Ventikos, *Simulations of flow through open cell metal foams using an idealized periodic cell structure.* International Journal of Heat and Fluid Flow, 2003. **24**(6): p. 825-834.

109.   Dupuit, A.J.E.J., *Etudes Theoriques et Pratique sur le Mouvement des Eaux*. 1863, Paris.

110. Boomsma, K. and D. Poulikakos, *The Effects of Compression and Pore Size Variations on the Liquid Flow Characteristics in Metal Foams.* Journal of Fluids Engineering, 2001. **124**(1): p. 263-272.
111. Agnew, B., *Comments on wind tunnel tests*. 2016.
112. Dukhan, N., *Metal foams: fundamentals and applications*. 2013, Lancaster, U.S.A.: DEStech Publications, Inc.
113. Liu, J.F., et al., *Measurement and correlation of friction characteristic of flow through foam matrixes.* Experimental Thermal and Fluid Science, 2006. **30**(4): p. 329-336.
114. Kamath, P.M., C. Balaji, and S.P. Venkateshan, *Experimental investigation of flow assisted mixed convection in high porosity foams in vertical channels.* International Journal of Heat and Mass Transfer, 2011. **54**(25–26): p. 5231-5241.
115. Bodla, K.K., J.Y. Murthy, and S.V. Garimella, *Microtomography-Based Simulation of Transport through Open-Cell Metal Foams.* Numerical Heat Transfer, Part A: Applications, 2010. **58**(7): p. 527-544.
116. Brun, E., *De l'imagerie 3D des structures a l'etude des mecanismes de transport en milieux cellulaires*. 2009.
117. Calmidi, V.V. and R.L. Mahajan, *Forced Convection in High Porosity Metal Foams.* Journal of Heat Transfer-transactions of The Asme, 2000. **122**(3).
118. Mancin, S., et al., *Air forced convection through metal foams: Experimental results and modeling.* International Journal of Heat and Mass Transfer, 2013. **62**: p. 112-123.
119. Pielichowska, K. and K. Pielichowski, *Phase change materials for thermal energy storage.* Progress in Materials Science, 2014. **65**: p. 67-123.
120. Hargrave, J., *It's alive: Can you imagine the urban building of the future*, ARUPForesight, Editor. 2013.
121. Duocel. *Duocel foam application guide*. 2011 [cited 2015 2 June]; Available from: http://www.ergaerospace.com/Material-Applications-guide.html.
122. Druma, A., K. Alam, and C. Druma, *Surface area and conductivity of open-cell carbon foams.* Minerals & Materials Characterisation & Engineering, 2006. **5**(1): p. 73-86.
123. Kumar, J., et al., *Effect of X-ray computed tomography scanning parameters on the estimated porosity of foam specimens*, in *2011 2nd International Conference on Mechanical, Industrial, and Manufacturing Technologies (MIMT 2011)*. 2011.
124. Richard, A.K. and D.C. William, *Acquisition, optimization and interpretation of X-ray computed tomographic imagery: applications to the geosciences.* Comput. Geosci., 2001. **27**(4): p. 381-400.
125. Hwang, J.J., et al., *Measurement of Interstitial Convective Heat Transfer and Frictional Drag for Flow Across Metal Foams.* Journal of Heat Transfer, 2001. **124**(1): p. 120-129.
126. Dierick, M., et al., *Recent micro-CT scanner developments at UGCT.* Nuclear Instruments and Methods in Physics Research Section B: Beam Interactions with Materials and Atoms, 2014. **324**(0): p. 35-40.
127. GeneralElectric. *Phoenix v|tome|x L 300*. 2015; Available from: https://www.gemeasurement.com/inspection-ndt/radiography-and-computed-tomography/phoenix-vtomex-l-300.
128. OsiriX. *About OsiriX*. [cited 2015 24 June]; Available from: http://www.osirix-viewer.com/AboutOsiriX.html.

129. Fagerlund, G., *Determination of specific surface by the BET method.* Matériaux et Construction, 1973. **6**(3): p. 239-245.

130. Kang, S., *Advanced cooling for power electronics*, in *International Conference on Integrated Power Electronics Systems*. 2012: Nuremberg.

131. Thermacore. *Complete thermal solutions for today's power electronics*. 2015 [cited 2015 09 July]; Available from: http://www.thermacore.com/applications/power-electronics-cooling.aspx.

132. Sharma, A., et al., *Review on thermal energy storage with phase change materials and applications.* Renewable and Sustainable Energy Reviews, 2009. **13**(2): p. 318-345.

133. Tian, Y. and C.Y. Zhao, *A numerical investigation of heat transfer in phase change materials (PCMs) embedded in porous metals.* Energy, 2011. **36**(9): p. 5539-5546.

134. Moreno, P., et al., *Corrosion of metal and metal alloy containers in contact with phase change materials (PCM) for potential heating and cooling applications.* Applied Energy, 2014. **125**(0): p. 238-245.

135. AluminiumPechiney. *AlSiMg0.3 and AlSi7Mg0.6 alloys particularly suitable for modification with sodium*. 2003 [cited 2015 09 July]; Available from: www.affimet.fr/images/up/fiche_pdf/2/Pech3.1E.pdf.

136. Xiao, X., P. Zhang, and M. Li, *Preparation and thermal characterization of paraffin/metal foam composite phase change material.* Applied Energy, 2013. **112**(0): p. 1357-1366.

137. Munson, B.R., *Fundamentals of Fluid Mechanics 6th Edition with WileyPlus 5th Edition Set*. 2008: John Wiley & Sons Canada, Limited.

138. Hughes, T.A., *Measurement and Control Basics (4th Edition)*. 2007: ISA.

139. Standard, B., *Temperature measurement - Part 4: Guide to the selection and use of thermocouples*. 1999, BSi.

140. Smith, C.L., *Basic Process Measurements*. 2009, New Jersey: Wiley.

141. TCDirect, *Guide to thermocouple and resistance thermometry*. 6.1 ed. 2009.

142. Perry, R.H., D.W. Green, and J.O. Maloney, *Perry's Chemical engineers' handbook*. 1984, New York: McGraw-Hill.

143. Xiao, X., P. Zhang, and M. Li, *Effective thermal conductivity of open-cell metal foams impregnated with pure paraffin for latent heat storage.* International Journal of Thermal Sciences, 2014. **81**(0): p. 94-105.

144. Lytron. *Electronics cooling case study*. 2015 [cited 2015 07 July]; Available from: http://www.lytron.com/Tools-and-Technical-Reference/Application-Notes/Electronics-Cooling-Case-Study.

145. Huang, L., et al., *Subcooling in PCM emulsions—Part 1: Experimental.* Thermochimica Acta, 2010. **509**(1–2): p. 93-99.

146. Tao, Y.B. and Y.L. He, *Numerical study on thermal energy storage performance of phase change material under non-steady-state inlet boundary.* Applied Energy, 2011. **88**(11): p. 4172-4179.

147. Hawlader, M.N.A., M.S. Uddin, and M.M. Khin, *Microencapsulated PCM thermal-energy storage system.* Applied Energy, 2003. **74**(1–2): p. 195-202.

148. Yang, H.D. and Y.K. Oh, *EFFECT OF ULTRASONIC VIBRATIONS ON ACCELERATING HEAT TRANSFER OF PCM.* International Journal of Modern Physics B, 2006. **20**(25n27): p. 4341-4346.

149. Ansys. *Ansys Fluent*. 2015 [cited 2015 29 June]; Available from: http://www.ansys.com/.

150. Comsol. *Comsol Multiphysics*. 2015 [cited 2015 29 June]; Available from: https://uk.comsol.com/products.

151. Shmueli, H., G. Ziskind, and R. Letan, *Melting in a vertical cylindrical tube: Numerical investigation and comparison with experiments.* International Journal of Heat and Mass Transfer, 2010. **53**(19–20): p. 4082-4091.

152. Laschet, G., et al., *Effective permeability and thermal conductivity of open-cell metallic foams via homogenization on a microstructure model.* Computational Materials Science, 2009. **45**(3): p. 597-603.

153. Faghri, A. and Y. Zhang, *6 - MELTING AND SOLIDIFICATION*, in *Transport Phenomena in Multiphase Systems*, A.F. Zhang, Editor. 2006, Academic Press: Boston. p. 421-530.

154. Voller, V.R. and C. Prakash, *A fixed grid numerical modelling methodology for convection-diffusion mushy region phase-change problems.* International Journal of Heat and Mass Transfer, 1987. **30**(8): p. 1709-1719.

155. Liu, Z., Y. Yao, and H. Wu, *Numerical modeling for solid–liquid phase change phenomena in porous media: Shell-and-tube type latent heat thermal energy storage.* Applied Energy, 2013. **112**: p. 1222-1232.

156. Veyhl, C., et al., *On the thermal conductivity of sintered metallic fibre structures.* International Journal of Heat and Mass Transfer, 2012. **55**(9–10): p. 2440-2448.

157. Petrasch, J., et al., *Tomography based determination of permeability, Dupuit–Forchheimer coefficient, and interfacial heat transfer coefficient in reticulate porous ceramics.* International Journal of Heat and Fluid Flow, 2008. **29**(1): p. 315-326.

158. Ansys. *Ansys Fluent Theory Guide R13*. 2012 [cited 2014 19 July]; Available from: http://www.ansys.com.

159. Boomsma, K. and D. Poulikakos, *On the effective thermal conductivity of a three-dimensionally structured fluid-saturated metal foam.* International Journal of Heat and Mass Transfer, 2001. **44**(4): p. 827-836.

160. Zhang, P., et al., *Heat transfer characteristics of a molten-salt thermal energy storage unit with and without heat transfer enhancement.* Applied Energy, 2015. **137**: p. 758-772.

161. Hong, S.T. and D.R. Herling, *Effects of Surface Area Density of Aluminum Foams on Thermal Conductivity of Aluminum Foam-Phase Change Material Composites.* Advanced Engineering Materials, 2007. **9**(7): p. 554-557.

162. Moeini Sedeh, M. and J.M. Khodadadi, *Thermal conductivity improvement of phase change materials/graphite foam composites.* Carbon, 2013. **60**: p. 117-128.

163. Seo Young, K., P. Jin Wook, and K. Byung Ha, *Thermal performance of aluminum-foam heat sinks by forced air cooling.* Components and Packaging Technologies, IEEE Transactions on, 2003. **26**(1): p. 262-267.

164. NASA. *Pitot-static tube: Prandtl tube*. 2015 [cited 2015 03 December]; Available from: https://www.grc.nasa.gov/WWW/K-12/airplane/pitot.html.

165. Thompson, D.W., *Fluid mechanics and transfer processes, J. M. Kay and R. M. Nedderman, 1985, 602 pages. Published by Cambridge University Press, $69.50 US (hardcover), $29.95 US (paperback).* The Canadian Journal of Chemical Engineering, 1987. **65**(3): p. 526-527.

166. Boomsma, K., D. Poulikakos, and F. Zwick, *Metal foams as compact high performance heat exchangers.* Mechanics of Materials, 2003. **35**(12): p. 1161-1176.

Appendices

A1 The second prototype

The second prototype was designed prior to the writing of this thesis and was completed at this point by Thermacore Ltd. (Figure A1 below). In this rig, the heat pipe evaporator was exposed to enable heating via a tape heater (variable wattage). The other end of the heat pipe (condenser) was attached to a fin stack for forced convection cooling.

Figure A1 The constructed second prototype.

The size limit of the rig was determined by the size of the vacuum oven in Newcastle University, where it will be used for impregnation with a paraffin PCM. Unfortunately, Thermacore at this point could not offer the modified design as due to equipment limitations. The prototype also showed a visible superficial defect. The design schematic is given in the following Figure A2. Tests will be carried out in a future project.
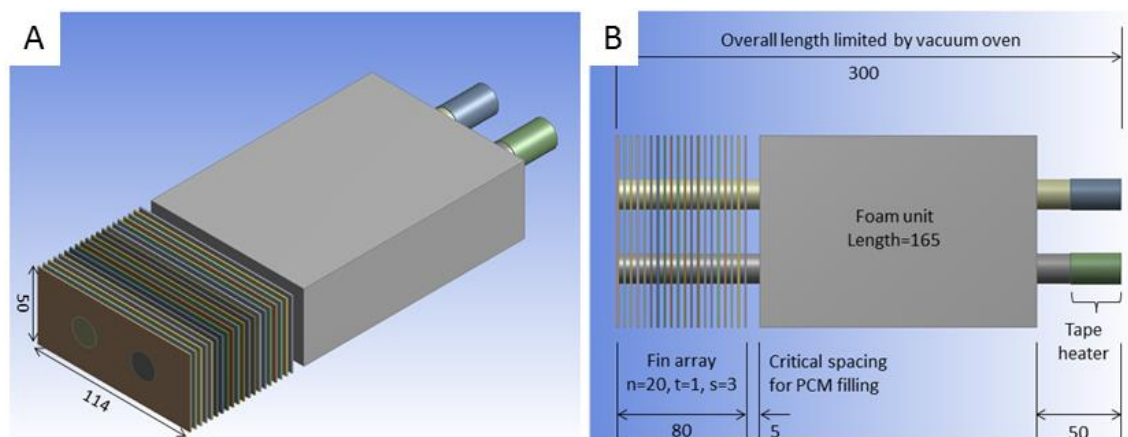
Figure A2 **Design schematic of the 2nd prototype** (**A**) isometric view, (**B**) plan view. Dimensions in mm.

A2 Description of the uncertainty analysis

Throughout the thesis, the uncertainty/error analysis was based on the combined random and systematic errors,

$$E_T = \sqrt{E_S^2 + E_R^2}$$

Where: E = error. The symbol δ was also used to represent uncertainty/error.

Where subscripts: T = total (combined), S = systematic, and R = random.

Therefore the combined error was the root mean square of the random and systematic errors.

A2.1. Random error

The random error is the standard deviation from the multiple replicates of the reading. For example, temperature (T) readings taken from a thermocouple were averaged into,

Mean temperature, $\overline{T} = \dfrac{1}{n}\sum\limits_{i=1}^{n} T_i$

Hence the random error, $\varepsilon_R = \sqrt{\dfrac{1}{n}\sum\limits_{i=1}^{n}\left(T_i - \overline{T}\right)^2}$

Where: n = number of replicates.

A2.2. Systematic error

Systematic errors occur due to the design of the experimental equipment. These errors shift the experimental readings away from their true values. The error values were in most cases provided by the equipment manufacturers. It can also be considered as ± half the scale resolution.

A2.3. A numerical example

Any measured variable such as temperature, T, was quoted as a mean value, T̄, plus or minus the combined error. For example, a thermocouple reading yielded,

Mean temperature, $\overline{T}$ = 58.60 °C.

Systematic error, E_S = 0.40 °C (from the uncertainty of the thermocouple, 0.75% of reading).

Random error, E_R = 1.92 °C (from standard deviation, derived from four replicates).

Therefore, combined error, E_T = √(0.40² + 1.92²) = 1.96 °C.

In percentage error terms (also known as the relative error),

$$\frac{\delta T}{\overline{T}} = \frac{E_T}{\overline{T}} = \frac{1.96\ ^\circ\text{C}}{58.60\ ^\circ\text{C}}\ x\ 100\% = 3.35\%$$

In quotation terms,

58.60 ± 1.96 °C (quoted as "mean ± standard deviation or *s.d.*").

In the previous example, the random error was larger in magnitude than the systematic error. This was representative of most of the cases.

A2.4. Error propagation

The discussion of error analysis for a measured variable was presented above (**A2.1 - 3**). Most equations used in the thesis involved multiple variables e.g. a, b, c, d, … with uncertainties of δa, δb, δc, δd, … Supposed a quantity, Q, was a function of a, b, c, and d, the uncertainty of Q was therefore the propagation of δa, δb, δc, and δd. The rules are given as follows:

1. For addition and/or subtraction,

$$Q = a + b + c - x - y - z$$

Then,

$$\delta Q = \sqrt{(\delta a)^2 + (\delta b)^2 + (\delta c)^2 + (\delta x)^2 + (\delta y)^2 + (\delta z)^2}$$

2. For multiplication and/or division,

$$Q = \frac{abc}{xyz}$$

Then,

$$\frac{\delta Q}{Q} = \sqrt{\left(\frac{\delta a}{a}\right)^2 + \left(\frac{\delta b}{b}\right)^2 + \left(\frac{\delta c}{c}\right)^2 + \left(\frac{\delta x}{x}\right)^2 + \left(\frac{\delta y}{y}\right)^2 + \left(\frac{\delta z}{z}\right)^2}$$

For the complete rules (e.g. for power, $Q = x^n$) and further reading, readers can refer to this online document,

Harvard University, *A summary of error propagation*, 2007, retrieved from, http://ipl.physics.harvard.edu/wp-uploads/2013/03/PS3_Error_Propagation_sp13.pdf. Accessed 21 October 2015.

A3 Equipment serial numbers and device settings

Here the list of all experimental equipment serial numbers and device settings are given for reference. All equipment are located / stored in Chemical Engineering and Advanced Materials' Process Intensification labs C18 and C13.

Equipment	Manufacturer	Serial number*	Device setting*
Foam sample	Thermacore	-	-
Vacuum oven	Gallenkamp	UNEW* serial: 1349	Vacuum, heating setting 56°C
Heater circulator	Haake analogue C10, 5L, 25-100°C, 0.01-0.04°C temp. stability	UNEW* serial: 121	Flow fixed at 12.5 L/min Flow temp. 50-60°C
Rotameter (variable area flowmeter) (x2)	Blue White Industries F440	1306	Outlet flow 4L/min
Computer	Windows PC	UNEW* serial: PC62000-1024	-
Data logger (x2) 8 channels each	PicoLog TC-08	A0001/756 and /827	-
Thermocouple (x16) TC01-TC16	TC Direct, mineral insulated, Type K, 1.5mm diameter, 1500mm long, pot seal, 1 metre lead	No serial numbers available, only "IEC-KXZ" etched on each wire lead.	-
Voltage controller	Digimess DC Power Supply HY3003	221703	Range was 0 – 12V
Hot wire anemometer	Testo 405	0560-4053	Range was -20 to 50°C
Pitot-static probe	Testo 512	AE060104/502	Range 0 – 2 hPa

* Should this be blank; this means that the serial number / device setting was not available and /or applicable.

* Some of the serial numbers are "UNEW" i.e. the numbers are University-based catalogue, not manufacturers'.

A4 Ice-water bath tests

Section 4.3.5.1 already discussed about the thermocouples involved - Type K, and the temperature cut-offs, or conditions that could render them to provide erroneous readings. Based on the BSi (British Standard) document (BS 1041: Part 4), junction drift was expected not to occur under the experimental conditions in this project (ambient - 60°C, short term usage). However, an ice-water bath test was carried out after experimentation to check their accuracy (against a known reference temperature; 0°C) as well as to assess any drift that could occur.

The procedure for the ice-water bath test followed the guidance in section 7.6 of the aforementioned BSi document [139]:

- For most thermocouples, crushed tap water-ice bath is quite suitable.
- The junctions are inserted in a glass tube into the melting crushed-ice contained in a wide mouth vacuum flask – in our case, it was carried out in a Styrofoam container to provide adequate insulation.
- A depth of immersion of about 15cm would be appropriate.
- Avoid to carry out the test with fresh ice, as more subtle is the error caused by the use of fresh ice, which may be initially be at a temperature considerably below 0°C.
- The ice should be wet but not swimming (Figure A3 below).
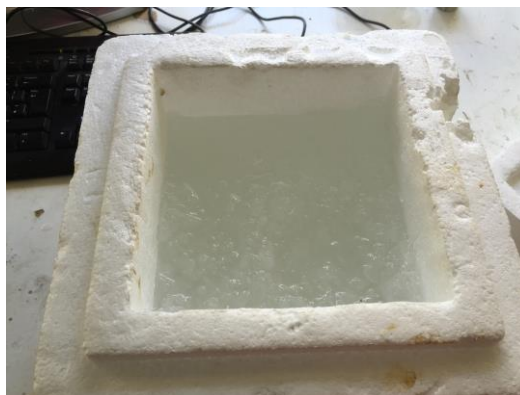
Figure A3 The ice-water bath condition for the tests.

Odd thermocouple numbers were tested i.e. TC01, 03, 05, 07, 09, 11, 13, 15. They were tested as a "unit" i.e. the metal sheated-junction, the cable, the data logger, and the computer as a connected unit.

The results were tabulated in the following table. Assuming the melting ice temperature to be 0.00°C, the temperature readings indicated a range of 0.50 – 1.10°C. The results were considered excellent considering the thermocouples have been stored for approximately 12 months after the experimentations ended.

TC no.	Temperature Reading (°C)				
	Test 1	Test 2	Test 3	Average	Standard Deviation
01	1.1	1.0	1.0	1.03	0.047
03	1.1	1.1	1.1	1.10	0.000
05	1.0	0.9	0.9	0.93	0.047
07	1.1	0.9	0.7	0.90	0.163
09	0.5	0.5	0.5	0.50	0.000
11	0.78	0.76	0.73	0.76	0.021
13	0.86	0.89	0.84	0.86	0.021
15	0.8	0.9	0.8	0.82	0.054

A5 MSDS for PCM salt hydrate S46

The following is the material safety datasheet (MSDS) for the phase change material salt hydrate S46 used in the Thesis.

Section 1: Identification of the substance/mixture and of the company/undertaking

1.1. Product identifier

Product name: PLUSICE S46

1.2. Relevant identified uses of the substance or mixture and uses advised against

1.3. Details of the supplier of the safety data sheet

Company name: Phase Change Material Products Ltd

Unit 32

Mere View Industrial Estate

Yaxley

Cambridgeshire

PE7 3HS

United Kingdom

Tel: +44 (0) 1733 245511

Fax: +44 (0) 1733 243344

Email: info@pcmproducts.net

1.4. Emergency telephone number

Section 2: Hazards identification

2.1. Classification of the substance or mixture

Classification under CHIP: This product has no classification under CHIP.

Classification under CLP: This product has no classification under CLP.

2.2. Label elements

Label elements under CHIP:

Hazard symbols: No significant hazard.

2.3. Other hazards

PBT: This substance is not identified as a PBT substance.

Section 3: Composition/information on ingredients

3.2. Mixtures

Hazardous ingredients:

SEPIOLITE

EINECS	CAS	CHIP Classification	CLP Classification	Percent
-	63800-37-3	Substance with a Community workplace exposure limit.	-	1-10%

[cont...]

FUMED SILICA

-	112945-52-5	Substance with a Community workplace exposure limit.	-	1-10%

Section 4: First aid measures

4.1. Description of first aid measures

Skin contact: Wash immediately with plenty of soap and water.

Eye contact: Bathe the eye with running water for 15 minutes.

Ingestion: Wash out mouth with water.

Inhalation: Consult a doctor.

4.2. Most important symptoms and effects, both acute and delayed

Skin contact: There may be mild irritation at the site of contact.

Eye contact: There may be irritation and redness.

Ingestion: There may be irritation of the throat.

Inhalation: There may be irritation of the throat with a feeling of tightness in the chest.

4.3. Indication of any immediate medical attention and special treatment needed

Immediate / special treatment: Not applicable.

Section 5: Fire-fighting measures

5.1. Extinguishing media

Extinguishing media: Suitable extinguishing media for the surrounding fire should be used.

5.2. Special hazards arising from the substance or mixture

Exposure hazards: In combustion emits toxic fumes.

5.3. Advice for fire-fighters

Advice for fire-fighters: Wear self-contained breathing apparatus. Wear protective clothing to prevent contact with skin and eyes.

Section 6: Accidental release measures

6.1. Personal precautions, protective equipment and emergency procedures

Personal precautions: Refer to section 8 of SDS for personal protection details.

6.2. Environmental precautions

Environmental precautions: Do not discharge into drains or rivers.

6.3. Methods and material for containment and cleaning up

Clean-up procedures: Wash the spillage site with large amounts of water.

6.4. Reference to other sections

Reference to other sections: Refer to section 8 of SDS.

Section 7: Handling and storage

7.1. Precautions for safe handling

Handling requirements: Avoid the formation or spread of dust in the air.

7.2. Conditions for safe storage, including any incompatibilities

Storage conditions: Store in cool, well ventilated area.

7.3. Specific end use(s)

Specific end use(s): No data available.

Section 8: Exposure controls/personal protection

8.1. Control parameters

Hazardous ingredients:

SEPIOLITE

Workplace exposure limits: — Respirable dust

State	8 hour TWA	15 min. STEL	8 hour TWA	15 min. STEL
EU	15 mg/m3	-	-	-

FUMED SILICA

UK	-	-	2.4 mg/m3	-

8.2. Exposure controls

Respiratory protection: Respiratory protective device with particle filter.

Hand protection: Protective gloves.

Eye protection: Safety glasses. Ensure eye bath is to hand.

Skin protection: Protective clothing.

Section 9: Physical and chemical properties

9.1. Information on basic physical and chemical properties

State: Solid

Colour: Pale brown

Odour: Characteristic odour

Solubility in water: Soluble

Boiling point/range°C: 100

Melting point/range°C: 46

Flash point°C: n/a

Autoflammability°C: n/a

Relative density: approx 1.6

pH: approx 7

9.2. Other information

Other information: Not applicable.

Section 10: Stability and reactivity

10.1. Reactivity

Reactivity: Stable under recommended transport or storage conditions.

[cont...]

10.2. Chemical stability

Chemical stability: Stable under normal conditions.

10.3. Possibility of hazardous reactions

Hazardous reactions: Hazardous reactions will not occur under normal transport or storage conditions.

Decomposition may occur on exposure to conditions or materials listed below.

10.4. Conditions to avoid

Conditions to avoid: Heat.

10.5. Incompatible materials

Materials to avoid: Strong oxidising agents. Strong acids.

10.6. Hazardous decomposition products

Haz. decomp. products: In combustion emits toxic fumes.

Section 11: Toxicological information

11.1. Information on toxicological effects

Toxicity values: Not applicable.

Symptoms / routes of exposure

Skin contact: There may be mild irritation at the site of contact.

Eye contact: There may be irritation and redness.

Ingestion: There may be irritation of the throat.

Inhalation: There may be irritation of the throat with a feeling of tightness in the chest.

Section 12: Ecological information

12.1. Toxicity

Ecotoxicity values: Not applicable.

12.2. Persistence and degradability

Persistence and degradability: Biodegradable.

12.3. Bioaccumulative potential

Bioaccumulative potential: No bioaccumulation potential.

12.4. Mobility in soil

12.5. Results of PBT and vPvB assessment

PBT identification: This substance is not identified as a PBT substance.

12.6. Other adverse effects

Other adverse effects: Negligible ecotoxicity.

Section 13: Disposal considerations

13.1. Waste treatment methods

NB: The user's attention is drawn to the possible existence of regional or national regulations regarding disposal.

[cont...]

Section 14: Transport information

Transport class: This product does not require a classification for transport.

Section 15: Regulatory information

15.1. Safety, health and environmental regulations/legislation specific for the substance or mixture

15.2. Chemical Safety Assessment

Chemical safety assessment: A chemical safety assessment has not been carried out for the substance or the mixture by the supplier.

Section 16: Other information

Other information

Other information: This safety data sheet is prepared in accordance with Commission Regulation (EU) No 453/2010.

* indicates text in the SDS which has changed since the last revision.

Legal disclaimer: The above information is believed to be correct but does not purport to be all inclusive and shall be used only as a guide. This company shall not be held liable for any damage resulting from handling or from contact with the above product.

[final page]

END